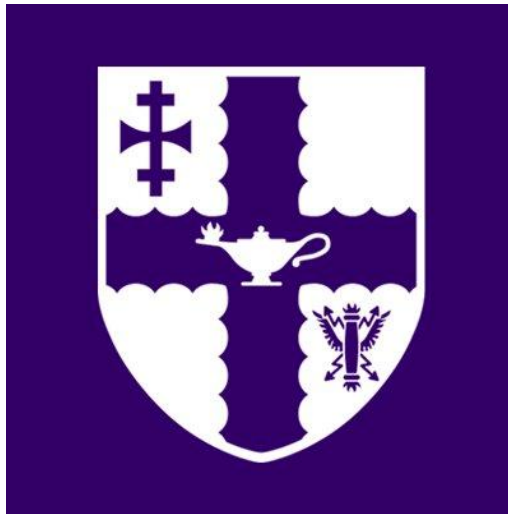


# **Development of superconducting thin films for use in SRF cavity applications.**

by

**Stuart Wilde**



**Doctoral Thesis**

**Submitted in accordance with the requirements for the award of  
Doctor of Philosophy of Loughborough University**

**December 2017**

**©Stuart Wilde 2017**



## Acknowledgements

I would like to express thanks to my three supervisors, Reza Valizadeh, Oleg Malyshev and Boris Chesca, for all of their support during my research. I feel I have been very fortunate to have had their guidance. I am grateful for the support from all the staff at ASTeC including Adrian Hannah, Mark Pendleton, Shrikant Pattalwar, Ninad Pattalwar, Keith Middleman, James Conlon and Joe Herbert. Particular thanks goes to Neil Pashley for all the technical advice and help with lifting heavy things! Thanks goes to Gavin Stenning for his continued support and arranging for me to access the facilities at the STFC ISIS laboratory. Similar thanks goes to Vladimir Vishnyakov for his advice, training and support. I would like to thank all of the other students from the ASTeC Vacuum Group, Paolo Pizzol, Sonal Mistry, Taaj Sian, Ruta Sirvinskaite, Nathan Lewis, Lewis Gurran and Sihui Wang, for their all of their support and for listening to me complain so much about everything. Finally, I would like to thank my parents and Nat. Don't think I could have done it without you all.



## Abstract

Superconducting thin films are a possible alternative to bulk niobium for superconducting radio frequency cavity applications. Thin film cavities have produced larger  $Q_0$  than bulk niobium at low accelerating voltages [1], are less susceptible to external magnetic fields and therefore require less magnetic shielding than bulk niobium cavities [2] and can benefit from substrates which conduct heat more effectively than bulk niobium [3]. The major drawback for current thin film cavity technology is the large  $Q$  slope which is observed above accelerating gradients of 6 – 7 MV/m. The mechanism for the  $Q$  slope is not yet fully understood. Theories have been suggested but are not accepted by everyone within the scientific community [2, 4, 5, 6, 7]. It is assumed that a better understanding of the physical properties of superconducting films is required before the origins of the sharp  $Q$  slope can be elucidated.

This study has been conducted to better understand the physical properties of superconducting thin films deposited by the magnetron sputtering process. In particular, superconducting niobium films have been deposited by high power impulse magnetron sputtering (HiPIMS) and tested by a wide range of analytical techniques as a function of the substrate temperature and applied bias during deposition. Analytical techniques which have been used include x-ray diffraction crystallography, Rutherford backscattering spectroscopy, scanning electron microscopy, residual resistance ratio, DC magnetometry and RF surface resistance measurements.

Results showed that the application of an applied bias during deposition resulted in increased energy of bombarding ions and enhanced rates of surface diffusion and defect annihilation within the microstructure of a growing niobium film. However, large numbers of random complex defects formed once the energy of bombarding ions becomes too large. The systematic approach that was described to investigate the changing morphological and DC superconducting properties of deposited films, as a function of the applied bias, allowed the identification of which process conditions produce the fewest random complex defects. The same systematic investigations could be applied to any HiPIMS deposition facility to provide similar results.

An important observation during the study is that the initial substrate conditions have a large influence on the properties of a deposited niobium film. Niobium films deposited onto polycrystalline copper substrate that was pre-annealed at 700 °C prior to deposition displayed more stable magnetic flux pinning, larger RRR and an enhanced resistance to the onset of flux penetration, than was observed for films deposited with a wide range of process conditions onto as received copper substrate.

Superconductors other than niobium have been successfully deposited by HiPIMS and tested. Niobium titanium nitride thin films displayed a superconducting transition temperature up to 16.7 K, with a normal state resistivity as small as  $45 \pm 7 \mu\Omega\text{cm}$ . The findings suggest that similar niobium titanium nitride thin films could produce smaller RF surface resistance than bulk niobium cavities at 4.2 K.



# Table of contents

List of Figures .....	xii
List of Tables .....	xxi
Symbols and Abbreviations.....	xxiii
1. Background .....	1
2. Superconducting Radio Frequency Cavities.....	5
2.1. Basics of superconductivity.....	5
2.2. Types of superconductor .....	7
2.3. Critical magnetic fields.....	7
2.4. Critical Current.....	8
2.5. RF Superconductivity .....	9
2.6. SRF Accelerating Cavities and the Quality Factor .....	10
3. Deposition Process.....	13
3.1. Magnetron Sputtering .....	13
3.2. Substrate Preparation.....	16
3.3. Thin Film Growth Mechanisms .....	17
3.4. Film Growth Parameters.....	19
3.5. Supplying energy to the growing film .....	22
4. State of the art superconducting thin film research.....	24
4.1. Benefits of thin film SRF cavities.....	24
4.2. The effects of substrate choice and substrate heating on deposited niobium thin films ....	24
4.3. Niobium thin film cavities deposited by conventional low ion to neutral ratio sputtering techniques.....	26
4.4. Niobium thin films deposited by energetic condensation methods .....	31
4.5. Deposition of superconducting films other than niobium.....	35
4.6. Superconductor – insulator – superconductor multilayer films.....	37

4.7.	The origins of the thin film Q slope.....	39
5.	Analytical techniques .....	43
5.1.	Morphological Analysis.....	43
5.1.1.	X-ray diffraction crystallography.....	43
5.1.2.	Scanning electron microscopy and electron backscattering diffraction.....	45
5.1.3.	X-ray photoelectron spectroscopy.....	46
5.1.4.	Energy-dispersive x-ray spectroscopy.....	47
5.1.5.	Rutherford backscattering spectrometry .....	47
5.2.	Superconducting performance .....	48
5.2.1.	Four-point probe.....	48
5.2.2.	DC magnetometer measurements.....	50
6.	Experimental Setup.....	54
6.1.	Deposition System .....	54
6.2.	Cryostat and four-point probe.....	60
7.	Deposition of Niobium Thin Films.....	66
7.1.	Niobium films deposited by DC magnetron sputtering .....	66
7.2.	Niobium films deposited by HiPIMS .....	77
7.2.1.	Testing the effects of the substrate choice.....	77
7.2.2.	Testing the effects of substrate heating and an applied DC substrate bias when depositing onto as received polycrystalline copper substrate .....	84
7.2.3.	Testing the effects of substrate heating and an applied DC substrate bias when depositing onto pre-annealed copper substrate .....	140
7.2.4.	Comparison of the DC magnetic properties of thin film and bulk niobium.....	163
7.2.5.	RF surface resistance measurements of niobium thin films deposited by HiPIMS onto as received polycrystalline copper .....	168
8.	Superconducting materials other than niobium.....	173
8.1.	Niobium Nitride thin films .....	173
8.1.1.	Deposition of niobium nitride thin films.....	173

8.1.2.	Analysis of deposited niobium nitride thin films .....	173
8.2.	Niobium Titanium Nitride thin films .....	178
8.2.1.	Varying nitrogen partial pressure .....	178
8.2.2.	Varying the niobium or titanium cathode current.....	183
9.	Summary and future research .....	189
	List of Publications .....	192
10.	References .....	194



## List of Figures

Figure 2.1.	Depiction of a superconductor expelling an applied magnetic field. The magnetic field penetrates the superconductor when its temperature is above $T_c$ . The magnetic field is expelled from the bulk of the superconductor when the temperature is below $T_c$ .....	6
Figure 2.2.	Magnetisation against applied field for type I and II superconductors. The superheating field is shown only for a type II superconductor however it can also occur for type I superconductors. ....	8
Figure 2.3.	The relative motion of fluxoids, $v$ , within a superconducting thin film.....	9
Figure 2.4.	Schematic view of a pillbox shape accelerating cavity operating with the $TM_{010}$ RF mode. Magnetic fields are shown in red and are strongest at the cavity walls. The electric field is shown in black and is strongest on the beam axis.....	10
Figure 3.1.	Schematic view of a planar magnetron. $Kr^+$ are positive krypton ions and $T$ and $T^+$ are target atoms and ions respectively. Dashed lines denote the magnetic field lines which form an electron trap. $N$ and $S$ are the north and south poles of permanent magnets housed underneath the target. ....	13
Figure 3.2.	Peak power of HiPIMS pulses are two orders of magnitude higher than that of DC sputtering. Black lines are plasma current and red lines are the bias voltage supplied to the target cathode. ....	15
Figure 3.3.	Schematic representation of an adatom, ledge, kink and vacancy.....	18
Figure 3.4.	Tilt and twist boundaries between two different crystals A and B [39] (reproduced with permission from Springer). ....	18
Figure 3.5.	A Monte Carlo simulation of the formation of a screw dislocation [40] (reproduced with permission from John Wiley & Sons, Inc.).....	19
Figure 3.6.	Structure zone diagram for energetic condensation processes. Axis labels are the generalised temperature, $T^*$ , the normalised energy flux, $E^*$ , and the net thickness, $t^*$ [42] (reproduced with permission from Elsevier). ....	20
Figure 4.1.	Cross sectional SEM images of niobium films which have had a section removed using a FIB. The left image shows a niobium film deposited onto an oxidised copper surface. The right image shows a niobium film deposited onto a copper surface which has had the native oxide layer removed [51] (CC BY 3.0). ....	25
Figure 4.2.	Lattice parameter of niobium films measured either on the copper substrate or after the substrate was etched away. The lattice parameter of a bulk niobium sample is shown for comparison [63] (CC BY 3.0). ....	27
Figure 4.3.	The setup for depositing single cell cavities by DC magnetron sputtering at CERN [2] (reproduced with permission from Elsevier). ....	28
Figure 4.4.	The dependence of $R_{BCS}$ on the mean free path $l$ at 4.2 K. $\xi_0$ was assumed to be 33 nm. The solid line was the result of a theoretical calculation of $R_{BCS}$ [2] (reproduced with permission from Elsevier). ....	29
Figure 4.5.	FIB cross sections of witness samples deposited by DC bias diode onto different locations of a HI-SOLDE test cavity [67]. The upper film shows a densely packed grain structure whereas the lower image shows voids between grains. Both images were taken from different locations of the same deposited cavity (CC BY 3.0). ....	30
Figure 4.6.	Average ion energies in eV over time following the initiation of a HiPIMS pulse [73] (©2011 IEEE). ....	31
Figure 5.1.	Penetration depth of x-rays into a niobium thin film versus the grazing angle $\Phi$ . ....	44
Figure 5.2.	Typical experimental setup for RBS [113] (©IAEA 2000). ....	47

Figure 5.3.	Schematic diagram of the four-point probe setup. ....	48
Figure 5.4.	Representation of the three definitions of $T_c$ ; $T_c^0$ , $T_c^{ex}$ and $T_c^{on}$ . ....	49
Figure 5.5.	Schematic view of the physical principle of how a SQUID magnetometer works. ....	51
Figure 6.1.	Schematic view of the experimental deposition system.....	56
Figure 6.2.	Photograph of the entire deposition facility.....	56
Figure 6.3.	Schematic drawing produced during the design stage of the sample cartridge system.....	59
Figure 6.4.	The entire load lock chamber is shown in the left hand image and the 7 sample cartridge system is shown in the right image.....	60
Figure 6.5.	Different substrates placed onto a 100 mm copper disk. Shown are silicon, magnesium oxide and polycrystalline copper.....	60
Figure 6.6.	Temperature profile of the substrate when read from the thermocouple at the heater..	61
Figure 6.7.	The left hand image shows a schematic drawing of the cryostat which houses the four-point probe and the right hand image shows a photograph of the cryostat.....	62
Figure 6.8.	Schematic representation of the four-point probe sample holder.....	63
Figure 6.9.	Photographs of a) the four-point probe and b) the sample stick (insert).....	64
Figure 6.10.	Example of a resistance versus temperature curve including $R_{TC}$ and $T_{TC}$ . ....	65
Figure 7.1.	The current-voltage-power characteristics of the DC power supply for a krypton pressure of $7 \times 10^{-3}$ mbar.....	66
Figure 7.2.	Secondary electron SEM images of niobium thin films. Beam energy was set to 8 kV with beam diameter of 4 nm. Each niobium film was deposited by DC magnetron sputtering onto Si (100) substrate at varying powers and with either grounded or a substrate bias of -50 V. a) grounded 100 W, b) 100 W with -50 V substrate bias, c) grounded 200 W, d) 200 W with -50 V bias and e) 300 W with -50 V bias. ....	68
Figure 7.3.	Secondary electron SEM images of niobium thin films. Beam energy was set to 8 kV with beam diameter of 4 nm. Each niobium film was deposited by DC magnetron sputtering onto Si (100) substrate at varying powers and with either grounded or a substrate bias of -50 V. a) grounded 400 W, b) 400 W with -50 V substrate bias, c) grounded 500 W, d) 500 W with -50 V bias, e) grounded 600 W and f) 600 W with -50 V bias. ....	69
Figure 7.4.	The growth rate versus power supplied to the magnetron for niobium thin films deposited by DC magnetron sputtering onto a grounded substrate. ....	70
Figure 7.5.	Grazing incidence XRD measurements of films deposited by DC magnetron sputtering at room temperature on either a) a grounded substrate or b) a substrate bias of -50 V. ....	70
Figure 7.6.	Lattice constant versus power supplied to the magnetron for niobium thin films deposited by DC magnetron sputtering with either a grounded substrate or a substrate biased at -50 V. ....	72
Figure 7.7.	Average grain size versus power supplied to the magnetron for niobium thin films deposited by DC magnetron sputtering with either a grounded substrate or a substrate biased at -50 V. ....	72
Figure 7.8.	Electron backscatter diffraction image of a thin film deposited by DC magnetron sputtering at 600 W onto grounded silicon (100) substrate (measurement courtesy of V. Vishnyakov, MMU). ....	73
Figure 7.9.	XPS spectrum of a niobium thin film (green) deposited at room temperature by DC magnetron sputtering at 600 W onto grounded silicon (100) substrate. A bulk niobium sample (red) is also shown for comparison (measurement courtesy of S. Mistry, STFC). ....	73

Figure 7.10.	<i>RRR against DC power supplied to the magnetron for films deposited with either a grounded substrate or biased at -50 V.</i>	74
Figure 7.11.	<i>The normal state resistivity measured just above <math>T_c</math> against power for niobium films deposited by DC magnetron sputtering onto grounded substrate.</i>	75
Figure 7.12.	<i>XRD peaks of niobium thin films which correspond to the (110) grain orientation.</i>	78
Figure 7.13.	<i>DC Hysteresis curves for film A as deposited onto copper and silicon.</i>	80
Figure 7.14.	<i>DC Hysteresis curves for film B as deposited onto copper and silicon.</i>	81
Figure 7.15.	<i>DC Hysteresis curves for film B as deposited onto copper and silicon.</i>	82
Figure 7.16.	<i>Optical emission spectrums of: upper image, a DC magnetron sputtering process and lower, a HiPIMS process.</i>	85
Figure 7.17.	<i>RGA spectrum before process gas injection. Pressure against mass to charge ratio is shown.</i>	86
Figure 7.18.	<i>RGA spectrum of the process gas at a total pressure of <math>7 \times 10^{-7}</math> bar. Pressure against mass to charge ratio is shown.</i>	86
Figure 7.19.	<i>Rutherford backscattering spectrometry data for sample deposited at a) room temperature with an applied bias of -120 V and b) 700 °C with an applied bias of -120 V (measurement performed by E. Alves and N.P. Barradas, Lisbon, Portugal).</i>	87
Figure 7.20.	<i>Grazing incidence XRD data for samples deposited onto as received substrate at room temperature. Data is shown from a) 40 to 130 ° measured on copper, b) the (110) peak at approximately 44 - 46° measured on copper, c) 40 to 130 ° measured after the copper substrate was etched away and d) the (110) peak at approximately 44 - 46° measured after the copper substrate was etched away.</i>	90
Figure 7.21.	<i>Grazing incidence XRD data for samples deposited onto as received substrate at 500 °C. Data is shown from a) 40 to 130 ° measured on copper, b) the (110) peak at approximately 44 - 46° measured on copper, c) 40 to 130 ° measured after the copper substrate was etched away and d) the (110) peak at approximately 44 - 46° measured after the copper substrate was etched away.</i>	91
Figure 7.22.	<i>Grazing incidence XRD data for samples deposited onto as received substrate at 700 °C. Data is shown from a) 40 to 130 ° measured on copper, b) the (110) peak at approximately 44 - 46° measured on copper, c) 40 to 130 ° measured after the copper substrate was etched away and d) the (110) peak at approximately 44 - 46° measured after the copper substrate was etched away.</i>	92
Figure 7.23.	<i>Grazing incidence XRD data for samples deposited onto as received substrate at 800 °C. Data is shown from a) 40 to 130 ° measured on copper, b) the (110) peak at approximately 44 - 46° measured on copper, c) 40 to 130 ° measured after the copper substrate was etched away and d) the (110) peak at approximately 44 - 46° measured after the copper substrate was etched away.</i>	93
Figure 7.24.	<i>Lattice parameters <math>a_0</math> of niobium thin films a) after having the copper substrate etched away and b) with the copper substrate still in place.</i>	94
Figure 7.25.	<i>Average grain size against applied bias voltage during deposition of niobium thin films measured after the substrate was etched away.</i>	95
Figure 7.26.	<i>Average grain size against applied bias voltage during deposition of niobium thin films as measured on polycrystalline copper substrate.</i>	95
Figure 7.27.	<i>Planar SEM images of niobium thin film samples deposited a) at room temperature and no bias, b) at room temperature with -80 V bias, c) at 500 °C with no bias, d) at 500 °C and -80 V bias, e) at</i>	

	700 °C with no bias, f) at 700 °C with -80 V bias, g) at 800 °C with no bias and h) at 800 °C with -80 V bias. ....	97
Figure 7.28.	The surface contour map of an uncoated polycrystalline copper substrate. ....	98
Figure 7.29.	Contour map of the surface of niobium thin films deposited onto polycrystalline copper substrate at room temperature and with a bias voltage ranging from 0 to -120 V DC. ....	99
Figure 7.30.	Contour map of the surface of niobium thin films deposited onto polycrystalline copper substrate at 500 °C and with a bias voltage ranging from 0 to -120 V DC. ....	99
Figure 7.31.	Secondary electron detector SEM images of the films deposited at a) room temperature with an applied bias of -80 V and b) 500 °C with applied bias of -80 V. The surface topography of the sample deposited at room temperature matches that of the underlying copper substrate whilst a “blistered” surface is seen for the film deposited at 500 °C. ....	100
Figure 7.32.	Contour map of the surface of niobium thin films deposited onto polycrystalline copper substrate at 700 °C and with a bias voltage ranging from 0 to -120 V DC. ....	100
Figure 7.33.	Contour map of the surface of niobium thin films deposited onto polycrystalline copper substrate at 800 °C and with a bias voltage ranging from 0 to -120 V DC. ....	101
Figure 7.34.	Secondary electron detector SEM image of the films deposited at 700 °C with applied bias of -120 V. The surface displays larger and more frequent “blisters” at the surface than was observed for any other film. ....	102
Figure 7.35.	SEM cross section of a niobium thin film deposited at 700 °C with -100 V bias. a) displays 3500 X magnification and b) 35000 X magnification. ....	102
Figure 7.36.	SEM cross section of a niobium thin film deposited at 800 °C with -80 V bias. a) displays 10000 X magnification and b) 50000 X magnification. ....	102
Figure 7.37.	a) Resistance versus temperature from 0 to 100 K and b) RRR versus temperature for niobium films deposited onto as received polycrystalline copper substrate at room temperature with bias voltages ranging from 0 to -120 V. ....	104
Figure 7.38.	a) Resistance versus temperature from 0 to 100 K and b) resistance versus temperature of the superconducting transition for niobium films deposited onto as received polycrystalline copper substrate at 500 °C with bias voltages ranging from 0 to -120 V. ....	105
Figure 7.39.	a) Resistance versus temperature from 0 to 100 K and b) resistance versus temperature of the superconducting transition for niobium films deposited onto as received polycrystalline copper substrate at 700 °C with bias voltages ranging from 0 to -120 V. ....	107
Figure 7.40.	a) Resistance versus temperature from 0 to 100 K and b) resistance versus temperature of the superconducting transition for niobium films deposited onto as received polycrystalline copper substrate at 800 °C with bias voltages ranging from 0 to -120 V. ....	108
Figure 7.41.	RRR values versus applied bias voltage for all films deposited onto as received polycrystalline copper substrate. ....	109
Figure 7.42.	$T_c$ versus applied bias voltage for all niobium films deposited onto as received copper substrate. ....	110
Figure 7.43.	DC magnetic moment versus applied magnetic field of niobium thin films versus. Films were deposited onto as received polycrystalline copper substrate at (a) room temperature, and (b) 500 °C. ....	112
Figure 7.44.	DC magnetic moment versus applied magnetic field of niobium thin films versus. Films were deposited onto as received polycrystalline copper substrate at (a) 700 °C, and (b) 800 °C. ....	112

Figure 7.45.	An example of a) the raw DC magnetisation data from a measurement of a niobium thin film deposited at 700 °C with -80 V applied bias. The dashed lines denote either $H_{dev}$ , $H(M_{max})$ or $H_{C2}$ and b) the RMSE against applied field for the same measurement. ....	114
Figure 7.46.	$H_{dev}$ (as defined in Fig. 7.46) versus applied bias voltage. ....	116
Figure 7.47.	$H_{C2}$ versus applied bias voltage for each film deposited onto as received polycrystalline copper substrate. ....	117
Figure 7.48.	The maximum recorded magnetisation $H(M_{max})$ versus applied bias voltage for each film deposited onto as received polycrystalline copper substrate. ....	117
Figure 7.49.	The normalised DC magnetic moment versus applied magnetic field for samples deposited at room temperature with a DC substrate bias of 0 to – 120 V. ....	118
Figure 7.50.	The normalised DC magnetic moment versus applied magnetic field for samples deposited at 500 °C with a DC substrate bias of 0 to – 120 V. ....	119
Figure 7.51.	The normalised DC magnetic moment versus applied magnetic field for samples deposited at 700 °C with a DC substrate bias of 0 to – 120 V. ....	120
Figure 7.52.	The normalised DC magnetic moment versus applied magnetic field for samples deposited at 800 °C with a DC substrate bias of 0 to – 120 V. ....	120
Figure 7.53.	Compilation of the measured $M/M_i$ versus applied bias voltage $-V_B(V)$ for every sample at magnetic fields of 300, 600, 1000 and 1800 Oe. ....	122
Figure 7.54.	DC magnetisation data for two films deposited using the same deposition process. Measurement labelled 1 piece was deposited for 8 hours and contained only one piece of film whilst the measurement labelled 3 pieces was deposited for 4 hours and contained 3 overlapped pieces of the same film. ....	123
Figure 7.55.	Comparison of $M/M_i$ versus applied magnetic field for both 1 piece and 3 pieces of niobium film deposited with similar process conditions. ....	124
Figure 7.56.	Comparison of the DC magnetic moment versus applied magnetic field of a film with copper substrate still in place and after the substrate has been removed by etching. ....	125
Figure 7.57.	Comparison of the $M/M_i$ versus applied magnetic field of a film with copper substrate still in place and after the substrate has been removed by etching. ....	126
Figure 7.58.	Repeated $M/M_i$ versus applied magnetic field measurements of niobium thin film samples deposited at 500 °C with -100 V DC bias. Film was cut from different parts of the sample for each measurement. Small differences are seen in each measurement of the order of the magnitude of the flux jumps. ....	127
Figure 7.59.	Repeated $M/M_i$ versus applied magnetic field measurements of niobium thin film samples deposited at 500 °C with -120 V DC bias. Film was cut from different parts of the sample for each measurement. Small differences are seen in each measurement of the order of the magnitude of the flux jumps. ....	127
Figure 7.60.	Repeated $M/M_i$ versus applied magnetic field measurement of niobium thin film samples deposited at 700 °C with -50 V DC bias. Film was cut from different parts of the sample for each measurement. Large differences are seen in each measurement of the order of the magnitude of the flux jumps. ....	128
Figure 7.61.	Repeated $M/M_i$ versus applied magnetic field measurement of niobium thin film samples deposited at 800 °C with -120 V DC bias. Film was cut from different parts of the sample for each measurement. Large differences are seen in each measurement of the order of the magnitude of the flux jumps. ....	128

Figure 7.62.	SEM and EDX data of copper dust found at the surface of some niobium thin films after cutting with the circular saw. The copper dust produced small GI-XRD peaks for the measured spectra. ....	132
Figure 7.63.	Schematic representation of magnetic field lines for (a) superconducting sample parallel to the applied magnetic field lines and (b) superconducting sample inclined with angle $\alpha$ . ....	137
Figure 7.64.	Grazing incidence XRD data for samples deposited onto pre-annealed substrate at room temperature and 500 °C. Data is shown in a) 40 to 130 ° measured on copper for films deposited at room temperature, b) the (110) peak at approximately 44 - 46° measured on copper for films deposited at room temperature, c) 40 to 130 ° measured on copper for films deposited at 500 °C and d) the (110) peak at approximately 44 - 46° measured on copper for films deposited at 500 °C. ....	142
Figure 7.65.	Lattice parameter versus applied bias voltage of niobium films deposited onto either as received or pre-annealed polycrystalline copper substrate. ....	143
Figure 7.66.	Average grain size against applied bias during deposition of niobium thin films deposited onto pre-annealed copper substrate. ....	144
Figure 7.67.	SEM images of niobium thin film samples deposited at a) room temperature without bias onto as received substrate, b) room temperature without bias onto pre-annealed substrate, c) 500 °C without bias onto as received substrate and d) 500 °C without bias onto pre-annealed substrate. ....	145
Figure 7.68.	SEM images of niobium thin film samples deposited at a) room temperature with -80 V substrate bias onto as received substrate, b) room temperature with -80 V substrate bias onto pre-annealed substrate, c) 500 °C with -80 V substrate bias onto as received substrate and d) 500 °C with -80 V substrate bias onto pre-annealed substrate. ....	146
Figure 7.69.	SEM images of niobium thin film samples deposited at a) room temperature with -120 V substrate bias onto as received substrate, b) room temperature with -120 V substrate bias onto pre-annealed substrate, c) 500 °C with -120 V substrate bias onto as received substrate and d) 500 °C with -120 V substrate bias onto pre-annealed substrate. ....	147
Figure 7.70.	SEM images of niobium thin films samples deposited at a) room temperature with -80 V substrate bias onto as pre-annealed substrate, b) room temperature with -120 V substrate bias onto pre-annealed substrate, c) 500 °C with -80 V substrate bias onto as pre-annealed substrate and d) 500 °C with -120 V bias onto pre-annealed substrate. ....	148
Figure 7.71.	3D Optical microscope images of the surface of niobium thin films deposited by HiPIMS at room temperature with bias voltages of 0 to -120 V onto pre-annealed substrate. ....	149
Figure 7.72.	3D Optical microscope images of the surface of niobium thin films deposited by HiPIMS at 500 °C with bias voltages of 0 to -120 V onto pre-annealed substrate. ....	149
Figure 7.73.	a) Resistance versus temperature from 0 to 100 K and b) RRR versus temperature for niobium films deposited onto pre-annealed polycrystalline copper substrate at room temperature with bias voltages ranging from 0 to -120 V. ....	151
Figure 7.74.	a) Resistance versus temperature from 0 to 100 K and b) RRR versus temperature for niobium films deposited onto pre-annealed polycrystalline copper substrate at 500 °C with bias voltages ranging from 0 to -120 V. ....	152
Figure 7.75.	RRR versus applied bias voltage for niobium films deposited onto as received and pre-annealed polycrystalline copper substrate. ....	153
Figure 7.76.	DC magnetic moment versus applied magnetic field for niobium thin film samples which were deposited at a) room temperature and b) 500 °C onto copper substrate which had been pre-annealed at 700 °C for 12 hours. ....	154

Figure 7.77.	<i>H<sub>c2</sub> versus applied bias voltage for each deposited niobium thin film deposited onto either as received or pre-annealed copper substrate.....</i>	<i>155</i>
Figure 7.78.	<i>H<sub>dev.</sub> (as defined in figure 7.46) versus applied bias voltage for samples deposited at room temperature and 500 °C onto either as received copper substrate or pre-annealed copper substrate. ....</i>	<i>155</i>
Figure 7.79.	<i>M/M<sub>i</sub> versus applied magnetic field for niobium films deposited at room temperature onto copper substrate which was annealed at 700 °C prior to deposition.....</i>	<i>156</i>
Figure 7.80.	<i>M/M<sub>i</sub> versus applied magnetic field for niobium films deposited at 500 °C onto copper substrate which was annealed at 700 °C prior to deposition.....</i>	<i>157</i>
Figure 7.81.	<i>Compilation of the measured M/M<sub>i</sub> versus applied bias voltage for niobium thin films at magnetic fields of 300, 600, 1000 and 1800 Oe. The bias voltage of each sample is denoted as -V<sub>B</sub> (V). ...</i>	<i>158</i>
Figure 7.82.	<i>Resistance versus temperature for a niobium thin film deposited onto a-plane sapphire at 800 °C with -80 V DC bias. Sample displayed the smallest normal state resistance of any sample tested during the study at 0.0006 mΩ. ....</i>	<i>164</i>
Figure 7.83.	<i>DC magnetic moment versus applied magnetic field of a niobium film with RRR of 229 deposited onto a-plane sapphire. ....</i>	<i>165</i>
Figure 7.84.	<i>M/M<sub>i</sub> versus applied magnetic field of niobium thin films deposited onto both sapphire or copper substrate and a theoretical line for a bulk niobium sample. ....</i>	<i>166</i>
Figure 7.85.	<i>R<sub>s</sub> versus magnetic field strength of a flat thin film niobium sample which was deposited at 800 °C with a grounded substrate. R<sub>s</sub> of the host cavity and the predicted R<sub>B<sub>CS</sub></sub> of niobium at 1.6 K are also shown (measurement performed by J.T. Maniscalco, Cornell University). ....</i>	<i>169</i>
Figure 7.86.	<i>R<sub>s</sub> versus magnetic field strength of a flat thin film niobium sample which was deposited at 500 °C with -100 V substrate bias. R<sub>s</sub> of the host cavity and the predicted R<sub>B<sub>CS</sub></sub> of niobium at 1.6 K and 1.8 K are also shown (measurement performed by J.T. Maniscalco, Cornell University). ....</i>	<i>170</i>
Figure 7.87.	<i>Temperature map during RF surface resistance test of flat thin film niobium sample which was deposited at 500 °C with -100 V substrate bias (measurement performed by J.T. Maniscalco, Cornell University). ....</i>	<i>170</i>
Figure 8.1.	<i>Resistance versus temperature curves for niobium nitride thin films deposited with a range of nitrogen partial pressures. a) displays the curve between 0 and 100 K whilst b) displays the superconducting transition. ....</i>	<i>174</i>
Figure 8.2.	<i>The T<sub>c</sub> of niobium nitride thin films deposited with varying nitrogen partial pressure. ....</i>	<i>175</i>
Figure 8.3.	<i>XRD data for a niobium nitride thin film with the largest measured T<sub>c</sub> of 15.35±0.03 K. ....</i>	<i>176</i>
Figure 8.4.	<i>SEM image of a niobium nitride thin film with the largest measured T<sub>c</sub> of 15.35±0.03 K. ....</i>	<i>176</i>
Figure 8.5.	<i>Rutherford backscattering spectroscopy data showing the elemental composition of the niobium nitride film with the largest T<sub>c</sub>. Measurement was performed using a hydrogen beam with 10° angle of incidence, 165° scattering angle and 25° exit angle (measurement performed by E. Alves and N.P. Barradas, Lisbon, Portugal). ....</i>	<i>177</i>
Figure 8.6.	<i>Resistance versus temperature curves for niobium titanium nitride thin films deposited with a range of nitrogen partial pressures. a) displays the curve between 0 and 100 K whilst b) displays the superconducting transition. ....</i>	<i>179</i>
Figure 8.7.	<i>The T<sub>c</sub> of niobium titanium nitride thin films with varying nitrogen partial pressure during deposition.....</i>	<i>180</i>

Figure 8.8.	SEM image of a niobium titanium nitride thin film deposited with a niobium cathode current of 590 mA, a titanium cathode current of 960 mA and a nitrogen partial pressure of 20 %. $T_c$ of the sample was $16.67 \pm 0.01$ K. ....	180
Figure 8.9.	XRD data for niobium titanium nitride thin films deposited with a niobium cathode current of 590 mA, titanium cathode current of 960 mA and nitrogen partial pressure of either 14 or 20 %. ...	181
Figure 8.10.	Rutherford backscattering spectroscopy measurement of a niobium titanium nitride thin film deposited with a niobium cathode current of 590 mA, a titanium cathode current of 960 mA and a nitrogen partial pressure of 20 %. $T_c$ of the sample was $16.67 \pm 0.01$ K. RBS measurement was performed using a hydrogen beam with $10^\circ$ angle of incidence, $165^\circ$ scattering angle and $25^\circ$ exit angle. Inset is a summary of two RBS measurements displaying the nitrogen partial pressure, $N_2$ P%, $T_c$ , and at.% of niobium, titanium and nitrogen (measurement performed by E. Alves and N.P. Barradas, Lisbon, Portugal).....	182
Figure 8.11.	Resistance versus temperature profiles for niobium titanium nitride thin films deposited with a range of niobium cathode currents. a) displays the curve between 0 and 100 K whilst b) displays the superconducting transition. ....	185
Figure 8.12.	Resistance versus temperature profiles for niobium titanium nitride thin films deposited with a range of titanium cathode currents. a) displays the curve between 0 and 100 K whilst b) displays the superconducting transition. ....	186
Figure 8.13.	The $T_c$ of niobium titanium nitride thin films with varying niobium cathode current during deposition.....	187
Figure 8.14.	The $T_c$ of niobium titanium nitride thin films with varying titanium cathode current during deposition.....	187



## List of Tables

<i>Table 4.1</i>	<i>Material parameters of a selection of superconducting materials [17].</i>	<i>35</i>
<i>Table 7.1.</i>	<i>Table of the measured and calculated data taken from the GI-XRD measurements shown in figure 7.5.</i>	<i>71</i>
<i>Table 7.2.</i>	<i>Table describing the HIPIMS power supply settings used to deposit niobium thin film samples.</i>	<i>77</i>
<i>Table 7.3.</i>	<i>Data taken from the magnetisation measurement shown in figure 7.46. The RMSE begins a continuous increase at 654 Oe (<math>H_{dev}</math>) indicating that flux has entered the sample at that field.</i>	<i>115</i>
<i>Table 7.4.</i>	<i>Niobium thin film samples deposited at a range of deposition temperatures and bias voltage using either the HIPIMS, DC or pulsed DC power supply.</i>	<i>163</i>



## Symbols and Abbreviations

$(\Delta V/V)_M$	Relative volume of each sample into which the applied magnetic field had penetrated
$\Delta$	Gap energy
AC	Alternating current
AFM	Atomic force microscopy
$\vec{B}$	Magnetic field
bcc	Body centred cubic
BCS	Bardeen - Cooper - Schrieffer
$d$	Interplanar distance
$D$	SIS layer thickness
DC	Direct current
$d_m$	Molecular gas diameter
$E_{acc}$	Acceleration Gradient
ECR	Electro cyclotron resonance
EDS	Energy dispersive x-ray spectroscopy
$\vec{F}$	Lorentz force
fcc	Face centred cubic
FIB	Focussed ion beam
$h$	Planck's constant
$H$	Magnetic field strength
$\hbar$	$h/(2\pi)$
$H(M_{max})$	Maximum magnetisation
$H_C$	Thermodynamic critical field
$H_{C1}$	First critical field
$H_{C2}$	Second critical field
$H_{dev}$	First detected flux entry into a sample
HiPIMS	High Power Impulse Magnetron Sputtering

$H_{SH}$	Superheating field
$I$	Current
$\vec{j}$	Current density
$\bar{l}$	mean free path
LEP-2	Large Electron - Positron Collider
LHC	Large Hadron Collider
LHe	Liquid Helium
$L_{probe}$	Distance between voltage probes
$m$	Mass
$M$	Measured magnetic moment
$M_i$	Magnetic moment of a sample that is still in the Meissner state
$n_e$	Density of normal conducting electrons
$N_n(E_F)$	Density state for electrons at the Fermi energy
$n_s$	Density of superconducting electrons
OFHC	Oxygen free high conductivity
$p$	Pressure
$P_a$	Dissipated Power
$p_F$	Fermi momentum
$q$	Charge
Q Factor	Quality factor
$Q(E)$	Q factor as a function of accelerating voltage
$R$	Normal state resistance
$R_{BCS}$	BCS resistance
RBS	Rutherford backscattering spectroscopy
RF	Radiofrequency
RGA	Residual gas analyser
RRR	Residual resistivity ratio

$R_{RT}$	Room temperature resistance
$R_S$	Surface resistance
RT	Room temperature
$R_{TC}$	Normal state resistance at just above $T_C$
$s$	Entropy
SEM	Scanning electron microscope
SIS	superconductor - insulator - superconductor
SRF	Superconducting Radio Frequency
$T$	Temperature
$t$	Film thickness
$T^*$	Generalised temperature
$T_C$	Superconducting transition temperature
$T_h$	Homologous temperature
$T_m$	Melting temperature of deposited material
$T_{pot}$	Temperature shift caused by the potential energy of arriving particles
$T_{TC}$	Temperature at which $R_{TC}$ is recorded
$U$	Stored energy
$V$	Voltage
$v_s$	Superfluid velocity
$W$	Sample width
XPS	X-Ray photoelectron spectroscopy
XRD	X-Ray diffraction
$\vartheta_{dif}$	Diffraction angle
$\kappa$	Ginzburg - Landau parameter
$\kappa_B$	Boltzmann constant
$\lambda_L$	London penetration depth
$\mu_0$	Permeability of free space

$\xi_0$	Coherence length
$\rho_n$	Resistivity
$\omega_0$	Phonon frequency
$\omega_{RF}$	RF frequency

# 1. Background

Large particle accelerators allow us to push the boundaries of nuclear and high energy physics research at facilities such as the LHC and XFEL. Smaller particle accelerators are widely used in other applications such as medical and defence applications. A key component of high energy particle accelerators is the radio frequency (RF) accelerating cavity. RF cavities are resonating structures which operate at microwave frequencies to provide energy to charged particles. Normal conducting RF cavities operate with high losses due to heating of the cavity structure whereas superconducting RF (SRF) accelerating cavities allow more efficient operation when operated with high duty cycle or in the continuous wave regime.

There are three parameters which can be used to rate SRF cavity performance, the maximum attainable acceleration gradient  $E_{acc}$ , above which the cavity will quench, the attainable quality factor  $Q$ , as a function of the accelerating field and its maximum  $Q_0$ .

Current superconducting accelerator technology is dominated by the use of bulk niobium SRF cavities. High field non-linear dissipation could explain the monopoly of bulk niobium since it has the highest value of the first critical field  $H_{C1}$  (around 175 mT at a temperature of 2K) among all superconductors; high  $H_{C1}$  material is mandatory to prevent early vortex penetration at surface defects. The theoretical limit of  $E_{acc}$  is capped at the superheating field  $H_{SH}$  as it is the upper limit to which a superconducting material can remain in the Meissner state. Current technology already allows bulk niobium test cavities to reach accelerating fields which are close to the  $H_{SH}$  of niobium [8]. New surface treatments such as nitrogen doping have improved the quality factor of bulk niobium cavities at the expense of a reduced  $E_{acc}$  [9].

Superconducting thin films have been proposed as an alternative to bulk niobium cavities. In fact, niobium thin film SRF accelerating cavities have already been successfully implemented in sections of the LHC and LEP-2. Benefits of using superconducting thin films are the use of a relatively cheap substrate such as copper, the high thermal conductivity of the copper substrate and less sensitivity to trapped flux for superconducting thin films when compared to bulk niobium [2].

Bulk niobium cavities usually operate at or below 2 K. However, accelerator operation becomes considerably cheaper at 4.2 K and above. Superconductors with superconducting transition temperature  $T_c$  that is larger than niobium can have comparatively smaller BCS resistance  $R_{BCS}$  and therefore larger  $Q$  at operating temperatures of  $\geq 4.2$  K. Attempts to use superconductors with higher  $T_c$  or upper critical field  $H_{C2}$  have failed so far, due to their low values of  $H_{C1}$ , that allows early penetration of magnetic vortices and high surface dissipation.

A new method of implementation of superconducting thin films was suggested by Gurevich in [10]. The theory suggests that multilayer superconductor-insulator-superconductor (SIS) films can utilise magnetic shielding to increase both  $E_{acc}$  and  $Q$  factor.

The current capabilities of thin film SRF technology is limited to the use of niobium for low field operation.  $Q$  factors become unacceptably low after around  $15 \text{ MVm}^{-1}$ . There are theories regarding the mechanisms which explain the sharp  $Q(E)$  slope however none are widely accepted as unequivocally proven [2, 4, 5, 6, 7]. It is therefore imperative that superconducting thin films are fully characterised using a wide range of analytical techniques to fill in the gaps in our scientific understanding towards the goal of erasing the  $Q$  slope and increasing  $E_{acc}$ .

The objective of this study was to systematically develop the process of superconducting thin film deposition. Particularly, high impulse magnetron sputtering (HiPIMS) has been studied whilst varying the deposition temperature and applied DC substrate bias during deposition. HiPIMS is a variant of the commonly used pulsed DC sputtering. However, HiPIMS achieves much higher target currents by using short pulses and comparatively long off times. The resulting HiPIMS plasma can have peak currents which are up to two orders of magnitude larger than for DC sputtering, producing a large ion to neutral ratio of the target material [11]. The application of a substrate bias voltage will therefore accelerate charged material towards the substrate and alter the surface mobility and diffusion mechanisms within the growing film [12].

Thin films grown from superconducting materials such as niobium, niobium nitride and niobium titanium nitride have been deposited and tested for both their superconducting and morphological properties. Analytical techniques which have been used to test deposited films include a low temperature four-point probe, DC magnetometer, scanning electron microscopy (SEM), optical microscopy, x-ray diffraction crystallography (XRD), x-ray photoelectron spectroscopy (XPS) and Rutherford backscattering spectroscopy (RBS). The observed results were then analysed and described in detail so that the effects of the tested process conditions on the physical properties of the deposited superconducting materials can be better understood. It is hoped that studies such as this, which test superconducting thin films that have a wide range of different properties, will one-day lead to an explanation of the origins of the sharp  $Q$  slope.

The dissertation is organised as follows:

- Chapter 2 introduces the theory of superconductivity.
- Chapter 3 describes thin film deposition by magnetron sputtering, including the theoretical basis of the film growth dynamics.
- Chapter 4 is a review of the most recent research in the field of SRF thin film technology, focussing primarily on sputtered films.

- Chapter 5 describes the techniques typically used to analyse superconducting thin films.
- Chapter 6 describes the experimental setup used in the investigation.
- Chapter 7 presents the results and conclusions towards the process development of niobium thin films for SRF application.
- Chapter 8 presents the results and conclusions towards the process development of materials other than niobium for use in thin films for SRF application.
- Chapter 9 is a summary of the conclusions from the entire study, including suggestions for future work.



## 2. Superconducting Radio Frequency Cavities

### 2.1. Basics of superconductivity

Superconductivity was first discovered by Heike Kamerlingh Onnes in 1911 [13]. Onnes discovered that when he cooled mercury below  $T_C$ , then it allowed a DC electrical current to flow without resistance; he called the current a supercurrent. Superconductors therefore conduct electricity with no resistance. This means that, unlike the more familiar conductors such as copper or steel, a superconductor can carry a current indefinitely without losing any energy. In addition, they have other important properties, such as the Meissner effect. Superconductivity has been explained in a class of superconductors called conventional superconductors or BCS-superconductors after Bardeen, Cooper, and Schrieffer (BCS) published their theory [14]. However, in all other types of superconductors, called unconventional, like cuprates, heavy-fermion superconductors, ruthenates, etc, there is no widely accepted theory among physicists able to explain superconductivity.

Normal electrons act like Fermions that cannot exist with a single energy state according to the Pauli Exclusion Principle. In the case of BCS superconductivity, negatively charged electrons pass through the crystal lattice of a superconductor and deform it, creating regions which are locally positively charged. The repulsive force between positive lattice and negative electrons create a weak binding force between pairs of electrons, called the gap energy  $2\Delta$ , and allows them to combine to become a Cooper pair. Cooper pairs can act as bosons where each electron has the same energy state.

The speed of the electrons in the Cooper pairs is defined by the Fermi velocity  $v_F$  and effects their spatial separation, known as the coherence length  $\xi_0$ ; as described using equation 2.1.

$$\xi_0 = -\frac{2\hbar v_F}{\pi\Delta} \quad (2.1)$$

The lengths of Cooper pairs are much longer than the lattice spacing of the superconducting material and therefore the pairs overlap into a condensation of boson like particles. More energy is required to scatter an electron from the condensate than can be provided by phonon lattice vibrations at very low temperatures and therefore the Cooper pairs carry a current without resistance.

$T_C$  is the temperature at which normal conducting electrons will first condense into Cooper pairs at zero magnetic field. If the phonon frequency  $\omega_o$  ( $\approx$  Debye Frequency), the density state of electrons at the Fermi energy  $N_n(E_F)$  and the Cooper pair coupling potential  $V_{CP}$  are known, then  $T_C$  can be calculated using equation 2.2.

$$T_C = 1.13 \frac{\hbar\omega_0}{k_B} \exp\left(-\frac{1}{N_n(E_F)V_{CP}}\right) \quad (2.2)$$

Not all electrons condense into Cooper pairs unless the superconductor is cooled to a temperature  $T$  of 0 K. If the number of superconducting electrons  $n_s$  is known, then the number of normal conducting electrons  $n_e$  can be estimated using equation 2.3.

$$n_e = 2n_s(T = 0) \exp\left(\frac{\Delta(T)}{k_B T}\right) \text{ where } T < \frac{T_c}{2} \quad (2.3)$$

Thus, there is always a finite probability that some pairs of electrons will be split by thermal excitations that are larger than  $2\Delta$  if  $T > 0$  K.

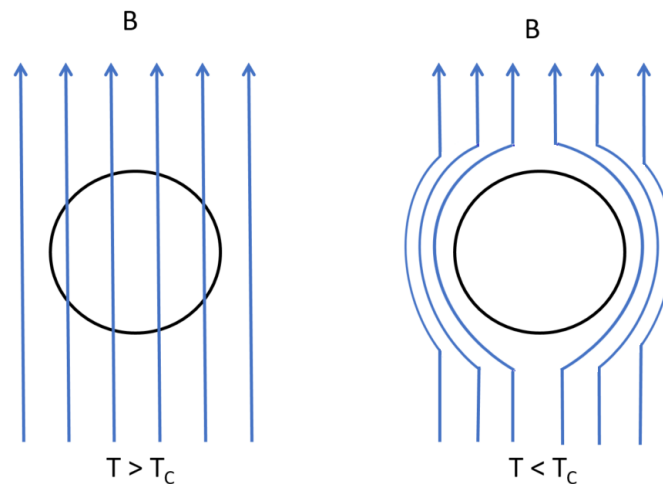


**Figure 2.1.** Depiction of a superconductor expelling an applied magnetic field. The magnetic field penetrates the superconductor when its temperature is above  $T_c$ . The magnetic field is expelled from the bulk of the superconductor when the temperature is below  $T_c$ .

Superconductors are affected by interactions with magnetic fields. When a weak magnetic field is applied to a superconductor then the superconductor reacts by generating screening currents which expel the magnetic field from all but a shallow surface layer of the material, as shown in figure 2.1.

The depth that the magnetic field can penetrate into the superconductor is called the London penetration depth  $\lambda_L$ . If the density of superconducting charge carriers  $n_s$  is known, then  $\lambda_L$  can be calculated using equation 2.4, where  $m$  and  $q$  are the mass and charge of the charge carriers respectively [15].

$$\lambda_L = \sqrt{\frac{m}{\mu_0 q^2 n_s}} \quad (2.4)$$

A superconductor is said to be in the Meissner state when no field has penetrated into the bulk of the superconductor, i.e. penetrating deeper than  $\lambda_L$  of the material.

## 2.2. Types of superconductor

There are two main classes of low temperature superconductor, known as type I and type II. The type of superconductor is primarily determined by the dominant length scale of the material, either  $\xi$  or  $\lambda_L$ . It is possible to determine the type of a superconductor by calculating its Ginzburg – Landau (GL) parameter  $\kappa$  using equations 2.5, 2.6 and 2.7.

$$\kappa = \frac{\lambda_L}{\xi_0} \quad (2.5)$$

$$\kappa < \frac{1}{\sqrt{2}} \quad \textit{Type I} \quad (2.6)$$

$$\kappa > \frac{1}{\sqrt{2}} \quad \textit{Type II} \quad (2.7)$$

## 2.3. Critical magnetic fields

Type I superconductors have positive surface energy and remain in the Meissner state so long as an applied magnetic field does not rise above the temperature dependant critical field  $H_C$ . Type II superconductors remain in the Meissner state at magnetic fields up to  $H_{C1}$  and allow a mixed superconducting – normal conducting state, known as the Shubkinov state, between  $H_{C1}$  and  $H_{C2}$ . The mixed superconducting state allows normal conducting cores to exist in the form of magnetic vortices that occur at either lattice imperfections or elemental impurities called pinning centres. Each vortex contains a quantised amount of magnetic flux denoted by the flux quantum,  $\Phi_0 = 2.1 \times 10^{-15}$  Wb. The number of vortices contained in the superconductor rises if the external field is increased.

A metastable state called the superheating field  $H_{SH}$  can theoretically allow a superconductor to remain in the Meissner state above  $H_C$  in type I superconductors and above  $H_{C1}$  in type II superconductors. A potential barrier allows the expulsion of magnetic flux up to an absolute limit of  $H_{SH}$ . It is possible for  $H_{SH}$  to be significantly larger than  $H_{C1}$  for some type II superconductors. The dependence of the superheating field on  $\kappa$  and  $H_C$  can be seen in equations 2.8, 2.9 and 2.10. Thus, superconductors with large  $H_C$  would be expected to have large  $H_{SH}$  and can theoretically remain in the Meissner state up to very high magnetic fields.

$$H_{SH} \approx \frac{0.89}{\sqrt{\kappa}} H_C \quad \kappa \ll 1 \quad (2.8)$$

$$H_{SH} \approx 1.2 H_C \quad \kappa \approx 1 \quad (2.9)$$

$$H_{SH} \approx 0.75 H_C \quad \kappa \gg 1 \quad (2.10)$$

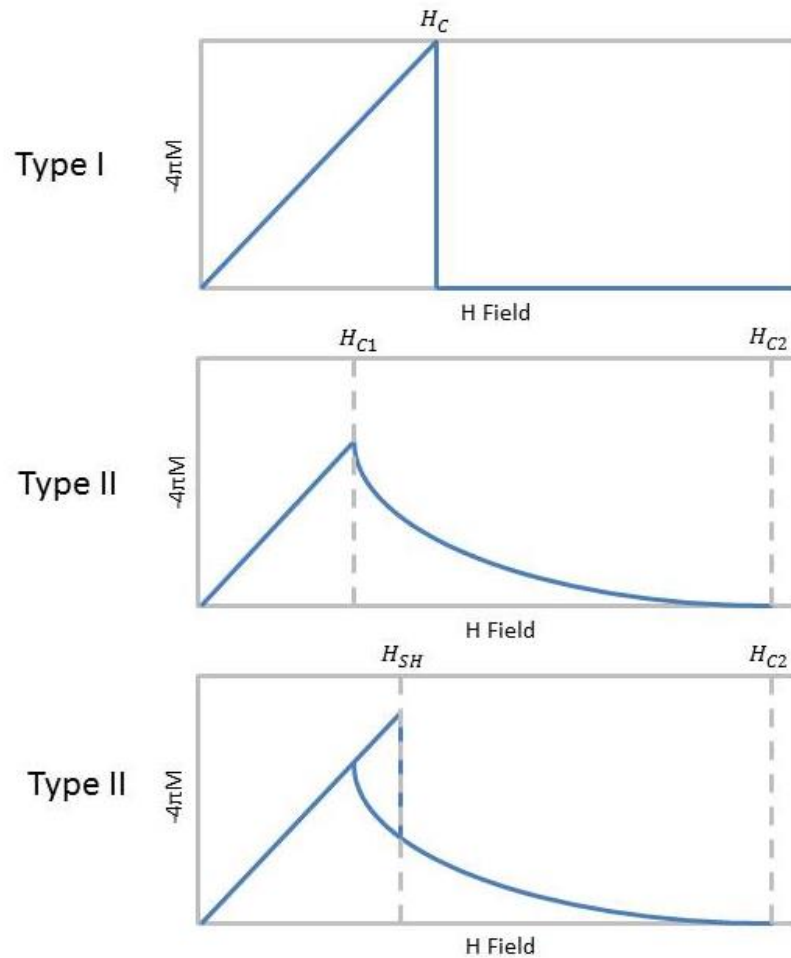


Figure 2.2. Magnetisation against applied field for type I and II superconductors. The superheating field is shown only for a type II superconductor however it can also occur for type I superconductors.

## 2.4. Critical Current

Figure 2.3 shows how the motion of vortices can be affected by a current passing through a superconductor. The current density  $\vec{j}$  exerts a force due to the Lorentz force,  $\vec{F} = \vec{j} \times \vec{B}$ , and so the vortices move in a direction perpendicular to both the magnetic field and electrical current. The vortices shift as a viscous motion which generates heat and removes energy from the supercurrent in the form of flux flow resistance [16]. If the vortex motion is at such a rate that the number of Cooper pairs that are broken at the front edge of the moving vortex is greater than the number formed at the back edge of the moving vortex then flux flow resistance will occur. Flux flow resistance allows local electric fields to act on unpaired electrons and a resistance is seen that is dependent on the normal resistance of the material. A critical current is reached when the motion of the vortices creates enough thermal energy that lattice vibrations can bridge the energy gap of Cooper pairs. The critical current

in general is limited by the volume of grain boundaries therefore large grain superconductors have higher critical currents [15].

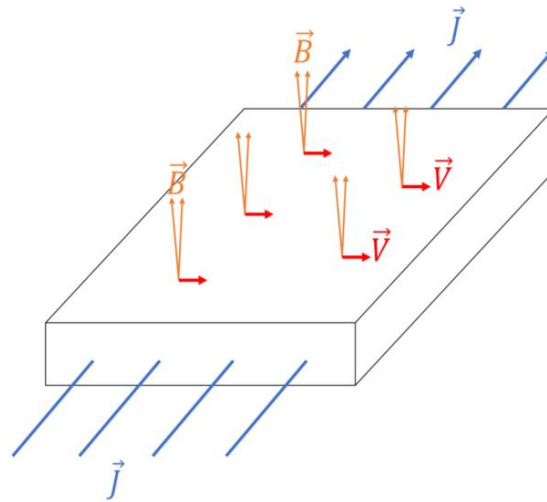


Figure 2.3. The relative motion of fluxoids,  $\vec{v}$ , within a superconducting thin film.

## 2.5. RF Superconductivity

Superconductors in DC magnetic fields can apply perfect screening of unpaired electrons. There is no longer perfect screening in the case of an AC magnetic field due to its changing direction and the resulting oscillations of Cooper pairs which have their own inertia. The imperfect screening results in a small surface resistance  $R_S$  of the superconductor. If we consider the case of an alternating magnetic field with RF frequency  $\omega_{RF}$ , then the application of the two-fluid model approximates  $R_S$  as shown in equation 2.11; where  $T \leq T_C/2$ . Equation 2.11 suggests that  $R_S$  drops exponentially to zero at  $T = 0$  K.

$$R_S \approx \omega_{RF}^2 e^{\left(-\frac{\Delta(T)}{\kappa_B T}\right)} \quad (2.11)$$

The total surface resistance is a sum of two different sources of resistance, the BCS resistance  $R_{BCS}$  and the residual resistance  $R_{RES}$ .

$$R_S = R_{BCS} + R_{RES} \quad (2.12)$$

$R_{RES}$  is temperature independent and therefore  $R_S$  can never actually vanish.  $R_S$  is attributed to intrinsic parasitic losses such as the purity of the superconductor, material defects, trapping of external magnetic fields on cooldown and other as yet unknown sources. Parasitic losses can also

occur due to damage, residues and dust left on material surfaces during assembly.  $R_{RES}$  has been proposed to be proportional to  $\sqrt{\rho_n}$  where  $\rho_n$  is the normal state resistivity [17].

Equation 2.13, where  $A$  is a constant that is weakly dependent on the material, describes an approximation of  $R_{BCS}$  that is valid for  $T \leq T_C/2$  and  $\hbar\omega < 2\Delta$ . It is clear that  $R_{BCS}$  is small for materials with relatively small  $\rho_n$  and relatively large  $T_C$ . Frequency is also a factor; where the  $R_s$  of very high frequency superconducting resonators is usually dominated by  $R_{BCS}$ .

$$R_{BCS} = A\sqrt{\rho_n} \frac{e^{\frac{-\Delta}{k_B T}}}{\sqrt{sT_C(1+e^{\frac{-\Delta}{k_B T}})^2}} \omega_{RF}^2 \ln\left(\frac{\Delta}{\hbar\omega_{RF}}\right) \quad (2.13)$$

## 2.6. SRF Accelerating Cavities and the Quality Factor

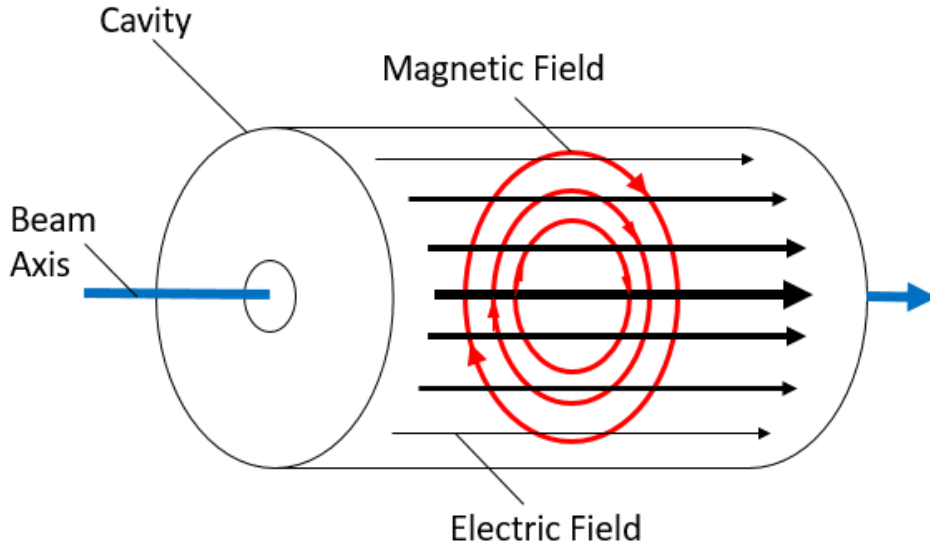


Figure 2.4. Schematic view of a pillbox shape accelerating cavity operating with the  $TM_{010}$  RF mode. Magnetic fields are shown in red and are strongest at the cavity walls. The electric field is shown in black and is strongest on the beam axis.

SRF accelerating cavities act as resonators for the RF electromagnetic waves which are used to accelerate charged particles within particle accelerators. Figure 2.4 illustrates an elliptical cavity working with the  $TM_{010}$  mode. The electric field is transverse through the accelerating cavity, with maximum amplitude at the central axis, and the magnetic field is orientated in the azimuthal direction, with maximum amplitude at the cavity wall.

The stored energy  $U$  within the SRF accelerating cavity is a function of the magnetic field strength  $H$  and the permeability of free space  $\mu_0$ , as described by equation 2.14.

$$U = \frac{1}{2} \mu_0 \int_v |H|^2 dv \quad (2.14)$$

Thus,  $U$  is the integral of the field energy density over the whole volume of the cavity.

The dissipated power  $P_a$  and the magnetic field strength  $H$  are related to  $R_S$  as shown in equation 2.15.

$$P_a = \frac{1}{2} R_S \oint_S |H|^2 ds \quad (2.15)$$

Thus,  $P_a$  is the integral of the resistive wall losses over the entire surface of the cavity wall.

The  $Q$  factor of a resonator describes the number of oscillations which it takes for  $U$  to reach zero. The  $Q$  factor for an SRF accelerating cavity is a function of both  $U$  and  $P_a$ , as described by equation 2.16.

$$Q = \frac{\omega_{RF} U}{P_a} \quad (2.16)$$

It can be useful to describe  $Q$  as a function of  $R_S$  rather than  $P_a$ , as  $R_S$  describes the specific material wall losses without consideration of the cavity shape. A geometry factor  $G$  is required to solve equation 2.16 for  $R_S$ .  $G$  is calculated using equation 2.17.

$$G = \frac{\omega \mu_0 \int_V |H|^2 dv}{\oint_S |H|^2 ds} \quad (2.17)$$

Finally, the  $Q$  factor of an SRF cavity is described using equation 2.18 and is therefore inversely proportional to  $R_S$  [18].

$$Q = \frac{G}{R_S} \quad (2.18)$$

The  $Q$  factor is considered to be the standard by which cavity performance is rated. Specifically, equation 2.18 describes the unloaded  $Q$  factor. The unloaded  $Q$  factor is the  $Q$  factor of the cavity in isolation. The loaded  $Q$  factor can be measured by also considering the losses attributed to any measurement system which is used to define the  $Q$  factor.

Accelerators are typically designed with a minimum  $Q$  at a desired accelerating voltage  $E_{acc}$ . Thus, the ideal accelerating cavity will reach the highest  $Q$  at the largest possible  $E_{acc}$ . The current technological capabilities of both  $Q$  and  $E_{acc}$  will be discussed in more detail in the literature review section of this report.



### 3. Deposition Process

#### 3.1. Magnetron Sputtering

Physical vapour deposition (PVD) is a vacuum coating technique which works on the basis of vaporising a solid target with the intention of the vapour re-condensing onto a nearby substrate in the form of a thin film. The most common form of PVD is magnetron sputtering and has been used extensively to produce thin metallic films for industry due to its ease of scalability and high deposition rates.

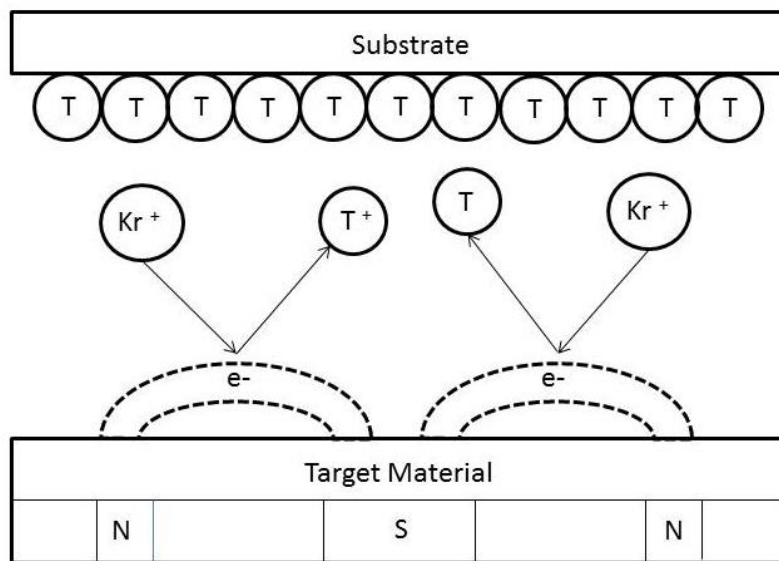


**Figure 3.1.** Schematic view of a planar magnetron.  $Kr^+$  are positive krypton ions and  $T$  and  $T^+$  are target atoms and ions respectively. Dashed lines denote the magnetic field lines which form an electron trap.  $N$  and  $S$  are the north and south poles of permanent magnets housed underneath the target.

A typical planar magnetron is shown in figure 3.1. A sputtering process begins by injecting a process gas, usually a noble gas, into the vacuum chamber at low pressure, typically between  $10^{-3}$  to  $10^{-1}$  mbar. The target of the magnetron is biased with a large negative voltage so that electrons can be emitted into the vacuum via field emission. If an electron and gas atom collide with sufficient energy then the gas atom will become positively ionised and release a secondary electron. The probability for ionisation to occur is increased if there are large numbers of both electrons and gas atoms confined to a small volume. Therefore, magnets are housed under the target of the magnetron to create an electron trap utilising closed  $E \times B$  drift currents close the target surface i.e. where they are most needed. Positively charged gas ions are then accelerated towards the negatively charged target with enough impact energy to eject (sputter) target atoms. More secondary electrons are emitted from the target as atoms are sputtered away. The secondary electrons released from the

target surface are accelerated through the target potential and arrive at the plasma with high kinetic energies and can initiate further ionisation of the process gas. Thus, sputter rates are largest directly beneath the  $E \times B$  drift in a region of the target known as the racetrack [19]. Ejected target atoms follow a parabolic trajectory towards the substrate material. If the target material is ejected with enough energy, or the plasma is dense enough, then the target material can become ionised.

Magnetrons can be in either a planar or cylindrical design however both operate using the same principles. Variations of the planar magnetron are typically used to deposit on a flat substrate whereas a cylindrical magnetron would be better suited to depositing on the inside of a curved surface, such as an RF cavity.

There are a number of different power supplies which can be used to control the magnetron sputtering process. Direct current (DC) is the simplest. A DC power supply is used to provide a constant voltage to negatively bias the target of the magnetron. DC Magnetron sputtering provides uniformity of coating and high deposition rates but does not produce sputtered material with high kinetic energies.

Pulsed DC magnetron sputtering is an adaption of DC sputtering which applies the DC sputter voltage as pulses rather than a constant voltage. Pulsed DC magnetron sputtering was first developed to enable reactive sputtering of dielectrics that were unsuitable for use with DC sputtering. A pulsed DC power supply operates by providing a pulsed negative sputtering voltage to the target, and then a positive voltage, of the order of 5 to 20 % of the sputter voltage, is applied between each negative pulse. Thus, the alternating polarity of the voltage allows the surface of a dielectric target to partially discharge and helps to prevent arcs [20]. Pulsed DC magnetron sputtering can also be effective to deposit conducting materials as current densities at the target surface can be up to double of those produced by DC magnetron sputtering [21]. Pulsed DC discharges are typically characterised by the duty cycle of the process. The duty cycle is given as a percentage equal to 100 times the length of a pulse multiplied by its frequency. Pulsed DC magnetron sputtering usually operates with a duty cycle of approximately 50 to 90 %.

RF magnetron sputtering is another technique developed to sputter dielectric material. RF power supplies operate at 13.56 MHz and supply an AC voltage to the target. The biasing of the cathode results in a plasma containing both sputter gas ions and electrons. The heavy sputter gas ions are not mobile enough to alternate from cathode to anode before the polarity of the RF field changes. The lighter electrons can switch between cathode and anode before the polarity of the RF field changes and results in the target being negatively biased with respect to the substrate and chamber due to the relatively small surface area of the target [22].

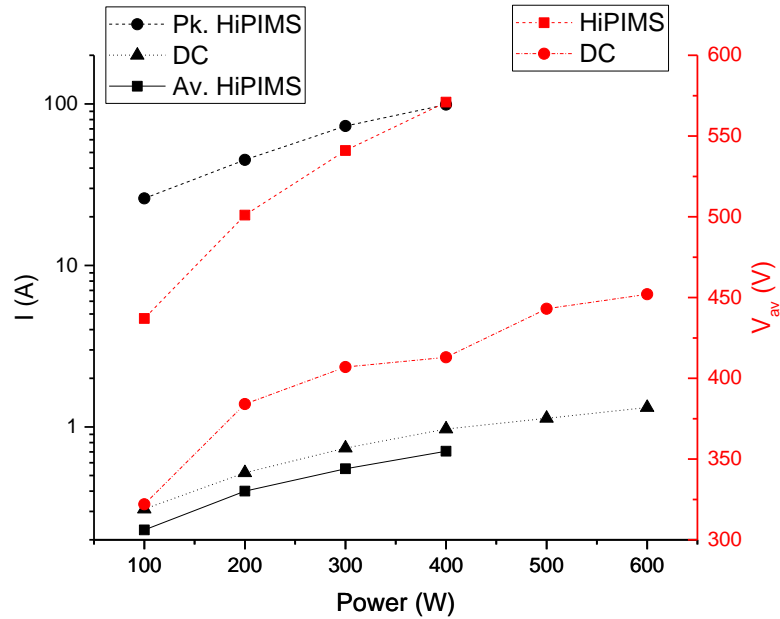


Figure 3.2. Peak power of HiPIMS pulses are two orders of magnitude higher than that of DC sputtering. Black lines are plasma current and red lines are the bias voltage supplied to the target cathode.

HiPIMS is a variant of pulsed DC magnetron sputtering which utilises long off times to achieve very large plasma currents. The duty cycle of a HiPIMS discharge is typically as small as 0.1 to 5 %, but the peak plasma current can be as much as two orders of magnitude larger than that of DC magnetron sputtering, as shown in figure 3.2. The evolution of a HiPIMS discharge is quite well understood. Normal operation of HiPIMS uses off times that are so long that there is no longer an  $E \times B$  drift between pulses because of the lack of an  $E$  field. Thus, the plasma density decreases during the off time. The high voltage at the beginning of each pulse causes the low density plasma to become highly negative, containing large numbers of secondary electrons with energies of up to 100 eV [23]. This initial stage lasts for approximately 10  $\mu$ s. The next phase of the discharge is a rapid increase in the plasma density as the high energy electrons become trapped in the renewed  $E \times B$  drift; resulting in increased sputtering rate, more secondary electrons and ramping of the plasma current [24]. The plasma current stops ramping once the number of neutrals is diminished [25]. Self-sputtering can occur as large fractions of the target material become ionised [26]. After the peak, the plasma current starts to drop till the end of the pulse.

Benefits of the HiPIMS process are reported to be dense films with few voids and with good film adhesion [27]. The main downside of the process is a small deposition rate a sensitivity to the process gas pressure and the pulse settings i.e. length of pulse and repetition rate. A stable plasma cannot be maintained if the off time is set to too long. Pre-ionisers can be used to maximise the length of the off time by maintaining a low density plasma between pulses.

### 3.2. Substrate Preparation

Substrate preparation is very important for any thin film coating process. One of the main reasons for a quench of an SRF cavity is due to field emission of electrons at defects on the RF surface. A smooth defect free surface is therefore preferred so that field emission can be minimised. The roughness of a thin film can be defined on the nm scale whereas the roughness of the substrate will usually be of the order of  $\mu\text{m}$  scales. This concludes that the substrate surface will usually define the surface roughness of a thin film.

Surface polishing can be performed using mechanical polishing, chemical polishing and electropolishing. Mechanical polishing uses abrasives to remove surface material. The abrasive will be used to scratch material away from the surface to be polished and the size of the abrasive will determine the volume of material that will be removed. Successively smaller abrasives are used which produce progressively smaller scratches until the surface becomes smooth enough for the required application. Mechanical polishing is usually performed on flat surfaces however barrel polishing can allow elliptical cavities to be polished [28]. Diamond turning can produce optically flat sample substrates with average surface roughness (Ra) of less than 10 nm [29].

Electropolishing is a process which is the reverse of electroplating. The workpiece which is to be polished is immersed in an electrolyte and acts as an anode. Another electrode is immersed into the electrolyte and acts as a cathode. A current is then passed from anode to cathode where metal at the surface of the workpiece is oxidised and dissolved into the electrolyte. The dissolved material is then deposited onto the cathode surface in a reduction reaction. Phosphoric acid is typically used as the electrolyte when electropolishing a copper workpiece [30]. Chemical polishing uses chemicals to etch the surface of a workpiece. Alternatively, buffered chemical polishing can be used, which is similar to chemical polishing, but where material is removed at a smaller rate to result in a smoother surface [31]. Studies have shown that electro polishing can produce surfaces which have an Ra of 20 nm as compared to 200 nm for chemical polishing [32]. Both chemical and electropolishing allow for more complex shapes to be polished than mechanical polishing.

The substrate surface must be clean and free of contamination before a film is deposited. A contaminant is any substance which is detrimental to the processing of the film / substrate coupling. Different types of contaminant are naturally occurring layers such as oxides, adsorbed layers such as hydrocarbons or particulate matter. Typical cleaning solvents are ultrasonic baths of acetone, isopropanol and methanol [33]. Solvents should not be allowed to dry before rinsing with deionised water; failure to do this can lead to surface staining. Surface staining can lead to unsatisfactory adhesion of the film to the substrate and even film delamination [34] [35].

Final cleaning can be performed in vacuum by techniques such as plasma cleaning and sputter cleaning. Species such as oxygen, nitrogen and carbon may be trapped below the surface of a substrate and can only be removed by baking [36]. Care should be taken when choosing a bake temperature as heating a substrate can alter its physical properties.

### **3.3. Thin Film Growth Mechanisms**

Physical vapour deposition is a process which produces a vapour consisting of atoms and ions of a material which are to be deposited onto a surface. Clusters of deposited atoms form as the first atoms arrive. The atoms in the clusters start to bond together by either metallic bonding in the case of metals or by chemisorption for reactive elements such as oxygen, nitrogen and carbon [37].

Nucleation occurs once a cluster of atoms reaches a critical size that is large enough to reduce the Gibbs free energy at the cluster surface. The critical cluster size increases with temperature and decreases with deposition rate. A continuous film is established once the clusters become large enough that they can coalesce. The surface of the film lattice has a potential energy which arises because bonds need to be broken in order for the film surface to become larger as more atoms are adsorbed from the vapour. The potential surface energy can be minimised by adatom diffusion into the most energetically stable lattice locations. Diffusion will occur faster if more energy is supplied to the growing film. Both substrate heating and ion bombardment will speed up diffusion rates by breaking bonds between film atoms. However, very high temperatures increase the desorption rate, therefore reducing the diffusion length, and ion bombardment can produce defects if the impact energy is too high. Crystals have the lowest surface energy when atoms are arranged in close packed planes of the materials preferred crystal orientation [38].

The electrons at the surface of a continuous film will react to the absence of atoms above the surface, causing the applied forces to change with respect to those within the bulk of the film. The act of applying different forces to surface atoms creates either compressive or tensile stresses as the film grows. The film can react to the applied stress by forming defects and dislocations within the crystal lattice, acting to lower the energy stored within the film. Defects and dislocations have the side effect of creating further film stresses, however, their creation should always coincide with a net drop in stored energy [39]. Dislocations can be grain boundaries, adatoms, surface ledges, kinks or vacancies, as shown in figure 3.3. More complex dislocations such as tilt boundaries, twist boundaries and twist dislocation are shown in figures 3.4 and 3.5. Dislocations within a superconducting lattice can produce regions containing normal conducting electrons which act as pinning centres and contribute to  $R_{RES}$ .

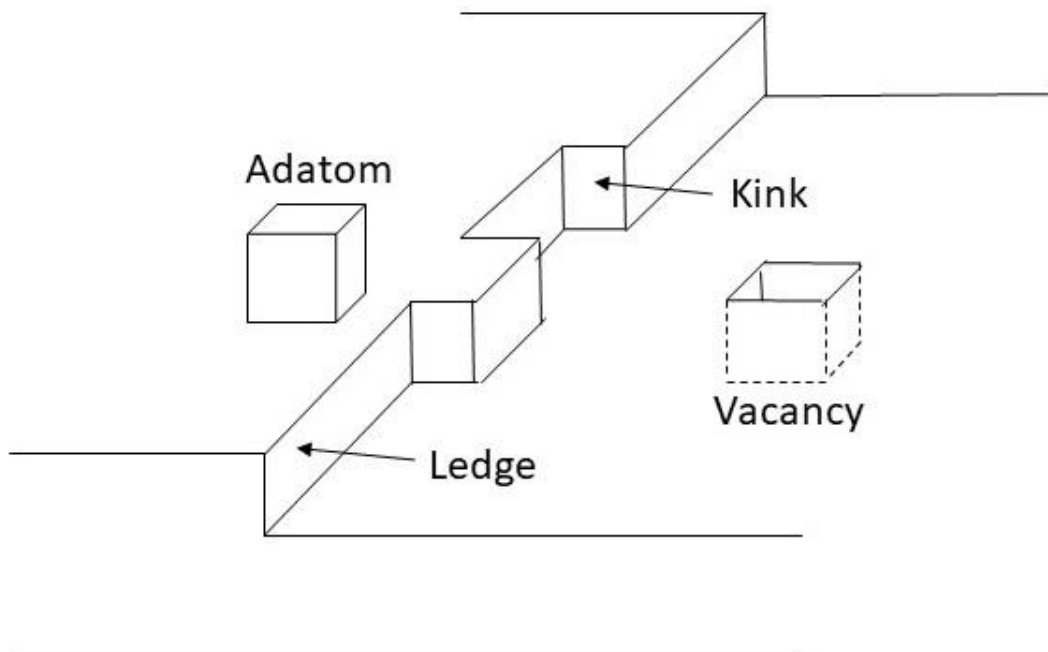
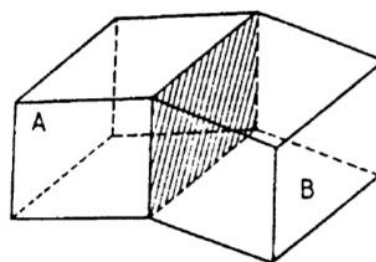
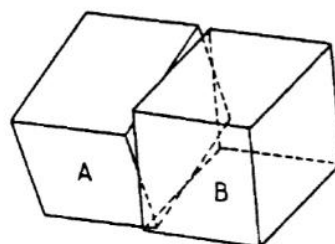


Figure 3.3. Schematic representation of an adatom, ledge, kink and vacancy.



Tilt boundary



Twist boundary

Figure 3.4. Tilt and twist boundaries between two different crystals A and B [39] (reproduced with permission from Springer).

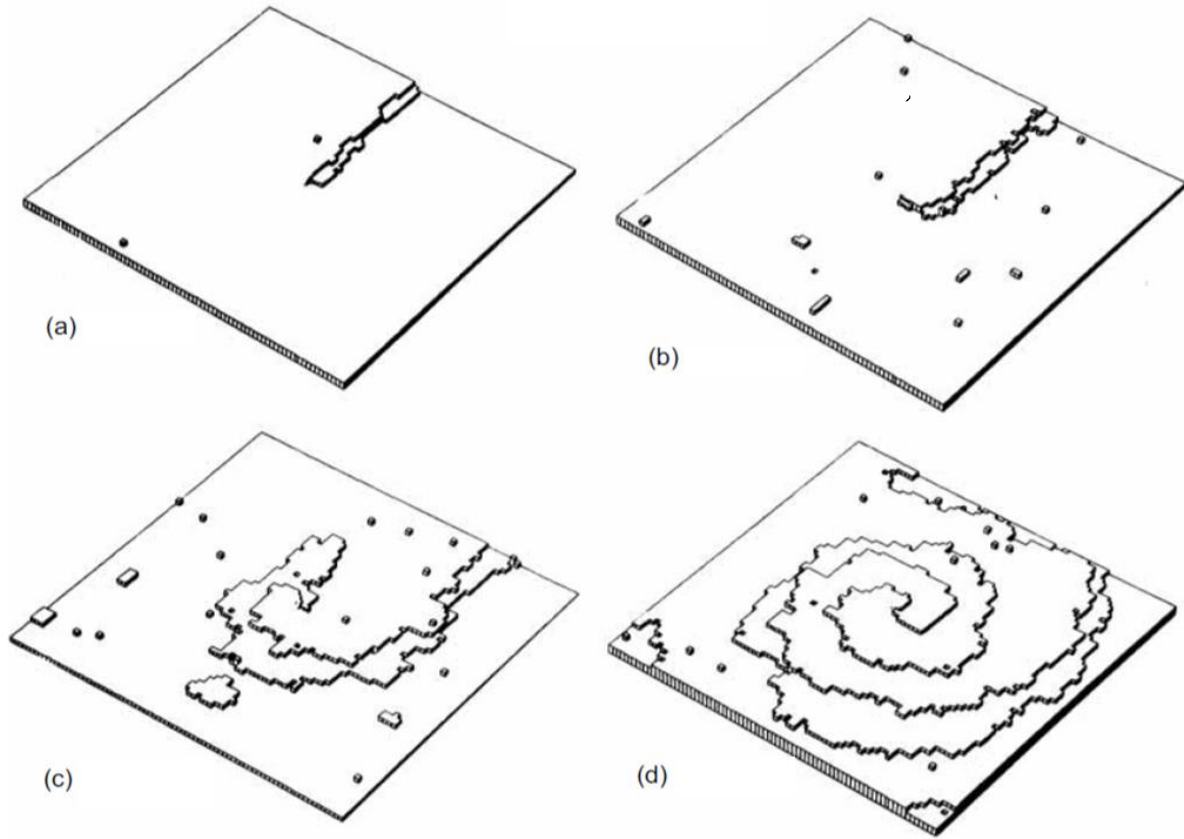


Figure 3.5. A Monte Carlo simulation of the formation of a screw dislocation [40] (reproduced with permission from John Wiley & Sons, Inc.).

### 3.4. Film Growth Parameters

It is useful to define common features of thin films so that deposition conditions can be compared effectively for different materials, such as to use a structure zone diagram (SZD). SZD's typically have an axis describing the temperature of the system, the energy of the arriving material and the thickness of the film.

An effective way to describe the temperature conditions of an evaporative deposition process is to use the homologous temperature  $T_h$ .  $T_h$  is a ratio of both the substrate temperature  $T$  and the melting temperature of the sputtered material  $T_m$ , as described by equation 3.1 [41].

$$T_h = \frac{T}{T_m} \quad (3.1)$$

$T_h$  is only valid for low energy deposition processes. Particles which arrive with high energy have their own potential energy  $E_{pot}$ . Thus, there is a temperature shift  $T_{pot}$  at the surface of the growing film, caused by the number of arriving particles  $N$  with significant  $E_{pot}$ .  $T_{pot}$  is described by equation 3.2.

$$T_{pot} = \frac{E_{pot}}{kN_{moved}} \quad (3.2)$$

Both  $T_h$  and  $T_{pot}$  can be combined to give a generalised temperature  $T^*$  which considers all methods of heating the deposited material, as described by equation 3.3 [42].

$$T^* = T_h + T_{pot} \quad (3.3)$$

Figure 3.6 is an example of a SZD which uses  $T^*$  to describe the temperature conditions. The energy axis is labelled with the normalised energy flux  $E^*$ .  $E^*$  describes the displacement and heating effects caused by the kinetic energy of bombarding atoms and ions. The  $z$  axis of the SZD is the net thickness  $t^*$  and describes how the film thickness changes by either densification or ion etching.

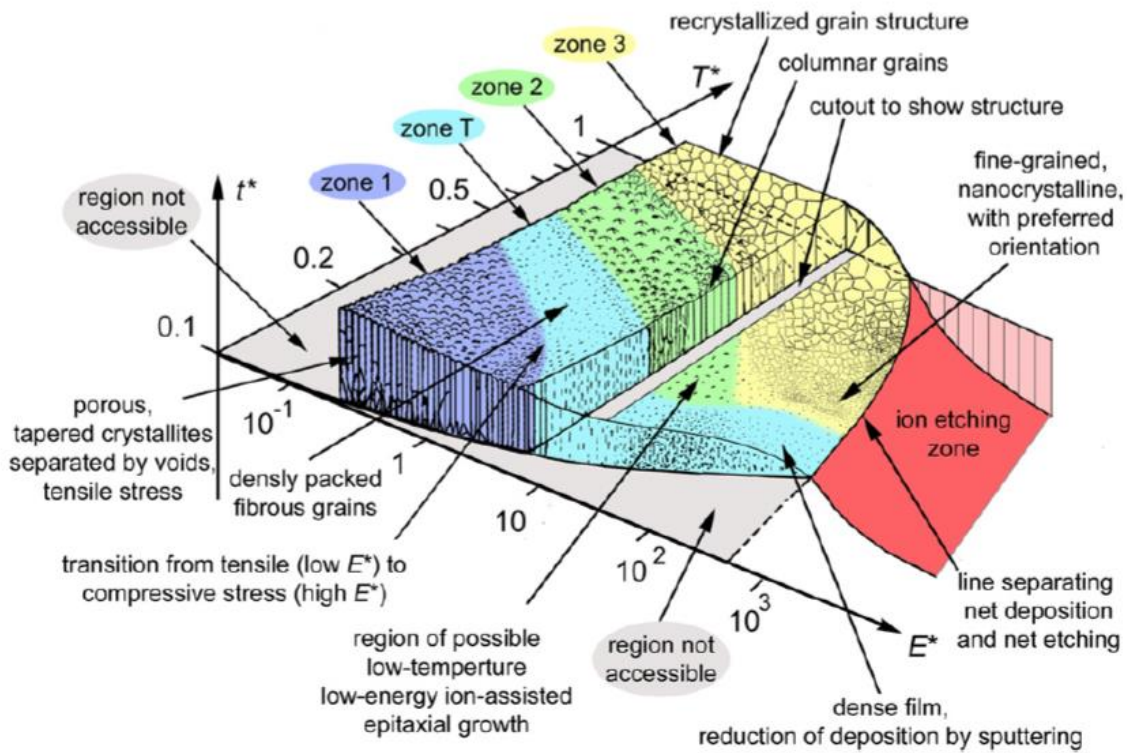


Figure 3.6. Structure zone diagram for energetic condensation processes. Axis labels are the generalised temperature,  $T^*$ , the normalised energy flux,  $E^*$ , and the net thickness,  $t^*$  [42] (reproduced with permission from Elsevier).

The SZD is characterised by different zones. Zone one occurs for  $T^* < 0.3$ ; where adatom mobility is low and the nucleation of grains continues throughout the thickness of the growing film. Zone one produces films which are fibrous and contain many voids. The fibrous grains have domed tops which point in the direction of the arriving particles. Columns are not formed from single grains and can become porous with limited diffusion between grains [43].

Zone T is the transition zone and occurs for  $0.2 < T^* < 0.4$ . Zone T has more densely packed grains than zone one. The higher film temperature with respect to zone 1 causes grain coarsening during the island coalescence stage by the formation of islands with relatively larger surface to volume ratios, grain boundaries are immobile. The random size and orientation of grains determines their growth behaviour and is representative of competitive growth with neighbouring grains. Competitive growth promotes the formation of energetically favourable v-shaped columns with a continuously changing surface topology as a function of film thickness. Adatom surface diffusion does occur to allow local epitaxy, however, the kinetically disadvantaged columns become overgrown. The tops of columns become faceted due to shadowing and initiates surface roughening that becomes more pronounced with film thickness [44].

Zone two occurs at  $0.4 < T^* < 0.7$ . Bulk diffusion becomes significant and grain boundary migration takes place throughout the full thickness of the film. Orientation is selected during the coalescence stage and is more pronounced, resulting in a decrease in the total grain boundary area. Large grains with low surface and interface energy grow instead of small unfavourably oriented grains. Secondary recrystallization can occur where the film structure becomes homogenous in the growth direction. Grains become columnar with flat surfaces that display grooves at grain boundaries.

Zone three occurs at  $T^* > 0.7$  and is characterised by bulk diffusion and recrystallization leading to the largest grain sizes. The grains become enlarged because the high temperature allows heightened and continuous adatom mobility to dominate over the effects of ion bombardment.

The effect of increasing  $E^*$  is to reduce the  $T^*$  required for films to form in each of the zones, T, two and three. Non-penetrating particles can have enough energy to promote surface diffusion of adatoms. If the energy of arriving particles is within a window between the surface displacement energy and bulk displacement energy, then epitaxial growth is promoted with no formation of defects within the bulk of the film. Particles that arrive with extremely high kinetic energy can initiate displacement cascades followed by a local thermal spike. The thermal spike creates large amplitude thermal vibrations and promotes diffusion, but can also cause interstitials and vacancies to migrate inside grains. Thus, the bombardment by energetic particles can promote both defect annihilation and defect generation. The film surface is etched once the kinetic energies reach a critical value which is between 400 eV and 1400 eV for most elements [42].

### 3.5. Supplying energy to the growing film

Substrate heating is usually provided by a resistive heater. Any resistive heater is adequate for most PVD applications so long as the heater is designed in such a way that a metallic deposit cannot cause the heater to short circuit.

Changing the energy of sputtered material can be a complex problem that is difficult to control. The kinetic energy of particles which arrive at the substrate can be modified due to a variety of factors which are discussed next.

Collisions between two moving particles will reduce their energy. The distance between the target and substrate dictates the distance through which sputtered material must travel during a deposition process. Shortening the travel distance reduces the chance of particle collisions.

Ideally, the gas pressure within a sputtering chamber should be so low that the average distance between particles is longer than the distance between vacuum chamber walls. Thus, allowing the target material to arrive at the substrate with the maximum possible energy. Equation 3.4 describes the mean free path,  $\bar{l}$ , of particles inside a vacuum chamber; where  $d_m$  is the molecular gas diameter, and  $p$  is the pressure [45]. Equation 3.4 shows that the mean free path is just below 1 mm for a typical magnetron sputtering process using krypton sputter gas at a temperature of 273 K and pressure of  $5 \times 10^{-3}$  mbar.

$$\bar{l} = \frac{k \cdot T}{\sqrt{2} \cdot \pi \cdot p \cdot d_m^2} \quad (3.4)$$

A mean free path of approximately 1mm for most magnetron sputtering processes suggests that sputtered atoms and ions will collide many times before arriving at the substrate. Thus, changing the process gas pressure can have dramatic effects on the deposited film. Altering the numbers of collisions within the sputtering chamber alters the kinetic energy of arriving material and changes the deposition rate. It is even possible to preferentially sputter different regions of a deposition chamber at different sputter gas pressure [46].

Finally, applying a DC or RF bias to the substrate can accelerate ions arriving at the surface of a growing film. The magnitude of the bias voltage dictates the extent by which ions will be accelerated. The applied bias can also affect the angle at which ionised material impinges on the substrate.



## 4. State of the art superconducting thin film research

### 4.1. Benefits of thin film SRF cavities

The operation of a particle accelerator at 4.2 K is less costly than operation at 2 K. Thin film cavities are preferred over bulk niobium cavities for low frequency and  $\approx 4.2$  K operation because  $R_{BCS}$  is smallest for thin films at those operating parameters [47].

Copper substrate is typically used for thin film SRF cavities. The thermal conductivity of copper at 4.2 K is  $300 - 2000 \text{ Wm}^{-1}$  as opposed to  $75 \text{ Wm}^{-1}$  for niobium. The high thermal conductivity of copper therefore allows heat to be dissipated efficiently and reduces the chance of a thermal quench [17].

Thin film niobium cavities have been shown to be less sensitive than bulk niobium cavities to flux trapping of the Earth's magnetic field [17, 48].  $R_s$  resulting from trapping of the Earth's magnetic field was as low as  $1 \text{ n}\Omega \text{ Gs}^{-1}$  for thin film cavities as oppose to  $100 \text{ n}\Omega \text{ Gs}^{-1}$  for bulk niobium cavities. Thus, thin film cavities do not require complex magnetic shielding to be installed within cryomodules.

Thin film niobium cavities are not used at high accelerating voltage as there is the large Q slope above 15 MV/m. Thus, eradication of the steep Q slope for thin film SRF technology is of great interest to the community.

### 4.2. The effects of substrate choice and substrate heating on deposited niobium thin films

The first step to producing a quality niobium film is to choose and prepare the substrate. Niobium films which have been deposited onto the native oxide layer of polycrystalline copper will form primarily with the body centred cubic (bcc) (110) orientation. Pre-heating polycrystalline copper at  $650 \text{ }^\circ\text{C}$  for up to 24 hours will fully remove the native oxide layer, outgas the substrate and anneal the substrate before deposition. Once the oxide layer is removed from the polycrystalline copper surface then niobium films grow in both the bcc (110) and (211) orientations [49]. Lattice parameters  $a_0$  were measured for films deposited onto the native oxide of copper and oxide free copper, producing similar  $a_0$  of  $3.3240$  and  $3.3184 \text{ \AA}$  respectively [50]. Niobium films grown on the oxidised copper substrate form grains which measure approximately 100 nm across, whereas grain size is the order of microns on the oxide free substrate, resulting in larger RRR [2, 51]. Surprisingly, it was found that the large grained films deposited onto the oxide free substrates produced more fluxon induced and residual RF losses than for the films deposited onto the native oxide layer.

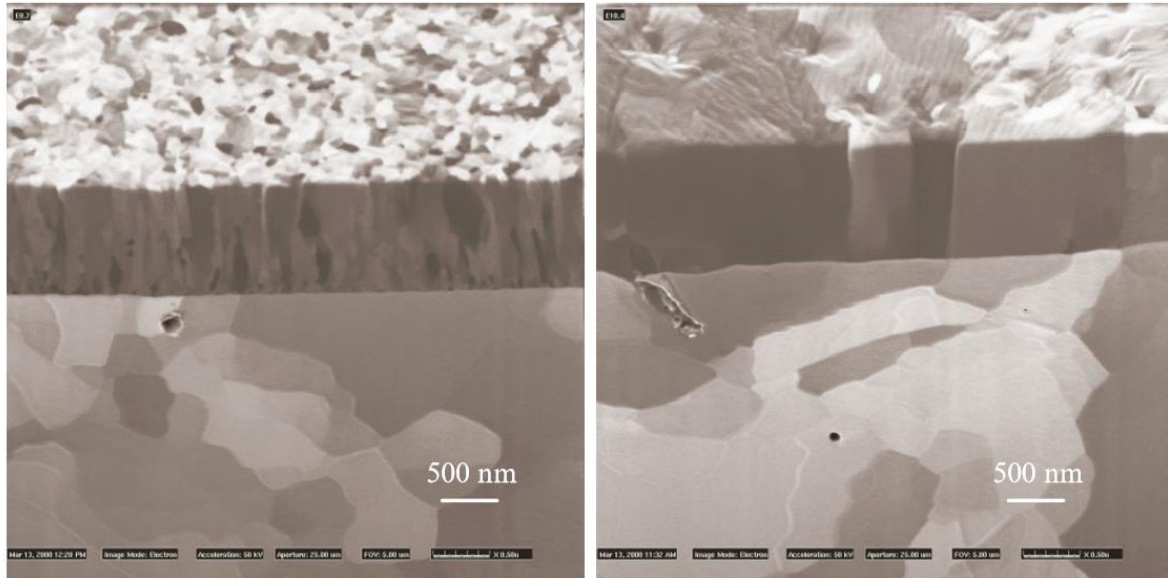


**Figure 4.1.** Cross sectional SEM images of niobium films which have had a section removed using a FIB. The left image shows a niobium film deposited onto an oxidised copper surface. The right image shows a niobium film deposited onto a copper surface which has had the native oxide layer removed [51] (CC BY 3.0).

Single crystal niobium films have been formed when deposited onto single crystal copper substrate which was first pre-heated to 350 °C for twenty-four hours to dissolve the native copper oxide layer into the bulk of the substrate. The crystal orientation of the copper substrate dictated the orientation of the growing niobium film. Single crystal bcc niobium (110) grew onto both face centred cubic (fcc) (100) and (111) single crystal copper substrate whilst single crystal bcc niobium (200) grew on single crystal fcc (110) copper substrate [52]. Heating the oxide free single crystal copper substrate up to 150 °C during deposition increased the film grain size and resulted in a sharper superconducting transition than was observed for films deposited with similar conditions at room temperature [53].

The major limitation of copper substrate is its relatively small melting temperature, 1085 °C, when compared to that of niobium, 2469 °C. Copper cavity substrates are typically deposited at temperatures no larger than 700 °C; for example, a niobium film was deposited onto a copper cavity at 635 °C in [54]. Heating the substrate up to 635 °C would theoretically produce a film in zone T of the structure zone diagram. Magnesium oxide and sapphire have been used as test substrates with higher melting temperatures than copper, at 2852 °C and 2030 °C respectively, and could therefore produce films in zone 2 of the structure zone diagram.

A-plane sapphire has a similar lattice structure to niobium (110) with a mismatch of 1.7 % whilst magnesium oxide has a larger mismatch of 10.9 % [55]. Niobium films deposited onto a-plane sapphire have been reported to grow with the (110) orientation at ranges from room temperature to 700 °C [56]. Sapphire and niobium both have similar thermal expansion coefficients which help to

minimise stress due to thermal expansion [57]. Niobium films were deposited onto single crystal magnesium oxide substrate which was annealed and then deposited at a range of temperatures. The study showed that films grew in the niobium (110) orientation at 150 °C, then changed to a mixture of both (110) and (100) at 500 °C and finally a pure (200) film at 700 °C [58]. Other work studied the DC magnetic properties of niobium films which grew with either the bcc (110) or (100) orientation onto magnesium oxide at 600 °C. The niobium (100) growth direction consistently exhibiting larger  $H_{c1}$  than the (110) growth direction; the larger  $H_{c1}$  was presumed to result from the larger grain size of the niobium (100) films [53]. Although the superconducting performance is promising for films deposited onto magnesium oxide and sapphire, both materials are unsuitable for cavity fabrication and can only be used in proof of principle experiments.

### **4.3. Niobium thin film cavities deposited by conventional low ion to neutral ratio sputtering techniques**

Superconducting niobium thin films have been successfully used in accelerator facilities such as the LEP-II (352 MHz at 4 K). Niobium films were deposited onto copper cavity substrates using the magnetron sputtering technique. The cavity substrates were prepared using a mixture of sulfamic acid, hydrogen peroxide, n-butanol and ammonium citrate (SUBU) to polish the surface before it was rinsed in sulfamic acid, water and alcohol [59]. The cathode of the magnetron was made from a stainless steel cylinder that was coated in a high quality niobium liner. Solenoid magnets were located within the cathode tube to confine the plasma during deposition. The substrate and magnetron cathode were mounted within a class 100 clean room. The vacuum system was baked for 150 °C for 24 hours prior to the start of the deposition. Sputtering was performed with a substrate temperature of 170 to 190 °C in an argon atmosphere of approximately  $5 \times 10^{-4}$  mbar and with a plasma current of 3.0 -5.5 A. Each sputtered film had a thickness between 1.2 and 1.5  $\mu\text{m}$  [60]. A common cause of cavity failure was blistering of the niobium film due to insufficient adhesion to the copper substrate, usually where the copper substrate was contaminated by particulate matter or stains left from the chemicals used to prepare the substrate. Steps were taken to include further visual inspections of the copper surface before deposition so that fewer cavities were rejected [61].

Sixteen single cell 400 MHz cavities are used in the LHC with design parameters:  $Q_0$  of  $2 \times 10^9$  at  $E_{acc}$   $5.5 \text{ MVm}^{-1}$  and temperature of 4.5 K. The cavities were deposited at CERN and are described by S. Calatroni in [62]. The researchers at CERN deposited each cavity using a cylindrical magnetron consisting of a niobium tube with a permanent magnet housed inside. The copper cavity acted as the vacuum chamber. A test cavity was used during the development of the LHC 400 MHz cavities which

allowed witness samples to be deposited at various locations around the equator of a 500 MHz cavity. Three witness samples were deposited at temperature of either 150, 250 or 350 °C with argon process gas at  $9 \times 10^{-4}$  mbar [63]. RRR measurements of the witness samples displayed a linear increase with the substrate temperature, from RRR of 13 to 40. XRD measurements were used to calculate the lattice parameter of each deposited film with the results shown in figure 4.2. The lattice parameter of the niobium films became shorter as the substrate temperature was increased, ranging from 3.3264 to 3.3198 Å when measured on copper. The lattice parameter of each film became shorter after the substrate was etched away.

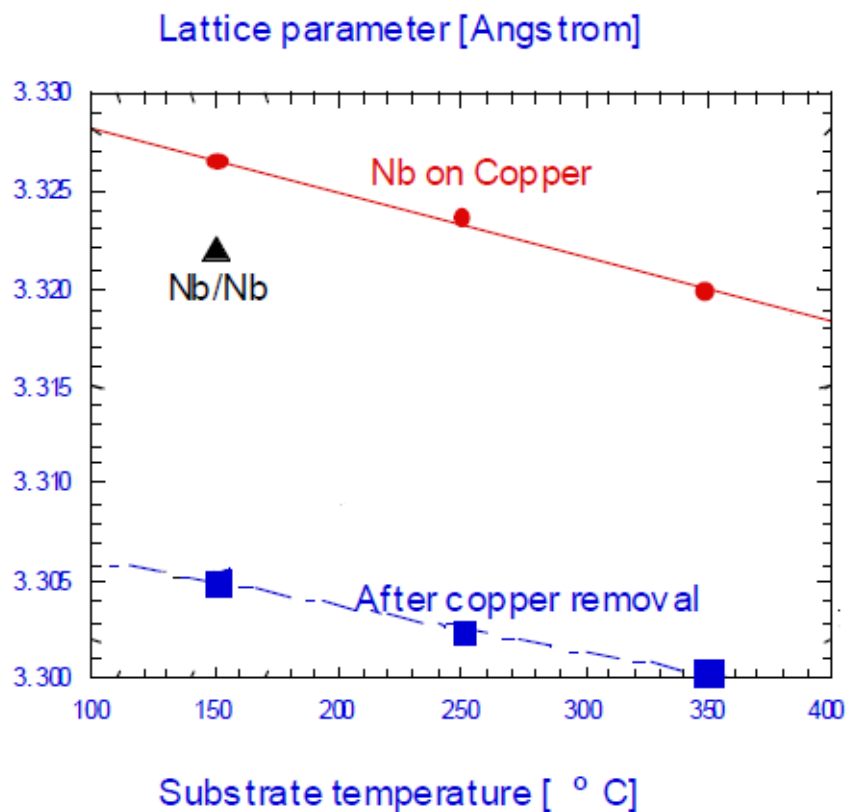


Figure 4.2. Lattice parameter of niobium films measured either on the copper substrate or after the substrate was etched away. The lattice parameter of a bulk niobium sample is shown for comparison [63] (CC BY 3.0).

The effect of flux trapping due to the inclusion of sputter gasses into niobium thin films was tested in detail for niobium films deposited onto 1.5 GHz copper cavities. Each copper cavity substrate was deposited by DC magnetron sputtering. A niobium tube was used as the cathode of the magnetron and a magnet was housed inside the cathode to confine the plasma during deposition, as shown in figure 4.3 [2]. Study of the  $R_{res}$  of each deposited film as a function of the deposition process conditions showed inconsistent results. The study ultimately found that the preparation of the copper cavity surface had a largest impact on the magnitude of  $R_S$  [64]. Films grown on spun copper provided smaller  $R_S$  than those grown on hydroformed copper cavities. Electropolishing of the copper cavity surface

was preferred over chemical polishing as the former did not leave pin hole defects at the surface of the copper. Cavities that were high pressure rinsed using ultra-pure water and then mounted into the deposition system within a dust free environment prior to the start of a deposition produced films with a factor 2 improvement in the maximum  $E_{acc}$  and factor of 3 reduction in the  $R_{res}$  relative to cavities that were deposited without prior rinsing and assembly in the dust free environment. Another interesting observation of the project was the comparison of the measured and theoretical values of  $R_{BCS}$  as a function of the mean free path  $l$  of the niobium material, as shown in figure 4.4.  $R_{BCS}$  was measured for a number of different cavities and was shown to have good correlation with the theoretical predictions, displaying a minimum  $R_{BCS}$  when  $l$  was comparable to  $\xi_0$  [2]. This is an important result as it shows that  $R_{BCS}$  has a minimum 4.2 K value for a  $l$  which is typical of niobium thin films, corresponding to RRR of approximately 30 [65].

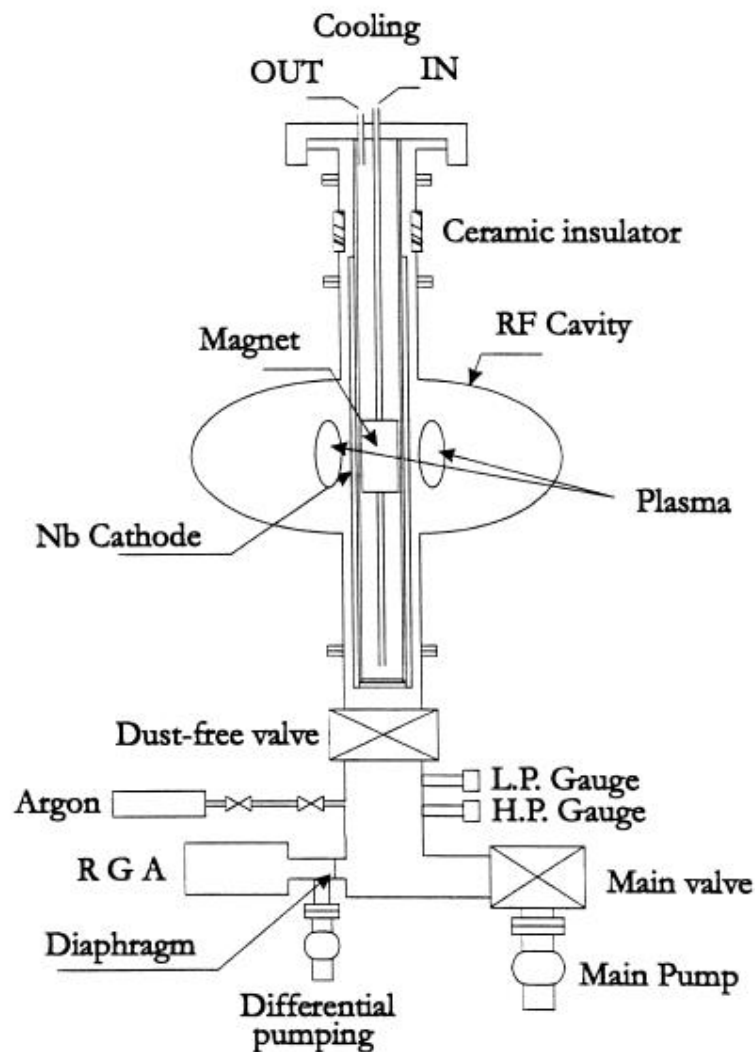


Figure 4.3. The setup for depositing single cell cavities by DC magnetron sputtering at CERN [2] (reproduced with permission from Elsevier).

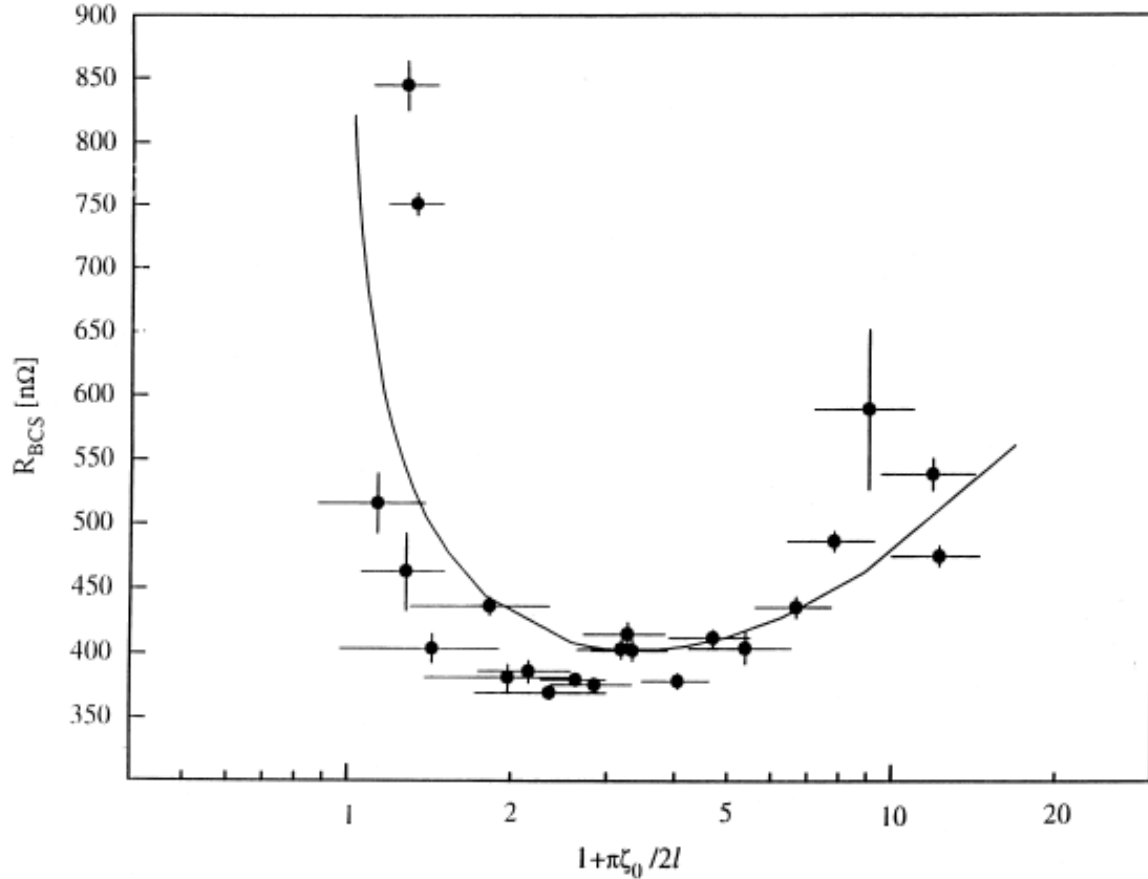


Figure 4.4. The dependence of  $R_{BCS}$  on the mean free path  $l$  at 4.2 K.  $\xi_0$  was assumed to be 33 nm. The solid line was the result of a theoretical calculation of  $R_{BCS}$  [2] (reproduced with permission from Elsevier).

Niobium thin film quarter wave resonators (QWR) were produced by DC bias diode sputtering to reach accelerating gradients up to  $4.5 \text{ MVm}^{-1}$  [66]. The OFHC substrates used for the niobium thin film QWR were first polished by tumbling and then electropolished. The substrate was then baked inside the deposition chamber for a few days at  $700 \text{ }^\circ\text{C}$ . It was found that the vacuum was slightly deteriorated due to residual gases that were released from the brazed joints of the cavity substrate during baking.

The most recent interest in thin film cavity technology is for the HIE-ISOLDE project at CERN, which requires 32 superconducting QWR [67]. Each cavity has a design frequency of 101 MHz and will be operated at 4.5 K with an  $E_{acc}$  of  $6 \text{ MVm}^{-1}$  and  $Q_0$  of  $4.5 \times 10^8$ . The cavity substrate is OFHC copper which is first chemically polished using SUBU before passivation with sulfamic acid [68]. The substrate is then cleaned using an 8 bar ultrapure water rinse in a class 100 cleanroom. The substrate is then baked under vacuum at between  $635$  and  $655 \text{ }^\circ\text{C}$  for 48 hours. Finally, a non-evaporative getter pump is activated inside the deposition chamber to better pump the vacuum system before the deposition

starts. Films are coated by DC bias diode sputtering in an argon pressure of 0.2 mbar using 8kW power and a substrate temperature between 315 and 625 °C. The deposition temperature must be smaller than the substrate baking temperature so that the substrate does not outgas as the film is being deposited. Thus, residual gasses such as hydrogen are less likely to contaminate the film [1]. The deposition is halted once the temperature gets too high, and the cavity is allowed to cool before sputtering is started again. Early test cavities have been produced which have performed better than the design specifications for the machine, with  $Q_0$  of  $2 \times 10^{-9}$  at  $6 \text{ MVm}^{-1}$  [54]. A dummy cavity was used to deposit on witness samples at different regions of the complex QWR geometry and showed that the deposited niobium film quality varied from region to region; particularly, the film formed with voids between grains opposite the edge of the cathode [67].

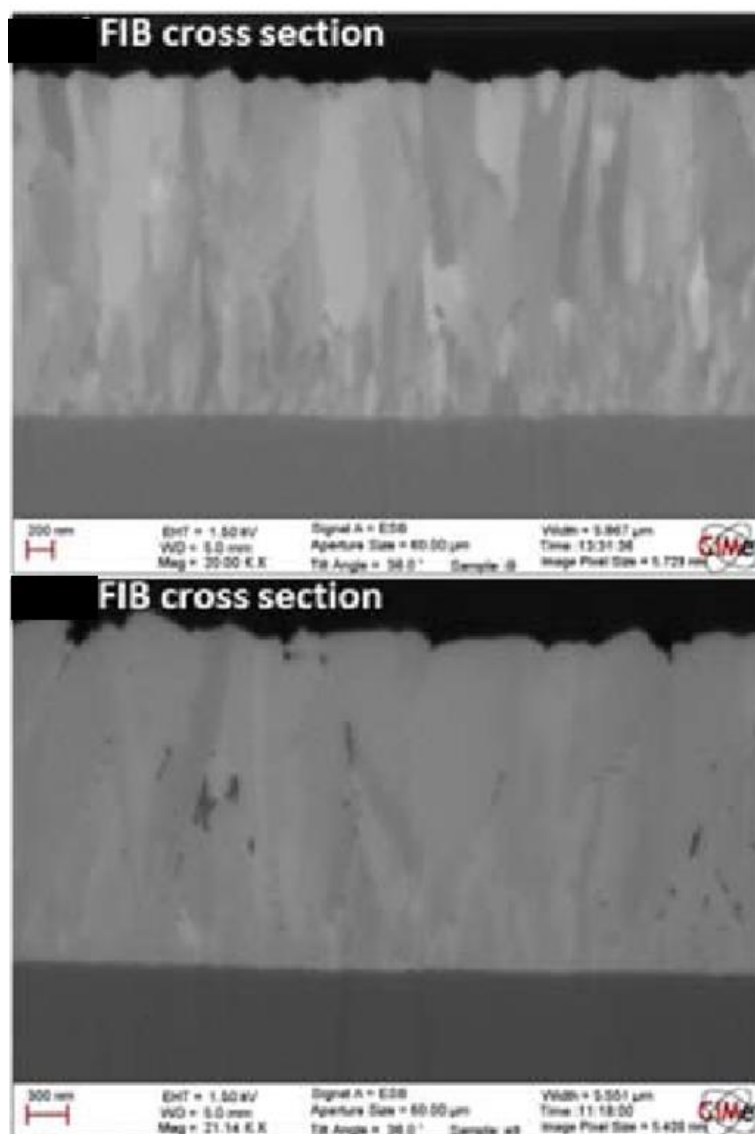


Figure 4.5. FIB cross sections of witness samples deposited by DC bias diode onto different locations of a HI-SOLDE test cavity [67]. The upper film shows a densely packed grain structure whereas the lower image shows voids between grains. Both images were taken from different locations of the same deposited cavity (CC BY 3.0).

#### 4.4. Niobium thin films deposited by energetic condensation methods

Energetic condensation is a term used to describe a wide range of deposition processes where a significant fraction of the target species becomes ionised with energies of approximately 10 eV or greater. The high energy bombarding ions can activate surface and subsurface diffusion processes. Ions can be implanted into the film once their energy is large enough. Implanted ions promote displacement cascades that are followed by a thermal spike and atomic scale heating. The atoms in the affected volume can be considered as a transient fluid and have a high mobility. Large amplitude thermal vibrations occur once the atoms find a fixed place. The thermal vibrations promote further diffusion and migration of dislocations or interstitials and adatom mobility at the film surface. If the energy of the sub-planted ions becomes too large then defects are generated that can increase the intrinsic film stresses [69]. Typically, high energy ion bombardment should be tailored so that the arriving ions have energies between the surface displacement and bulk displacement energy of the deposited material. Thus, relatively defect free films can be deposited which exhibit epitaxial growth [70]. All forms of energy from the bombarding ions contribute to non-local heating of the deposited film and shift the process conditions into a higher homologous temperature. Thus, the ion bombardment replaces conventional substrate heating and allows dense films to be formed at relatively low temperatures [71].

HiPIMS is an energetic condensation technique which allows gasless sputtering for materials that have large sputter yield [72]; attempts to self-sputter niobium have been unsuccessful. Collisions between sputtered ions and the process gas account for the energy tail displayed in figure 4.6 [73]. Thus, each HiPIMS pulse produces a range of different ion energies.

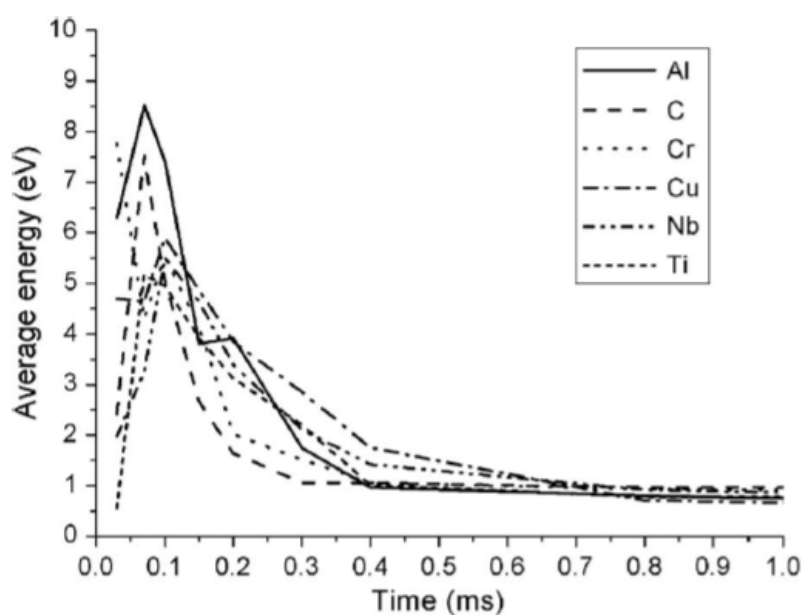


Figure 4.6. Average ion energies in eV over time following the initiation of a HiPIMS pulse [73] (©2011 IEEE).

Study of the minimum sputter gas pressure that can be used to ignite a stable HiPIMS plasma is discussed in [74]. The study found that the pulse repetition rate was crucial in determining the required gas pressure when using argon process gas. The minimum gas pressure was approximately  $8.4 \times 10^{-4}$  mbar for a repetition rate of 1 – 2 kHz. Krypton has since been proposed as “preferable to argon as a HiPIMS process gas as the former tends to damp plasma instabilities [75].”

HiPIMS has been used to deposit niobium films whilst observing the plasma characteristics and resulting film morphology [76]. The authors of the study performed optical emission spectroscopy in a small test facility using a planar magnetron with pulse durations of between 50 and 200  $\mu$ s and at frequencies of between 50 and 500 Hz. Samples that were to be tested for morphological analysis were deposited using a cylindrical magnetron into a dummy cavity containing copper coupons at various locations. The study found that the plasma was made up of both  $\text{Nb}^{1+}$ ,  $\text{Nb}^{2+}$ ,  $\text{Ar}^{1+}$  and  $\text{Ar}^{2+}$  ions with a ratio of roughly 10:1 of the 1+:2+ ions in both cases. The ratios of  $\text{Nb}^{2+}$  and  $\text{Nb}^{1+}$  within the plasma were plotted as a function of both the peak plasma current and pulse duration using the relative intensities of observed optical emission lines. The largest ratios of high energy niobium ions occurred for the largest powers and smallest pulse durations. XRD examination of the samples deposited with  $\text{Nb}^{2+}/\text{Nb}^{1+}$  ratios of  $\geq 0.65$  preferentially grew in the (110) orientation with small peaks relating to the (211) and (220) orientations. The authors quoted that the presence of the (211) and (220) peaks were evidence of enhanced disorder in the niobium lattice. The study also presented SEM images taken of a range of films either deposited by low energy DC magnetron sputtering or HiPIMS with peak currents of 50, 150 or 200 A; the images appeared to show the level of disorder to be inversely proportional to the current density at the target surface.

A HiPIMS niobium film was deposited onto a copper cavity substrate by a collaboration between Sheffield Hallam University and CERN [77]. The deposition system used a cylindrical magnetron to deposit onto a 1.3 GHz cavity which acted as the vacuum chamber and anode. Krypton sputter gas was used during the deposition process at a pressure of  $4.3 \times 10^{-3}$  mbar. The HiPIMS power supply was set to pulse with a frequency of 500 Hz and a pulse duration of 200  $\mu$ s. The RF measurements revealed an initial surface resistance of 43 n $\Omega$  at 2 K which equated to a quality factor of  $6 \times 10^9$  at 2 MV/m. The quality factor then dropped linearly with increasing acceleration field before quenching at approximately 11 MV/m. The authors stated that the theoretical  $R_{BCS}$  at 2 K and 1.3 GHz is approximately 8 n $\Omega$  therefore the major fraction of the measured surface resistance is attributed to the residual resistance of the film. The same film displayed approximately an order of magnitude smaller quality factor at 4.2 K. Further study of the niobium film described a  $T_c$  of 9.4 K, RRR of 16.7, mean free path of 42 nm and London penetration depth at 0 K of 50 nm. The surface resistance of the same cavity was later tested after different cooling cycles and a cavity bake at 150  $^\circ$ C for 50 hours

[78]. Cooling rates of 236 mK/s and 72 mK/s were tested for the unbaked cavity and rates of 330 mK/s and 113 mK/s for the baked cavity. The authors of the study concluded that  $R_s$  was smaller by approximately 20 % for the faster cooling rates in both instances. Baking the cavity increased  $R_s$  relative to measurements performed before baking.

The HiPIMS 1.3 GHz cavity deposition system was later adapted, by adding earthed anodes close to the upper and lower extremities of the cylindrical cathode, so that a -20 V bias could be applied to the cavity substrate [79]. RRR of the deposited film increased from 21 for a film deposited onto a grounded substrate to 30 for a film deposited onto the biased substrate. The niobium grain size was larger for films deposited with an applied bias relative to those deposited onto a grounded substrate. The same deposition setup was used to deposit witness substrates at angles of 0, 45 and 90 degrees relative to the direction of the target [80]. The authors found that the incident angle of the arriving sputtered material dictated the direction of growth of columnar film grains when deposited by DC magnetron sputtering with either a grounded or biased substrate and for films deposited by HiPIMS onto a grounded substrate. Films deposited by HiPIMS with an applied bias of either -50 or -100 V resulted in more densely packed grains which exhibit no preferred growth direction, all other films grew with grains oriented towards the target.

A novel proposal for using HiPIMS to deposit onto a biased cavity structure was proposed in [81]. Two magnetrons are used instead of one and allows the second magnetron to act as the anode. The polarity of each magnetron is changed with the same frequency as the HiPIMS pulse. The cavity itself no longer participates in the plasma discharge process and therefore can be biased by an independent power supply.

A range of niobium films have been deposited using vacuum arc deposition onto both copper and aluminium oxide. The vacuum arc produces multiply charged niobium ions, typically +3, and with energies larger than 100 eV [82]. Films displayed RRR of between 20 and 60.  $T_c$  was measured between 8.70 and 9.26 K but seemed to show no trends that linked  $T_c$  to changes in the process conditions. The films displayed relatively large grains with few intra-grain defects and strain when compared to films deposited by DC magnetron sputtering [83].

Electron cyclotron resonance (ECR) is an energetic condensation technique which has been showing promising results for niobium thin film samples. The ECR process begins with a neutral niobium vapour that is produced by irradiating a target with an electron beam. A combination of both perpendicular magnetic and RF electrical fields then ionise the neutral niobium atoms in the vapour. The niobium ions are almost always singly charged with energy of 64 eV. Thus, the application of a substrate bias allows the ECR process to tune the energy of deposited ions to a desired value as oppose

to producing a range of ion energies [84]. An ECR film was deposited onto a flat copper substrate and tested for  $R_s$  using the quadrupole resonator at CERN [85]. The copper substrate was first heated to 1050 °C to recrystallize and anneal defects. The substrate was heated to 360 °C during the deposition. The deposition proceeded in two phases. The first phase used high energy niobium ions at 184 eV to deposit a film thickness of 100 nm and nucleate the grains. The second phase reduced ion energy to 64 eV so that the overlying film was relaxed and contained few internal stresses. The process resulted in a substrate / film interface which spanned 31.8 nm, whereas films deposited at lower ion energy have an interface of approximately 10 nm. The thicker interface produces a dense and strong link between film and substrate with good adhesion. The resulting ECR film had a RRR of 67 and grain sizes of up to 50  $\mu\text{m}$ . Surface resistance measurements of the thin film sample at 400 MHz showed a  $Q$  slope which was similar in shape to that of a bulk niobium sample with RRR of 47. However, the thin film exhibited  $R_s$  of approximately 70 n $\Omega$  compared to 45 n $\Omega$  for the bulk sample. A third niobium / copper film deposited using the CERN DC magnetron sputtering process was tested for comparison and displayed similar  $Q_0$  to the ECR film but with a much sharper  $Q$  slope.

Niobium films have been deposited by ion-beam-assisted deposition to test the effects of ion bombardment with very high energy ions up to 1000 eV [86]. Ion energies of 0, 250, 500 and 1000 eV were tested resulting in ion to atom ratios of 0 to 0.4. The ion beam was orientated at 50 ° to the plane of the substrate and resulted in columns inclined towards the incident ion direction at the highest tested energy of 1000 eV. Columnar grains with domed tops grew for all energies however the column width increased with ion energy and film thickness. The largest ion energies resulted in porous films with high surface roughness. Films deposited with ion to atom ratios of less than 0.16 resulted in smoother surfaces than standard deposition techniques such as DC magnetron sputtering. The authors state the preferential re-sputtering of grains grown in certain directions relative to the incident beam lead to the enhanced porosity and roughness at the highest energies.

#### 4.5. Deposition of superconducting films other than niobium

Table 4.1 Material parameters of a selection of superconducting materials [17].

Material	$T_c$ (K)	$\rho_n$ ( $\mu\Omega\text{cm}$ )	$H_c(0)$ (T)	$H_{c1}(0)$ (T)	$H_{c2}(0)$ (T)	$\lambda$ (nm)	$\Delta$ (meV)	$\xi$ (nm)
Nb	9.23	2	0.2	0.18	0.28	40	1.5	35
NbN	17.3	70	0.23	0.02	15	200-350	2.6	3 - 5
NbTiN	17.8	35	-	0.03	15	150-200	2.8	5
Nb <sub>3</sub> Sn	18	8-20	0.54	0.05	28	80-100	3.1	4
V <sub>3</sub> Si	17	4	0.72	0.072	24.5	179	2.5	3.5
Nb <sub>3</sub> Al	18.7	54	-	-	33	210	3	-
Mo <sub>3</sub> Re	15	10-30	0.43	0.03	3.5	140	-	-
MgB <sub>2</sub>	40	0.1-10	0.43	0.03	3.5-60	140	2.3-7.2	5
Pnictides	30-55	-	0.5-0.9	30	50-135	200	10 - 20	2

As discussed in section 2, good candidate superconductors for SRF application should have as high  $T_c$  and low  $\rho_n$  as possible so that  $R_{BCS}$  can be minimised and  $Q$  factor can be maximised. A large  $H_{SH}$  is also preferred as it allows large accelerating gradients. Table 4.1 details a selection of promising materials for SRF application.

Figure 4.7 displays the predicted  $R_{BCS}$  at 4.2 K for a 500 MHz SRF cavity that was built using a selection of the materials described in table 4.1 [87, 88]. Figure 4.7 highlights how certain materials can perform better than niobium when used in SRF cavities at 4.2 K.

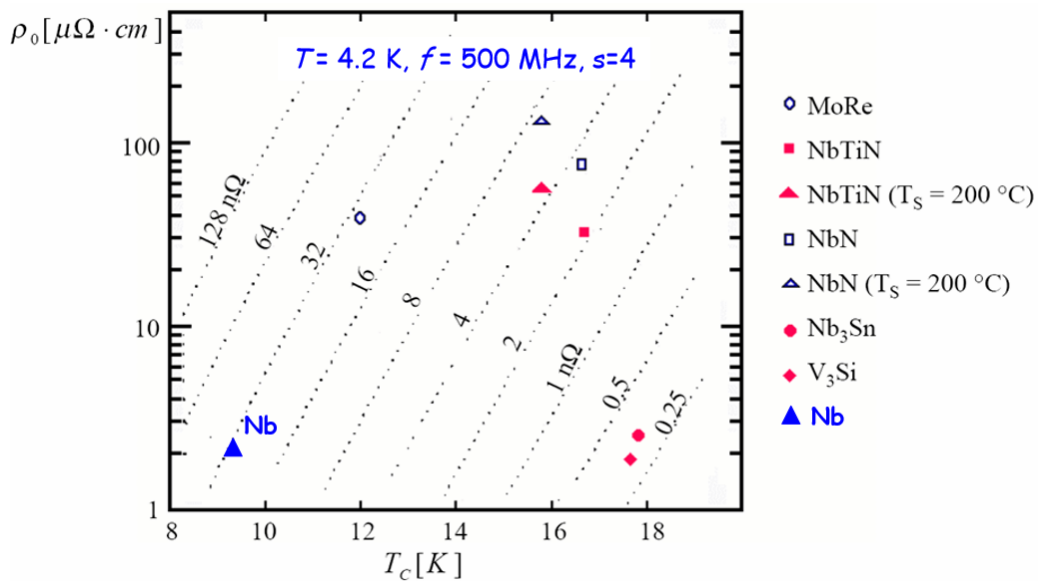


Figure 4.7. Model of  $R_{BCS}$  at 500 MHz as a function of  $T_c$  and normal state resistivity for many superconducting materials [89] (CC BY 3.0).

Niobium nitride (NbN) is a B1 binary compound which has an NaCl structure. The material can form with many different phases however the cubic phase with  $T_C$  of up to 17.3 K and a lattice parameter of 4.388 Å is the only thermodynamically stable phase at room temperature [17]. Thermal diffusion of nitrogen into niobium at 1400 °C was used to produce niobium nitride SRF cavities in [90]. Films have also been successfully deposited by reactive magnetron sputtering in [91]. The sputtered films were deposited at 600 °C and had  $T_C$  of 17 K. However, the films had extremely high normal state resistivity. The high resistivity was thought to occur because of weakly bounded grains that are separated by many voids and is typical of sputtered niobium nitride thin films.

Niobium titanium nitride (NbTiN) has a  $T_C$  of up to 17.8 K and has  $\rho_n$  as low as 35  $\mu\Omega\text{cm}$ . Reactive sputtering has been used to deposit niobium titanium nitride in [92].  $\rho_n$  was below what is typically exhibited by niobium nitride and was found to drop as the nitrogen content was increased. The small  $\rho_n$  when compared to niobium nitride is most likely caused by a reduction in the number of nitrogen vacancies, as titanium is a good getter of nitrogen. A 1.5 GHz copper cavity was deposited with niobium titanium nitride at CERN [93]. The cavity was seamless and treated with SUBU chemical polishing. The film was deposited by reactive magnetron sputtering in an argon and nitrogen atmosphere using a cylindrical magnetron; the target was a niobium<sub>0.35</sub> / titanium<sub>0.65</sub> alloy. The cavity substrate was maintained at 265 °C during deposition. The measured  $R_{BCS}$  of the cavity was 55 n $\Omega$  at 4.2 K. The maximum accelerating voltage was limited to 10 MV<sup>-1</sup>.

Niobium tin (Nb<sub>3</sub>Sn) is an A15 superconducting material with  $T_C$  of 18 K and a  $\rho_n$  as low as 8  $\mu\Omega\text{cm}$ . The niobium tin A15 phase occurs over the range of 18 to 25 at.% tin; however, the smallest  $\rho_n$  and highest  $T_C$  is expected to occur for niobium tin that is formed close to 25 at.% tin. Niobium tin is of particular interest for SRF application as it has a theoretically large  $H_{SH}$  of 545 mT [94]. Vapour phase diffusion has been used to produce niobium tin SRF cavities. 1.5 GHz bulk niobium cavities were heated within a vacuum furnace to approximately 1200 °C within a tin vapour to produce a niobium tin layer at the cavity surface which was a few microns thick [45]. The cavity had a  $Q_0$  of just above 10<sup>10</sup>, before the onset of Q drop at 15 MVm<sup>-1</sup>.

Vanadium silicon (V<sub>3</sub>Si) is an A15 compound with  $T_C$  up to 17 K and  $\rho_n$  as low as 4  $\mu\Omega\text{cm}$ . The superconducting A15 phase occurs between 19 and 25 at.% silicon however the highest  $T_C$  and RRR values are obtained at 25 at.% silicon [88]. A consideration of using vanadium silicon for SRF application is the large diffusion coefficient of vanadium into niobium. Therefore, a niobium substrate cannot be used without a protective interlayer. Vanadium silicon films were deposited by magnetron sputtering to produce films with  $T_C$  of 16.3 K and resistivity of 3 – 5  $\mu\Omega\text{cm}$ .  $R_{BCS}$  of the sputtered film

was measured at 4.2 K using a stripline resonator at 3.5 GHz and was smaller than for a bulk niobium sample [95].

Magnesium diboride ( $MgB_2$ ) is a superconducting material with high  $T_c$  of 39 K and has a double band gap of 2.7 meV and of 6.7 meV [96]. The best performing magnesium diboride thin films have been deposited by hybrid physical / chemical vapour deposition [97]. Magnesium diboride films that were tested for RF performance using a 10 GHz stripline resonator displayed a  $Q_o$  of  $10^4$  at 20 K [17].

#### 4.6. Superconductor – insulator – superconductor multilayer films

Superconductor – insulator – superconductor (SIS) multilayer films have been proposed as a method of providing magnetic shielding to an underlying superconducting layer [98]. SIS multilayers can theoretically allow for higher accelerating gradients. Figure 4.8 shows the distribution of the magnetic field in each superconducting layer. The magnetic field penetrates into each superconducting layer. However, the underlying layers are shielded from those above and effectively see a weaker magnetic field. Thermomagnetic avalanches throughout the whole multilayer are inhibited as each superconducting layer is decoupled from the next by an insulating layer. Consideration must be taken for the thickness of the insulating layers so that they cannot act as Josephson junctions.

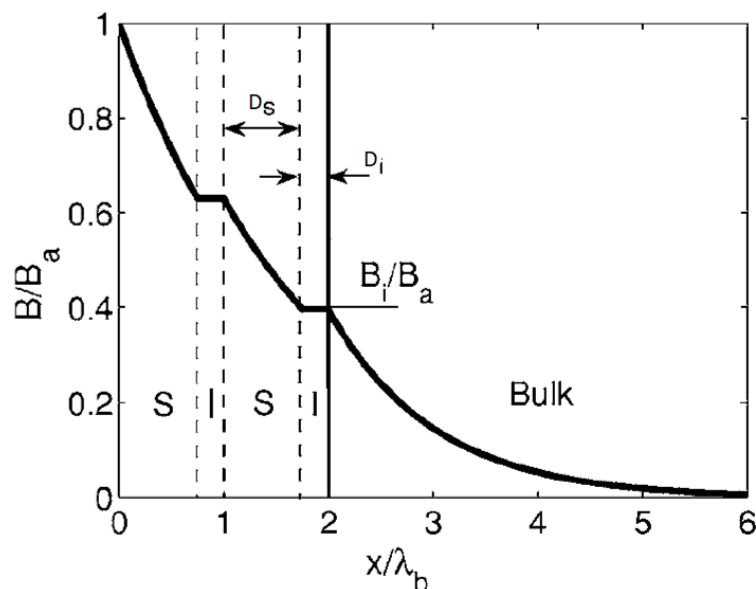


Figure 4.8. Distribution of the total magnetic field  $B_o$  in each layer of an SIS multilayer film.  $D_S$  is the superconducting layer thickness and  $D_I$  is the insulating layer thickness. Only a  $0.4 B_o$  reaches the bulk underlying superconductor in this particular SIS model. The bulk layer can either be a bulk superconductor or thick superconducting film [98] (reproduced with permission from AIP).

If the shielding superconducting layers have a thickness  $D$  which is less than  $\lambda_L$  of the material, then equation 4.1 applies. Superconductors with  $\xi < \xi^{Nb}$  provide the best screening layers in an SIS multilayer because they can have  $B_{C1}$  that is much larger than that of Nb if the layer is thinner than  $\lambda_L$ . The enhancement of  $B_{C1}$  relative to film thickness for a selection of superconductors with  $\xi < \xi^{Nb}$  is shown in figure 4.9.

$$B_{C1} = \frac{2\phi_0}{\pi d^2} \ln \frac{d}{1.07\xi} \quad d < \lambda \quad (4.1)$$

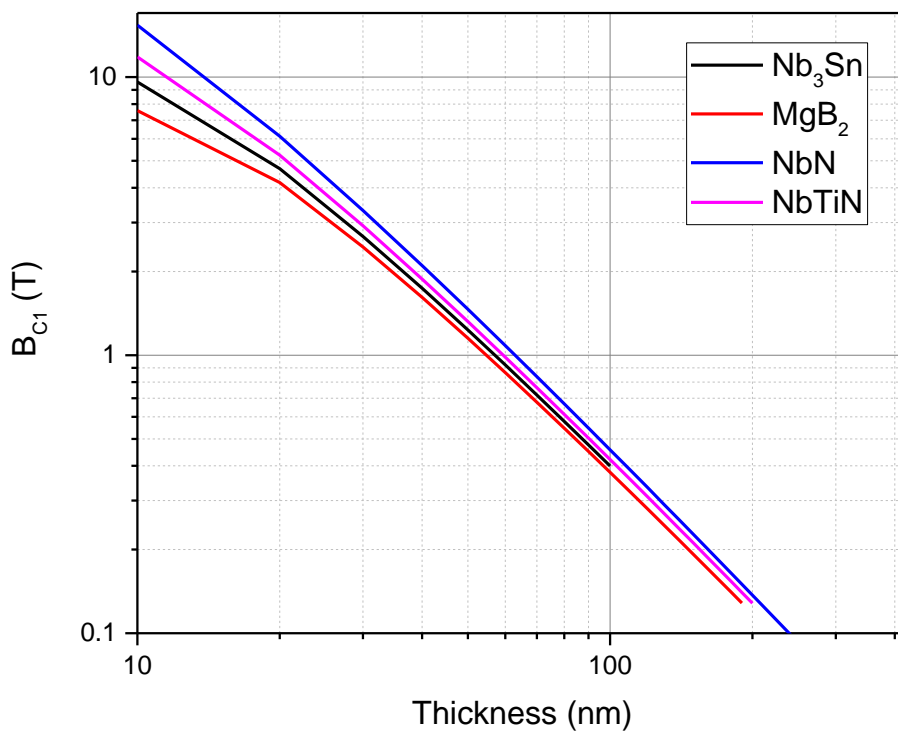


Figure 4.9. Enhancement of  $B_{C1}$  for a range of thin films made up of materials with  $\xi < \xi^{Nb}$ . The theoretical  $B_{C1}$  approaches approximately 10 T for films which are 10 nm thick.

It is impossible to have perfect screening of the bulk superconducting layer if the shielding S layers have a thickness smaller than  $\lambda$ . Thus, the optimum thickness of the S layer can be modelled so that there is both significant decay of the magnetic field, but the film should still be thick enough to protect the bulk layer. Such optimisation has been modelled for various materials in [99].

#### 4.7. The origins of the thin film Q slope

A receding Q slope is observed for both bulk niobium and thin film niobium cavities as acceleration gradient increases. The shape of the slope for each is shown in figure 4.10. Niobium thin films deposited onto copper cavities have produced very high Q factor at low accelerating voltage. However, Q drops below that of bulk niobium at around 15 MV/m.

Bulk niobium cavities had previously suffered from steep Q drop at medium and high fields. However, quench fields up to 40 MV/m are now possible through both optimisation of the cavity geometry and preparation. The cavity geometry is designed so as to reduce multipacting. Standard procedure for bulk niobium cavity preparation is to electropolish the niobium surface, followed by low temperature baking at 120 °C for 24 to 48 hours and a final a HF rinse. The electropolishing is performed to reduce field emission at sharp edges. The 120 °C bake is performed to reduce the mean free path of the bulk niobium and therefore reduce  $R_{BCS}$ . The final HF rinse is performed to remove a small increase in  $R_{res}$  that is caused by the 120 °C bake [100]. Nitrogen doping is an alternative treatment which allows for the highest bulk niobium Q factor with the disadvantage of a slightly reduced peak accelerating gradient [101].

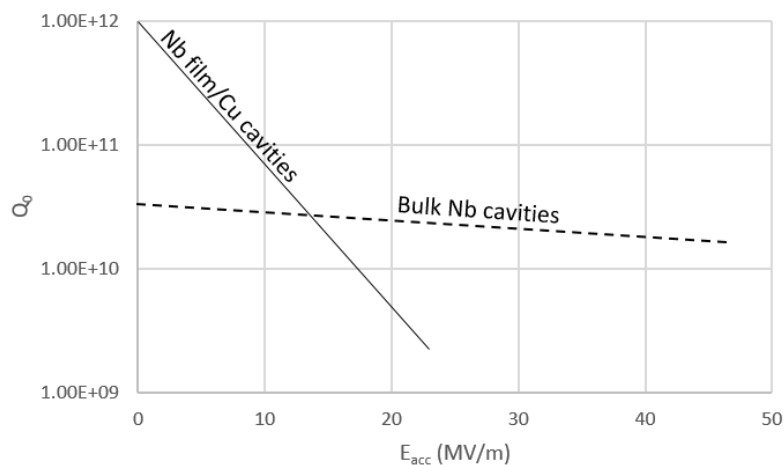


Figure 4.10. Typical Q factor versus accelerating voltage for both bulk Nb and thin film Nb/Cu cavities.

Theories have been proposed to describe the mechanism leading to the sharp Q drop for thin film cavities, however, none are universally accepted. A selection of proposed Q drop mechanisms for thin film cavities are discussed next.

The first Q drop mechanism to be discussed is for losses due to magnetic pinning at non-superconducting inclusions of trapped process gasses which can cluster into solid form. Any external field can become pinned at the normal conducting inclusions and induce losses when subjected to RF fields [50]. However, experiments have been performed which argue against this hypothesis. Films deposited with xenon, krypton or argon process gas have displayed similar residual losses, even

though the volume of trapped argon was approximately 35 times larger than xenon or krypton [2]. Thus, any increase in magnetic pinning that could have occurred at the non-superconducting argon inclusions did not result in an increase in  $R_{res}$ , as might be expected. A possible reason for this observation is that the small dimension of the gas inclusions, 3 nm across when compared to  $\approx 36$  nm for  $\xi_0$ , will not affect the formation of Cooper pairs.

The relatively large volumes of grain boundaries within thin films has been proposed as a possible source of the  $Q$  slope. Thin films generally form from smaller grains than bulk niobium, creating a situation where the grain boundaries within the film could act like many weakly linked Josephson junctions. The smaller grained thin films could therefore have a reduced critical current when compared to that of the larger grain bulk material [102, 103, 104]. However, it has been reported that large grain niobium films have a measured  $R_{res}$  which is larger than that of small grain films. Thus, the observations were the opposite of what would be expected if the Josephson junction model for  $Q$  drop was correct [51]. A proposed reason for the worse RF performance for large grain niobium films in [51] is a diminished volume of impurities and dislocations which can act as nitrogen traps. When no nitrogen traps are present then the bulk of the thin film is able to form with hydrides. Hydrides have been shown to increase  $R_{res}$  once the atomic hydrogen percentage reaches 1.4 % [105].

The next  $Q$  drop mechanism to be considered is dependent on the change in superconducting energy gap with changing acceleration field [106]. As the current density of the supercurrent increases up to the maximal current density, then the superfluid velocity  $v_S$  also increases. Equation 4.2 describes the relationship between the energy gap and  $v_S$ ;  $p_F$  is the Fermi momentum and  $m$  is the mass of an electron.

$$\frac{1}{2}m\left(\frac{p_F}{m+v_S}\right)^2 - \frac{1}{2}m\left(\frac{p_F}{m-v_S}\right)^2 > 2\Delta \quad (4.2)$$

Thus, equation 4.2 describes how the superconducting state becomes unstable against Cooper pair creation when  $v_S p_F > \Delta$  i.e. Cooper pairs are more likely to break at high accelerating voltage where the current density and therefore superfluid velocity is large. Cooper pair breaking leads to resistive losses that would cause  $Q$  to drop.

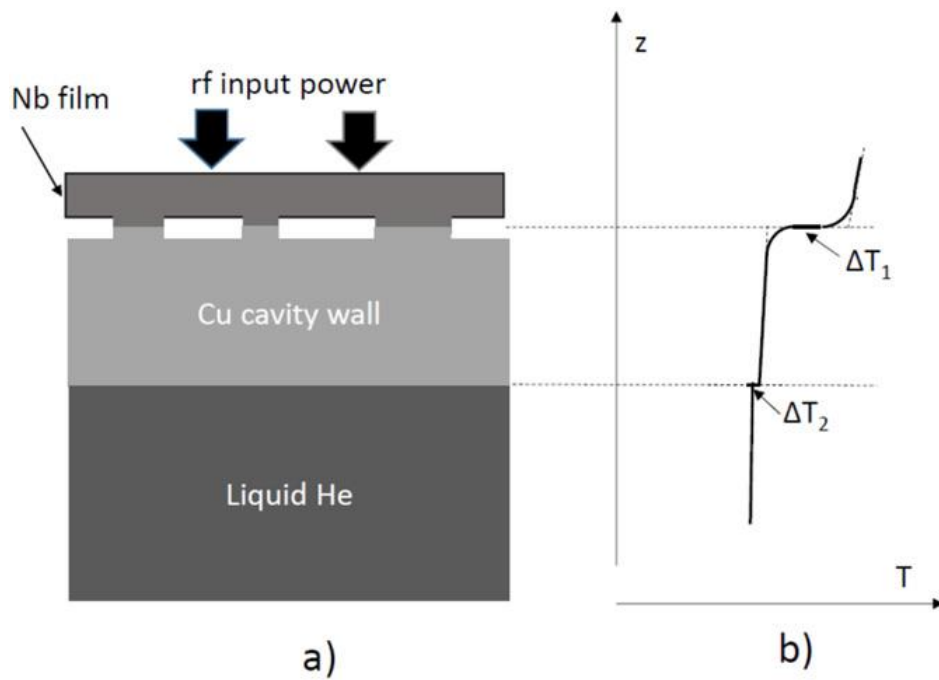


Figure 4.11. A schematic representation of heating due to poor thermal contact of a niobium thin film deposited onto a copper cavity. a) RF input power heats the film surface and b) the related temperature profile through the depth of the RF surface, including the temperature difference at the interfaces between the film and substrate and substrate and liquid helium bath, labelled  $\Delta T_1$  and  $\Delta T_2$  respectively [65] (CC BY 3.0).

A final notable theory leading to  $Q$  drop is due to thermal contact resistance at the interface between niobium film and copper substrate for thin film cavities [65]. The theory describes how  $Q$  drop should be steep for thin film cavities if there is poor thermal contact of the film to the copper cavity substrate material. Figure 4.11 shows how poor thermal contact could lead to temperature differences across the niobium / copper and copper / LHe interfaces. If the theory is correct, then a small temperature increase of the superconducting film relative to the LHe results in elevated  $R_S$  and quenches at relatively low fields, as is experimentally observed.



## 5. Analytical techniques

### 5.1. Morphological Analysis

#### 5.1.1. X-ray diffraction crystallography

XRD analysis is used for characterising crystalline materials. XRD can provide information on crystal orientation, crystal grain size, strain, stress and defect structure. The basis of the technique is to bombard a crystalline solid with x-rays so that they can be scattered by the atoms of the sample. Most x-rays can scatter in any direction and therefore destructively interfere. Constructive interference only occurs when certain geometric requirements are met, as described by Bragg's law.

Bragg's law is defined using the wavelength of the x-rays  $\lambda$ , the spacing between crystal planes  $d$  and the diffraction angle  $\vartheta_{dif}$ , as shown in Equation 5.1; where  $n$  is an integer.

$$n\lambda = 2d \sin\theta_{dif} \quad (5.1)$$

Constructive interference of x-rays will only occur for certain  $\vartheta_{dif}$  and if  $\lambda$  remains constant. Thus,  $\vartheta_{dif}$  can be measured and used to calculate  $d$  [107].

A range of different information can be obtained once  $d$  is known; most importantly the lattice plane orientations of the sample. The plane orientations of a cubic system are defined by the three integers,  $h$ ,  $k$  and  $l$ , known as the Miller indices. If we assume that a unit cell has three axes,  $a$ ,  $b$ , and  $c$ , then  $h$  will cut the  $a$  axis,  $k$  will cut the  $b$  axis and  $l$  will cut the  $c$  axis. The Miller index of the lattice planes is given by equation 5.2. Equation 5.2 includes the lattice parameter  $a_0$  which is equal to the lengths  $a = b = c$  for cubic systems.

$$a_0 = \frac{d_{hkl}}{(h^2+k^2+l^2)} \quad (5.2)$$

$a_0$  is well documented for most elements and therefore the Miller index can be obtained directly from  $d$  using a database (usually provided with the XRD device). If  $a_0$  is unknown, then it is still possible to solve equation 5.2 for all possible  $h$ ,  $k$ , and  $l$ .

Conversely, measurement of  $d$  can allow the calculation of  $a_0$  assuming that the crystal orientation of the sample is known. Comparing small sample to sample shifts in  $a_0$  can be a useful tool to define relative differences in internal stresses. Shifts to longer  $a_0$  imply the presence of tensile stress whilst shifts to shorter  $a_0$  implies a compressive stress.

Another important physical property which can be obtained from XRD spectra is the average grainsize of the crystallites. The full width half maximum of each reflection peak  $B$  is inversely

proportional to the average crystallite size  $L$ , as shown in equation 5.3; where  $K$  is a constant depending on the material being analysed [108].

$$B(2\theta) = \frac{K\lambda}{L\cos\theta} \quad (5.3)$$

It should be stressed that equation 5.3 is intended for use with measurements of powder samples. Measurements of thin film samples can exhibit a component of line broadening due to internal stress or strain and therefore effects the accuracy of the calculated value [32].

Typical XRD devices use monochromatic x-ray sources. When analysing using the conventional Bragg – Brentano configuration to perform XRD then the x-ray beam moves through an angle,  $\vartheta$ , which is relative to the plane of the sample surface. As the orientation of the beam is moved through  $\vartheta$  then the angle of a scintillation detector is moved through  $2\vartheta$  and the intensity of x-rays are measured. The x-rays will only show intensity spikes at angles equal to  $2\vartheta_{diff}$ . There is usually a strong signal from the substrate material when using the Bragg – Brentano configuration to analyse thin film samples as x-rays can be detected from up to microns into the surface of the sample.

Alternatively, grazing incidence XRD can be performed with the x-ray beam fixed at between 1 and 10 °; only the scintillation detector is moved. The shallow incident angle of the x-ray beam reduces its penetration depth and allows the very surface of the sample (10's to a few hundred's on nm) to be probed. Figure 5.1 illustrates the penetration depth of x-rays into niobium with incidence angles between 0 and 2 ° [109]. The shallow penetration depth of grazing incidence XRD allows thin films to be measured without a signal arising from the substrate material.

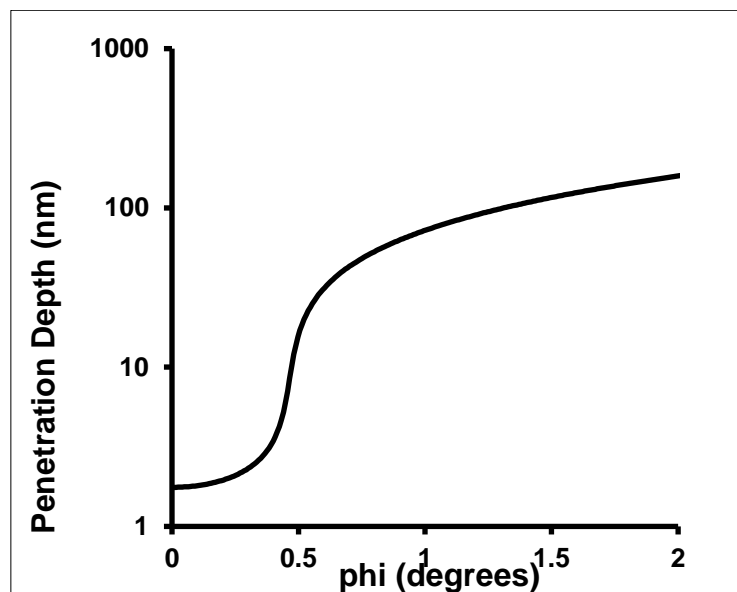


Figure 5.1. Penetration depth of x-rays into a niobium thin film versus the grazing angle Phi.

All XRD or grazing incidence XRD measurements performed during this study used one of the following two devices. A Rigaku SmartLab device using a copper x-ray source to produce x-rays with wavelength  $K\alpha_1$  of 1.54059 Å and  $K\alpha_2$  of 1.54441 Å, with a ratio  $K\alpha_2/ K\alpha_1$  of 0.5; or a Bruker D8 Discover device using a cobalt X-Ray source to produce x-rays with wavelength  $K\alpha_1$  of 1.78901 Å and  $K\alpha_2$  of 1.79290 Å with ratio  $K\alpha_2/ K\alpha_1$  of 0.5. The step size between measurement points was 0.01 °. All grazing incidence XRD measurements were performed with a grazing angle of 2 °. All calculations of  $a_0$  were performed using  $\vartheta$  that was equal to the maximum intensity of the largest diffraction peak from each measurement and using the wavelength of  $K\alpha_1$ .

Possible errors in the XRD technique arise from the specimen not being centred correctly on the axis of the diffractometer, the roughness of the sample surface, the divergence of the x-ray beam and the width of the diffraction peaks; all of which affect the accuracy of the measurement of  $\vartheta_{dif}$  and any subsequent calculations. The error in the measurement of peak position was therefore set to  $\pm 0.01$  ° for all XRD or grazing incidence XRD measurements performed during this research project. The major component of the measurement uncertainty was considered to be the relatively broad diffraction peaks, ranging from approximately 0.3 to 1.5 °, for all deposited films.

### **5.1.2. Scanning electron microscopy and electron backscattering diffraction**

A SEM is used to produce reconstructed images of a surface with a resolution of up to 5 nm. The first principle of operation is to scan an electron beam across the surface to be imaged. The electron beam interacts with the surface atoms of the sample and results in either backscattering of electrons or the release of secondary electrons. Computer software is then used to reconstruct an image based on the energies of electrons that arrive at various different detectors.

Secondary electrons are emitted from very near to the surface of the sample. They usually have low energy and occur due to inelastic interactions between the electron beam and the sample. Secondary electron detectors are used to analyse the topography of the sample surface.

A backscattered electron detector analyses electrons which originate from elastic collisions between atoms and electrons within a wide region of the beam interaction volume. Larger atoms can scatter many more electrons than lighter elements due to the relative cross sections of the atoms. The number of scattered electrons can also vary due to the relative direction of the crystal lattice of the sample relative to the detector; the effect is called channelling contrast. Thus, the channelling contrast allows grain boundaries to be distinguished on an image.

Electron backscatter diffraction (EBSD) is used to characterise sample microstructure in more detail than a regular backscattered electron detector. For EBSD, samples are tilted 70 ° from horizontal

and then bombarded by the electron beam. The atoms within the sample scatter a fraction of the arriving electrons, forming divergent electron sources close to the sample surface. The electrons which are incident from atomic planes satisfy the Bragg law, where  $\lambda$  is the wavelength of the bombarding electrons. The scattered electrons are used to produce characteristic Kikuchi patterns on a fluorescent phosphorus screen and can be imaged by a camera within the EBSD detector. Computer software is then used to index the crystal orientations that are observed in the image and can be presented as an orientation map [110].

SEM images presented during this study were taken using either an FEI Quanta 3D microscope fitted with a field emission gun and Oxford Instruments SDD EDX detector with the Oxford Instruments quantification software, or using a Zeiss Ultra 55 microscope.

### 5.1.3. X-ray photoelectron spectroscopy

Surface analysis by XPS provides an analysis of the elemental composition and chemical state of atoms at the surface of a material. XPS is performed by first irradiating the sample with x-rays and then analysing the energy of the emitted electrons. Typical x-ray energies used to irradiate the sample are Mg K $\alpha$  (1253.6 eV), Al K $\alpha$  (1486.6 eV) or Al K $\alpha$  (1486.7 eV), where K $\alpha$  refers to electron transitions from a 2p orbital to the innermost K shell. The bombarding electrons interact with sample atoms and cause the emission of x-rays due to the photoelectric effect.

All emitted electrons have a kinetic energy  $KE$  which is a function of the photon energy  $h\nu$ , the binding energy of the atomic orbitals from where the electron was emitted  $BE$  and the spectrometer work function  $\phi_s$ .  $KE$  is calculated using equation 5.4.

$$KE = h\nu - BE - \phi_s \quad (5.4)$$

The binding energy can be thought of as the difference in energy between the initial and final state, before and after a photoelectron has left an atom. As each element has a unique set of binding energies then it is possible to identify and determine the relative elemental abundances and chemical states at the surface of a sample.

XPS spectra are made up from electrons released within the uppermost 10 nm of the sample. Thus, the small sampling depth of XPS requires the removal of surface oxide and carbon layers by ion bombardment before a bulk elemental composition can be obtained of a reactive material [111].

#### 5.1.4. Energy-dispersive x-ray spectroscopy

Energy-dispersive x-ray spectroscopy (EDX) is a technique which performs an elemental analysis of a sample surface. The sample is bombarded by a high energy electron beam to stimulate the emission of x-rays. X-rays are emitted by two mechanisms; either the electron beam ejects inner shell electrons from atoms at the surface of the sample or the beam interacts with the nucleus of the atoms at the surface of the sample to produce Bremsstrahlung radiation. Only the x-rays emitted by the ejection of an inner electron are useful for EDX analysis. After the inner shell electron is ejected, the hole is filled by an outer shell electron and the superfluous energy is released as an x-ray. Thus, the emitted x-rays have a characteristic energy that depends on the atomic number of the sample. A detector is used to measure the energy of the emitted x-rays and then the atomic number and relative abundance can be defined. Different spectral lines can be detected for the same element depending on the shell of the initial vacancy and the origin of the electron which fills the hole. The detection limits of the technique are determined by the signal to noise ratio; where the noise is made up of the Bremsstrahlung radiation. The accuracy of the technique can also be effected by overlapping spectral peaks [112].

EDX analysis during this study was performed using an FEI Quanta 3D microscope fitted with a field emission gun and Oxford Instruments SDD EDX detector with the Oxford Instruments quantification software

#### 5.1.5. Rutherford backscattering spectrometry

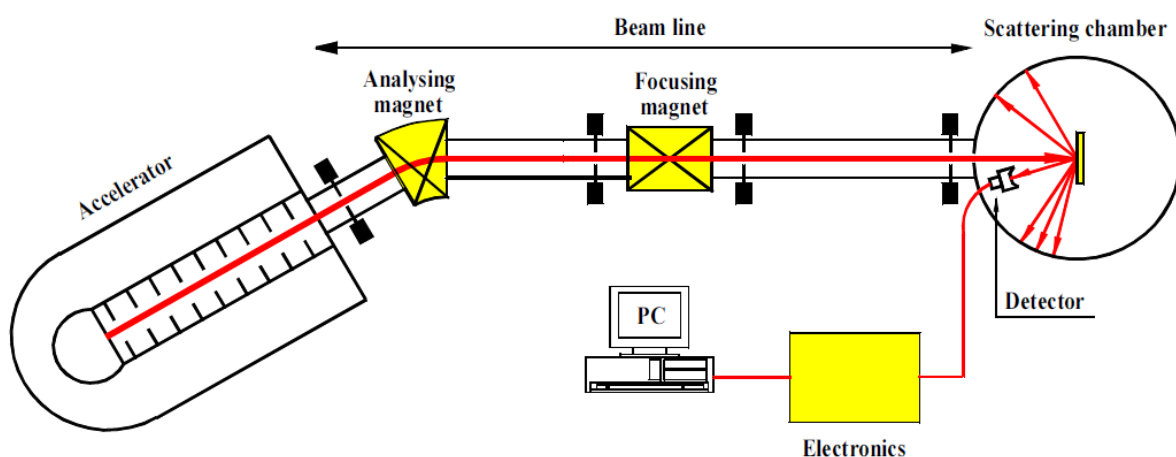


Figure 5.2. Typical experimental setup for RBS [113] (©IAEA 2000).

RBS is a technique used to determine the elemental composition of solid materials. The RBS technique works by bombarding a test sample with an ion beam, resulting in scattering of the beam

and sample atoms. A typical RBS setup is shown in figure 5.2. RBS requires a Van de Graph type accelerator that accelerates the ion beam through several diaphragms and quadruple magnets, used to collimate the beam to a size of approximately  $1 \times 1 \text{ mm}^2$ . The analysing magnet selects ions of a chosen energy. A detector located in the scattering chamber observes the energy spectrum of the backscattered ions. The energy spectrum describes the elemental composition of the sample with all the data handling performed by suitable electronics and a computer program. Bombarding ions are typically  $^4\text{He}^+$  or  $^1\text{H}^+$  with energy of a few MeV; heavier bombarding ions can be used to detect heavy elements [113].

All RBS measurements in this report were performed by E. Alves and N.P. Barradas at the Centre for Nuclear and Technological Sciences in Lisbon, Portugal. Each RBS measurement was performed using a hydrogen beam with  $10^\circ$  angle of incidence,  $165^\circ$  scattering angle and  $25^\circ$  exit angle.

## 5.2. Superconducting performance

### 5.2.1. Four-point probe

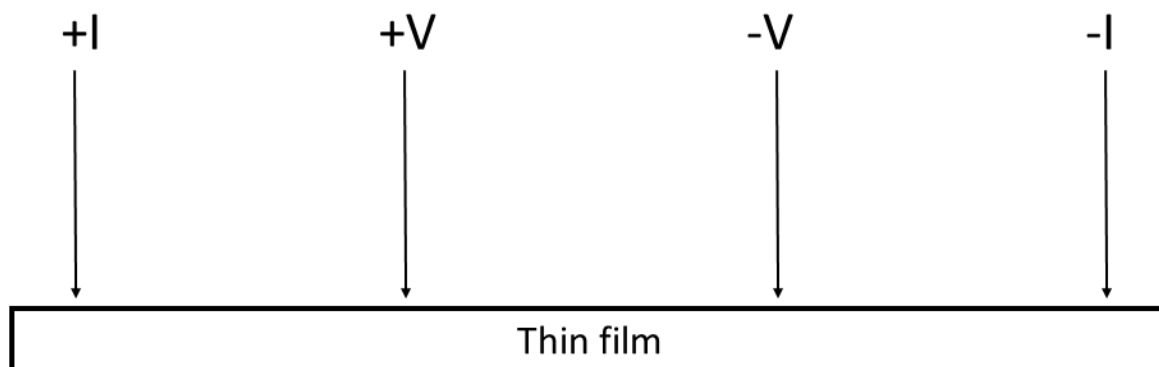


Figure 5.3. Schematic diagram of the four-point probe setup.

A four-point probe allows the measurement of a resistance across a thin film sample. A schematic representation of a four-point probe is shown in figure 5.3. A direct current flows between probes  $-I$  and  $+I$ . The resistance of the sample causes a drop in potential which can be measured across probes  $-V$  and  $+V$ . Thus, a sample can be assumed to be superconducting when the resistance across probes  $-V$  and  $+V$  drops to zero. A four-point probe can be used to measure both  $T_c$  and the residual resistivity ratio (RRR) of a superconducting thin film.

$T_C$  is measured at the transition from normal conducting to superconducting. Three definitions of  $T_C$  can be defined by different points of the superconducting transition as described by figure 5.4.  $T_C^0$  corresponds to the temperature at which resistance drops to zero,  $T_C^{ex}$  corresponds to the extrapolation of the steep transition slope and  $T_C^{on}$  is the onset of the transition [114]. All  $T_C$  values used in the results section of this report describe  $T_C^{on}$ .

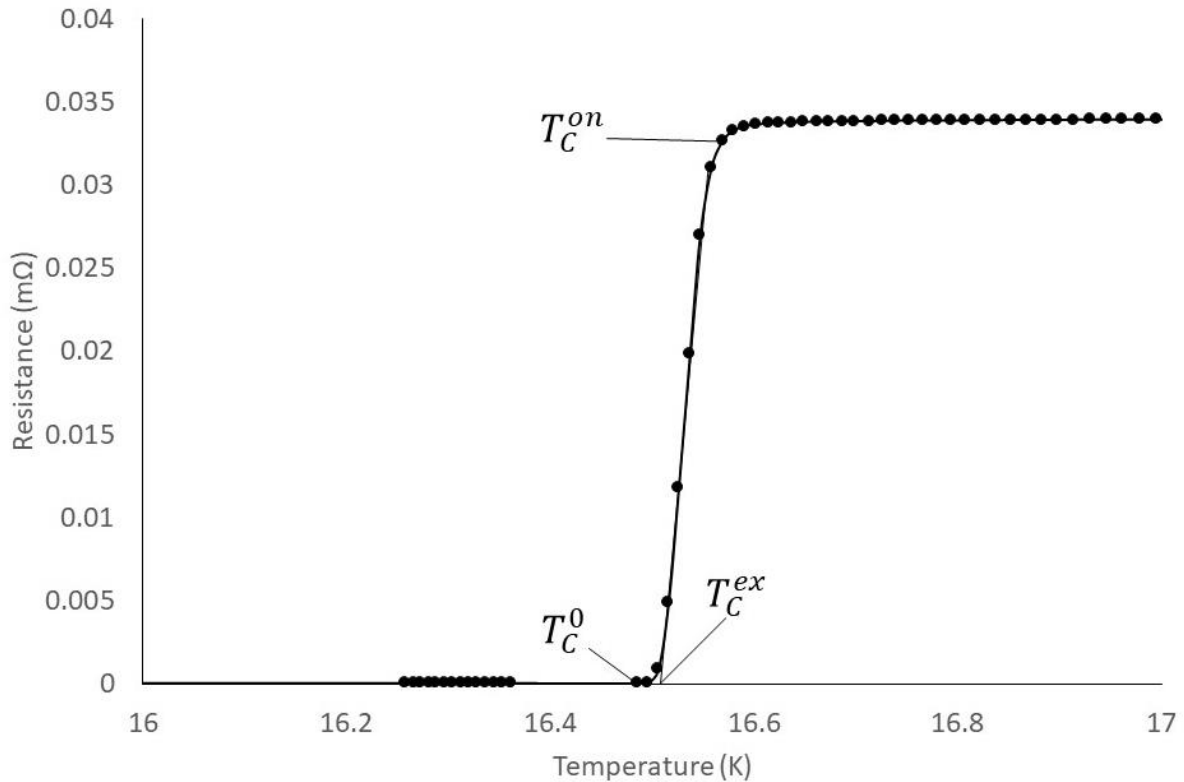


Figure 5.4. Representation of the three definitions of  $T_C$ ;  $T_C^0$ ,  $T_C^{ex}$  and  $T_C^{on}$ .

The RRR is a ratio of the resistance of a sample at 300 K  $R_{300K}$  and at 10 K  $R_{10K}$  as described by equation 5.5.

$$RRR = \frac{R_{300K}}{R_{10K}} \quad (5.5)$$

The resistance at 300 K is predominantly phonon – electron interactions. Lattice vibrations are much smaller at 10 K resulting in negligible phonon – electron collisions. The residual resistivity is much smaller than the phonon related resistivity at 300 K. However, the residual resistivity is temperature independent and accounts for the largest part of the measured resistance at 10 K. Since the residual resistivity is made up of electron scattering centres such as defects and impurities then the RRR can provide an estimate of the film purity. Thin films that contain many defects and impurities have the smallest RRR [32].

The measurement of the resistance across the voltage probes allows the resistivity of the sample to be calculated if the dimensions of the sample are known. If  $L_{probe}$  is the distance between the voltage probes,  $W$  is the width of the sample and  $t$  is the thickness of the film then resistivity  $\rho_n$  is calculated using equation 5.6.

$$\rho_n = \frac{R_{10K} \times W \times t}{L_{probe}} \quad (5.6)$$

The resistivity is a useful property to know as it is a material property rather than a measured value like the resistance. The resistivity of a superconducting thin film is usually quoted as  $\mu\Omega\text{cm}$ .

All four point probe measurements described in the results section of this report were performed using a purpose built four point probe which will be discussed in more detail in chapter 6.

### 5.2.2. DC magnetometer measurements

A DC magnetometer is used to measure the DC magnetic moment of a sample. The DC magnetometer operates by moving samples through a set of detection coils that are inductively coupled to a superconducting quantum interference device (SQUID). The SQUID comprises two parallel superconductors connected by a pair of Josephson junctions. The physics behind the SQUID relies on the reduced critical current across the Josephson junctions to periodically change the direction of the supercurrent flowing through the squid loop in response to an applied flux. A common setup of a DC magnetometer uses four detection coils which are wound with the upper coil in one direction, the two central coils in the opposing direction and the bottom coil in the same direction as the first, as shown in figure 5.5. Assuming that the sample size is smaller than the coils; the sample acts as a point source dipole that moves through the coils to produce a small current that is a function of the sample position. The current in the detection coils is inductively coupled to the instrument's SQUID, which acts as an extremely sensitive current to voltage converter. The software of the DC magnetometer then applies fitting algorithms to the output voltage to determine the magnetic moment of the sample. The DC magnetic moment is usually measured whilst varying either an applied magnetic field or the sample temperature [115].

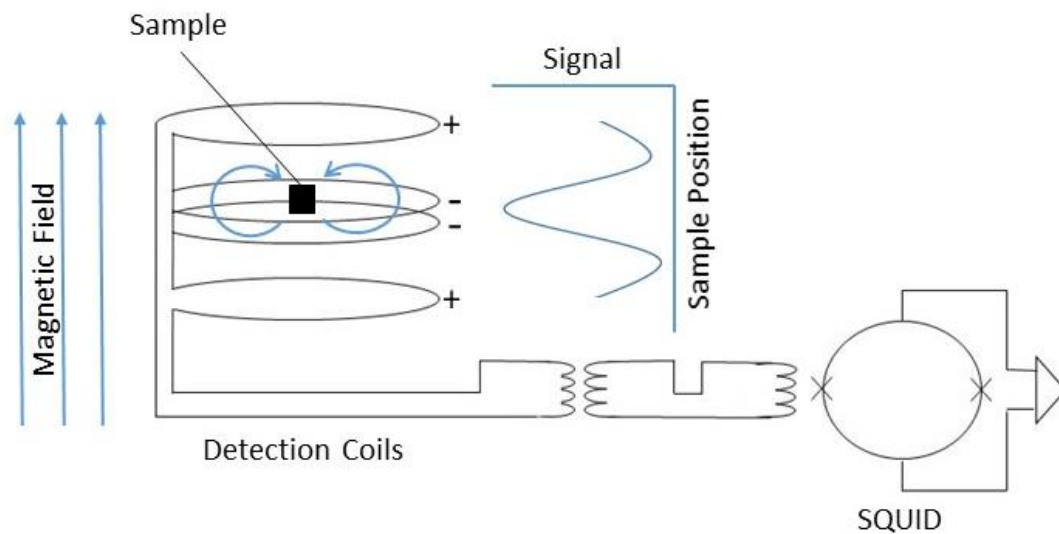


**Figure 5.5. Schematic view of the physical principle of how a SQUID magnetometer works.**

Accurate measurements of the DC magnetic moment rely on a large signal to noise ratio, the correct sample positioning and accurate sample alignment with the applied magnetic field.

The signal to noise ratio can be increased by ensuring the volume of the measured sample is as large as possible, since the magnitude of the measured moment is proportional to the sample volume.

The sample must be centred correctly at the start of each measurement. Sample centring can be done automatically however the raw data should be checked to ensure that the centring algorithm has worked correctly before proceeding with a measurement. Best practice when centring superconducting samples is to apply a magnetic field to the sample so that the measured moment is large during the centring process. However, a superconducting sample should then be warmed well past  $T_c$  so that any trapped field can completely escape. The sample is then cooled to the required temperature so that the measurement can commence.

Considerations should be made to ensure that the sample plane is aligned correctly with the applied magnetic field. The onset of flux penetration will happen at smaller fields if the sample and field are not aligned correctly when measuring the DC magnetic moment of a thin film with the applied field parallel to the plane of the film. Thus, the sample must be aligned parallel to the sides of the sample holder when the sample is inserted into the device. Error in sample alignment was  $\pm 1^\circ$  ( $\pm 17$  mrad) for all DC magnetometer measurements described in this report.

A range of useful information can be obtained from DC magnetisation data. The applied field can be kept constant whilst the temperature is changed, allowing the superconducting transition

temperature to be measured. The first measurable sign of flux penetration into the sample can be determined from the initial change in gradient of the measured moment as the applied field is increased; not to be confused with an accurate measurement of  $H_{C1}$  [116].  $H_{C2}$  can be determined as the point where the observed magnetic moment returns to zero (superconductivity is extinguished by the applied field). Finally, rapid jumps in the measured moment can provide information on the magnetic pinning properties of a sample. *A more detailed description of the analysis of DC magnetic measurements is given later in section 7.2.2.7.*



## 6. Experimental Setup

### 6.1. Deposition System

A deposition system was purpose built to deposit superconducting thin films for this study. A schematic view of the deposition system is shown in figure 6.1. Large components was first cleaned by wiping their internal surfaces with acetone and then isopropanol soaked wipes before installation. Some smaller components were cleaned ultrasonically in baths of acetone and then isopropanol. All UHV joints were sealed using copper CF gaskets for CF flange to flange seals or ¼ inch stainless steel pipes with Swagelok fittings for gas lines. All joints were later leak chased using an external helium gas source to ensure that helium leak rates were below  $1 \times 10^{-10}$  mBar l s<sup>-1</sup> as measured by an internal residual gas analyser (RGA).

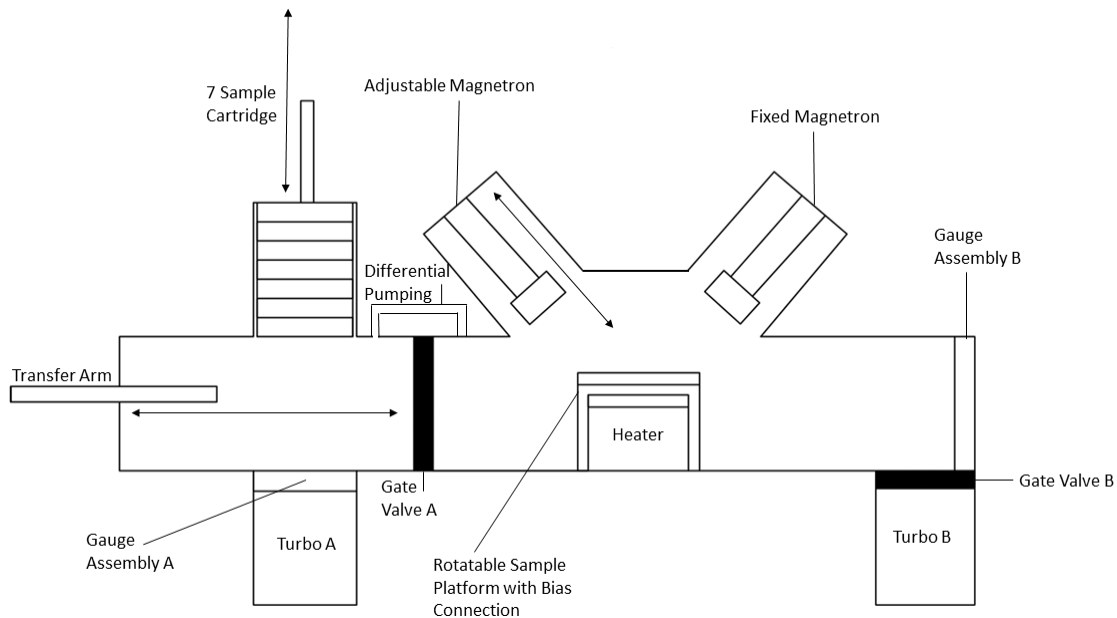


Figure 6.1. Schematic view of the experimental deposition system.



Figure 6.2. Photograph of the entire deposition facility.

The entire deposition facility can be seen in figure 6.2 and comprises two chambers; a load lock chamber and deposition chamber. The deposition chamber comprises an 18 inch diameter spherical chamber with nine ports and an adjoining six way cross piece which houses vacuum gauges and two turbomolecular pumps. A UHV Design ECP-9442-004 substrate heater and biasing stage is seated at the base of the spherical chamber. The substrate heater can heat sample substrates up to  $\approx 900$  °C and is powered by a Glassman Europe Limited LV 60 V -50 A DC Power Supply. The biasing stage allows the substrate to be either grounded using a 50 Ohm impedance RF block, or is DC or RF biased. Only DC biasing was tested during the study using a TDK-Lambda Genesys 1U power supply. The sample is insulated from the chamber walls when biased. The biasing stage rotates the sample at 4 rpm.

The deposition chamber contains ports which allow the installation of up to four magnetrons, however only two were used in this study, facing downwards towards the substrate at an angle of 45 °. Each magnetron is a 3 inch planar magnetron. One magnetron is mounted on an adjustable bellow allowing movement in the z direction between 50 and 250 mm from the substrate surface, the other magnetron is fixed at 150 mm from the substrate surface. The magnetrons are powered by either an Ionautics Hipster 1000 V HiPIMS power supply or a 3kW Advanced Energy Pinnacle + Pulsed DC / DC dual output power supply.

A quartz window is situated on one of the side ports of the deposition chamber and allows an ex-situ viewing lens to face the magnetron plasma. The viewing lens is connected via an optical cable to a Plasus Emicon multi-channel plasma emission monitoring and process control system that is used to identify ionised species within the magnetron plasma during deposition.

The deposition chamber contains an MKS 104220009 Penning gauge, an MKS 103170024SH Pirani gauge and an MKS 120AA-00001RAJ Baratron gauge. The Penning and Pirani gauges output to an MKS 937 B Gauge Controller and the Baratron to an MKS PR400B controller. The Penning gauge has a measurement range between  $10^{-3}$  to  $10^{-11}$  mbar, the Pirani gauge can measure between  $10^3$  and  $10^{-3}$  mbar and the Baratron gauge is accurate between  $10^{-1}$  and  $10^{-4}$  mbar [117].

Up to two different process gases can be injected into the deposition chamber by separate MKS 1179A12CS1BVB mass flow controllers, one calibrated for krypton and the other for nitrogen. The mass flow controllers have a flow range up to 100 sccm and are controlled by MKS Type 250B and MKS Model 247C control units. Pressure during deposition is typically  $10^{-3}$  mbar and is set by adjusting the flow rate through the mass flow controller, with a constant pumping speed, until the desired pressure is read from the Baratron.

Two Leybold 340M turbomolecular pumps are used to pump the deposition chamber. One turbomolecular pump is connected directly to an 8 inch diameter port and the other is connected to

a 2 inch diameter tube. A high pumping speed using both turbomolecular pumps preserves a low base pressure. A gate valve can seal off the pump connected directly to the 8 inch port, leaving only the pump connected through the 2 inch diameter tube, to restrict the pumping speed. The restricted pumping speed is used during deposition to conserve sputter gas. Each turbomolecular pump is backed up by a Leybold 10i scroll pump to maintain the backing line at  $10^{-2}$  mbar.

The loadlock chamber of the deposition facility is built around a six way cross piece with 8 inch diameter ports. The loadlock chamber houses similar Penning and Pirani gauges as described for the deposition chamber, plus an MKS MicroVision2 RGA. The RGA is a type of mass spectrometer that can measure the mass to charge ratio of residual gas ions. The mass to charge ratio can be used to determine the composition of the residual gasses within the vacuum system. The RGA can only work at pressures below  $10^{-5}$  mbar and is therefore unsuitable for use in the deposition chamber. A variable pumping system was installed between load lock and deposition chamber which allows a small volume of process gas to be sent through a leak valve for analysis by the RGA.

Up to 7 samples can be loaded into a retractable cartridge system within the load lock chamber (figure 6.4). The cartridge was designed so that it could maximise the number of samples which could be loaded into the available space within the load lock chamber. Design drawings of the cartridge system were made using AutoCAD software (figure 6.3) before each component part was machined by the STFC Daresbury Laboratory mechanical workshop. Sample substrates are disks that can be no larger than 100 mm in diameter and 10 mm thickness if they are to be installed within the cartridge system. Smaller substrates can be used with the cartridge but must be placed on top of a 100 mm copper disk as shown in figure 6.5. The cartridge is mounted on a rotatable z drive allowing a transfer arm to pick up a sample then transfer it to the deposition chamber. The use of the cartridge system requires that the load lock chamber only be baked once for every 7 samples which are deposited. It is possible to transfer samples which are up to 140 mm in diameter from load lock to deposition chamber; however such samples will not fit within the cartridge. Only one sample can be inserted into the system at a time when not using the cartridge.

The sample temperature during deposition was measured using a thermocouple located at the heater filament. Calibration curves were made so that the sample temperature was known accurately. The calibration curves were made by attaching separate thermocouples directly to the 100 mm disk and to a smaller sample substrate placed onto the 100 mm disk, the temperature on each thermocouple was then compared to what was read from the thermocouple at the heater filament. The calibration curve is shown in figure 6.6.

An efficient bakeout procedure, combining heater tapes and the substrate heater, was devised to minimise the lost process time when changing samples or changing the targets of the

magnetrons. The internal substrate heater can heat the walls of the spherical deposition chamber to 160 °C when at 80 % power and was left at this setting for the duration of the bake. 10 permanent heater tapes were added to other locations of the deposition system so that every outside surface reached at least 150 °C during baking. The bakeout would last for 36 hours to achieve a pressure of  $10^{-10}$  mbar.

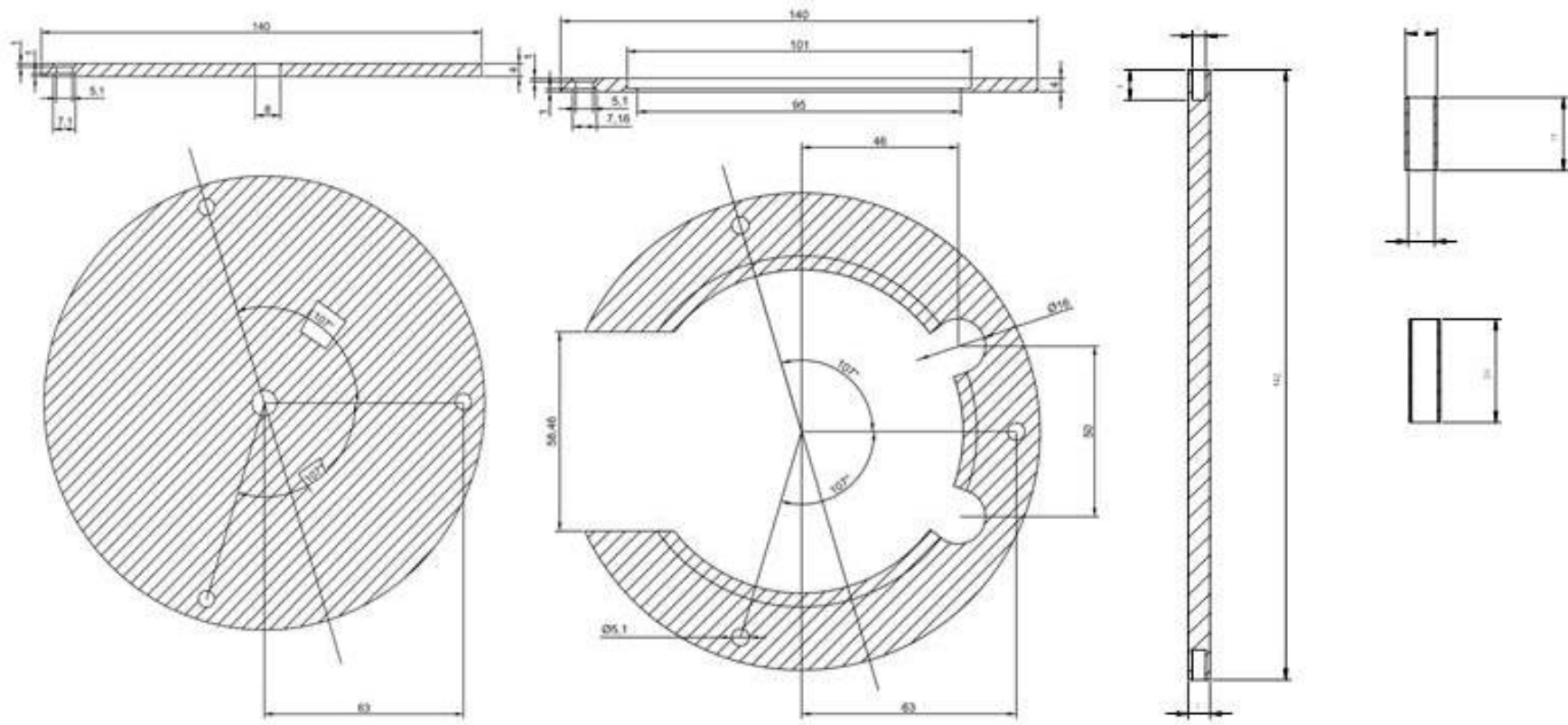


Figure 6.3. Schematic drawing produced during the design stage of the sample cartridge system.



Figure 6.4. The entire load lock chamber is shown in the left hand image and the 7 sample cartridge system is shown in the right image.

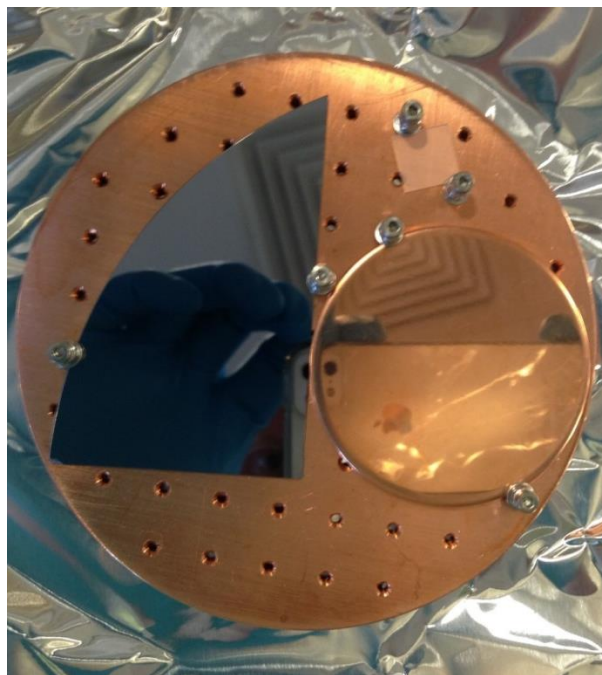


Figure 6.5. Different substrates placed onto a 100 mm copper disk. Shown are silicon, magnesium oxide and polycrystalline copper.

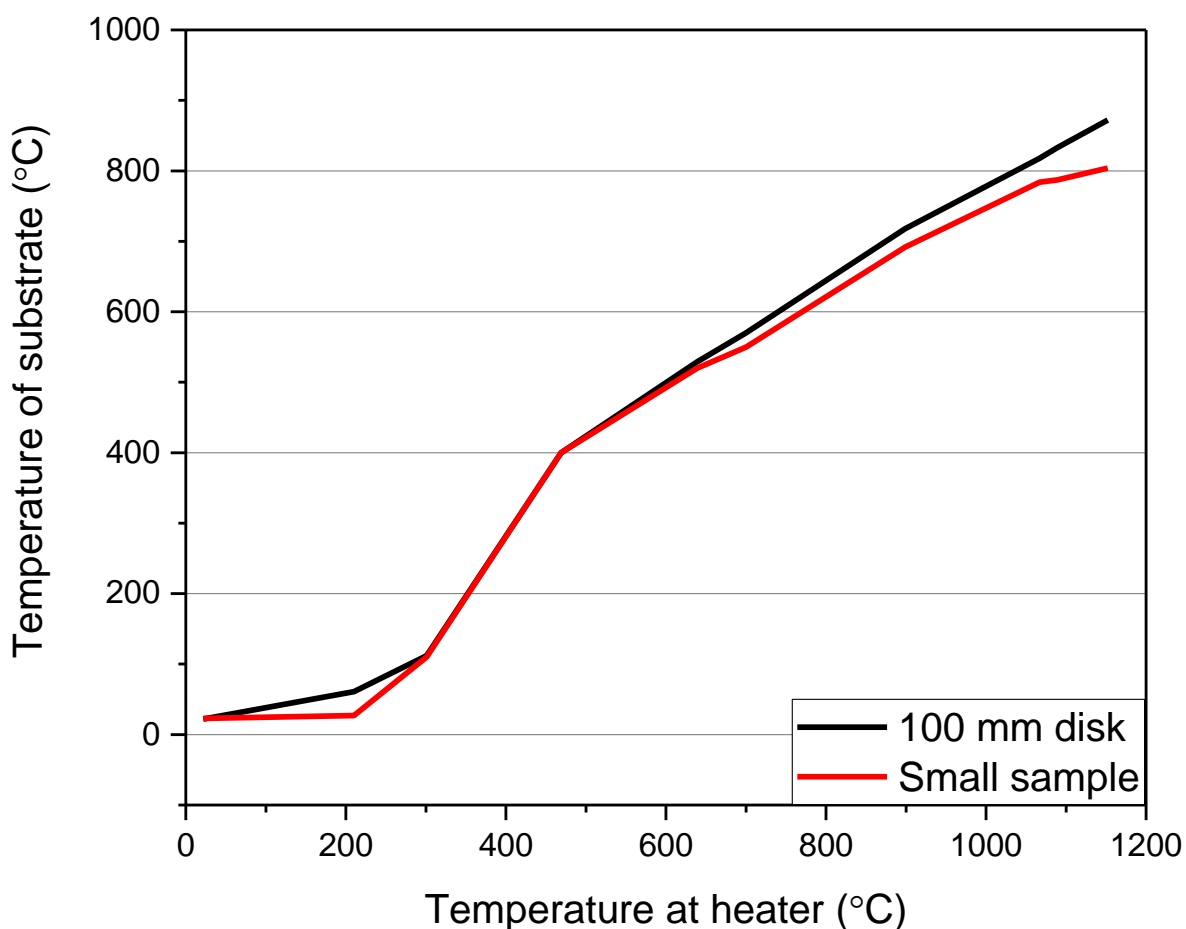


Figure 6.6. Temperature profile of the substrate when read from the thermocouple at the heater.

## 6.2. Cryostat and four-point probe

A four-point probe was used to measure resistance versus temperature curves at temperatures down to 5 K. The cryostat was designed by N Pattalwar and S Pattalwar at STFC Daresbury Laboratory. Machinable parts were built at the STFC mechanical workshop. Assembly and commissioning of the cryostat was performed by both N. Pattalwar and the author of this report. A schematic drawing of the cryostat is shown in figure 6.7. The outer vacuum chamber was pumped by an Alcatel Drytel 1025 vacuum pump to achieve a pressure of approximately  $10^{-3}$  mbar at room temperature and  $10^{-6}$  mbar when the system is cold with the application of rubber o-ring seals at all vacuum joints. The pressure in the cryostat is read from a Pfeiffer Vacuum Compact Full Range Gauge. A Sumitomo Heavy Industries Ltd RP-082B 4K Pulse Tube and a Sumitomo F-70 helium compressor are used to cool the system. The first cooling stage is maintained at a temperature of approximately 70 K and the second cooling stage is maintained at a temperature of approximately 4 K. A radiation shield, comprising a copper cylinder that is closed at one end and covered in multilayer insulation, is attached

to the first cooling stage. The temperature of each of the cooling stages was monitored by DT-670 silicon diode temperature sensors. All wiring connections and insulated copper wire with a diameter of 0.234 mm and used lead solder.

The benefit of using a pulse tube to cool the system is that no cryogenic liquids are necessary to cool the system; a drawback of pulsed cooling is that the temperature of the second cold stage is constantly oscillating by approximately  $\pm 1$  K. Early designs of the system used strongly coupled conduction to cool the sample and therefore the sample temperature was unstable. The final design utilised a sample space which cooled by weakly coupled conduction through helium gas and therefore provides a uniform and stable temperature.

The four-point probe is attached to a sample stick made from of a length of 6 mm thin wall stainless steel tubing with radiation baffles along its length. The sample space is pumped by a Leybold 10i scroll pump to reach a base pressure of  $10^{-2}$  mbar. Helium gas was injected into the sample space at a pressure of 30 mbar during testing to allow even cooling. The pressure in the sample space is read from a mechanical pressure gauge with a range from 1 mbar to 1500 mbar. Samples can be changed when the system is cold by venting the sample space with helium gas and allowing a steady flow of helium whilst the sample stick is removed. The sample space is then sealed using a KF-60 blank and the helium is pumped away. The sample space remains under vacuum until the sample stick is to be replaced. A tantalum wire coil is wrapped around the outer edge of sample space, in the approximate position of the sample, and acts as a resistive heater.

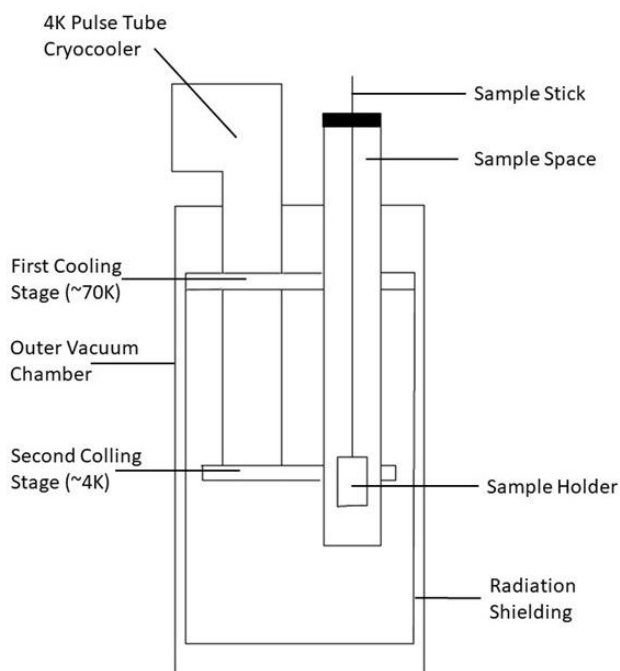


**Figure 6.7.** The left hand image shows a schematic drawing of the cryostat which houses the four-point probe and the right hand image shows a photograph of the cryostat.

A pre-requisite of the four-point probe was that the sample turnover should be as high as possible. Therefore, a sample holder was designed by the author of this report which did not require the use of either indium solder or conductive paint to attach the current and voltage probes. The sample holder is shown in figures 6.8 and 6.9. Three polychlorinated biphenyl (PCB) disks, usually used for circuit boards, were used to make the sample holder. Each PCB board has arrays of through holes where components can be soldered in place. PCB boards 1 and 2 hold two rows of four spring loaded test probes (RS Pro 2.54 mm Pitch Spring Test Probe with Needle tip) which are soldered into position; two PCB boards are preferred over just one as it adds rigidity to the assembly. PCB board 3 is used to press the sample onto the spring-loaded test probes. M2 bolts and nuts are used to hold each PCB board in the correct position. A Lakeshore Cernox temperature sensor is fixed permanently in place on the underside of PCB board 1 with a distance of 13 mm to each sample. The design of the sample holder allows sample changeover in only a few minutes.

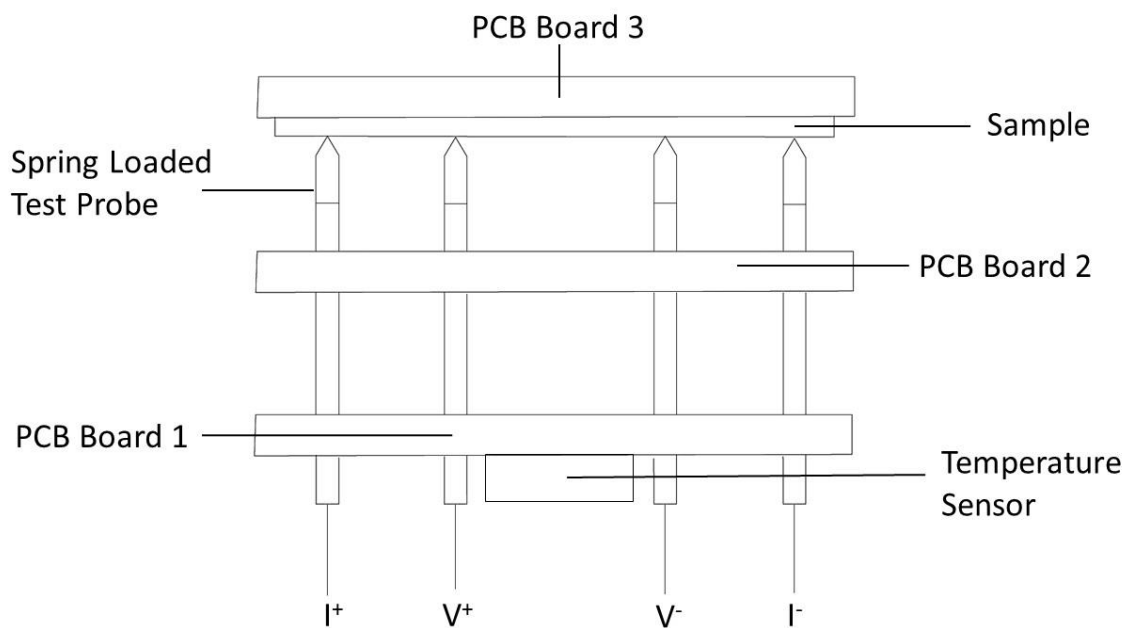


Figure 6.8. Schematic representation of the four-point probe sample holder.



Figure 6.9. Photographs of a) the four-point probe and b) the sample stick (insert).

The normal state resistance  $R$  of each sample is calculated by first applying a current  $I$  across probes  $I^*$  and  $I$  and measuring the voltage  $V$  across probes  $V^*$  and  $V$ , with the relation  $R = V / I$ . The current is supplied by a Keithley 6220 Precision Current Source and the voltage is measured using a HP 34401V Multi-meter.

The sample space is maintained at approximately 5 K before the room temperature samples are inserted. The samples are then allowed to cool in helium gas at 300 mbar. The system is partially automated; a constant current is set at the beginning of each measurement before simple LabView software logs the temperature and voltage of each sample every five seconds. The resistance versus temperature curves were used to calculate the RRR of each sample using equation 6.1, where  $RT$  is the room temperature in K,  $R_{RT}$  is the room temperature resistance,  $R_{TC}$  is the resistance at just above  $T_C$  and  $T_{TC}$  is the temperature at which  $R_{TC}$  was measured.

$$RRR = \frac{300\text{ K} - T_{TC}}{RT - T_{TC}} \times \frac{R_{RT}}{R_{TC}} \quad (6.1)$$

Figure 6.10 shows a typical resistance versus temperature curve including  $R_{TC}$  and  $T_{TC}$ . Using this technique, the error in the measured resistance is approximately 1 % and the error of the

calculated RRR is 2 – 3 % [118]. Repeated measurements like the one shown in figure 6.10 were made for a single sample during the initial testing of the four point probe described in figures 6.8 and 6.9, where the repeatability was within the 2 – 3 % error margin quoted in [118].

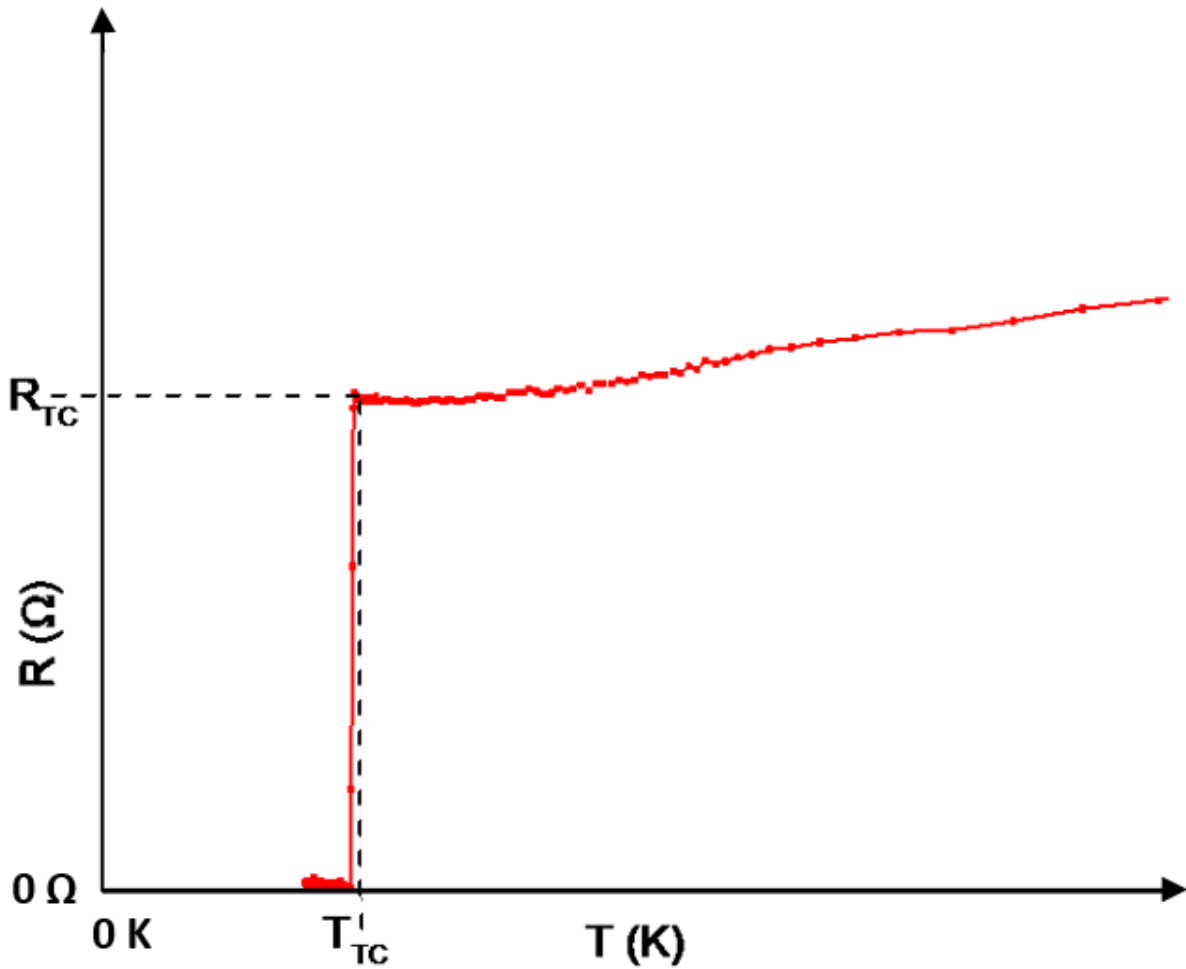


Figure 6.10. Example of a resistance versus temperature curve including  $R_{TC}$  and  $T_{TC}$ .



## 7. Deposition of Niobium Thin Films

### 7.1. Niobium films deposited by DC magnetron sputtering

The first films deposited during the study were produced using DC magnetron sputtering and allowed the deposition system to be tested using a deposition technique which is well documented in the literature [2, 17, 64]. The magnetron fixed at 150 mm from the substrate used to deposit each film and was fitted with a niobium target of 99.95 % purity. Films were deposited onto Strukturbericht designation A4 diamond structure silicon substrate at room temperature with either a grounded substrate or a substrate biased at -50 V DC and with a range of powers, between 100 and 600 W, supplied to the magnetron. Each silicon substrate wafer was 0.75 mm thick and cut to approximate dimensions of 20 x 50 mm. Sample substrates were all prepared with the same procedure; first cleaned in ultrasonic baths of acetone, then isopropanol, then rinsed in deionised water and blown dry using dry nitrogen gas. The deposition chamber was unbaked and reached a base pressure of approximately  $10^{-8}$  mbar. Krypton process gas was used during each deposition at a constant pressure of  $7 \times 10^{-3}$  mbar as read from the Baratron gauge. Samples were set to rotate at 4 rpm for the 2.5 hour duration of each deposition. No heating was provided to the substrate. The current voltage-power relation of the DC power supply is shown in figure 7.1. Only six measurements were used to produce figure 7.1 with the current and voltage read directly from the display of the power supply with an error of  $\pm 1$  V or  $\pm 0.01$  A. It should be stressed that the current and voltage was specific to the process that has been described. Altering process conditions such as the process gas pressure, pumping speed and even the shape of the target may have produced different current and voltage characteristics.

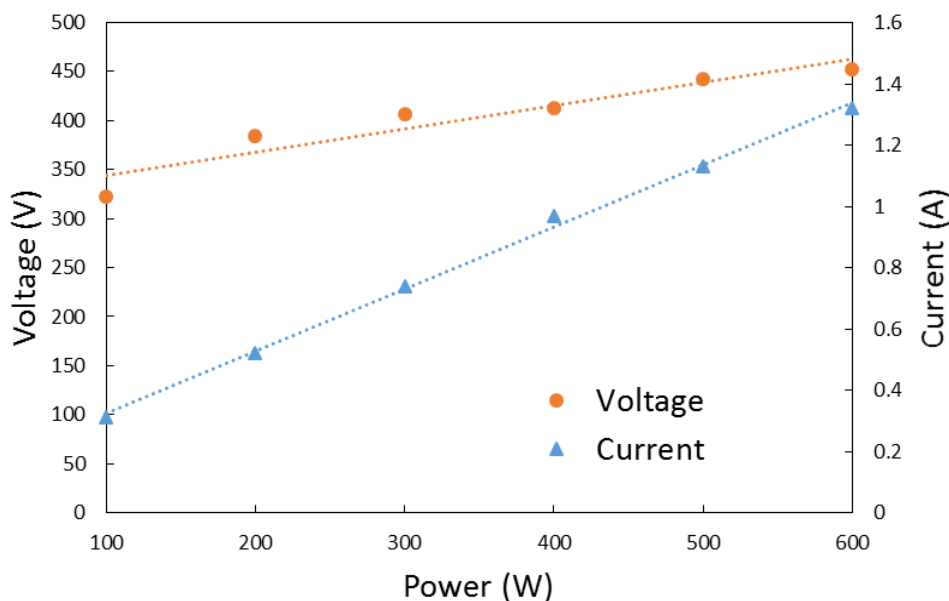


Figure 7.1. The current-voltage-power characteristics of the DC power supply for a krypton pressure of  $7 \times 10^{-3}$  mbar.

A range of films were imaged in cross section using SEM and are shown in figures 7.2 and 7.3. The images gave an insight into the microstructure of the deposited films and provided a measurement of the film thickness. The grounded films deposited with magnetron power of 100 and 200 W show columnar grains with sharp tops, grains with domed tops formed at 400 to 600 W. All films deposited onto a grounded substrate formed with many voids between grains. The films deposited with a -50 V bias appear to show more densely packed grains than for the grounded films at powers of 300 to 600 W. The film thickness, and therefore deposition rate, of the grounded films increase as a function of the applied power and is shown in figure 7.4. The thickness of the biased films could not be accurately measured as they did not always cleave with a visible cross section. This would indicate that some of the biased films were less brittle than the grounded films.

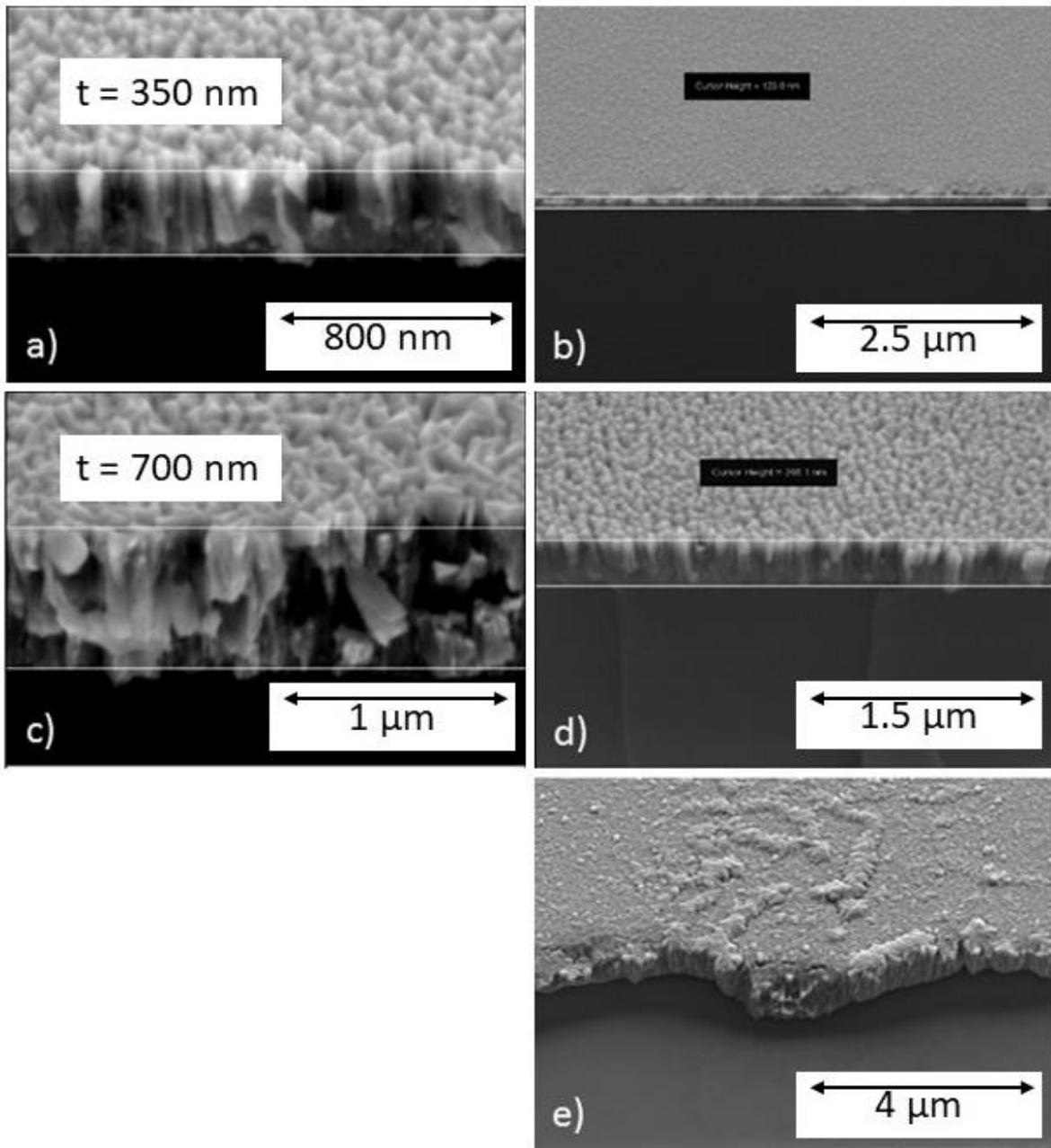


Figure 7.2. Secondary electron SEM images of niobium thin films. Beam energy was set to 8 kV with beam diameter of 4 nm. Each niobium film was deposited by DC magnetron sputtering onto Si (100) substrate at varying powers and with either grounded or a substrate bias of -50 V. a) grounded 100 W, b) 100 W with -50 V substrate bias, c) grounded 200 W, d) 200 W with -50 V bias and e) 300 W with -50 V bias.

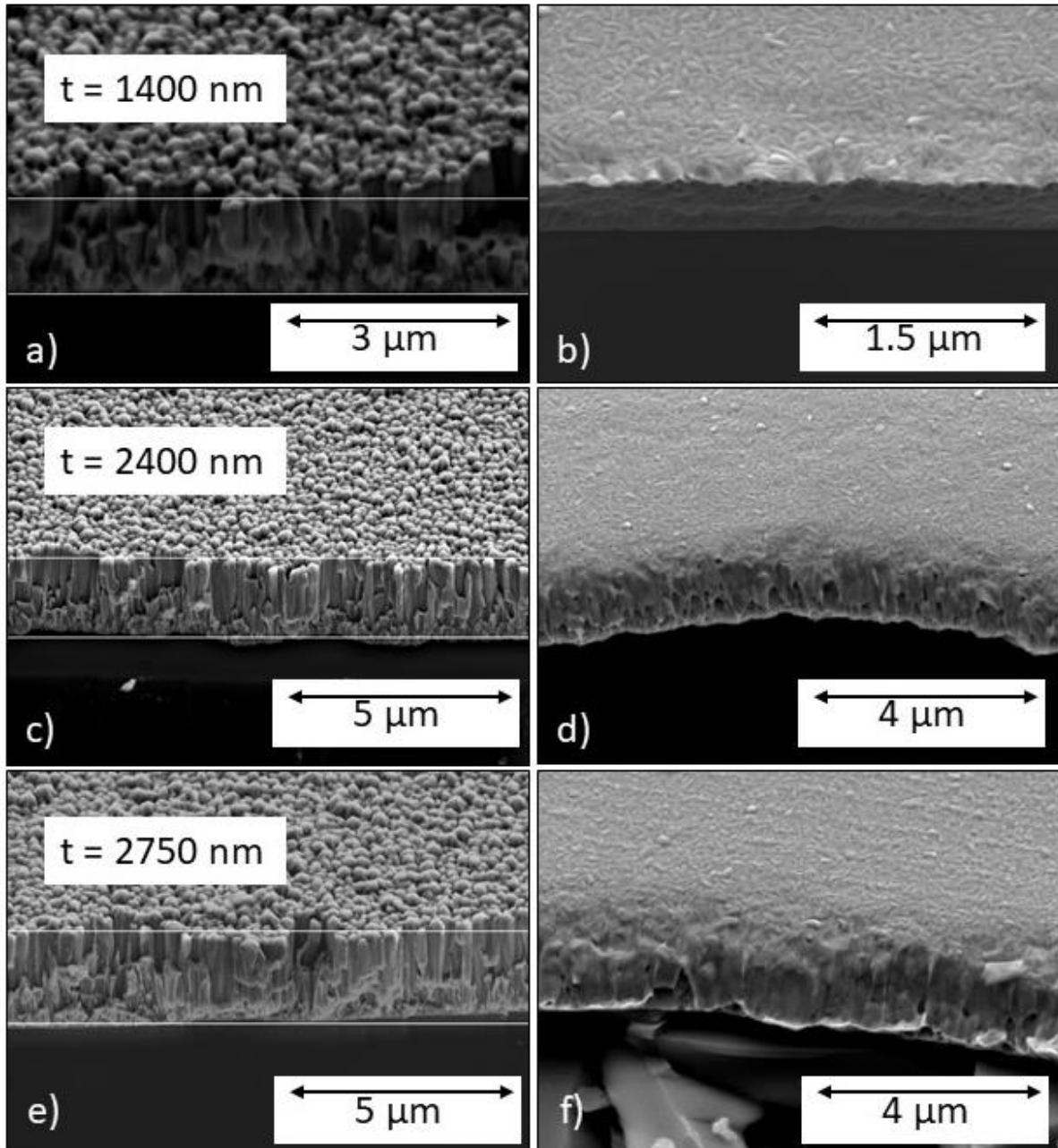


Figure 7.3. Secondary electron SEM images of niobium thin films. Beam energy was set to 8 kV with beam diameter of 4 nm. Each niobium film was deposited by DC magnetron sputtering onto Si (100) substrate at varying powers and with either grounded or a substrate bias of -50 V. a) grounded 400 W, b) 400 W with -50 V substrate bias, c) grounded 500 W, d) 500 W with -50 V bias, e) grounded 600 W and f) 600 W with -50 V bias.

Grazing incidence XRD measurements were performed for the niobium films deposited at room temperature using DC magnetron sputtering onto grounded substrate or substrate biased at -50 V. Grazing incidence XRD measurements were performed using a copper x-ray source to produce x-rays with a  $K\alpha_1$  wavelength of 1.54056 Å; the results are shown in figure 7.5. Each film grows with a preferred bcc (110) orientation. Smaller peaks are observed which correlate the (200), (211) and (220) orientations with the relative peak heights differing depending if the film is biased or not. Grounded

films displayed proportionately larger (220) peaks and films biased at -50 V displayed proportionately larger (200) and (211) peaks in every instance.

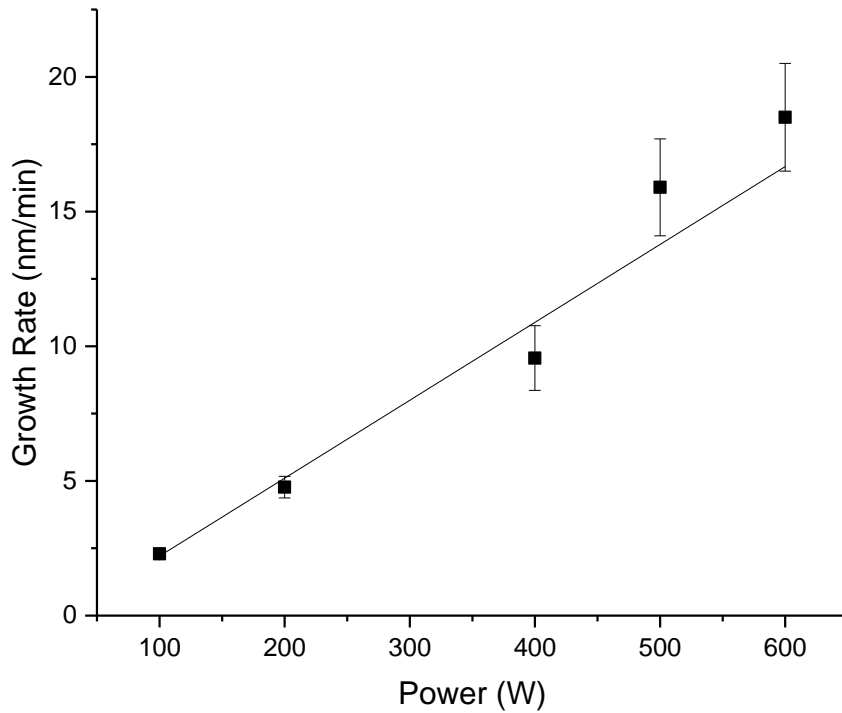


Figure 7.4. The growth rate versus power supplied to the magnetron for niobium thin films deposited by DC magnetron sputtering onto a grounded substrate.

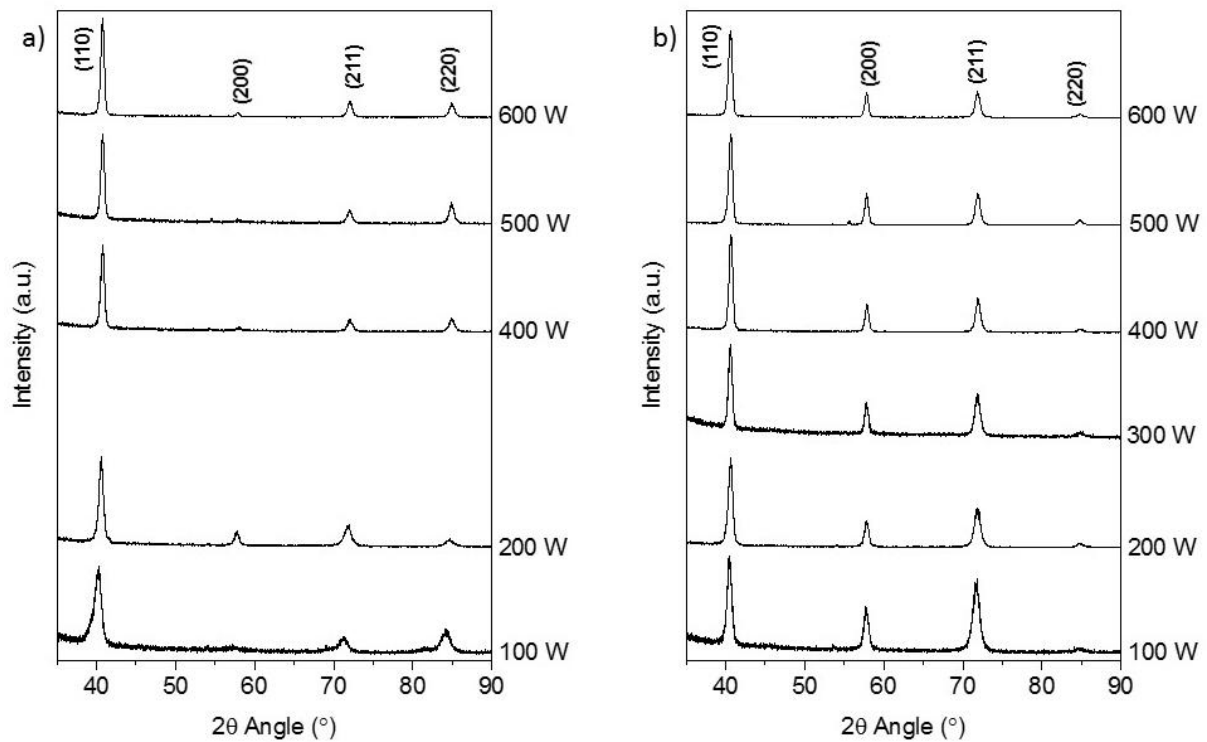


Figure 7.5. Grazing incidence XRD measurements of films deposited by DC magnetron sputtering at room temperature on either a) a grounded substrate or b) a substrate bias of -50 V.

The bcc (110) peak positions of each grazing incidence XRD measurement was used to first calculate the  $d$  spacing and  $a_0$  whilst the full width half maximum (FWHM) of each peak was used to estimate the average grain size (Table 7.1). The FWHM was defined as the difference between the two extremes of the (110) peak at half of its maximum intensity.

**Table 7.1.** Table of the measured and calculated data taken from the GI-XRD measurements shown in figure 7.5.

<b>Power (W)</b>	<b>Bias (-V)</b>	<b>(110) Peak Position (°)</b>	<b><math>d</math> Space (Å)</b>	<b>Lattice Constant (Å)</b>	<b>FWHM (°)</b>	<b>Average Grain Size (nm)</b>
<b>100</b>	0	40.25	2.24	3.17	1.05	10
<b>200</b>	0	40.56	2.22	3.14	0.66	17
<b>400</b>	0	40.80	2.21	3.13	0.54	20
<b>500</b>	0	40.80	2.21	3.13	0.50	22
<b>600</b>	0	40.79	2.21	3.13	0.52	21
<b>100</b>	50	40.51	2.23	3.15	0.66	17
<b>200</b>	50	40.65	2.22	3.14	0.63	17
<b>300</b>	50	40.60	2.22	3.14	0.52	21
<b>400</b>	50	40.68	2.21	3.13	0.52	21
<b>500</b>	50	40.66	2.22	3.14	0.55	20
<b>600</b>	50	40.61	2.22	3.14	0.55	20

The calculated lattice constant was observed to be approximately constant for all tested DC powers, ranging between  $3.15 \pm 0.005$  Å and  $3.13 \pm 0.005$  Å, for films deposited with a substrate bias of -50 V. The  $a_0$  of the grounded films ranged between  $3.14 \pm 0.005$  Å and  $3.13 \pm 0.005$  Å and was similar to the biased films with the exception of 100 W, which exhibited the longest  $a_0$  of  $3.17 \pm 0.005$  Å. The calculated  $a_0$  of each film is shown in figure 7.6. Error in the calculated value of the  $a_0$  is defined by the uncertainty in the measurement of peak position as described in more detail in section 5.1.1.

The maximum average grain size of between  $20 \pm 2$  nm and  $22 \pm 2$  nm was similar for both the grounded films and those biased at -50 V. The grain size was smallest for the films deposited at powers of either 100 or 200 W with a minimum value of  $10 \pm 1$  nm occurring for the film deposited at 100 W onto a grounded substrate. Each calculated average grain size is displayed in figure 7.7. Error in the calculation of average grain size is defined by the uncertainty in the measurement of peak position and with consideration to the fact that not all grains are of the same dimension within polycrystalline materials.

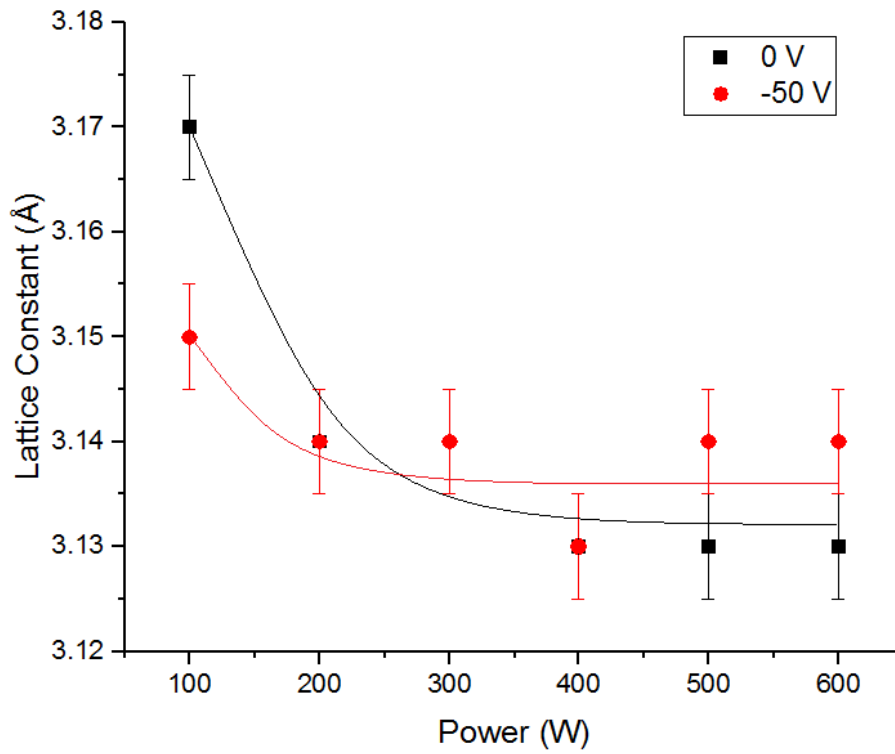


Figure 7.6. Lattice constant versus power supplied to the magnetron for niobium thin films deposited by DC magnetron sputtering with either a grounded substrate or a substrate biased at -50 V.

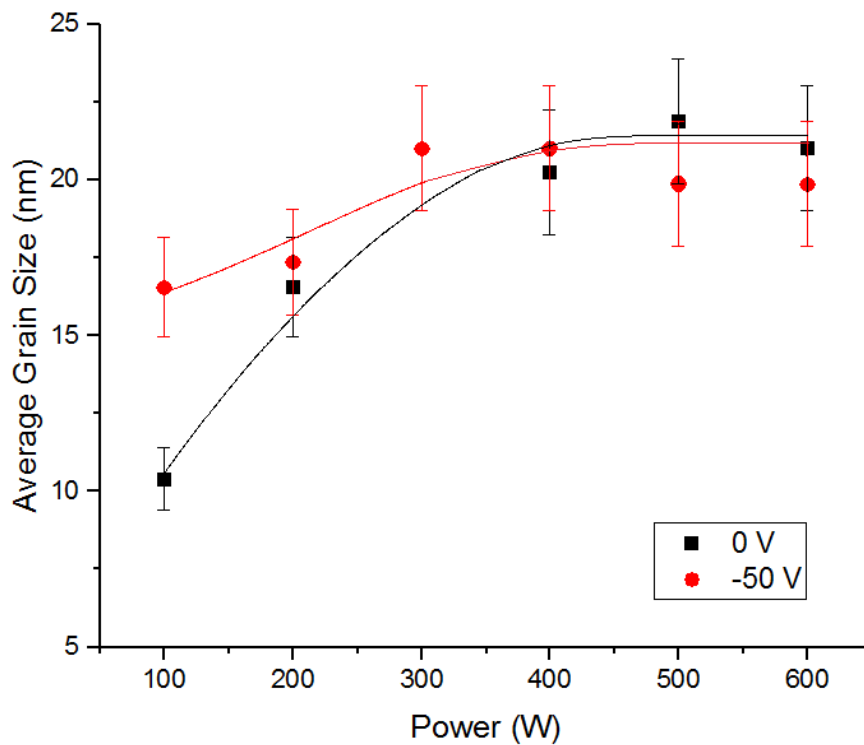


Figure 7.7. Average grain size versus power supplied to the magnetron for niobium thin films deposited by DC magnetron sputtering with either a grounded substrate or a substrate biased at -50 V.

A single film deposited by DC magnetron sputtering was imaged using EBSD analysis and is shown in figure 7.8; the film was deposited onto grounded silicon (100) substrate at 600 W. The image shows the largest grains of up to 250 nm across with a matrix of much smaller grains of approximately 10's of nm in diameter. The same sample was also tested by Sonal Mistry at STFC using XPS analysis with the results displayed in figure 7.9. The XPS analysis was used to measure the atomic percentages of elemental contaminants within the film after the surface had been sputtered with argon for 30 minutes. The elemental composition was calculated from the area under each of the Nb 1s, C 1s and Nb 3p peaks respectively. The thin film sample displayed 10 % atomic oxygen and no carbon whilst a reference bulk niobium sample displayed atomic oxygen at 16 % and atomic carbon at 21 % after the same 30 minute argon sputter.

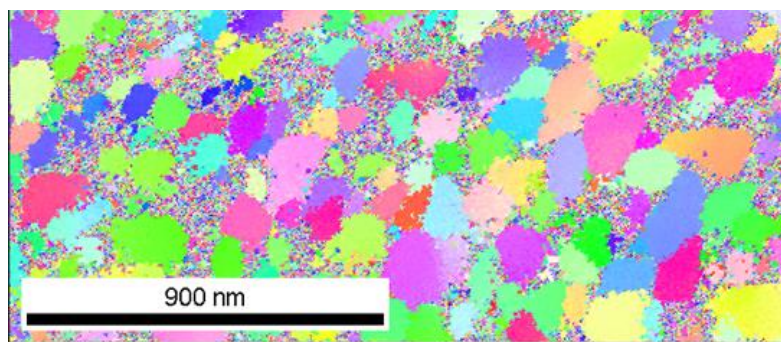


Figure 7.8. Electron backscatter diffraction image of a thin film deposited by DC magnetron sputtering at 600 W onto grounded silicon (100) substrate (measurement courtesy of V. Vishnyakov, MMU).

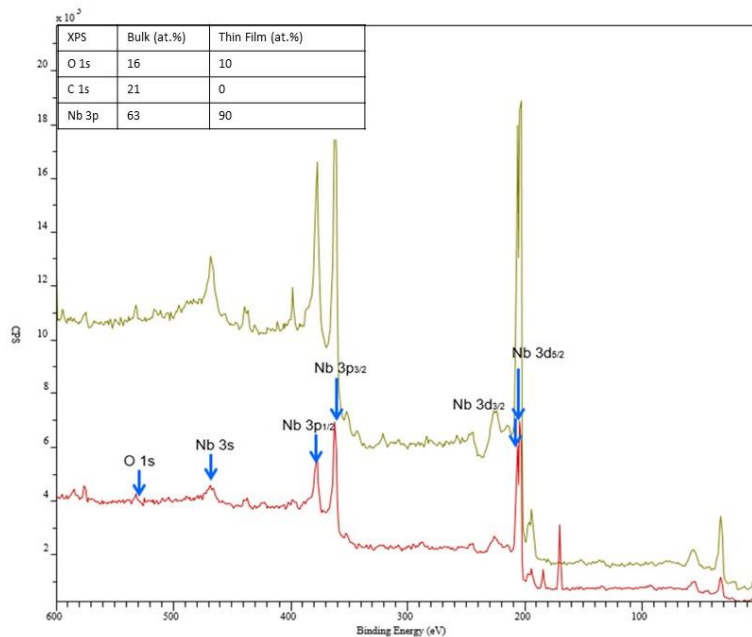


Figure 7.9. XPS spectrum of a niobium thin film (green) deposited at room temperature by DC magnetron sputtering at 600 W onto grounded silicon (100) substrate. A bulk niobium sample (red) is also shown for comparison (measurement courtesy of S. Mistry, STFC).

RRR was measured for all films deposited by DC magnetron sputtering and the results are displayed in figure 7.10. RRR ranged between 2 and 12 for all niobium films. RRR was observed to increase linearly with applied DC power to the magnetron. The RRR was larger in every instance for films deposited at the same power onto a biased substrate relative to a grounded substrate.

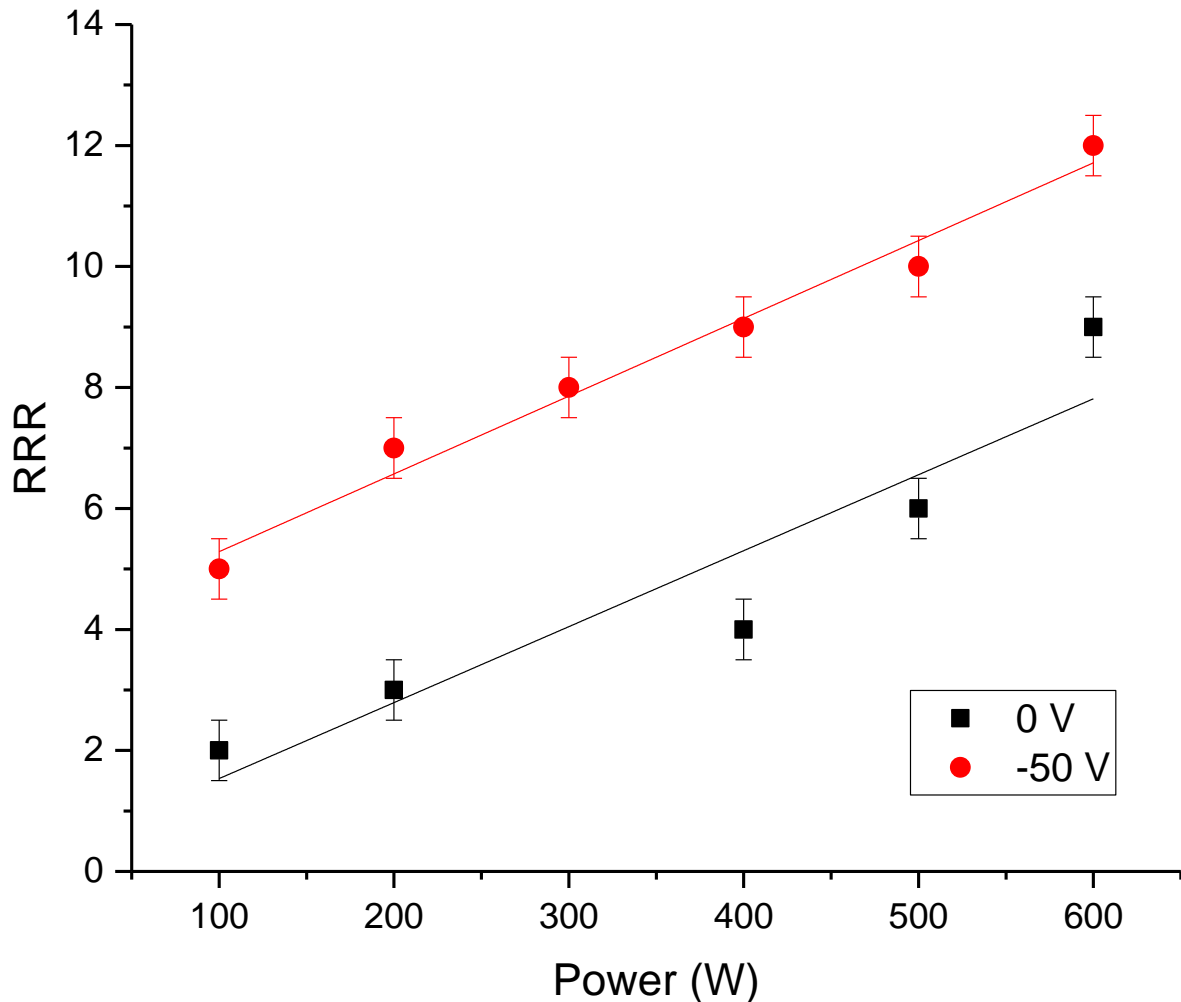


Figure 7.10. RRR against DC power supplied to the magnetron for films deposited with either a grounded substrate or biased at -50 V.

It was possible to calculate the normal state resistivity for films with a known thickness. The normal state resistivity for films deposited with a grounded substrate is shown in figure 7.11. There was a trend for a smaller normal state resistivity at larger DC magnetron power. The normal state resistivity could not be calculated for the biased films as the thickness was not accurately known.

The results show some distinct differences between films that are deposited by DC magnetron sputtering with and without an applied substrate bias. The SEM images in figure 7.3 show two very different types of microstructure, columnar grains with many voids in the case of the grounded substrate and more closely packed grains for the films deposited onto biased substrate at powers of

400 W and above. The microstructure of each of the grounded films is typical of zone 1 of the structure zone diagram of figure 3.6. Zone 1 films form at the smallest substrate temperatures with little energy supplied to the growing film by either substrate heating or the kinetic energy of the arriving particles. The closely packed grains of the films deposited with a -50 V bias at powers of 300 to 600 W have a microstructure typical of zone T of the structure zone diagram. The structure zone diagram shows how zone T can occur at a small substrate temperature so long as the kinetic energy of the arriving particles is large enough. The ion to atom ratio of DC magnetron sputtering is less than 5 % and therefore only very small [119], however the application of a bias still appears to have altered the growing film from zone 1 to T.

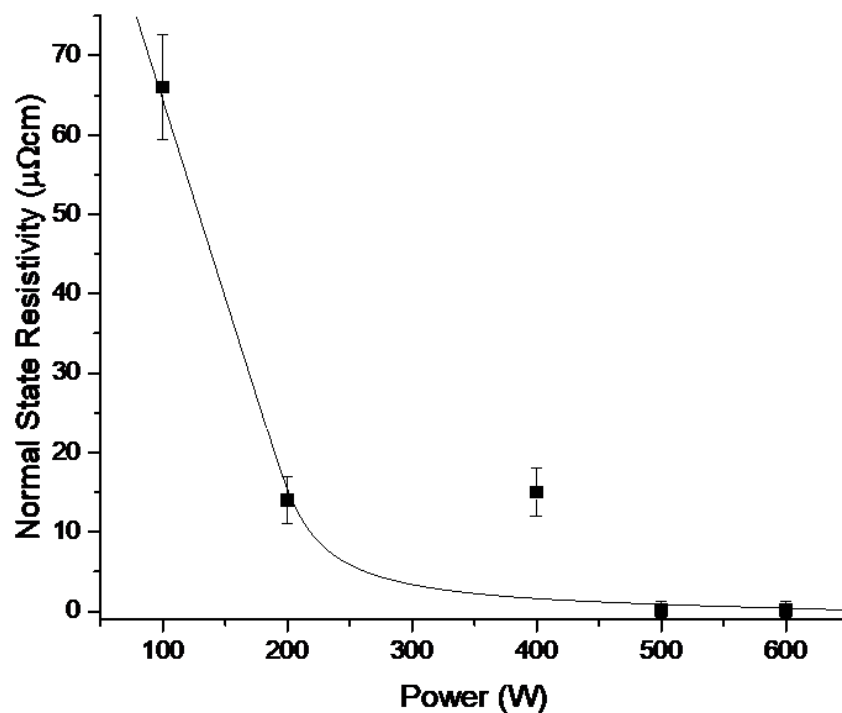


Figure 7.11. The normal state resistivity measured just above  $T_c$  against power for niobium films deposited by DC magnetron sputtering onto grounded substrate.

The application of a substrate bias does not only accelerate charged particles; it can also alter the angle at which sputtered ions arrive at the substrate. Previous studies have shown that porous niobium thin films form with columnar grains and domed tops when the incident angle of the sputtered material is well below  $90^\circ$  [84]. The setup of the thin film deposition facility used in the current study dictates that the angle between the magnetron and the substrate is  $45^\circ$ . All electrically neutral material will therefore arrive at the growing film at an angle of  $45^\circ$  whilst ionised material can arrive at steeper angles, up to  $90^\circ$  to the plane of the substrate if a bias is applied. The changing angle of arrival of the sputtered material can therefore also assist in the apparent densification of biased films as there will be less shadowing of grains in biased films relative to grounded films.

The niobium bcc (110) preferred growth orientation occurred for all films deposited by DC magnetron sputtering. However, there were notable differences in the sizes of the smaller reflection peaks if the substrate was grounded or biased. Grazing incidence XRD measurements showed that the application of a substrate bias resulted in relatively larger reflections of the (200) and (211) lattice orientation, and relatively smaller (220) when compared to films deposited onto grounded substrate. The change in the relative sizes of the peaks of the grazing incidence XRD spectrum correlate with the apparent densification of films in the SEM images. In contrast,  $a_0$  and average grain size of the deposited films display little difference between the grounded or biased films, except for at the smallest power of 100 W. Films deposited at 100 W have both longer  $a_0$  and smaller grain size than at all other tested powers. The relative disparity between  $a_0$  and grain size for the films deposited at 100 W with and without and applied -50 V bias may be a result of statistical error rather than the effects of the applied bias as only single measurements were performed in each instance. Film deposited onto both grounded and biased substrates at powers of 200 to 600 W have lattice constants between 3.13 and 3.14 Å and average grain size of 20 to 22 nm. Thus, the calculated  $a_0$  and grain size display no correlation which could explain the apparent densification in the SEM images.

The only sample imaged by EBSD, the film deposited onto a grounded substrate at 600 W DC power, shows that there are larger grains present than 22 nm however the matrix of smaller grains may explain the much lower average value. Another explanation to account for the large difference in average grain size and maximum grain size is that the FWHM of the grazing incidence XRD peaks can become broadened due to the presence of stresses contained within the film microstructure [32].

RRR increases linearly with applied power to the magnetron for films deposited onto a grounded substrate and those deposited onto a substrate biased at -50 V. The heightened RRR at larger powers can be linked to higher deposition rates. Firstly, a larger deposition rate can reduce the probability of impurity atoms, which originate from outgassing of the unbaked vacuum chamber, to become trapped within the growing film. Secondly, the larger deposition rate results in thicker niobium films. The RRR of niobium thin films has already been shown in the literature to increase with film thickness for similar deposition conditions [120, 121]. Models have been produced which indicate that RRR will ultimately plateau once the film reaches an optimum thickness and the film microstructure changes from fibrous, small grained crystals, to larger grains with higher crystalline order. The upper limit of RRR for niobium thin films is thought to occur at between 1.5-2 microns [122].

RRR results show that the electrical properties of the film improve with the application of an applied bias. The improved RRR most likely occurs due to the apparent decrease in the number of

voids visible in the SEM images. Similar lattice constant and average grain size of both grounded and biased films suggests that the stresses present in each type of film are similar and therefore cannot explain the difference in RRR.

Normal state resistivity is inversely proportional to the applied DC power due to the corresponding deposition rates. The normal state resistivity should become larger as the film thickness increases for the same reasons as already discussed for RRR.

## 7.2. Niobium films deposited by HiPIMS

### 7.2.1. Testing the effects of the substrate choice

HiPIMS niobium films were deposited onto Strukturbericht designation A4 diamond structure silicon substrate, polycrystalline copper and magnesium oxide (100) substrates allowing the effects of the choice of substrate to be compared. Copper substrates were standard oxygen free copper gaskets of 2 mm thickness and diameter of 50 mm, the magnesium oxide was 0.5 mm thick with dimensions of 10 mm x 10 mm and silicon substrates were the same as used in section 7.1. The same cleaning procedure as detailed in section 7.1 was used for all substrates prior to deposition. Prior to deposition, the entire deposition facility was baked to 150 °C for 4 days, the base pressure of  $5 \times 10^{-10}$  mbar was reached after cooling to room temperature. The magnetron fitted with an adjustable bellow was used for each deposition at a fixed distance of 150 mm from the substrate surface. The target material was 99.95 % purity niobium. Krypton was used as a sputter gas at a pressure of  $7 \times 10^{-3}$  mbar. Samples were set to rotate at 4 rpm during 4 hour deposition process. Samples were deposited at three different HiPIMS power supply settings and then analysed by four-point probe, XRD and DC magnetometer. Table 7.2 details the HiPIMS power supply settings which were used.

**Table 7.2.** Table describing the HiPIMS power supply settings used to deposit niobium thin film samples.

Setting	Power (W)	Temp (°C)	Pulse Width (µs)	Repetition Rate (Hz)	DC Bias (-V)	Peak Current (A)
A	400	330	100	300	100	26
B	300	330	100	200	100	27
C	300	330	150	100	100	37

XRD measurements in this section of the report were performed using a copper x-ray source to produce x-rays with wavelength of 1.54056 Å. Figure 7.12 shows the XRD data for film B as deposited onto all three substrates. Each film grew with the bcc (110) grain orientation however the peak location and FWHM shifted depending on the choice of substrate. The magnesium oxide substrate produced a peak at 38.23 ° with the smallest FWHM of 0.12 °, the copper substrate produced a peak at 38.31 ° with a FWHM of 0.23 ° whilst the silicon substrate produced a peak at 38.63 ° and the largest FWHM of 0.31 °. The peak locations and FWHM correspond to  $a_0$  of 3.33 Å and grain size of 90 nm for magnesium oxide substrate, 3.32 Å and 47 nm for copper substrate and 3.29 Å and 35 nm for the silicon substrate respectively.

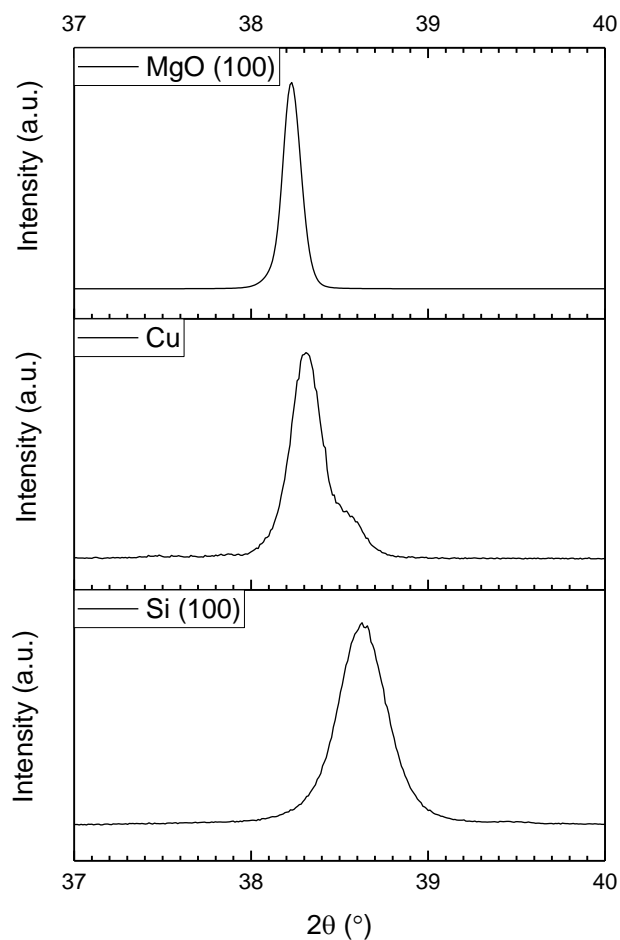


Figure 7.12. XRD peaks of niobium thin films which correspond to the (110) grain orientation.

Each of films A, B and C as deposited onto both silicon and copper were then tested by DC magnetometer to measure magnetic hysteresis loops in a DC magnetic field at 4.2 K, as shown in figures 7.13, 7.14 and 7.15. All samples were oriented as close to parallel to the plane of the magnetic field as was possible to achieve. The error in the sample alignment with the magnetic field was  $\pm 1^\circ$  ( $\pm 17$  mrad).

The sensitivity of the MPMS system is quoted to be  $10^{-7}$  emu however the noise level in the reported experiment was observed to be  $10^{-5}$  emu at zero field. Signal to noise ratio can be increased by increasing the sample volume. Since the volume of the deposited thin films is very small then copper substrates were first etched from the films using nitric acid so that the sample thickness could be reduced; allowing three  $5\pm 1$  mm x  $5\pm 1$  mm pieces of the same film to be placed one on top of another inside the MPMS measurement space. Measuring three pieces of the same film produces larger signal to noise ratio than measuring one piece alone. Films deposited onto silicon substrate were cut into pieces of similar size however the substrate was left in place.

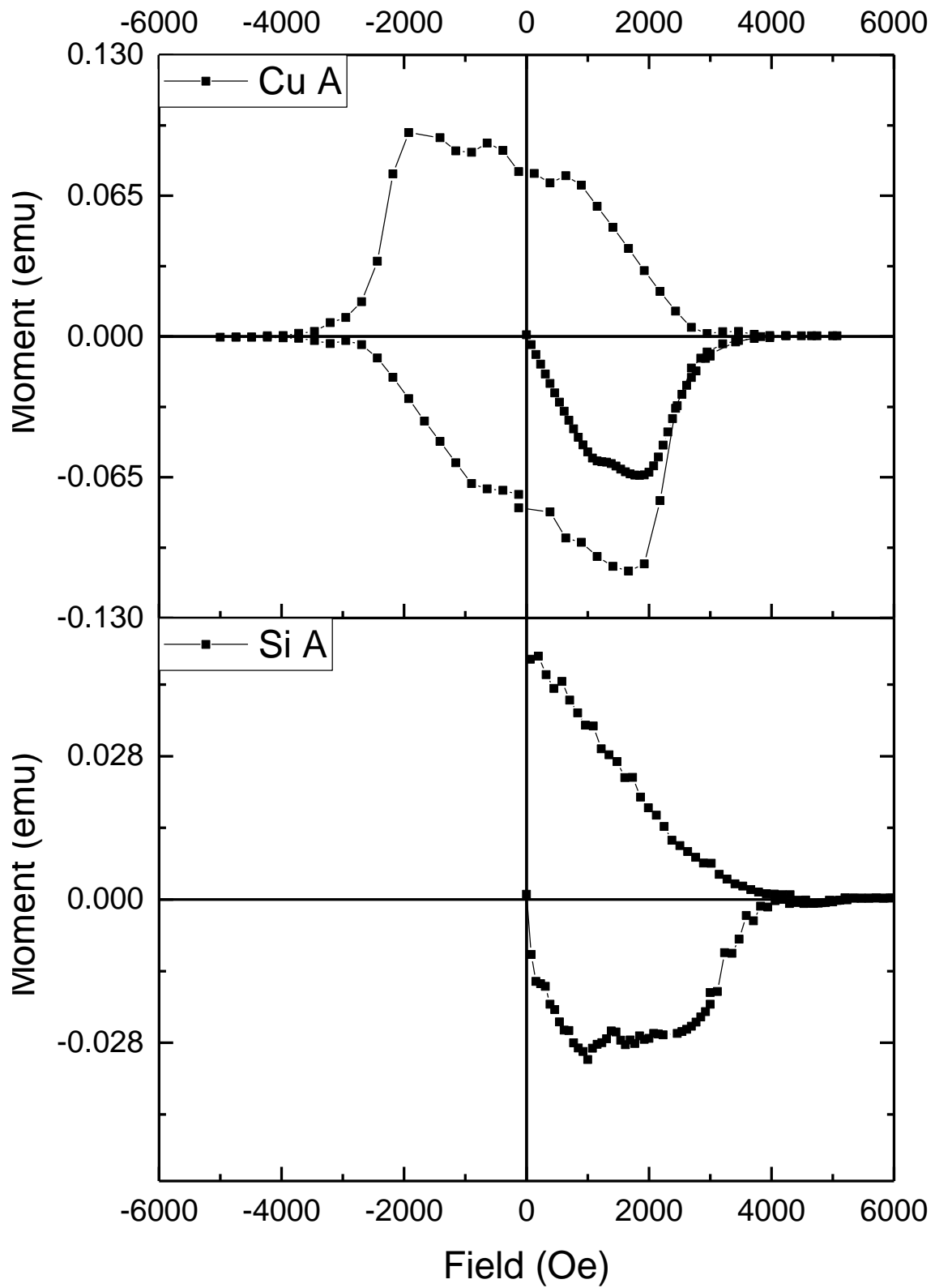


Figure 7.13. DC Hysteresis curves for film A as deposited onto copper and silicon.

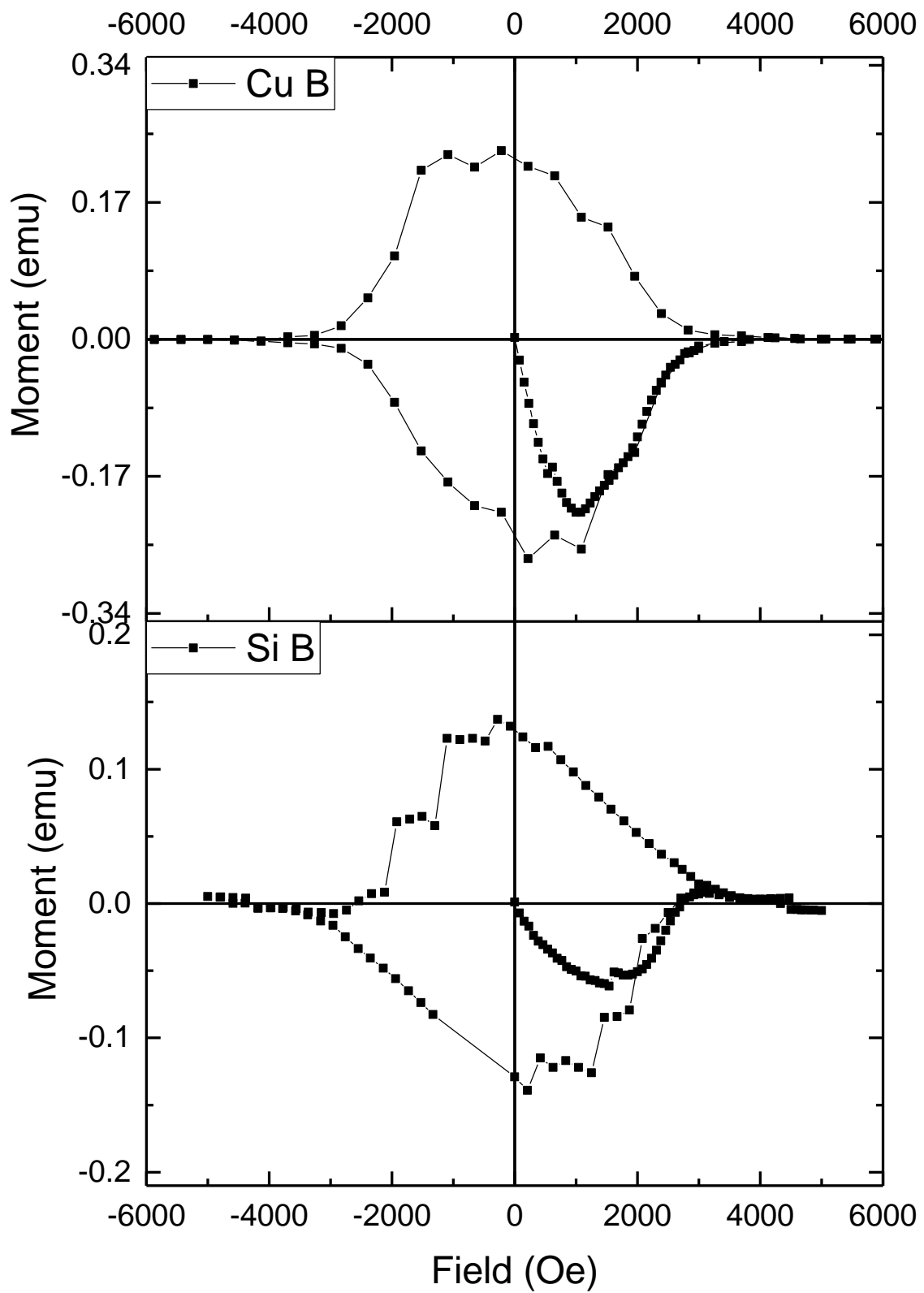


Figure 7.14. DC Hysteresis curves for film B as deposited onto copper and silicon.

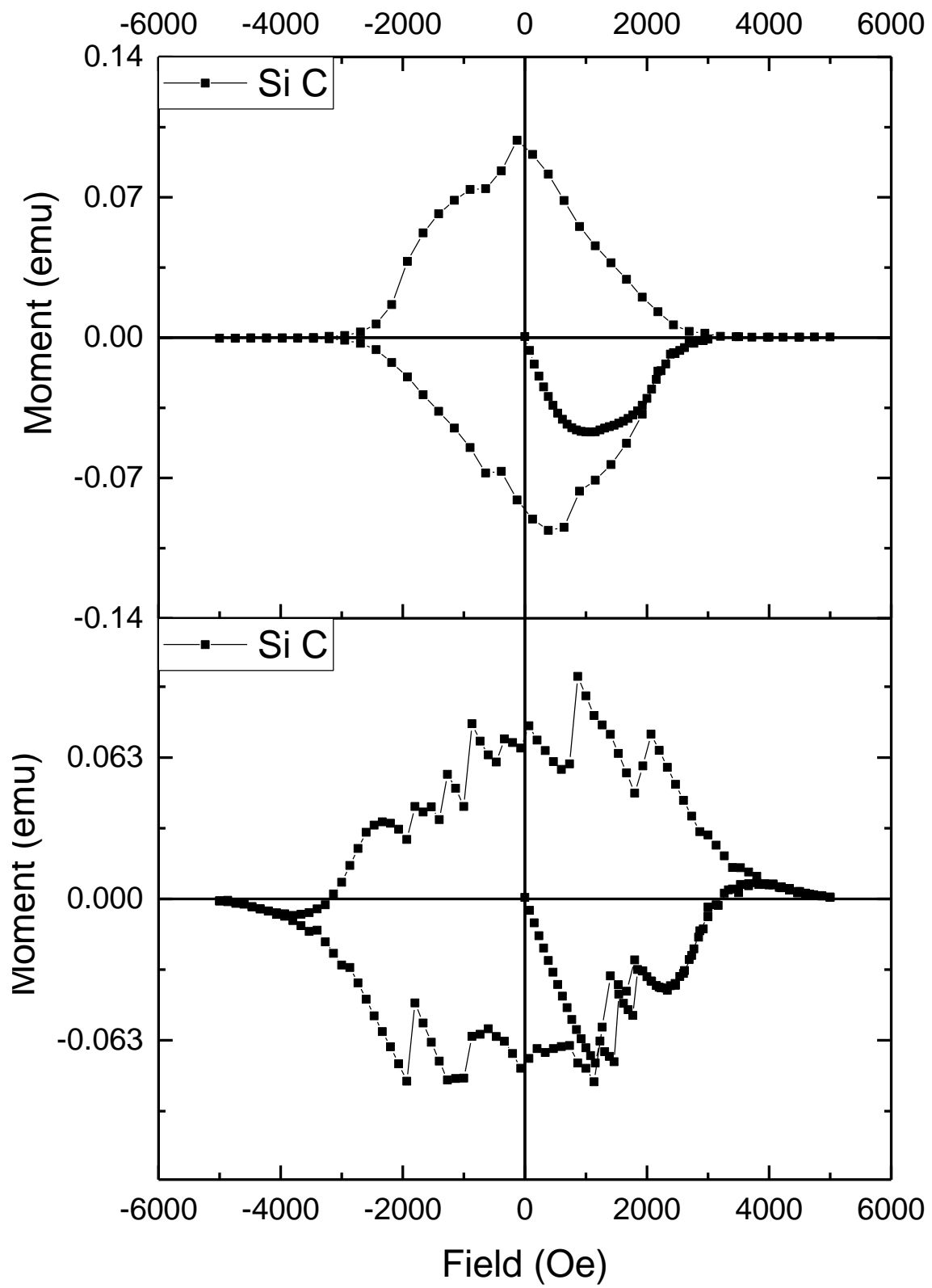


Figure 7.15. DC Hysteresis curves for film B as deposited onto copper and silicon.

The hysteresis curves of the films deposited onto silicon consistently displayed unstable flux pinning whereas the films which had been deposited onto copper showed a stable curve with few flux jumps. The films deposited onto silicon substrate therefore contained trapped magnetic field which was not as strongly pinned as for films deposited onto copper substrate.

The cause of the different pinning properties relates to the types of pinning centre which are present within the film. The fact that both silicon and copper substrates were deposited at the same time and in the same plasma rule out the possibility of differences in elemental impurities within the films and therefore leaves only lattice defects which could alter the pinning properties from sample to sample. The seemingly random nature of the flux jumps exhibited for films deposited onto silicon substrate, as the trapped flux shifts from one pinning centre to another, suggest that the defects formed within the film are also random and can be different from sample to sample. The smoother curves displayed for samples grown on copper substrate suggests a more regular dispersal of defects in those films. The exact nature of the defects is unclear from the results.

It should be reminded that the copper substrate was first etched from the films before performing the DC magnetometry and it has been reported in the literature that removing the substrate can release stresses trapped within the film caused by lattice mismatches at the interface [63]. However, the XRD measurements were performed when the films were still attached to the substrate with measured peak locations which were different for each substrate. The variation in peak position suggests that internal film stresses are be affected by the choice of substrate.

When considering both the XRD and DC magnetometry results then it is fair to conclude that the DC magnetic properties of the film depend on the nature of the defects which are present within the film and that the nature of the defects can be influenced by the substrate. It can be argued that films which contain fewer internal stresses contributing from the substrate / film interface provide the most stable flux pinning once the magnetic field has entered the niobium film.

### **7.2.2. Testing the effects of substrate heating and an applied DC substrate bias when depositing onto as received polycrystalline copper substrate**

The application of a substrate bias resulted in a change of the film microstructure and larger RRR when depositing niobium thin films by DC magnetron sputtering (discussed in section 7.1). The ion to atom arrival ratio is only very small for DC magnetron sputtering and therefore the application of a bias was expected to produce only minor changes in the deposited films. The next phase of the study of niobium thin film deposition was to deposit films by HiPIMS using an applied substrate bias. HiPIMS produces an ion to atom arrival ratio of between 30 and 100 % of the target material, compared to less than 5 % for DC magnetron sputtering, and should allow high energy ion bombardment of the film surface during deposition [75]. The kinetic energies of the bombarding ions will be larger if a bias is applied

The HiPIMS niobium thin films used to test the effects of a DC substrate bias were each deposited onto the same as received polycrystalline oxygen free copper substrates used in section 7.2.1 and followed the same cleaning procedure. The deposition system was prepared in similar fashion to achieve a base pressure of  $\approx 10^{-10}$  mbar. A 99.95 % purity niobium target was used at a fixed distance of 150 mm at a krypton process gas pressure of  $7 \times 10^{-3}$  mbar. Samples were set to rotate at 4 rpm during 4 hour deposition process.

The HiPIMS power supply was set to pulse with constant settings for every deposited film. The voltage was set to pulse at 200 Hz with pulse length of 100  $\mu$ s. The average current was maintained at 600 mA and resulted in peak target currents of approximately 40 A. The power supply settings were chosen as they should provide a stable plasma and produce large numbers of high energy niobium ions [19, 123].

Twenty-four samples were deposited in total. Two deposition parameters were varied, sample temperature and the DC bias applied to the sample substrate. Samples were deposited at room temperature, 500, 700 or 800 °C with either a grounded substrate or with an applied DC bias of -20, -50, -80, -100 or -120 V. Substrates were heated to the desired temperature which was then maintained for 30 minutes so that the temperature was homogeneous throughout the substrate before the start of the deposition. The system was vented with dry nitrogen when the samples were removed.

#### **7.2.2.1. Optical emission spectroscopy**

Plasma monitoring was performed during all deposition processes as a diagnostic tool. There were no differences between the emission spectrums of the tested HiPIMS processes. However, there was a difference between the spectrum of processes using either HiPIMS or the DC sputtering

technique, as shown in figure 7.16. Plasma monitoring confirmed the presence of more intensive niobium<sup>2+</sup> emission lines at between 309 and 319 nm in the case of HiPIMS. The niobium<sup>+</sup> emission line at 408 nm was more intensive in the case of DC sputtering than for HiPIMS. Both spectra contain the same krypton<sup>+</sup> emission lines at 760 and 810 nm respectively.

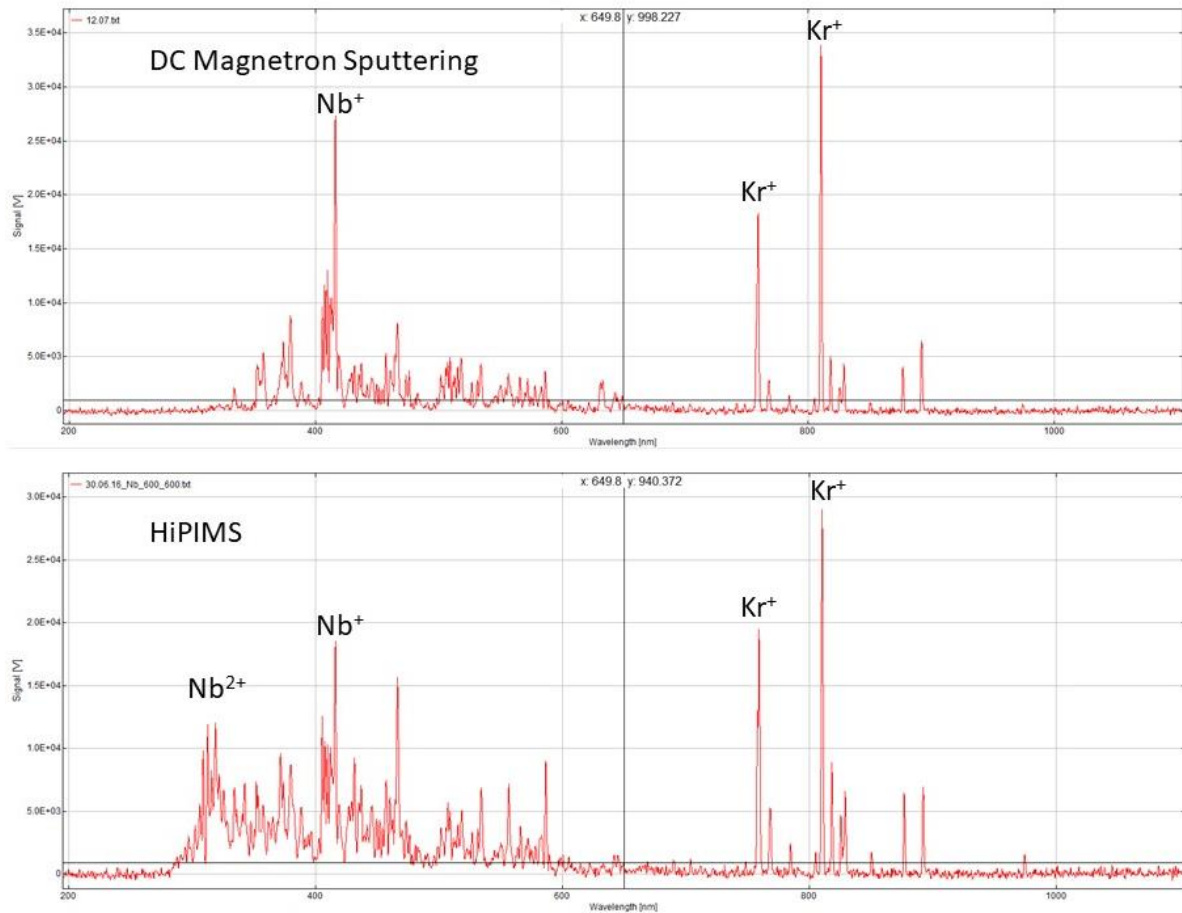


Figure 7.16. Optical emission spectrums of: upper image, a DC magnetron sputtering process and lower, a HiPIMS process.

### 7.2.2.2. Residual Gas Analysis

RGA analysis was performed to ensure that each deposition process progressed in as clean an environment as was possible. As already described, the base pressure of the deposition system was  $10^{-10}$  mbar after full bakeout. N5 (99.999% purity) krypton process gas was injected into the system to a pressure of  $7 \times 10^{-3}$  mbar during deposition. Some of the krypton process gas was sent through a leak valve to the RGA at a pressure of  $5 \times 10^{-7}$  mbar so that it could be analysed. Figures 7.17 and 7.18 show the RGA data that was typical of both before and after the process gas was injected. Cracking patterns for krypton gas appear after gas injection at 77 to 81 amu, 38 to 44 amu and 26 to 30 amu; the cracking patterns relate to the various isotopes of krypton in the singly, doubly and triply ionised

states respectively. The largest peaks relating to krypton were at the  $10^{-7}$  mbar range. Peaks relating to carbon at 12 amu and oxygen at 32 amu remain approximately the same before and after gas injection with partial pressures of approximately  $10^{-12}$  mbar. A peak at 14 amu relating to nitrogen can be seen after gas injection but is only very small at  $5 \times 10^{-13}$  mbar. The difference of 5 or more orders of magnitude between the partial pressure of the process gas and possible impurity elements suggests that impurities within the growing film would be less than 1 %. This value was approximated from estimations of the adsorption rate of residual gasses and the deposition rate of the HiPIMS process.

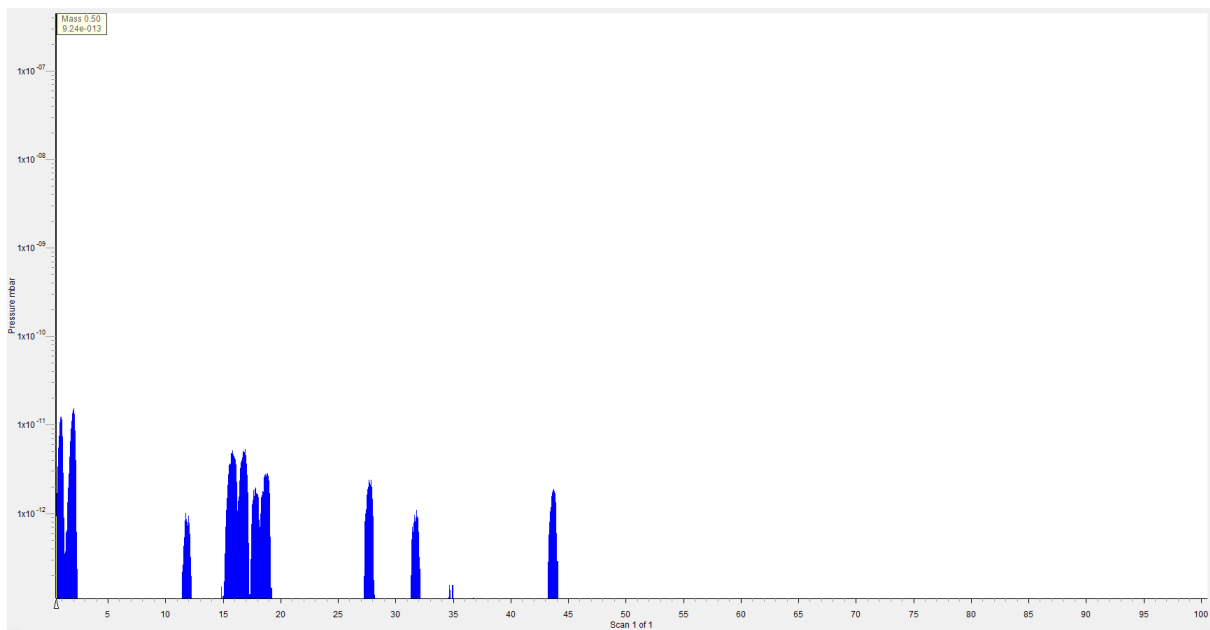


Figure 7.17. RGA spectrum before process gas injection. Pressure against mass to charge ratio is shown.

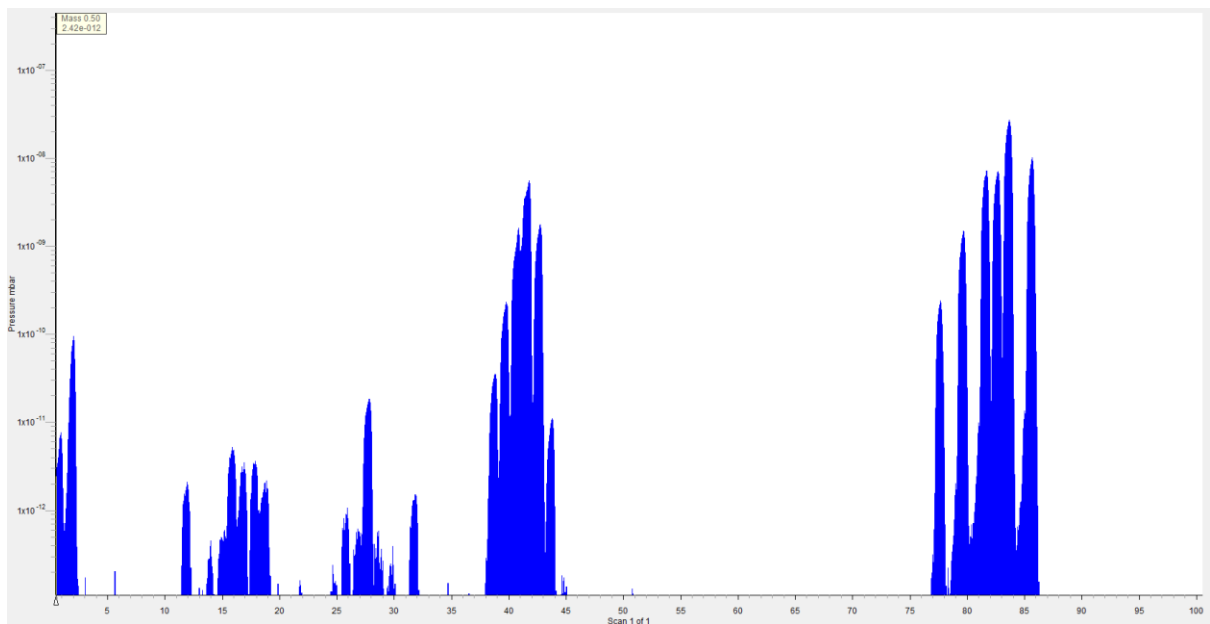


Figure 7.18. RGA spectrum of the process gas at a total pressure of  $7 \times 10^{-7}$  bar. Pressure against mass to charge ratio is shown.

### 7.2.2.3. Rutherford backscattering spectroscopy

Two of the deposited niobium films were sent for analysis by Rutherford backscattering spectroscopy (RBS) to probe the levels of elemental impurities within the films. The measurements were performed by E. Alves and N.P. Barradas at the Centre for Nuclear and Technological Sciences in Lisbon, Portugal. The measured films were deposited at room temperature with an applied bias -120 V and 700 °C with an applied bias of -120 V. Samples were chosen which had both high and low deposition temperatures and with the largest applied bias. Thus, elemental impurities generated by outgassing from the chamber walls and from ion implantation could be quantified. The RBS measurements are shown in figure 7.19. The red symbols are the measured data points, the blue line denotes a fitting line applied by the IBA DataFurnace NDF v9.6f software used after the analysis and the green lines deconvolute the elemental composition from the signal (copper substrate in light green and niobium film in dark green). Each RBS measurement was performed using a 2MeV helium beam with 10° angle of incidence, 165° scattering angle and 25° exit angle. The detector used 850 channels at 25 keV per channel. The measurements of both films describe 100 % niobium elemental composition.

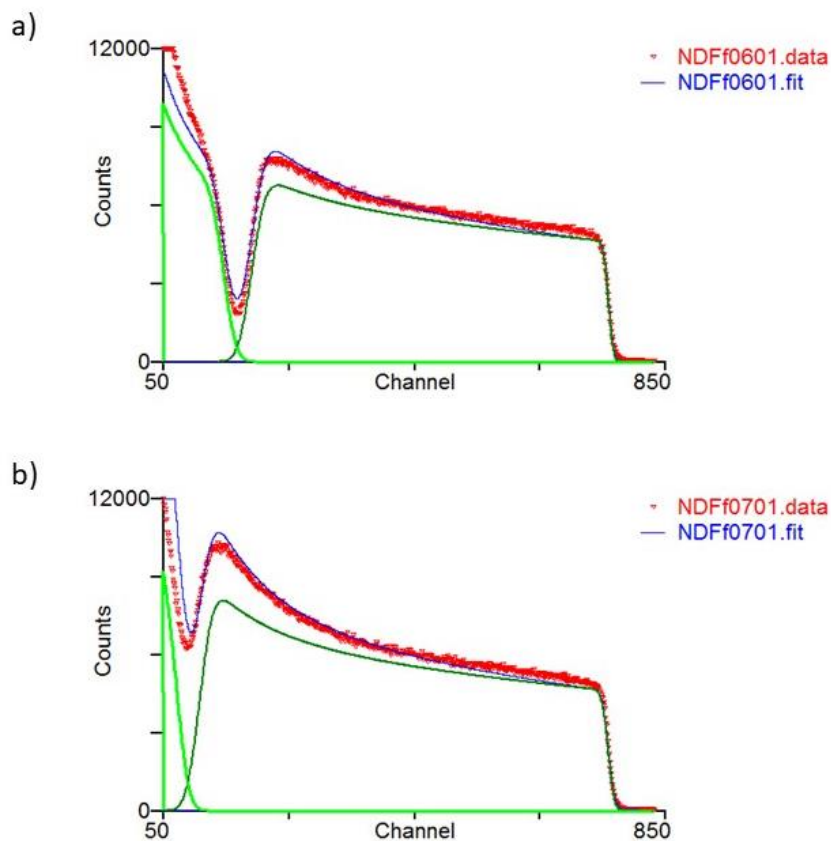


Figure 7.19. Rutherford backscattering spectrometry data for sample deposited at a) room temperature with an applied bias of -120 V and b) 700 °C with an applied bias of -120 V (measurement performed by E. Alves and N.P. Barradas, Lisbon, Portugal).

#### 7.2.2.4. Grazing incidence x-ray diffraction

Each of the films deposited by HiPIMS onto as received copper substrate was analysed using grazing incidence XRD to probe the structural properties of the niobium superconducting lattice. Grazing incidence XRD measurements were performed using a cobalt X-Ray source to produce an x-ray beam with  $K\alpha_1$  wavelength of 1.78901 Å. Each film was analysed when still attached to the substrate and then after having the substrate etched away, the substrate was etched using nitric acid.

Figures 7.20 to 7.23 display all the raw grazing incidence XRD data for the films deposited onto as received substrate with temperatures ranging from room temperature up to 800 °C and with an applied bias voltage ranging 0 to -120 V. All deposited films grew with the same bcc (110) preferred growth orientation with peaks between 44 and 46 °. Films deposited at room temperature and 500 °C show (110) peaks which have smooth almost Gaussian shapes, whereas the peaks become more irregular in shape at 700 and 800 °C. Smaller peaks denoting the following niobium bcc orientations were also observed in every deposited film; (200) at  $\approx 65^\circ$ , (211) at  $\approx 83^\circ$ , (220) at  $\approx 100^\circ$  and (310) at  $\approx 117^\circ$ . Small peaks at  $50^\circ$  relating to fcc copper (111) orientation were visible in a small number of measurements.

The niobium (110) peak locations were later used to calculate  $a_0$  for all deposited thin films, both on the copper substrate and after it had been etched away. The lengths of  $a_0$  are shown in figure 7.24. The length of  $a_0$  was different for all films when measured either with the substrate still in place or after it was removed.

$a_0$  as measured after the substrate has been removed will be described first. The samples display similar  $a_0$  of 3.31 to 3.33 Å for films deposited at room temperature with bias voltages of 0 to -100 V and at 500 °C with bias voltages of 0, -50, -80, -100 and -120 V. The films deposited at room temperature with -120 V bias and at 500 °C with -20 V bias have widely different  $a_0$  when compared to the other films deposited at those temperatures. The entire series of films deposited at either 700 or 800 °C display ranges of  $a_0$  of 3.35 to 3.38 Å or 3.32 to 3.35 Å respectively. Thus, the variability of  $a_0$  was smaller for films deposited at 700 and 800 °C relative to room temperature and 500 °C.

Now, the lengths of  $a_0$  for the films when still attached to the copper substrate will be described. Films that were deposited at room temperature show little variation in the lengths of  $a_0$  with all bias voltages ranging from 3.27 to 3.30 Å. Films deposited at 500 and 700 °C and with bias voltage of -50 to -100 V all show  $a_0$  between 3.27 and 3.29 Å and were like those of films deposited at room temperature. Films deposited at 500 and 700 °C and with applied bias of either 0, -20 or -120 V exhibit seemingly random distributions in the lengths of  $a_0$ . All films deposited at 800 °C appear to show no trends that link the length of  $a_0$  and the bias that was applied during deposition.

Average grain size was calculated using equation 5.1 and the grazing incidence XRD data. The average grain sizes are shown in figures 7.25 and 7.26. Average grain size was calculated at between 15 and 45 nm for all deposited films. There appear to be no trends linking the calculated values of grain size and the different process conditions.

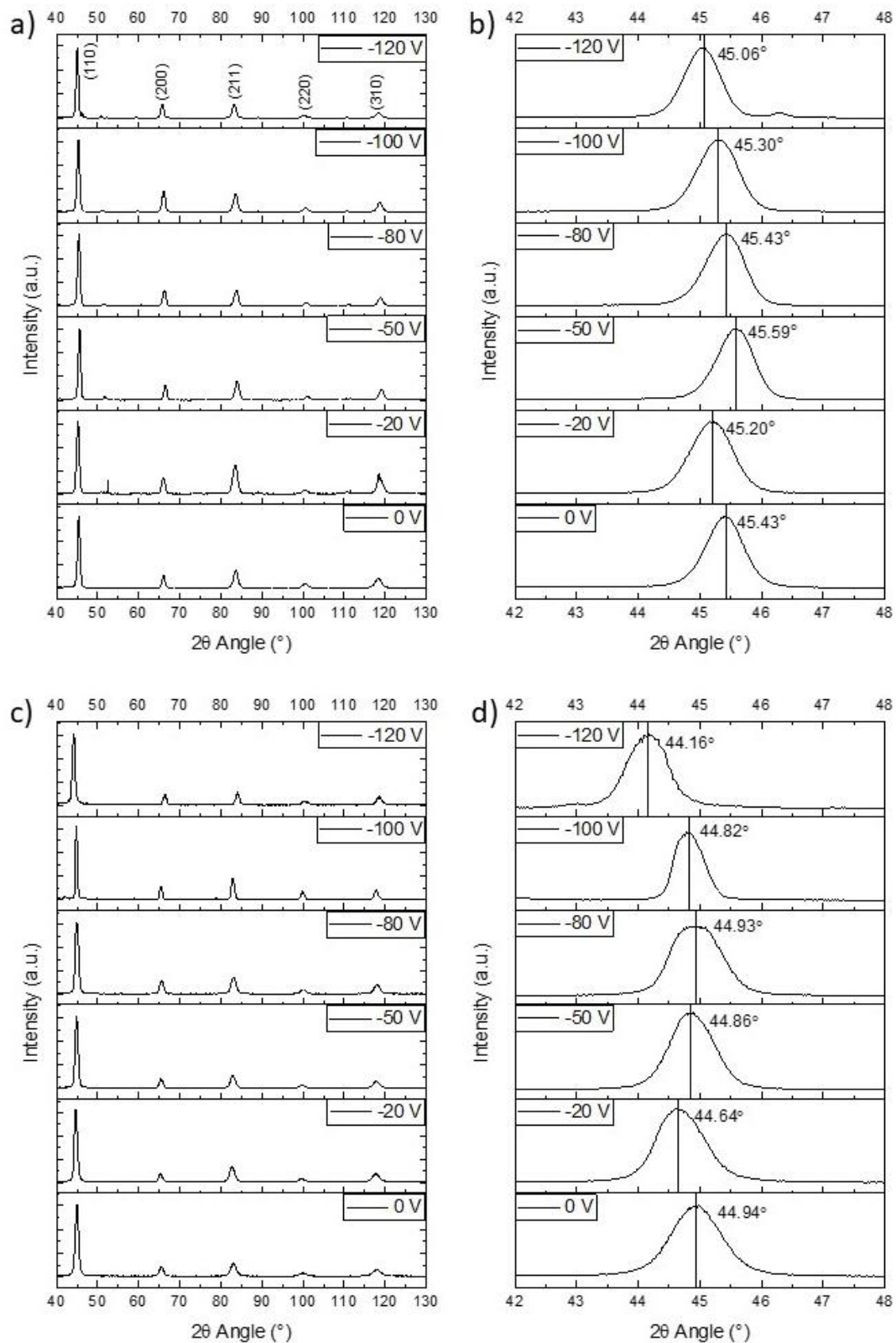


Figure 7.20. Grazing incidence XRD data for samples deposited onto as received substrate at room temperature. Data is shown from a) 40 to 130 ° measured on copper, b) the (110) peak at approximately 44 - 46° measured on copper, c) 40 to 130 ° measured after the copper substrate was etched away and d) the (110) peak at approximately 44 - 46° measured after the copper substrate was etched away.

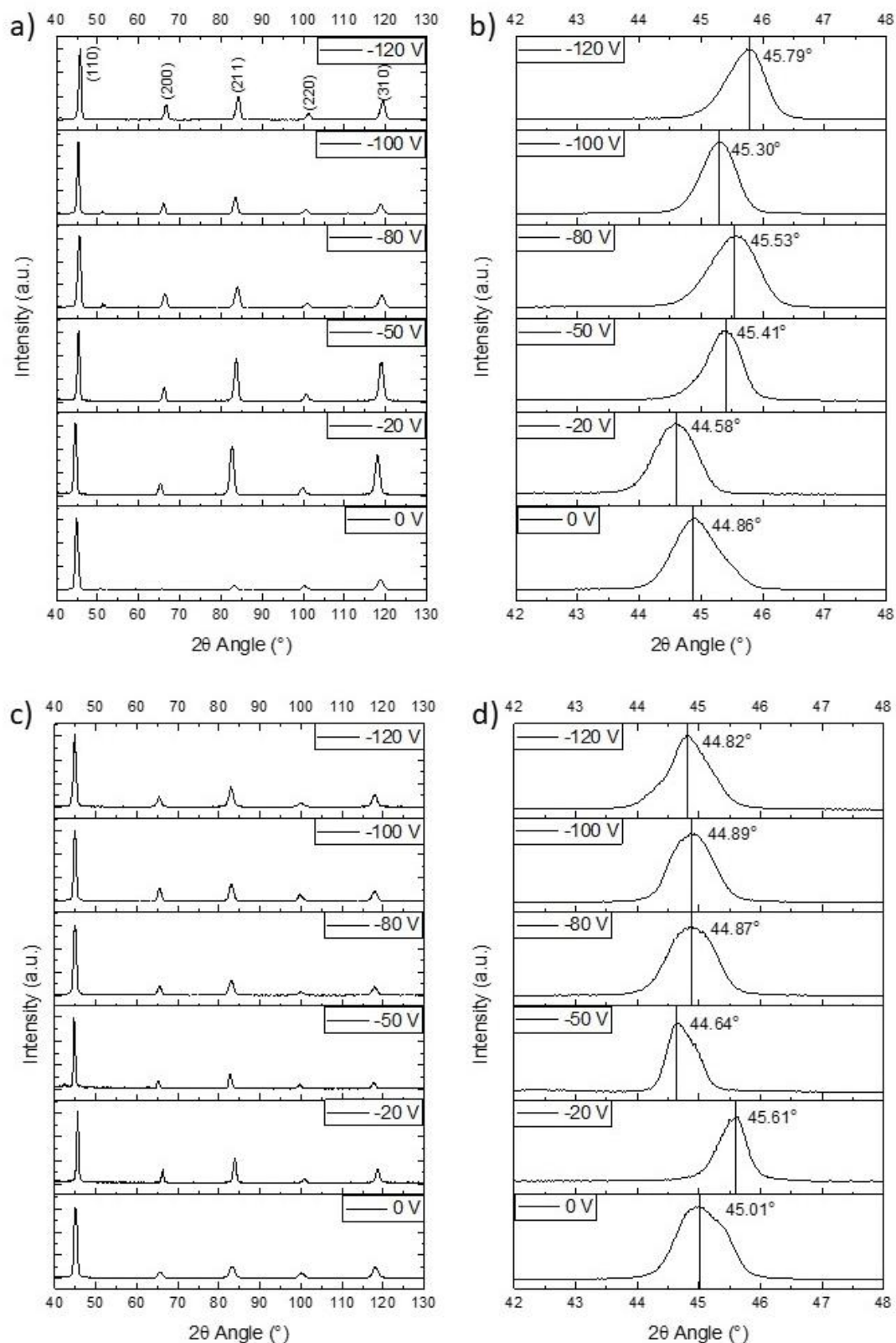


Figure 7.21. Grazing incidence XRD data for samples deposited onto as received substrate at 500 °C. Data is shown from a) 40 to 130 ° measured on copper, b) the (110) peak at approximately 44 - 46° measured on copper, c) 40 to 130 ° measured after the copper substrate was etched away and d) the (110) peak at approximately 44 - 46° measured after the copper substrate was etched away.

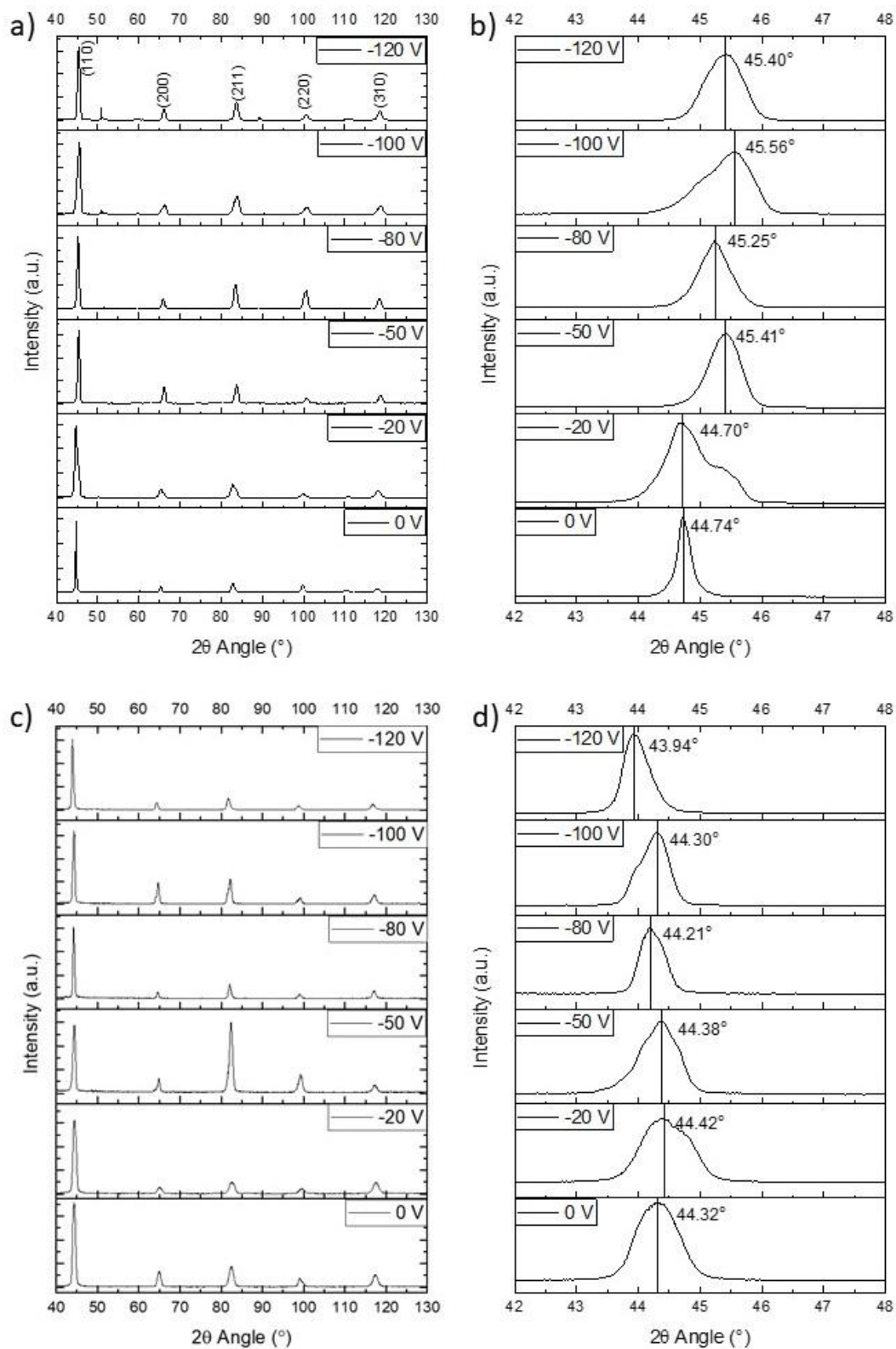


Figure 7.22. Grazing incidence XRD data for samples deposited onto as received substrate at 700 °C. Data is shown from a) 40 to 130 ° measured on copper, b) the (110) peak at approximately 44 - 46 ° measured on copper, c) 40 to 130 ° measured after the copper substrate was etched away and d) the (110) peak at approximately 44 - 46 ° measured after the copper substrate was etched away.

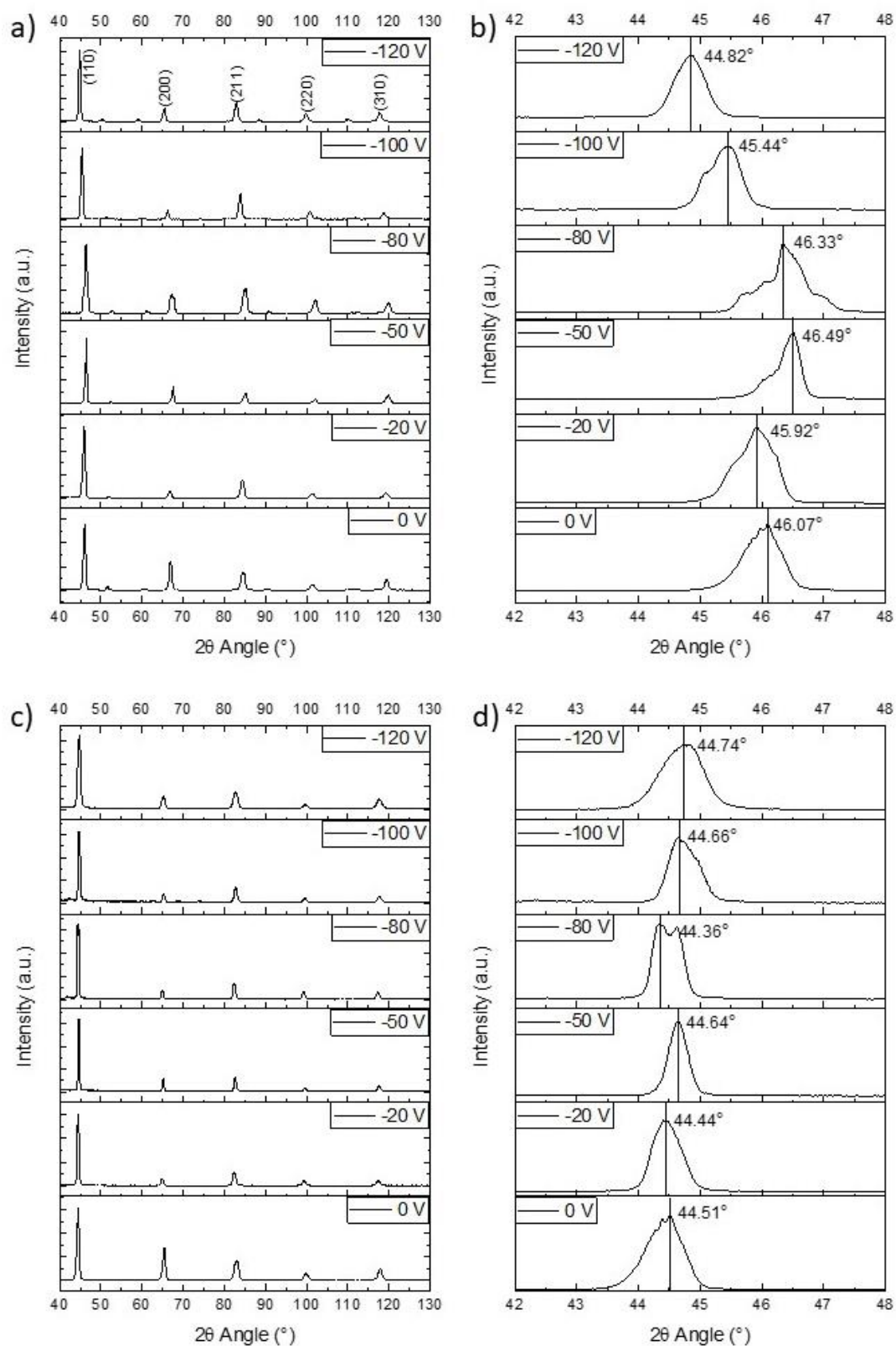


Figure 7.23. Grazing incidence XRD data for samples deposited onto as received substrate at 800 °C. Data is shown from a) 40 to 130 ° measured on copper, b) the (110) peak at approximately 44 - 46° measured on copper, c) 40 to 130 ° measured after the copper substrate was etched away and d) the (110) peak at approximately 44 - 46° measured after the copper substrate was etched away.

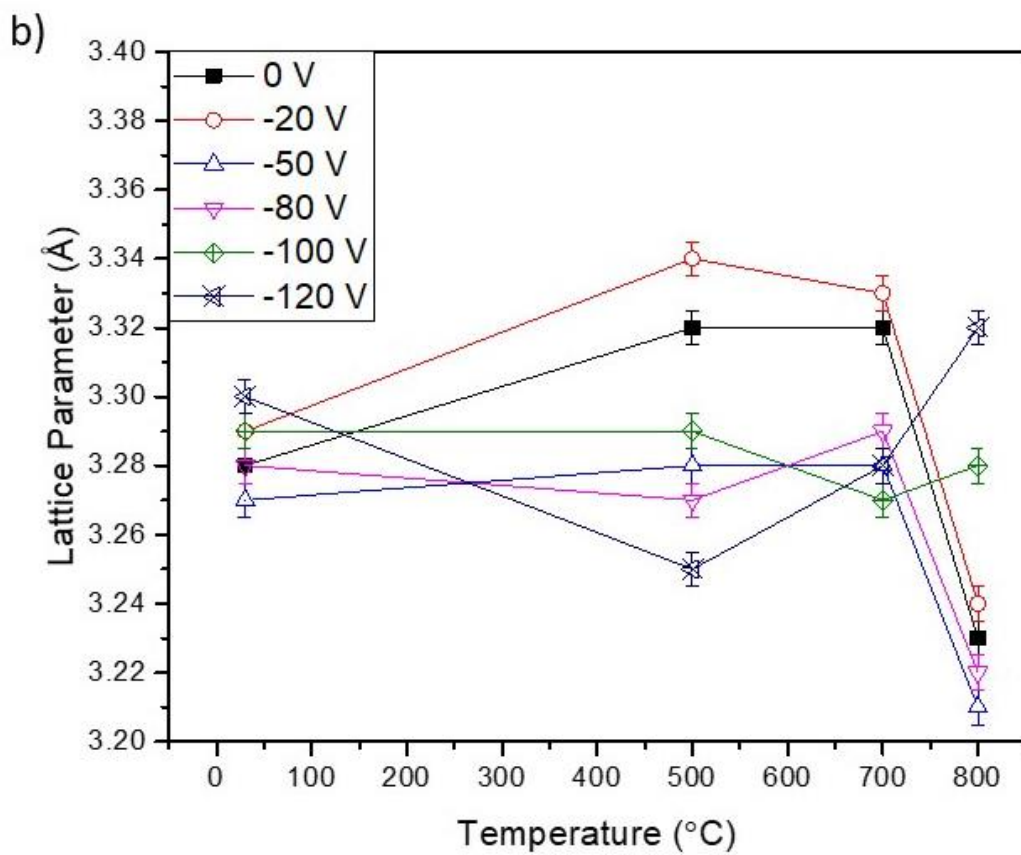
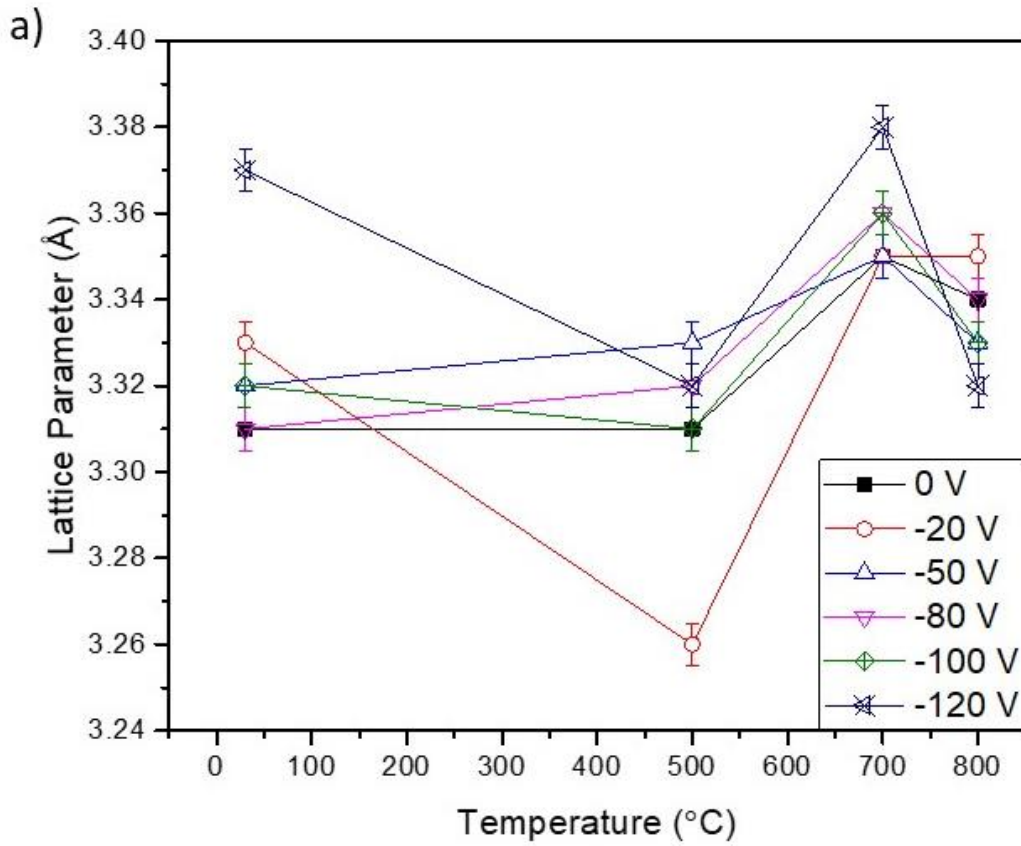


Figure 7.24. Lattice parameters  $a_0$  of niobium thin films a) after having the copper substrate etched away and b) with the copper substrate still in place.

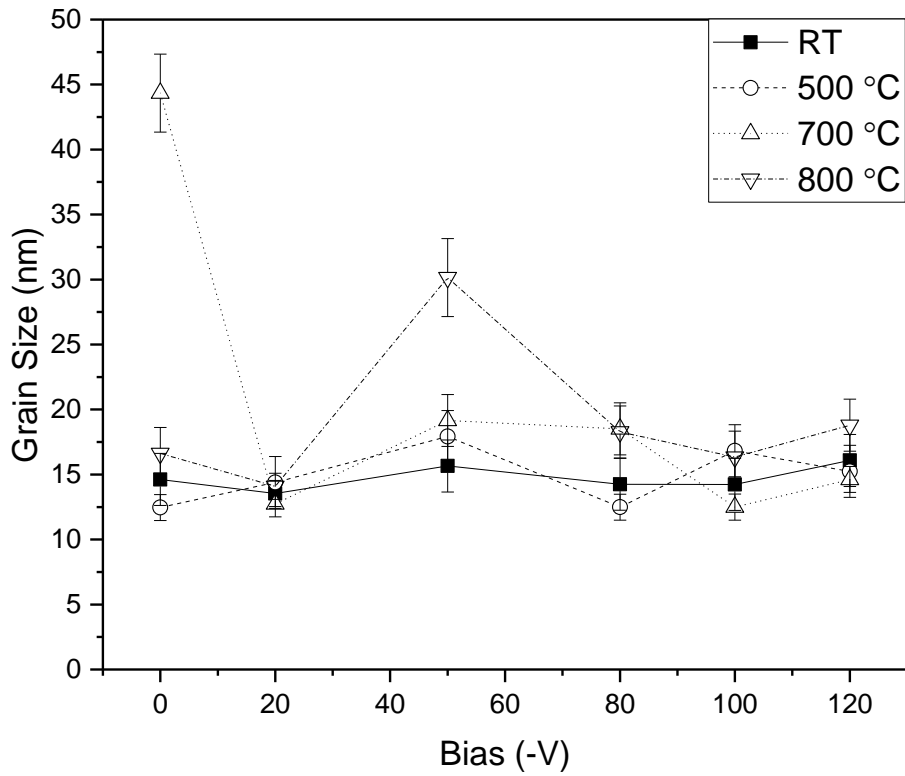


Figure 7.25. Average grain size against applied bias voltage during deposition of niobium thin films measured after the substrate was etched away.

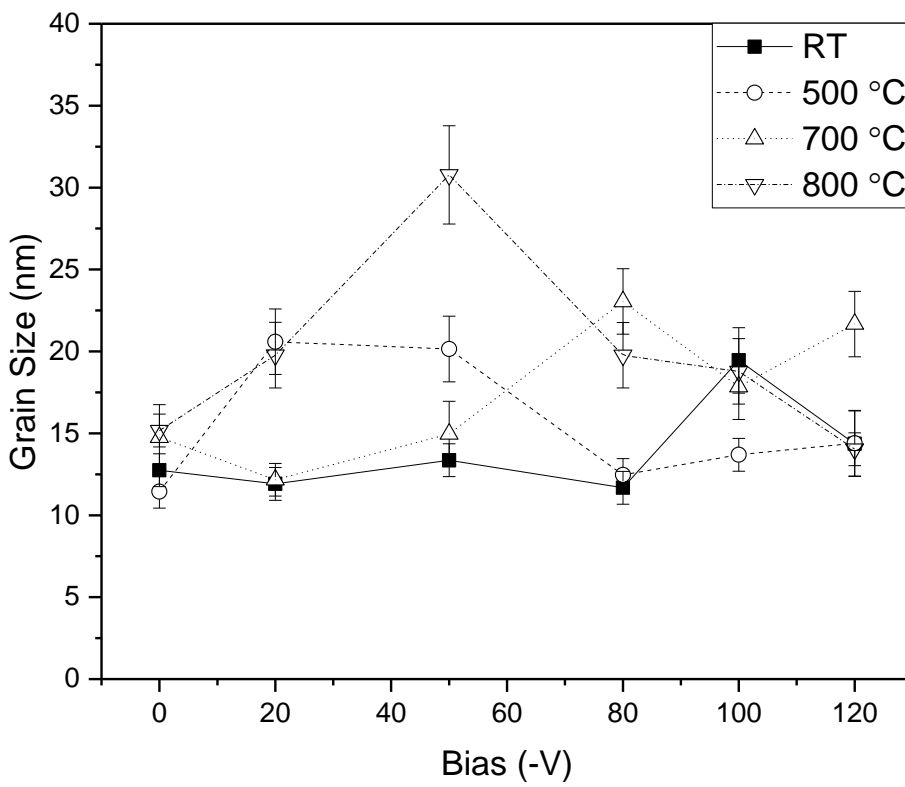


Figure 7.26. Average grain size against applied bias voltage during deposition of niobium thin films as measured on polycrystalline copper substrate.

### 7.2.2.5. Scanning electron microscopy and 3D optical microscopy

SEM images were taken of a selection of films deposited with substrate temperatures ranging from room temperature to 800 °C and with either a grounded substrate or with an applied bias of -80 V, the images are shown in figure 7.27. Figures 7.27 a to f are all backscatter detector images; a and c with a spot size of 3 nm and beam energy of 20 kV, b with a spot size of 4.5 nm and beam energy of 20 kV and d and f with a spot size of 3 nm and beam energy of 10 kV. Figures 7.27 g and h are secondary electron images performed with a beam energy of 1.5 kV. The images show that there is only a very small increase in grain size for grounded films deposited at 500 °C relative to room temperature; grain size is sub-microns in both instances. The films deposited at room temperature and 500 °C with an applied bias of -80 V display grains which appear to be larger and more densely packed together relative to the grounded substrate at the same temperature. Grain size becomes much larger, 1 – 2 microns across, for each film that was deposited at 700 and 800 °C.

It was apparent when viewing by eye that several of the samples had undergone some form of deformation process at the sample surface. Therefore, each sample was imaged using a Keyence VHX - 2000 3D optical microscope to find the extent of the deformation. The 3D optical microscope allows surface contour maps to be overlain onto images so that differences in the surface height can be evaluated with an accuracy of  $\pm 10$  nm. However, the error in height of the contour maps plotted for this study have been quoted at  $\pm 2$   $\mu\text{m}$  after considering that each image consists of 9 smaller images which are stitched together and that each image needed to be tilt corrected. Tilt correction is necessary for samples which do not have a perfectly flat base, such as the unpolished copper substrate which was used for niobium film deposition. Tilt correction is performed by the user, who defines 3 points on the stitched image which they believe to be of the same height, then the software corrects the tilt of the image. Each individual image has dimensions of approximately 240 x 270  $\mu\text{m}$  and the stitched images are 640 x 740  $\mu\text{m}$ . The surface height ranged from 0 to 20  $\mu\text{m}$  across all deposited samples. The surface contours of a reference uncoated polycrystalline copper substrate are shown in figure 7.28 where the maximum measured height was  $6 \pm 2$   $\mu\text{m}$  and minimum was  $0 \pm 2$   $\mu\text{m}$ .

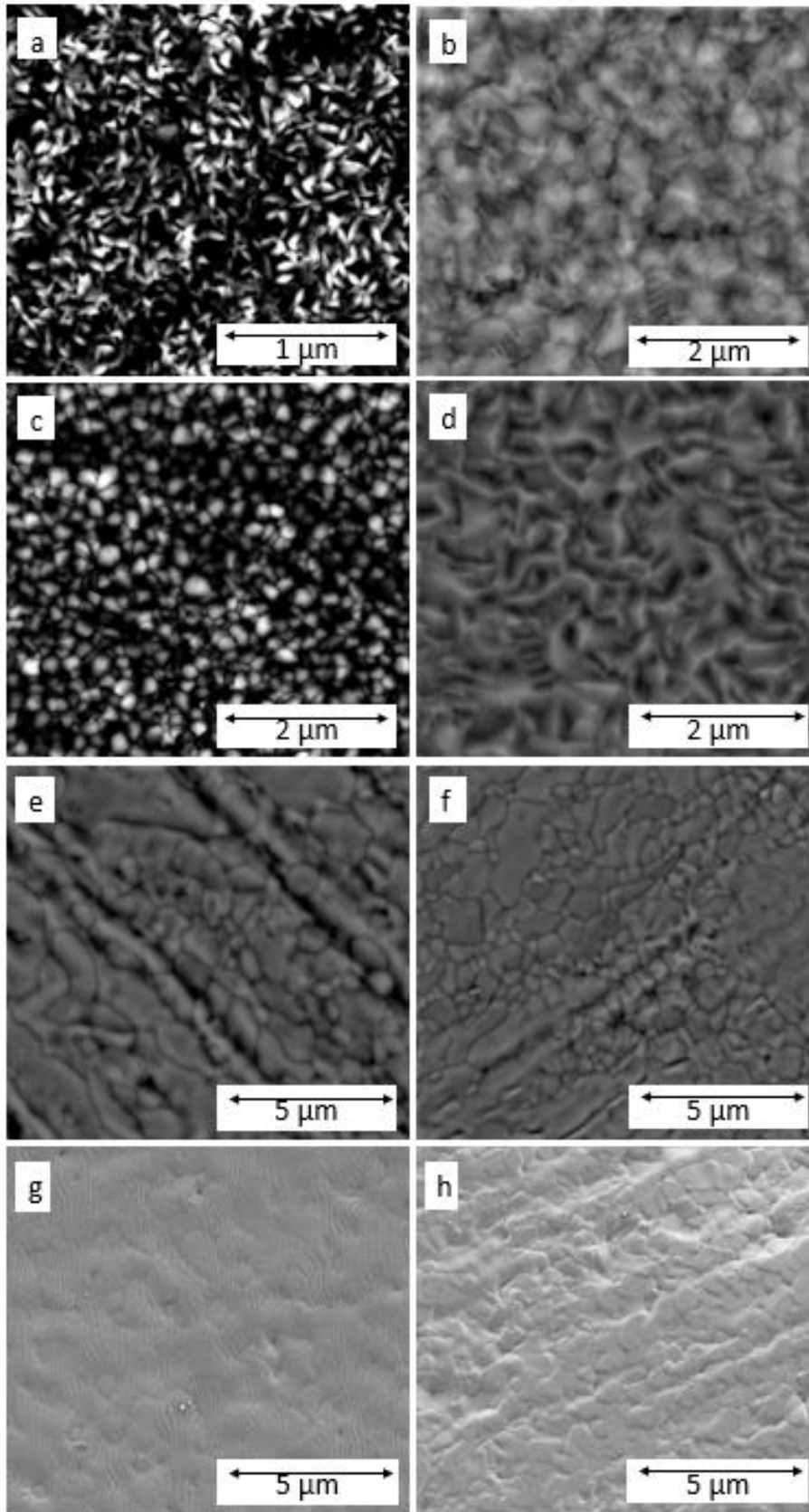


Figure 7.27. Planar SEM images of niobium thin film samples deposited a) at room temperature and no bias, b) at room temperature with -80 V bias, c) at 500 °C with no bias, d) at 500 °C and -80 V bias, e) at 700 °C with no bias, f) at 700 °C with -80 V bias, g) at 800 °C with no bias and h) at 800 °C with -80 V bias.

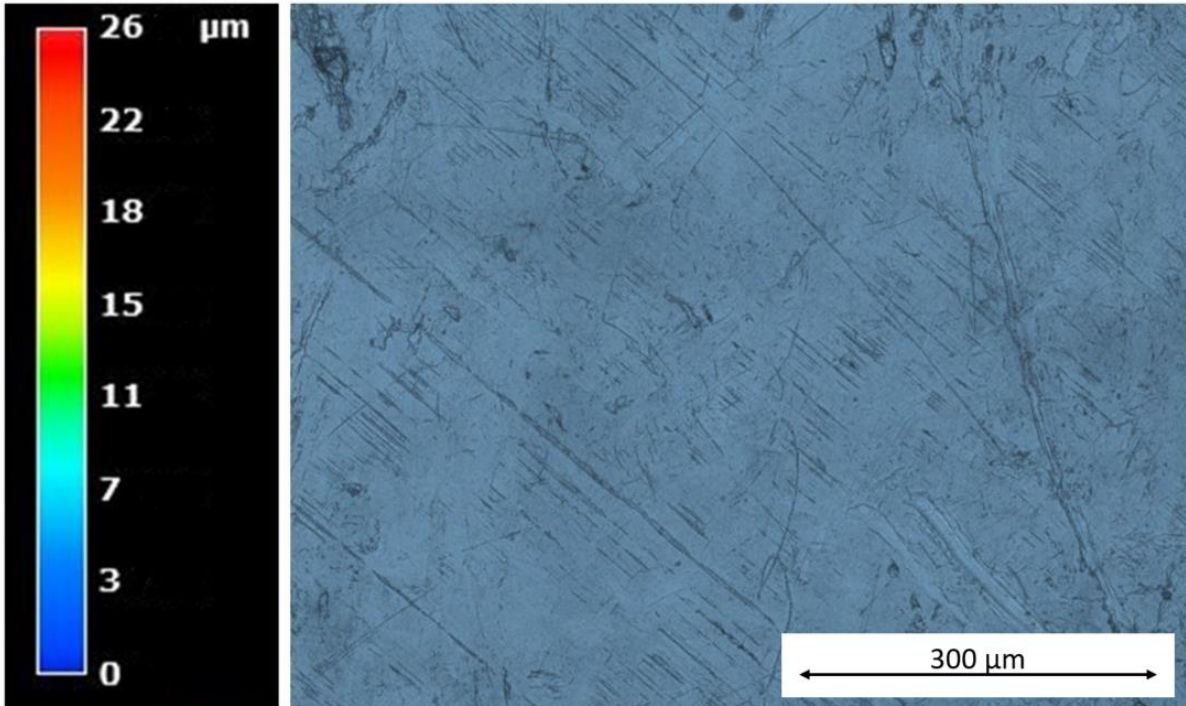


Figure 7.28. The surface contour map of an uncoated polycrystalline copper substrate.

The samples deposited at room temperature and 500 °C with bias voltages of 0 to -120 V can be seen in figures 7.29 and 7.30. Each sample deposited at room temperature, and those deposited at 500 °C with applied bias of 0, -20, -50, -100 and -120 V, resembles the surface contours of an uncoated copper substrate and show a variation in surface height of approximately  $6\pm 2$  to  $10\pm 2$   $\mu\text{m}$ . The film deposited at 500 °C with an applied bias of -80 V displays a different texture than the other films deposited at room temperature and 500 °C, with what appears to be “blisters” at the surface that are approximately 10 – 30  $\mu\text{m}$  in diameter. Figure 7.31 shows a secondary electron detector SEM image of both the films deposited with applied bias of -80 V at room temperature and 500 °C. Figure 7.31 highlights the difference between a film surface which matches the topography of the underlying copper substrate and a “blistered” surface.

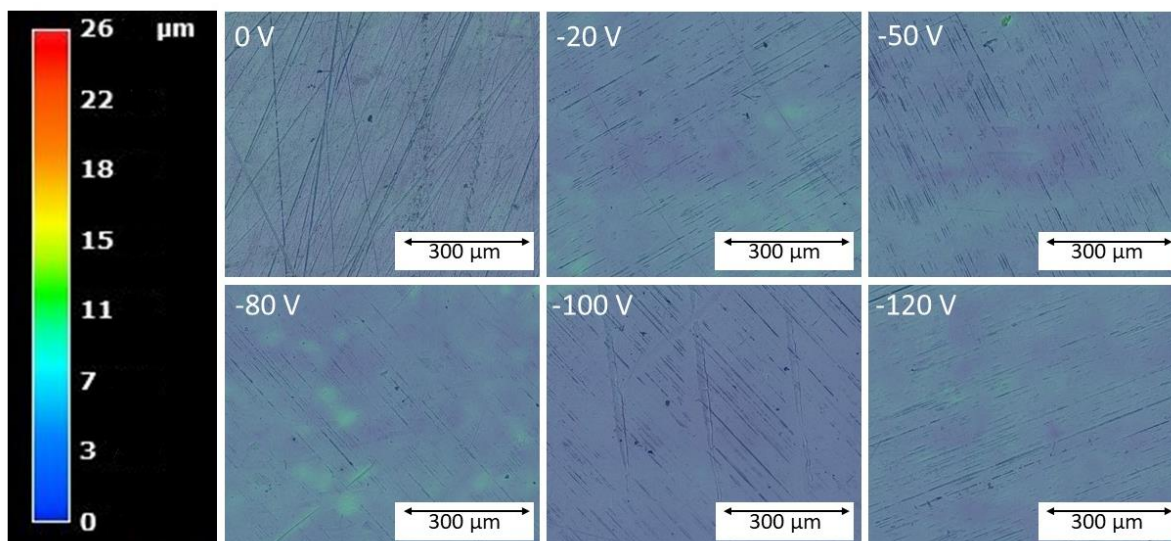


Figure 7.29. Contour map of the surface of niobium thin films deposited onto polycrystalline copper substrate at room temperature and with a bias voltage ranging from 0 to -120 V DC.

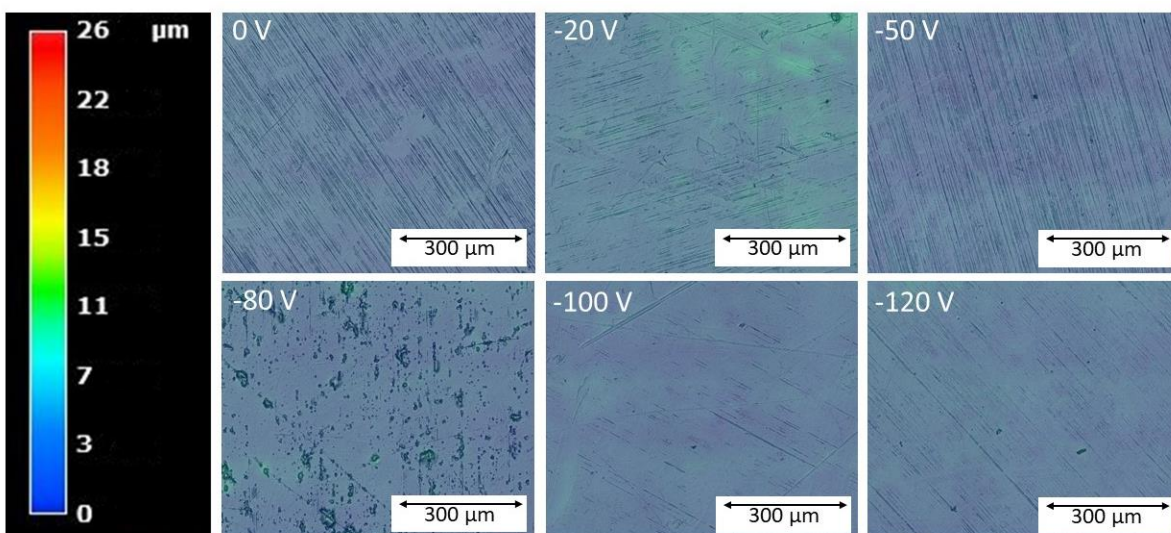


Figure 7.30. Contour map of the surface of niobium thin films deposited onto polycrystalline copper substrate at 500 °C and with a bias voltage ranging from 0 to -120 V DC.

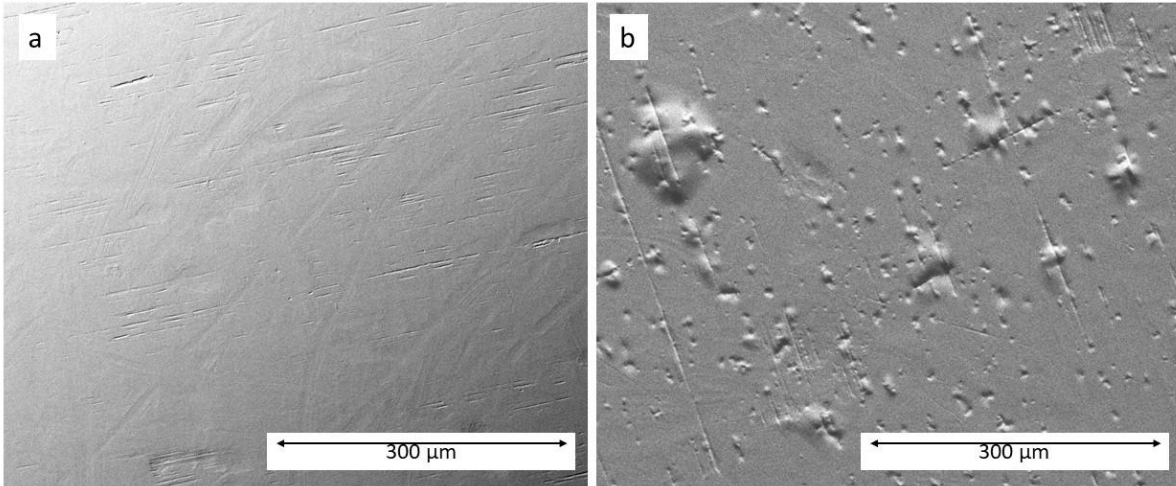


Figure 7.31. Secondary electron detector SEM images of the films deposited at a) room temperature with an applied bias of -80 V and b) 500 °C with applied bias of -80 V. The surface topography of the sample deposited at room temperature matches that of the underlying copper substrate whilst a “blistered” surface is seen for the film deposited at 500 °C.

The surface contour map and height profiles of samples deposited at both 700 and 800 °C with bias voltages ranging 0 to -120 V are shown in figures 7.32 and 7.33. It is apparent at each temperature that the surface texture changes as the bias voltage is increased. Raised “blisters” appear at the films surface when deposited at 700 °C with applied bias of -50 to -120 V and at 800 °C with an applied bias of -80 to -120 V. The raised “blisters” grow larger in height and diameter, with heights ranging  $10\pm 2$  to  $20\pm 2$   $\mu\text{m}$  and diameter ranging 50 to 250  $\mu\text{m}$ , and occur more frequently as the bias voltage is increased during deposition. Figure 7.34 displays a secondary electron SEM detector image of the film deposited at 700 °C with applied bias of -120 V and was the film which displayed the largest and most frequent “blisters” at the film surface.

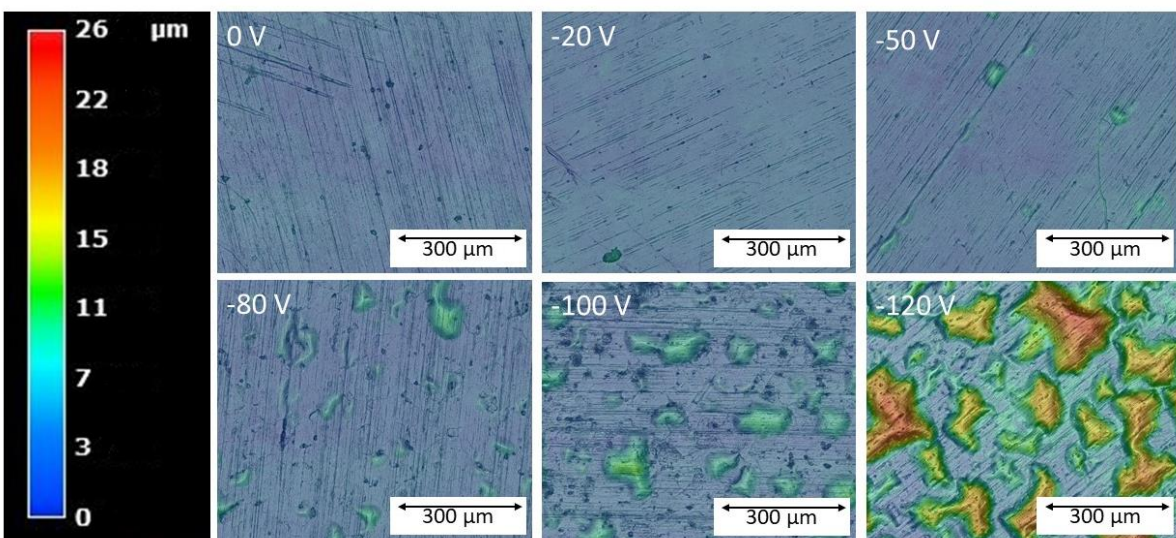


Figure 7.32. Contour map of the surface of niobium thin films deposited onto polycrystalline copper substrate at 700 °C and with a bias voltage ranging from 0 to -120 V DC.

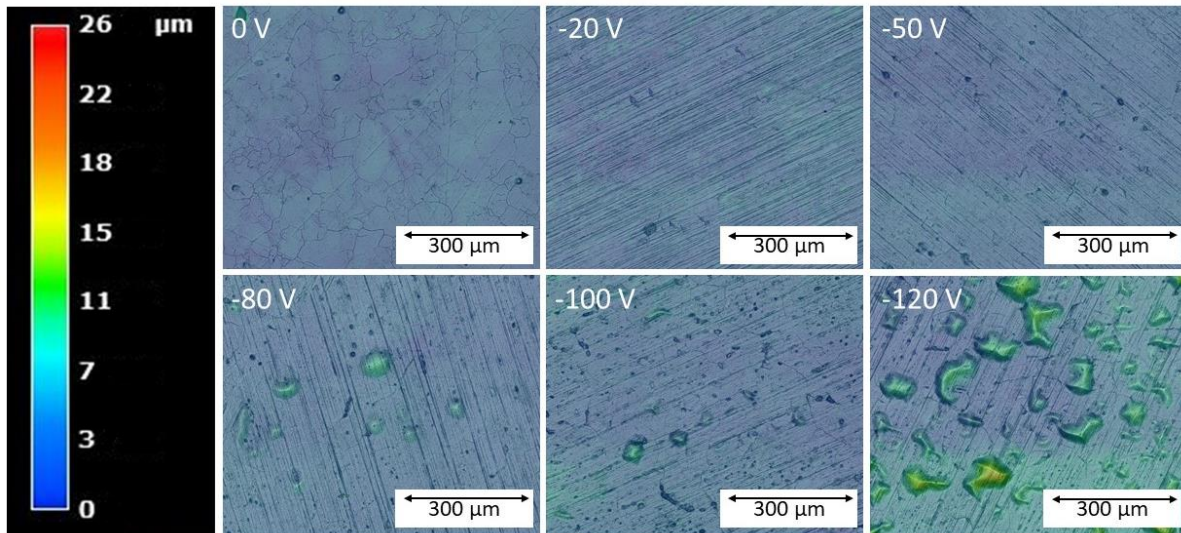


Figure 7.33. Contour map of the surface of niobium thin films deposited onto polycrystalline copper substrate at 800 °C and with a bias voltage ranging from 0 to -120 V DC.

Films deposited at 700 °C with -100 V bias and at 800 °C with -80 V bias (both displaying “blisters” at the surface) were imaged in cross section and are displayed in figures 7.35 and 7.36. The cross section was cut through numerous “blisters” and then mounted in conductive resin and mechanically polished to a mirror surface. No indication of the nature of the “blisters” was observed in the cross sectional SEM images. The cross-sectional images allowed the thickness of the films to be measured. Both films were 1.4 microns thick. It was therefore assumed that all films deposited with similar conditions, and for the same length of time by HiPIMS, should have approximately similar thickness of 1.4 micron.

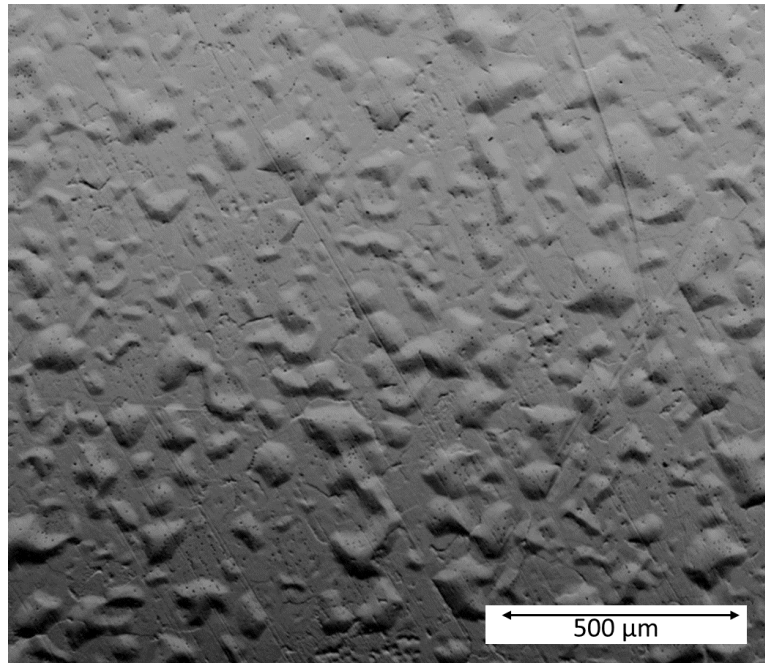


Figure 7.34. Secondary electron detector SEM image of the films deposited at 700 °C with applied bias of -120 V. The surface displays larger and more frequent “blisters” at the surface than was observed for any other film.

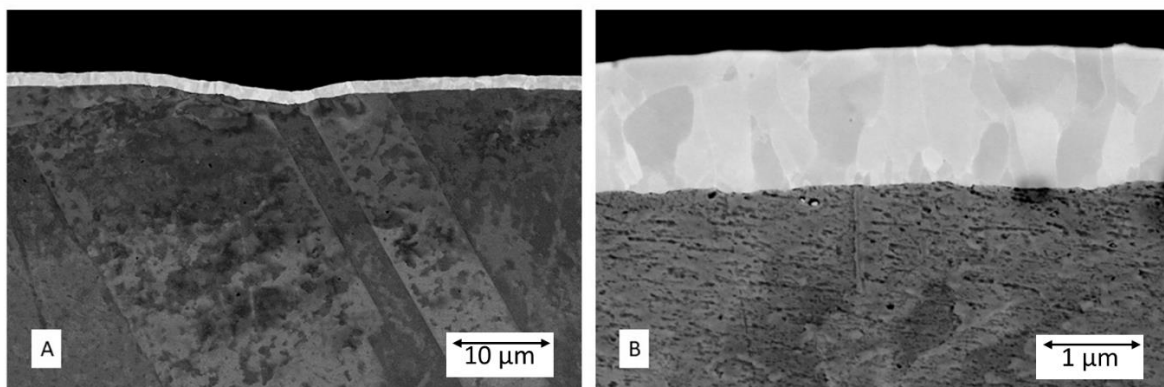


Figure 7.35. SEM cross section of a niobium thin film deposited at 700 °C with -100 V bias. a) displays 3500 X magnification and b) 35000 X magnification.

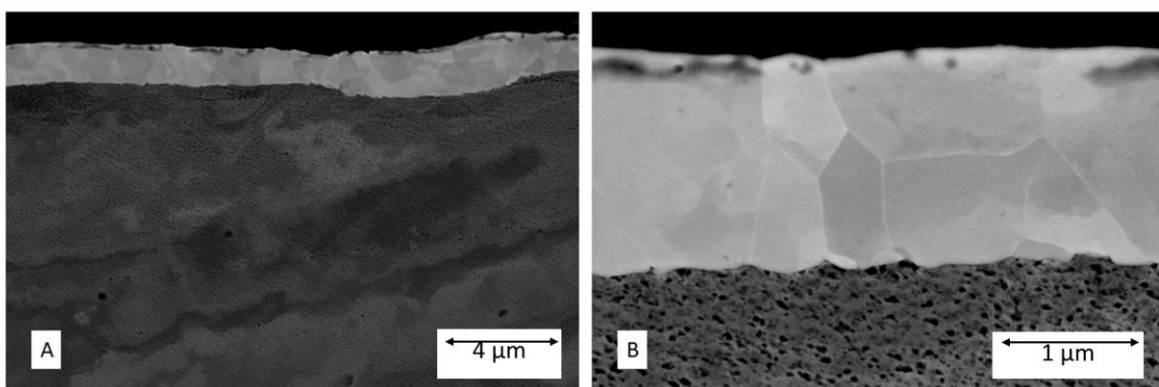


Figure 7.36. SEM cross section of a niobium thin film deposited at 800 °C with -80 V bias. a) displays 10000 X magnification and b) 50000 X magnification.

### 7.2.2.6. Resistance versus temperature curves

Resistance versus temperature curves were measured for each film using a four point probe. The copper substrate was first etched from each film so that a component of resistance from the copper was not measured. The measurements were performed by setting a constant current of 10 mA across the probe whilst the voltage was read at 5 second intervals as the sample cooled from room temperature to below  $T_c$ . The measured resistance was then used to calculate the RRR of each sample. The resistance of each sample has been plotted between 0 to 0.005 m $\Omega$  for all films at temperatures of 0 to 100 K. A small selection of films displayed larger resistance than 0.005 m $\Omega$  but have not been displayed in full to allow comparisons of the most useful datasets which exhibited the smallest resistance. Films which display very large DC resistance in the normal conducting state would be expected to show very large  $R_S$  in the superconducting state [17]. Each measurement is also plotted as RRR versus temperature from 10 to 100 K.

Figure 7.37a displays the measured resistance for the samples deposited at room temperature onto as received polycrystalline copper substrate. The sample with the largest resistance was the 0 V biased sample and displayed 0.0230 m $\Omega$  at just above  $T_c$ . Of the other bias voltages, -20 and -120 V films displayed similar resistances of approximately 0.0022 m $\Omega$ , -80 and -100 V displayed approximately 0.0018 m $\Omega$  and -50 V displayed the smallest normal state resistance of 0.0013 m $\Omega$ .

Figure 7.37b displays the RRR versus temperature data for the films deposited at room temperature. The smallest RRR at 10 K of all deposited samples was 9 and occurred for the sample deposited with 0 V bias. The -20 V biased film displayed RRR of 13 whilst those deposited with bias voltages of -50, -80, -100 and -120 V displayed RRR ranging 19 to 21.

Figure 7.38a displays the normal state resistance for the films deposited at 500 °C. Like the room temperature films, the 0 V biased sample displays the largest resistance at just above  $T_c$  at 0.0468 m $\Omega$ . The film biased at -120 V during deposition has the next largest resistance of 0.0032 m $\Omega$ , followed by -100 V at 0.0017 m $\Omega$  then -50 V at 0.0013 m $\Omega$ . The smallest normal state resistance of the films deposited at 500 °C occurred for those biased at -20 and -80 V with resistances of 0.0010 m $\Omega$ .

Figure 7.38b presents the RRR versus temperature data for the samples deposited at 500 °C. The smallest RRR at 10 K for the films deposited at 500 °C was 11 and occurred for the sample deposited with 0 V bias. RRR was measured at 18 for the film biased at -120 V, 24 for the film biased at -100 V and was largest for those biased at -20, -50 and -80 V which ranged 30 to 31. The largest RRR values at 500 °C were approximately 30 % larger than the largest value recorded for the films deposited at room temperature.

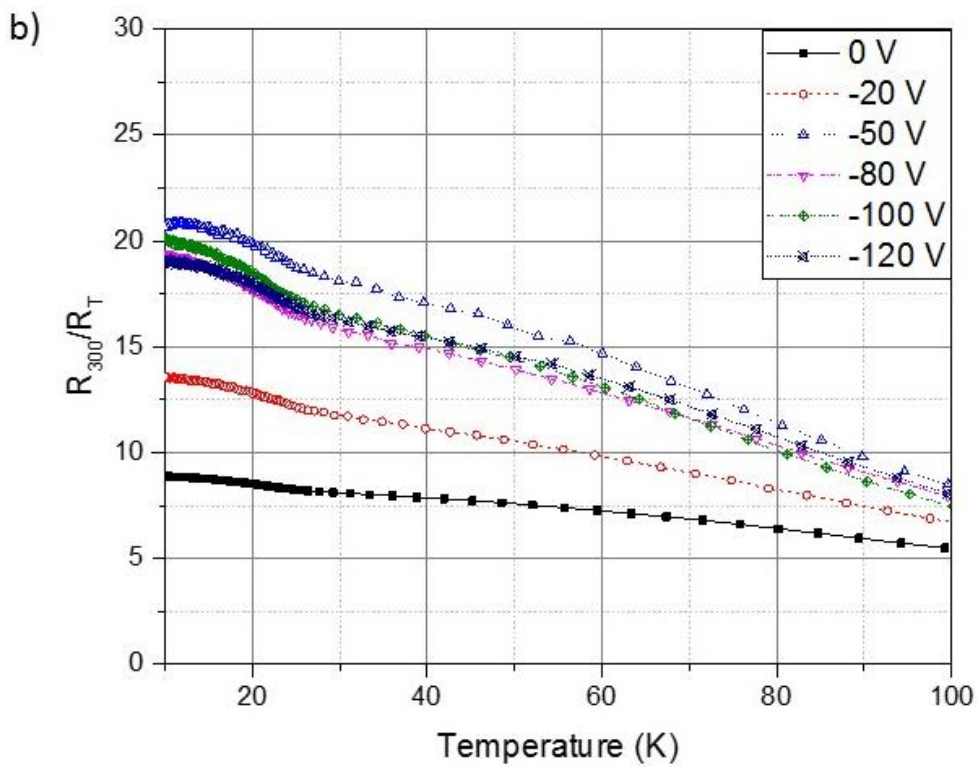
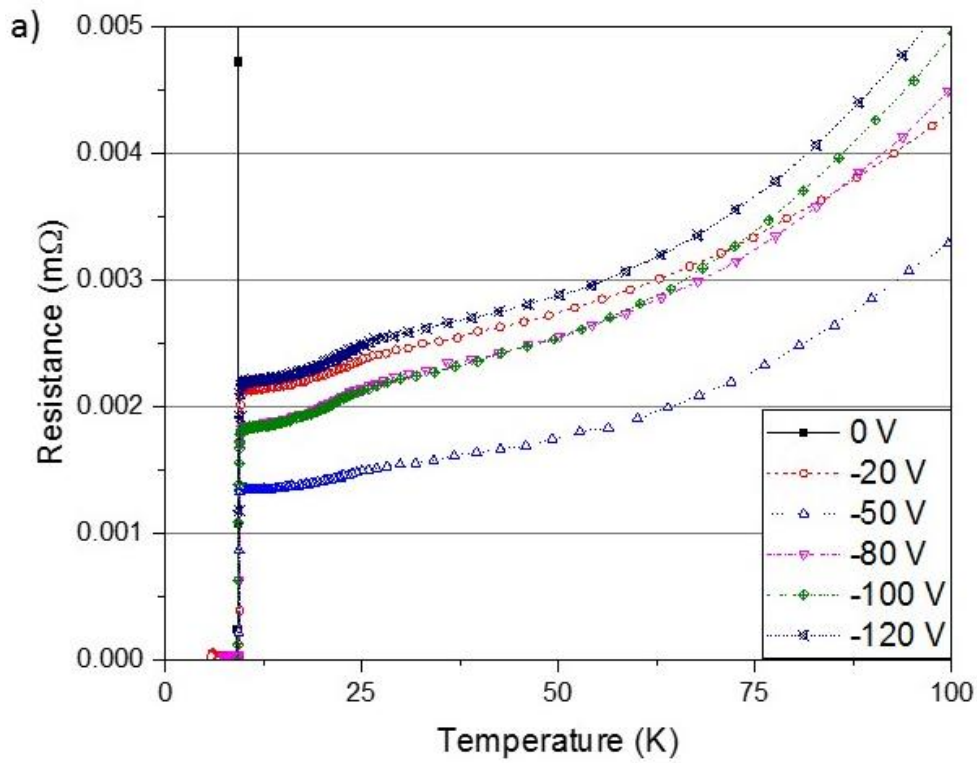


Figure 7.37. a) Resistance versus temperature from 0 to 100 K and b) RRR versus temperature for niobium films deposited onto as received polycrystalline copper substrate at room temperature with bias voltages ranging from 0 to -120 V.

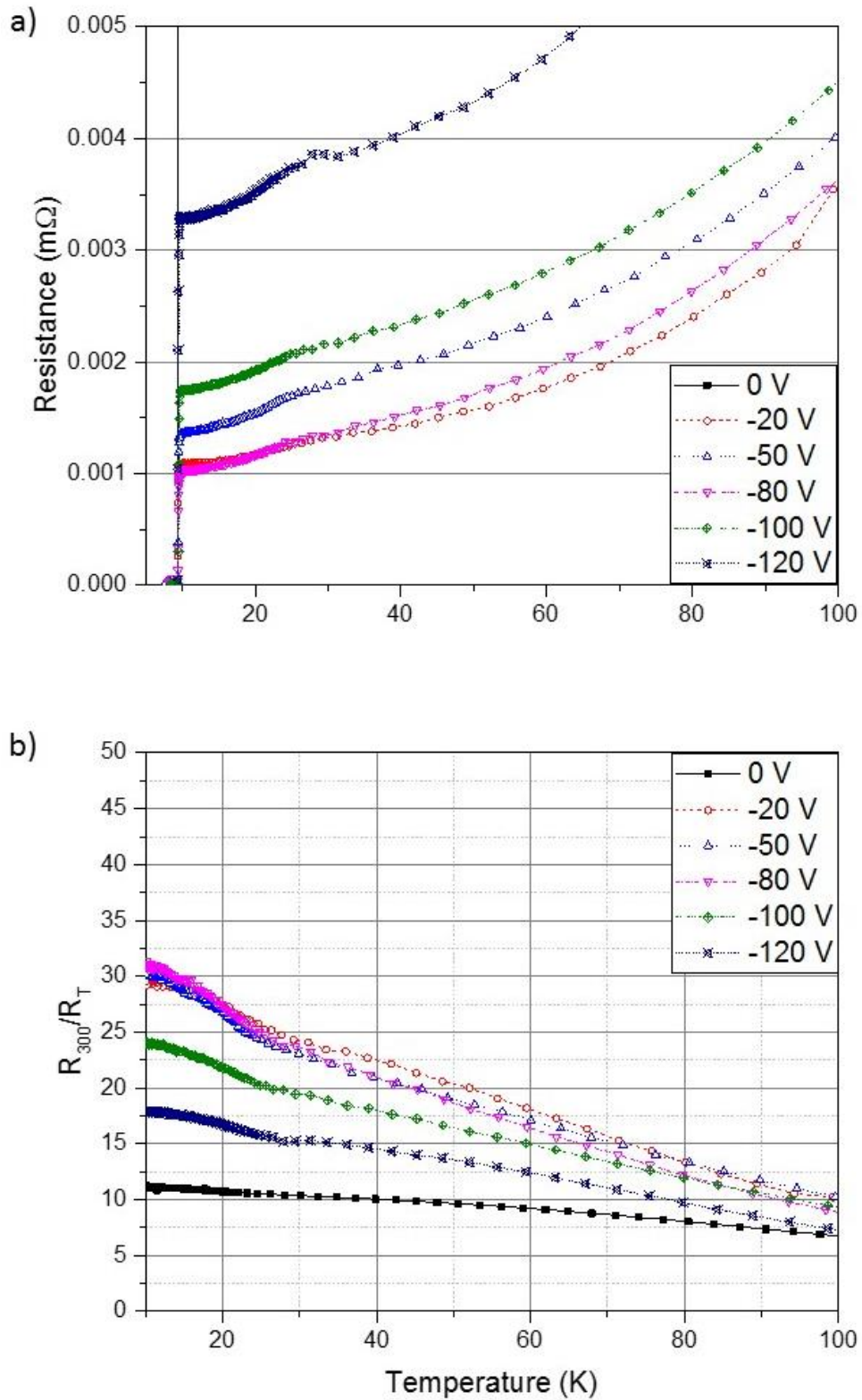


Figure 7.38. a) Resistance versus temperature from 0 to 100 K and b) resistance versus temperature of the superconducting transition for niobium films deposited onto as received polycrystalline copper substrate at 500 °C with bias voltages ranging from 0 to -120 V.

Figure 7.39a presents the normal state resistance data for the samples deposited at 700 °C. Except for the 0 V biased sample, the 700 °C films displayed the most consistency in measured resistance across the range of tested bias voltages. The largest resistance at just above  $T_c$  was 0.0018 mΩ and occurred for the film biased at 0 V during deposition. All other bias voltages displayed similar normal state resistances at just above  $T_c$  of between 0.0006 and 0.0008 mΩ.

The RRR versus temperature data for the films deposited at 700 °C is shown in figure 7.39b. The smallest measured RRR values at 700 °C were between 41 and 42 and occurred for the samples deposited with bias voltages of -20 and -100 V. All other films displayed similar RRR versus temperature curves with 10 K values ranging 52 to 55. The largest RRR at 700 °C was approximately 56 % larger than those measured at 500 °C and approximately 260 % larger than those deposited at room temperature.

The normal state resistance data for films deposited at 800 °C is shown in figure 7.40a. The largest normal state resistance at just above  $T_c$  was 0.0018 mΩ and occurred for the samples deposited with 0, -20 and -120 V bias. The film biased at -100 V displayed a minimum normal state resistance of 0.0011 mΩ, the film biased at -50 V measured 0.0008 mΩ and the smallest resistance occurred for the film biased a -80 V at 0.0005 mΩ.

The RRR versus temperature data for the films deposited at 800 °C is shown in figure 7.40b. The smallest RRR value for films deposited at 800 °C was 24 and occurred for 0 and -120 V bias. The next largest value was 35 and occurred for the film deposited with -100 V bias. The films deposited at 800 °C with -20, -50 and -80 V bias all displayed similar RRR versus temperature curves with maximum values of 49, 48 and 52 respectively. There was no increase in RRR for similar bias voltages, and in some cases a drop in RRR, when compared to films deposited at 700 °C.

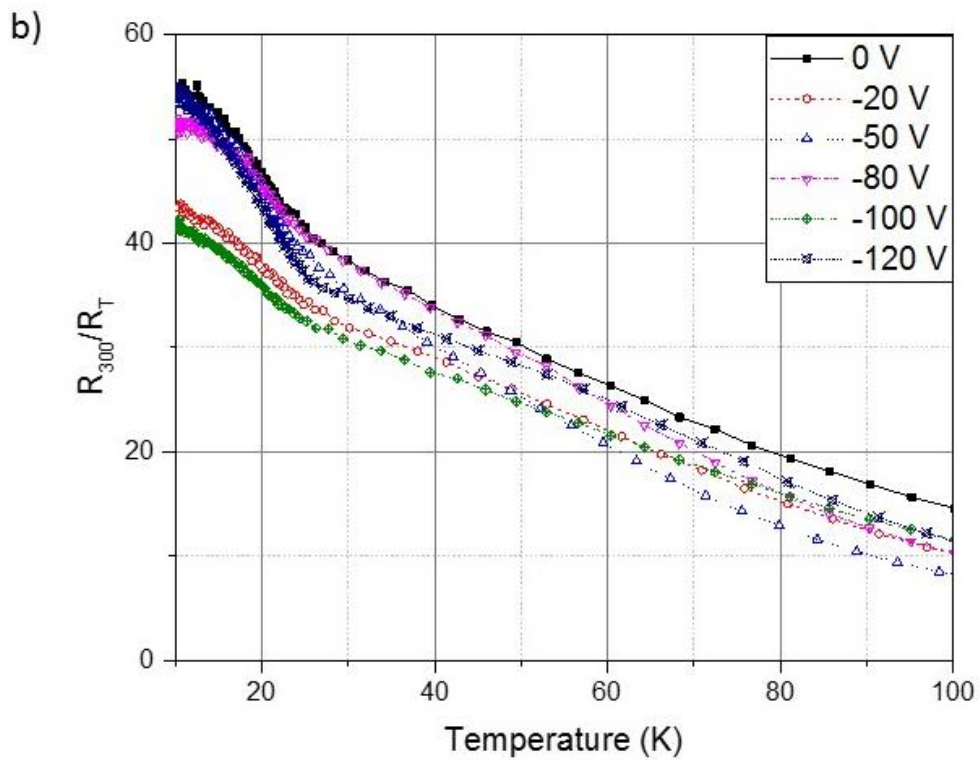
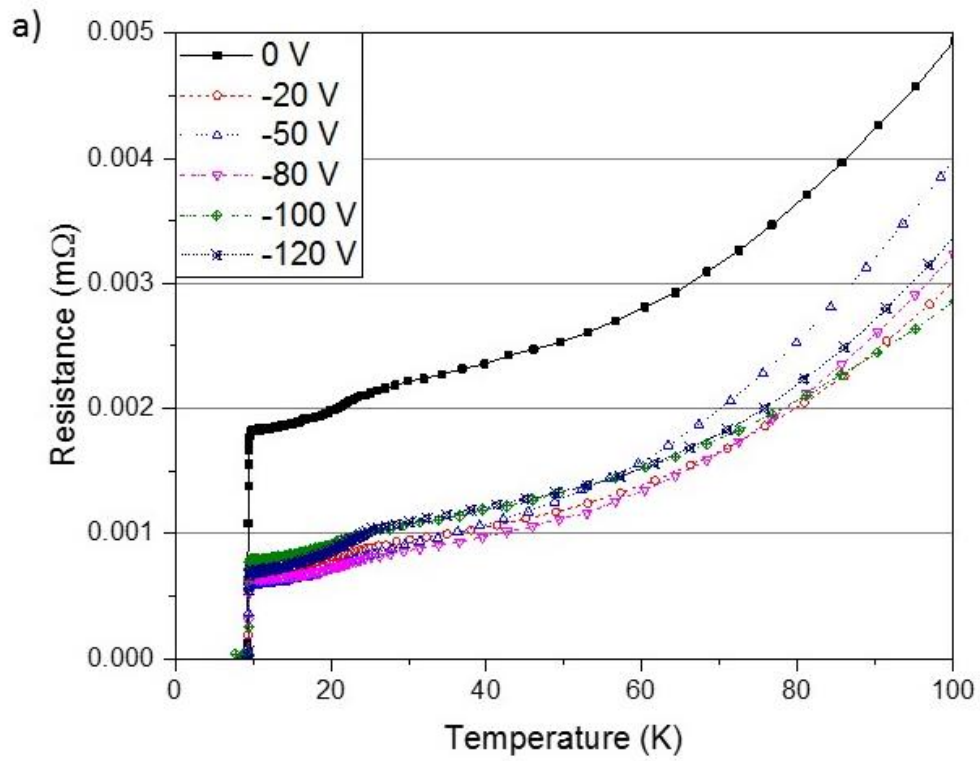


Figure 7.39. a) Resistance versus temperature from 0 to 100 K and b) resistance versus temperature of the superconducting transition for niobium films deposited onto as received polycrystalline copper substrate at 700 °C with bias voltages ranging from 0 to -120 V.

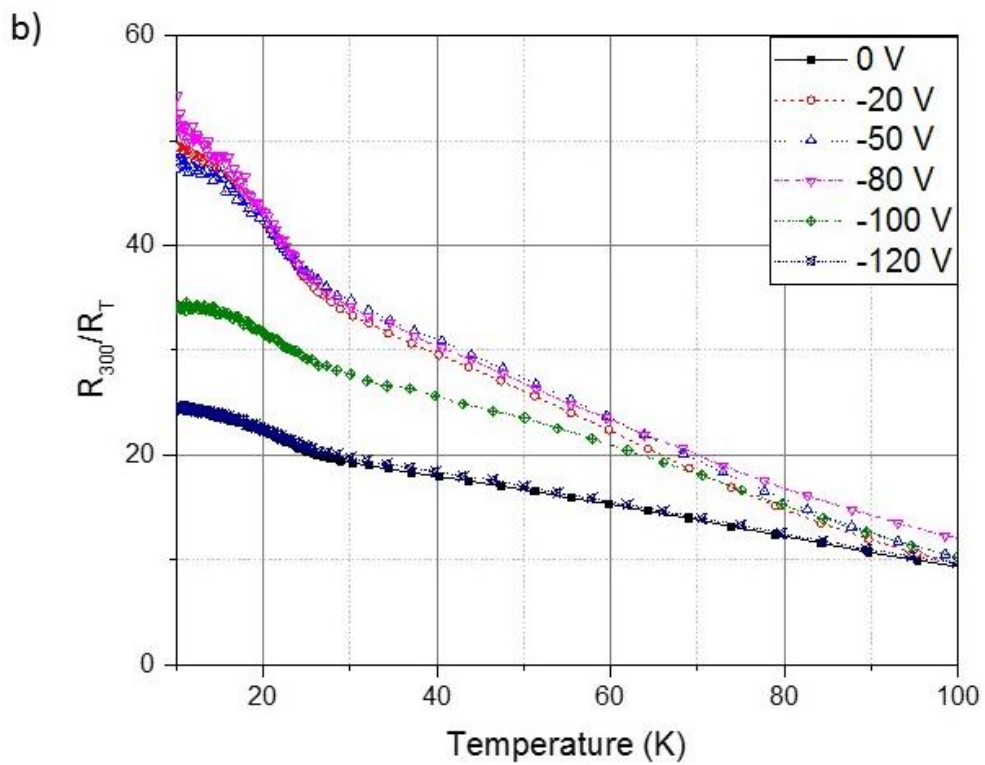
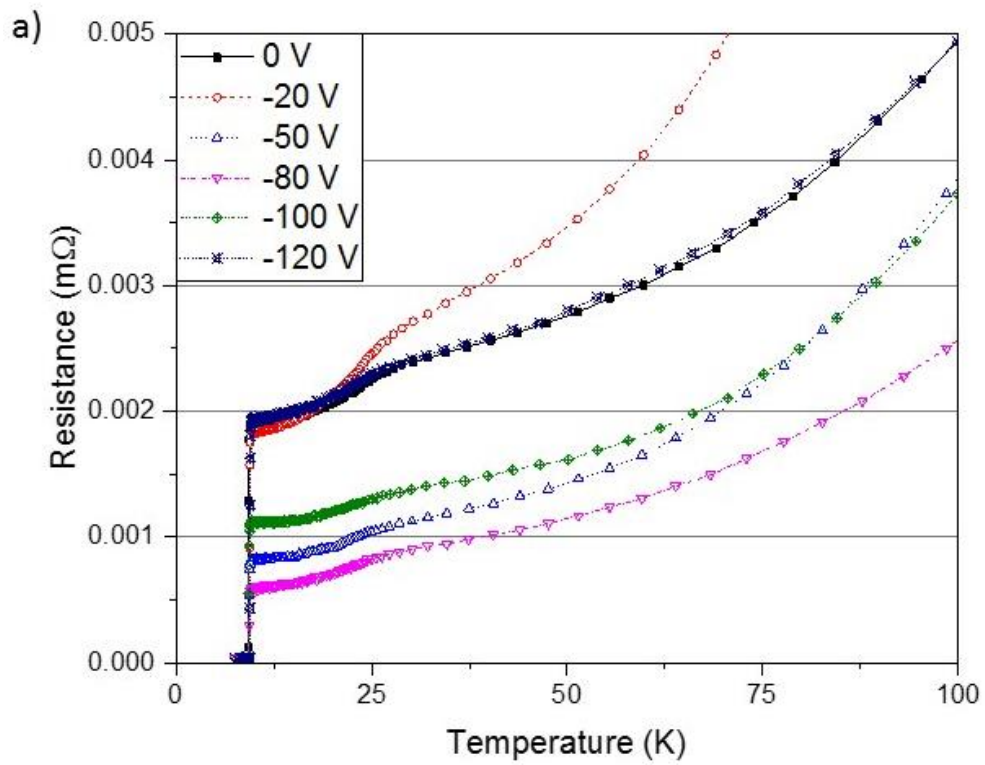


Figure 7.40. a) Resistance versus temperature from 0 to 100 K and b) resistance versus temperature of the superconducting transition for niobium films deposited onto as received polycrystalline copper substrate at 800 °C with bias voltages ranging from 0 to -120 V.

A summary of the RRR data for all samples is shown in figure 7.41. The calculated RRR was rounded up to the nearest whole number in each instance. The displayed error was calculated from the signal to noise ratio, calculated using the measured voltage across the sample when it was superconducting and at 10 K. The average error was 3 % and was applied to each measurement and then rounded up to the nearest whole number.

RRR across all samples deposited onto as received polycrystalline copper substrate ranged from 9 to 54. The samples deposited at room temperature had the smallest RRR for the 0 V biased sample, rising to 13 for the sample biased at -20 V and then plateauing between 19 and 20 for all other bias voltages. The films deposited at 500 °C had a RRR of 9 for the sample biased at 0 V and rose to between 29 and 31 for the films biased at -20 to -80 V. RRR then dropped to 23 and 18 for the films deposited at 500 °C and biased at either -100 V and -120 V respectively. RRR values for the samples deposited at 700 °C showed consistently large values for all bias voltages ranging from 51 to 54 for the samples deposited with bias voltages of 0, -50, -80 and -120 V and dropping to slightly smaller values of 42 and 41 for the samples deposited with -20 and -100 V bias. The samples deposited at 800 °C showed larger variation in RRR than those deposited at 700 °C. The films deposited at 800 °C with bias voltages of -20 to -80 V displayed RRR between 48 and 51, RRR of the film deposited with -100 V bias was smaller at 33 and RRR of the films biased at 0 and -120 V drop as low as 24.

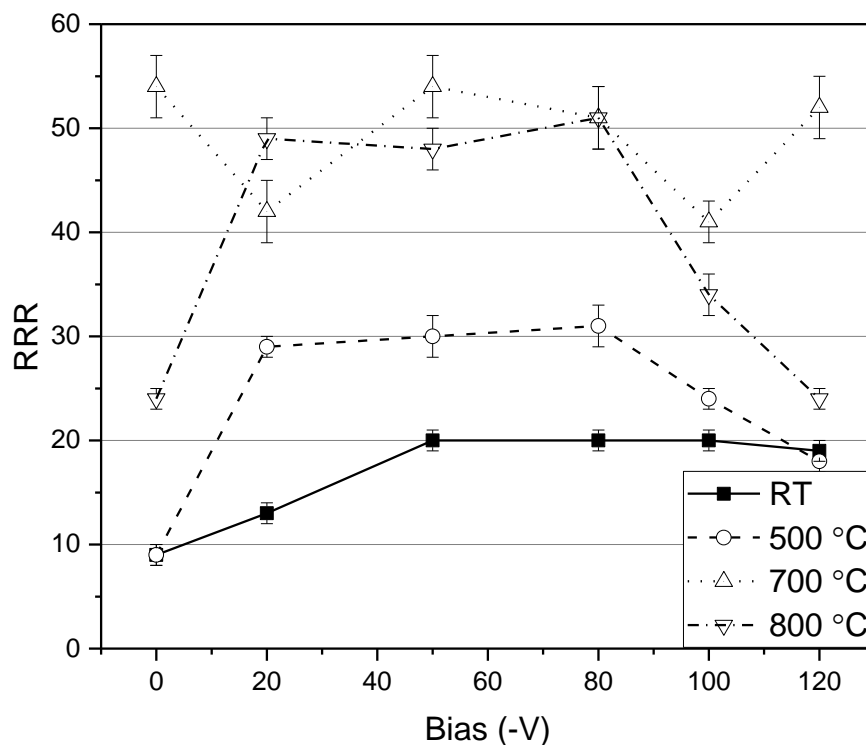


Figure 7.41. RRR values versus applied bias voltage for all films deposited onto as received polycrystalline copper substrate.

$T_C$  was measured from each resistance versus temperature curve and is summarised in figure 7.42.  $T_C$  of all films ranges from 9.28 to 9.52 K. Films deposited at room temperature and 700 °C display a  $T_C$  which increases as the bias voltage was increased during deposition, up to a bias of -100 V. However, films deposited at 500 and 800 °C display no consistent trends linking  $T_C$  to the deposition process conditions.

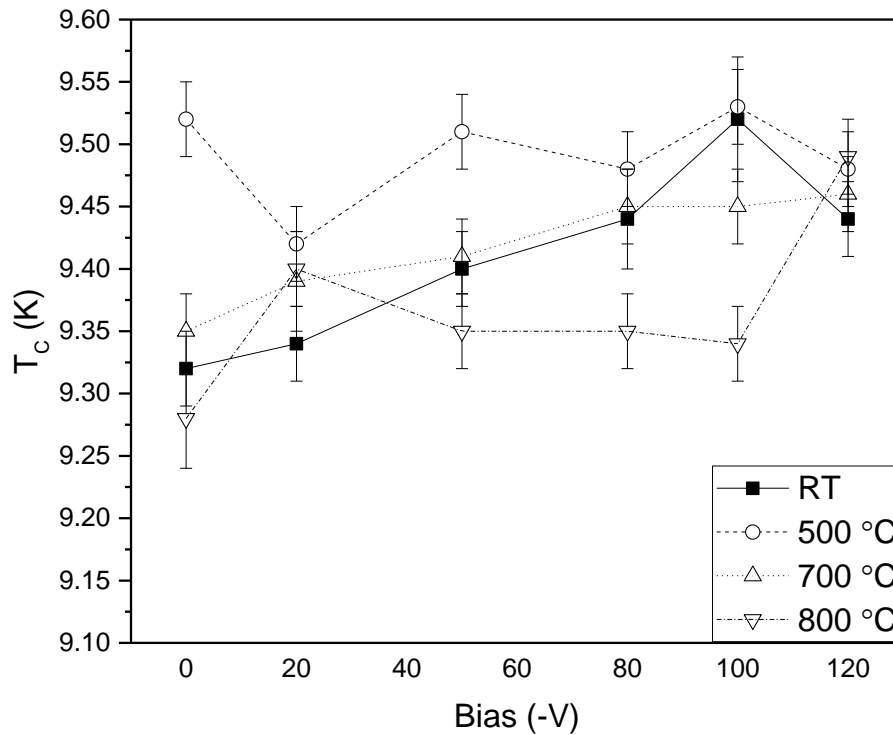


Figure 7.42.  $T_C$  versus applied bias voltage for all niobium films deposited onto as received copper substrate.

### 7.2.2.7. DC magnetisation measurements

DC magnetisation measurements were performed on all films deposited onto as received copper substrate. Samples were prepared for measurement by first etching away the substrate to allow 3 pieces of overlapped film to be inserted into the measurement space (as described in section 7.2.1 to increase signal to noise ratio of the technique). All samples were oriented as close to parallel to the plane of the magnetic field as was possible to achieve. The error in the sample alignment with the magnetic field was  $\pm 1^\circ$  ( $\pm 17$  mrad). The magnetic moment was measured at 4.2 K for each sample from 0 Oe to just above  $H_{C2}$ . The raw magnetisation data is shown in figures 7.43a, 7.43b, 7.44a and 7.44b for samples deposited at room temperature, 500, 700 and 800 °C, respectively. Each figure displays results for films deposited with applied bias voltages of 0 to -120 V. The measured magnetic moment  $M$  displays an initial linearity as a function of applied field  $H$ , followed by a varying rate of change in the measured moment, before reaching its maximum value and finally falling back to zero. Only a selection of samples exhibit smooth curves, deposited at either 700 °C with bias voltages of -80, -100 and -120 V and 800 °C with a bias voltage of -50 V. A small number of other samples, deposited at 800 °C with 0, -20, -80 and -100 V bias, show only one or two jumps in the measured magnetic moment. Multiple small value magnetic flux jumps can be observed in all other samples.

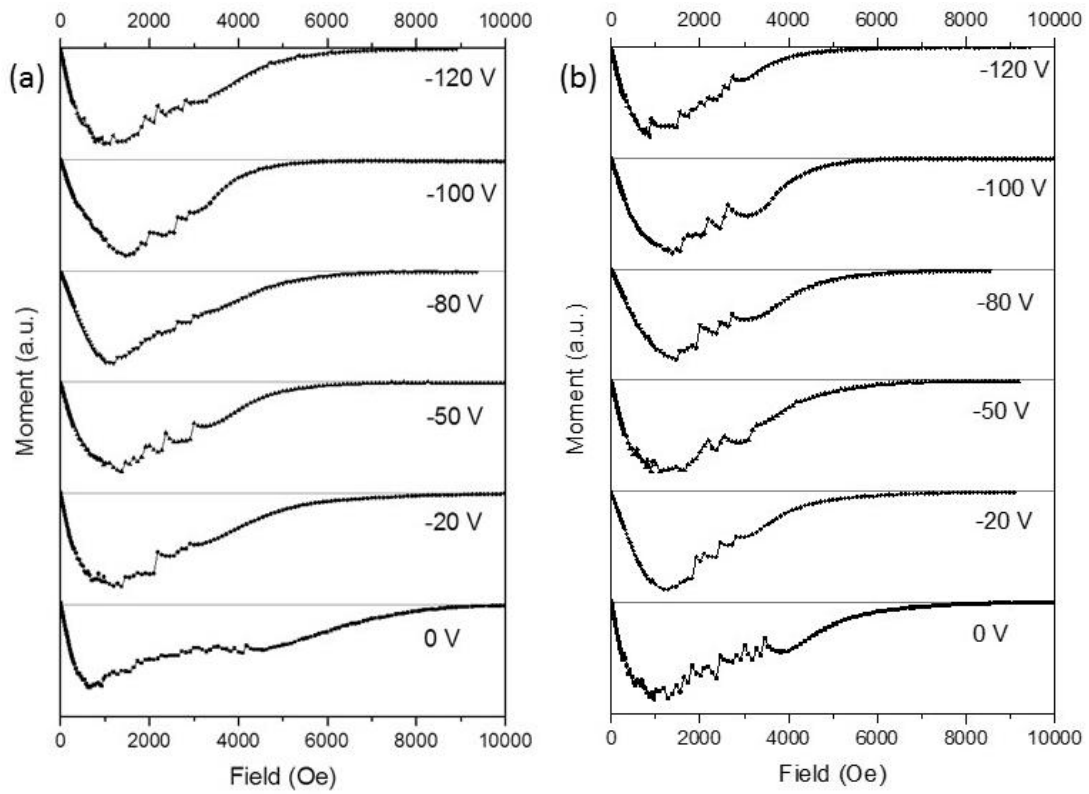


Figure 7.43. DC magnetic moment versus applied magnetic field of niobium thin films versus. Films were deposited onto as received polycrystalline copper substrate at (a) room temperature, and (b) 500 °C.

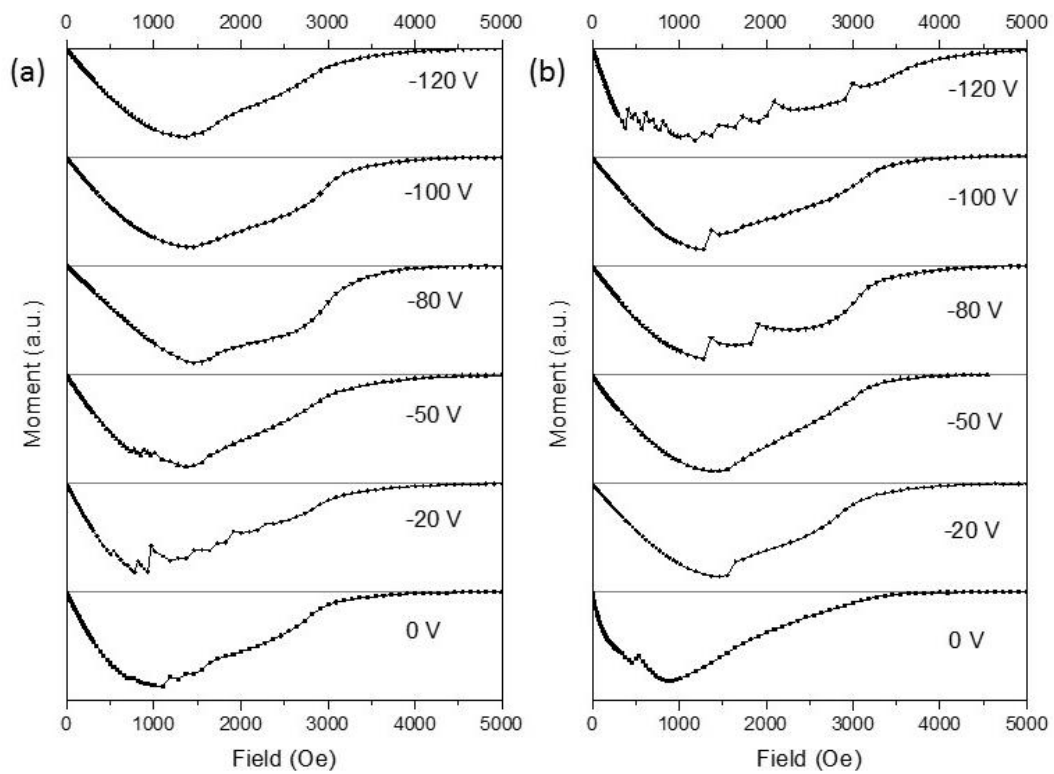


Figure 7.44. DC magnetic moment versus applied magnetic field of niobium thin films versus. Films were deposited onto as received polycrystalline copper substrate at (a) 700 °C, and (b) 800 °C.

When the sample is in the full Meissner state the magnetic moment  $M_i$  increases linearly with  $H$ , and can be described as,

$$M_i = \beta H \quad (7.1)$$

where  $\beta$  is proportional to the undefined sample volume.

The first detection of flux entry into a superconducting film occurs when the gradient of the hysteresis curve changes after an initial linear increase [124]. To find  $\beta$  for each sample; straight fitting lines were plotted for the linear section of the hysteresis curve and any deviation from the predicted moment was calculated using the root mean squares error (RMSE) method. The RMSE is initially large at low field due to small signal to noise ratio, before reaching a minimum during the linear section of the curve, then finally continuing to increase once flux begins to enter the sample. Table 7.3 gives the calculated RMSE for one measurement. The RMSE data from table 7.3 is plotted in Figure 7.45 b, where the minimum RMSE occurs between 101 and 615 Oe.

The field at which the magnetisation curve returns to zero is equivalent to the  $H_{C2}$  of a superconductor.  $H_{C2}$  is reached when the magnetic field becomes large enough to extinguish superconductivity.

An example of the first detected flux entry (first deviation from linear),  $H_{dev}$ , the maximum magnetisation,  $H(M_{max})$ , and  $H_{C2}$  are shown in Figure 7.45 a.

The error in the measured moment is larger when the moment is smaller, as has already been discussed, therefore the field at which the magnetisation effectively reaches zero has been quoted with an error set to  $\pm 10\%$ .

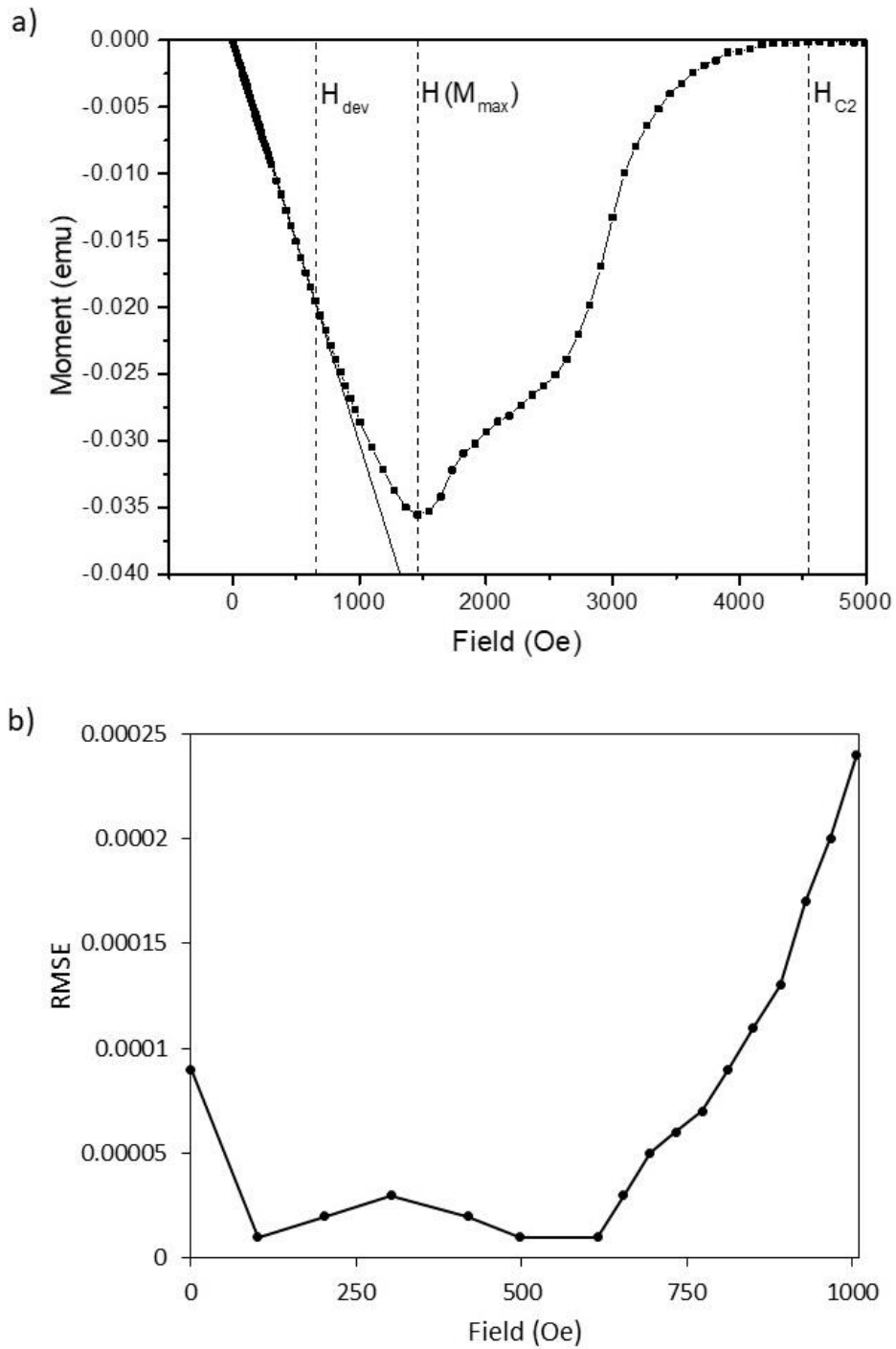


Figure 7.45. An example of a) the raw DC magnetisation data from a measurement of a niobium thin film deposited at 700 °C with -80 V applied bias. The dashed lines denote either  $H_{dev}$ ,  $H(M_{max})$  or  $H_{C2}$  and b) the RMSE against applied field for the same measurement.

**Table 7.3.** Data taken from the magnetisation measurement shown in figure 7.45. The RMSE begins a continuous increase at 654 Oe ( $H_{dev}$ ) indicating that flux has entered the sample at that field.

<b>Field [Oe]</b>	<b>Moment [emu]</b>	<b>Predicted Moment [emu]</b>	<b>Difference [emu]</b>	<b>RMSE [emu]</b>
<b>0</b>	0.00001	-0.00009	0.00009	0.00009
<b>101</b>	-0.00315	-0.00313	-0.00002	0.00001
<b>202</b>	-0.00624	-0.00615	-0.00009	0.00002
<b>303</b>	-0.00931	-0.00917	-0.00014	0.00003
<b>419</b>	-0.01274	-0.01265	-0.00009	0.00002
<b>498</b>	-0.01507	-0.01503	-0.00005	0.00001
<b>615</b>	-0.01846	-0.01854	0.00007	0.00001
<b>654</b>	<b>-0.01952</b>	<b>-0.01970</b>	<b>0.00018</b>	<b>0.00003</b>
<b>694</b>	-0.02062	-0.02092	0.00030	0.00005
<b>733</b>	-0.02172	-0.02208	0.00036	0.00006
<b>773</b>	-0.02285	-0.02328	0.00043	0.00007
<b>812</b>	-0.02387	-0.02444	0.00057	0.00009
<b>850</b>	-0.02487	-0.02560	0.00073	0.00011
<b>891</b>	-0.02591	-0.02681	0.00089	0.00013
<b>929</b>	-0.02680	-0.02795	0.00115	0.00017
<b>967</b>	-0.02768	-0.02910	0.00142	0.00020
<b>1006</b>	-0.02859	-0.03028	0.00169	0.00024

Figure 7.46 and 7.47 show plots of  $H_{dev}$  and  $H_{C2}$  data respectively for all samples deposited onto as received polycrystalline copper substrate.  $H_{dev}$  was at its maximum for all samples at  $654 \pm 40$  Oe for the sample deposited at  $700^\circ\text{C}$  with a  $-80$  V bias. A peak in  $H_{dev}$  occurred for films deposited at room temperature and  $500^\circ\text{C}$  with  $-80$  V bias, whilst  $H_{dev}$  peaked at  $-100$  V for films deposited at  $800^\circ\text{C}$ .

$H_{C2}$  peaked at  $10000$  Oe for films deposited at room temperature onto a grounded substrate or with a  $-20$  V bias and deposited at  $500^\circ\text{C}$  onto a grounded substrate.  $H_{C2}$  dropped to between  $8000$  and  $6000$  Oe for films deposited with all other bias voltages at room temperature and  $500^\circ\text{C}$ . The smallest  $H_{C2}$  values were between  $4000$  and  $5000$  Oe and occurred for all samples deposited at either  $700$  or  $800^\circ\text{C}$ .

The maximum magnetisation  $H(M_{max})$  was recorded for each deposited film. However, showed no consistent trends relating to either substrate temperature or applied bias, the results are displayed in Figure 7.48.

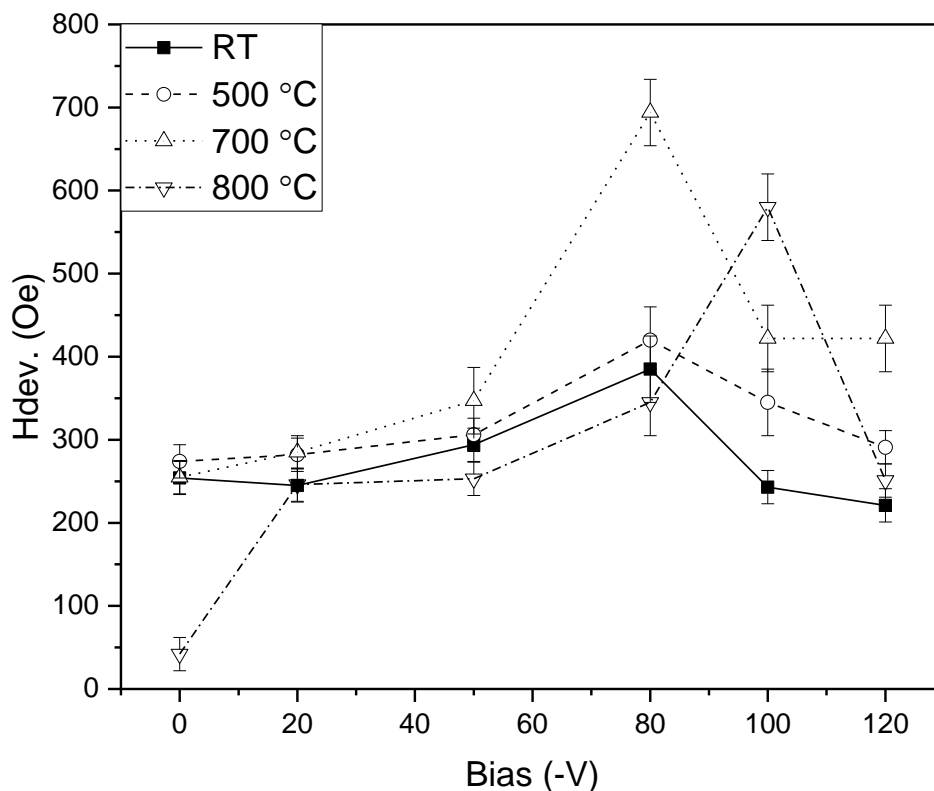


Figure 7.46.  $H_{dev}$  (as defined in Fig. 7.45) versus applied bias voltage.

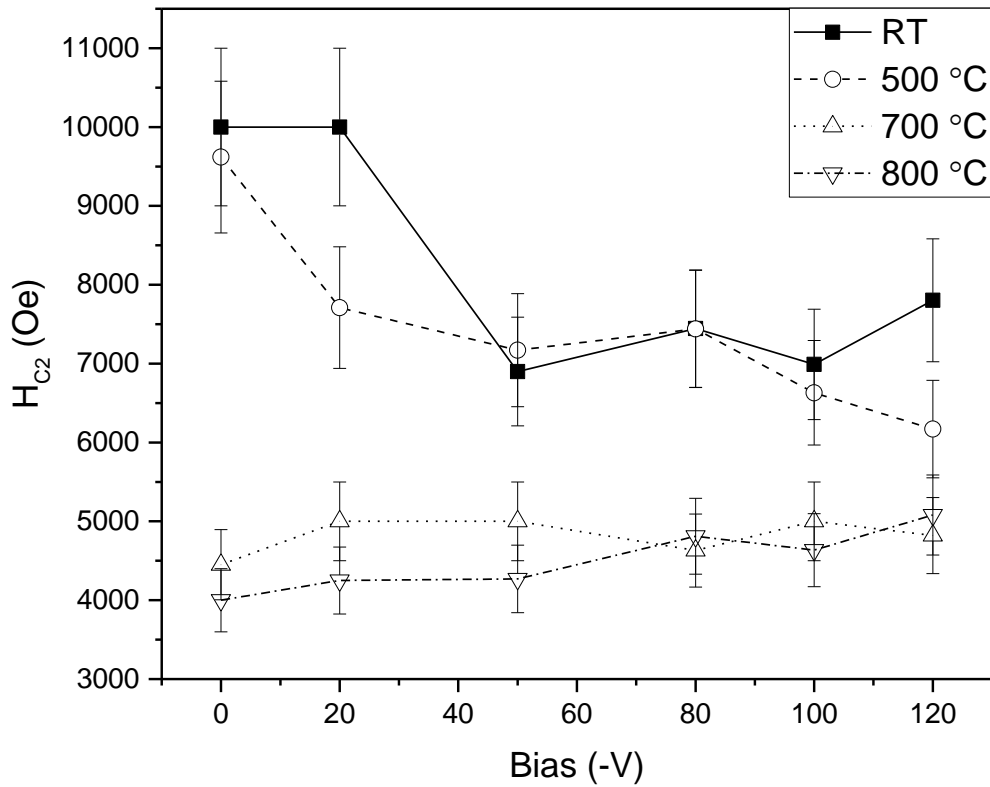


Figure 7.47.  $H_{C2}$  versus applied bias voltage for each film deposited onto as received polycrystalline copper substrate.

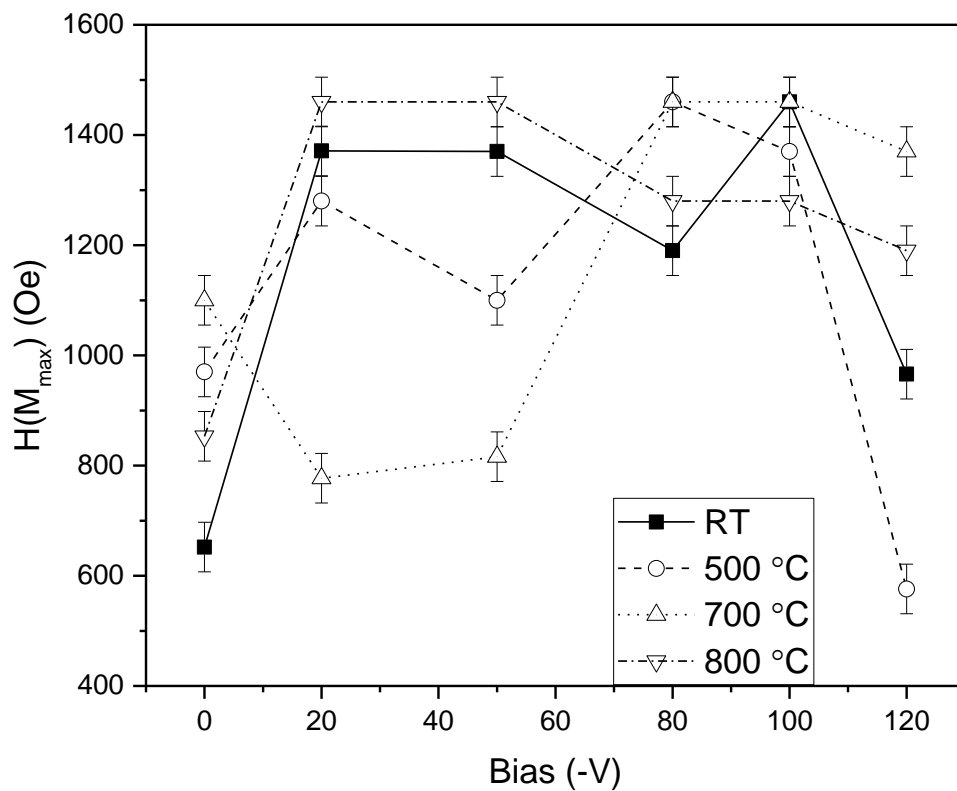


Figure 7.48. The maximum recorded magnetisation  $H(M_{max})$  versus applied bias voltage for each film deposited onto as received polycrystalline copper substrate.

### 7.2.2.8. Comparing the relative volume of niobium films which are penetrated by a DC magnetic field

The magnitude of a measured DC magnetic moment is proportional to the volume of the sample that is measured. It is difficult to compare sample to sample variation of raw DC magnetisation curves unless the volume of each sample remains constant. Although each sample was cut to approximately the same size, any small deviation in surface area could result in a large change in volume when considering the dimensions of a thin film. Thus, a simple algorithm was used to normalise each DC magnetisation curve so that they could be better compared. Coefficients  $\beta$ , as described in equation 7.1, allow the normalisation of each set of measurements  $M$  to the ideal moment  $M_i$  of the sample if it is in the Meissner state. Thus,  $M/M_i = 1$  corresponds to a sample in the Meissner state. Any deviation from  $M/M_i = 1$  will be proportional to the fraction of the sample volume which contains magnetic flux and is no longer in the Meissner state,  $(\Delta V/V)_M$ . The linear section of the raw data, where  $M/M_i = 1$ , was defined as the minimum RMSE as described for one sample in table 7.3. The error in  $M/M_i$  was  $\leq 1\%$  by considering the magnitude of the RMSE for each raw dataset and the error in the measured moment of  $10^{-5}$  emu. The results are shown in figures 7.49 to 7.52.

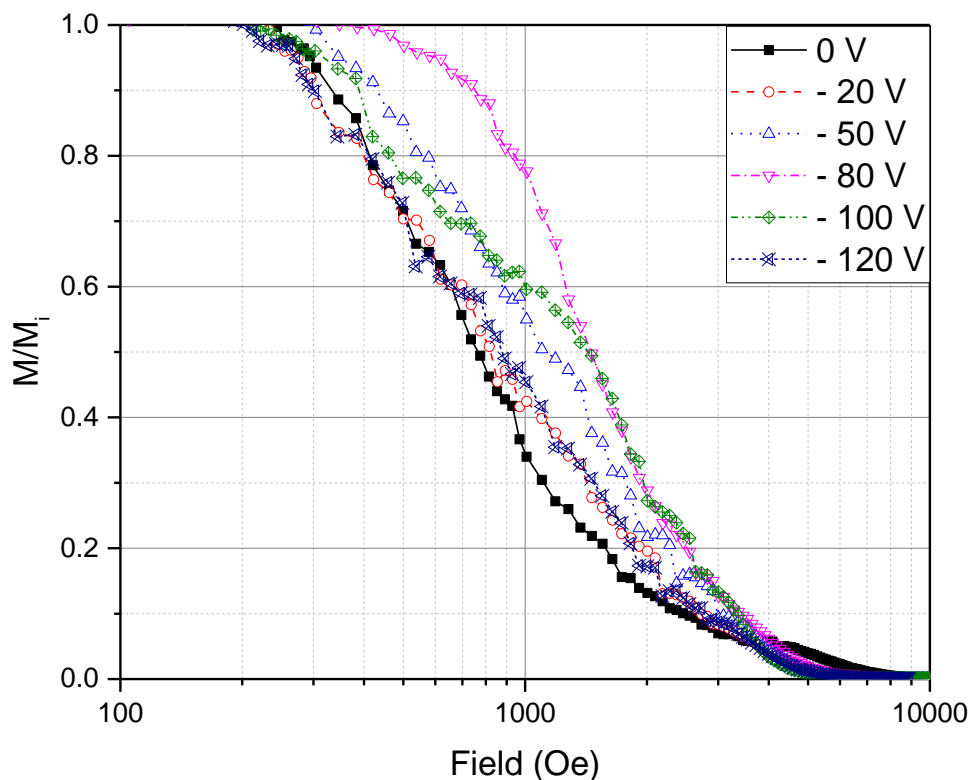


Figure 7.49. The normalised DC magnetic moment versus applied magnetic field for samples deposited at room temperature with a DC substrate bias of 0 to  $-120$  V.

$M/M_i$  for films deposited at room temperature are shown in Figure 7.49. The film deposited at room temperature and with a  $-80$  V bias displayed  $M/M_i$  which is consistently larger than for any

other film up to a magnetic field of 1500 Oe, at which point the films biased at -80 and -100 V converge. The films deposited with bias voltages of 0, -20 and -120 V display the smallest  $M/M_i$  up to fields of approximately 3500 Oe.

Films deposited with a substrate heated to 500 °C are presented in Figure 7.50.  $M/M_i$  was largest for the films deposited with a -80 V bias, and was similar to the film deposited at the same bias at room temperature. The films deposited at 500 °C without bias and with -120 V bias displayed the smallest average  $M/M_i$  of all films deposited at that temperature.

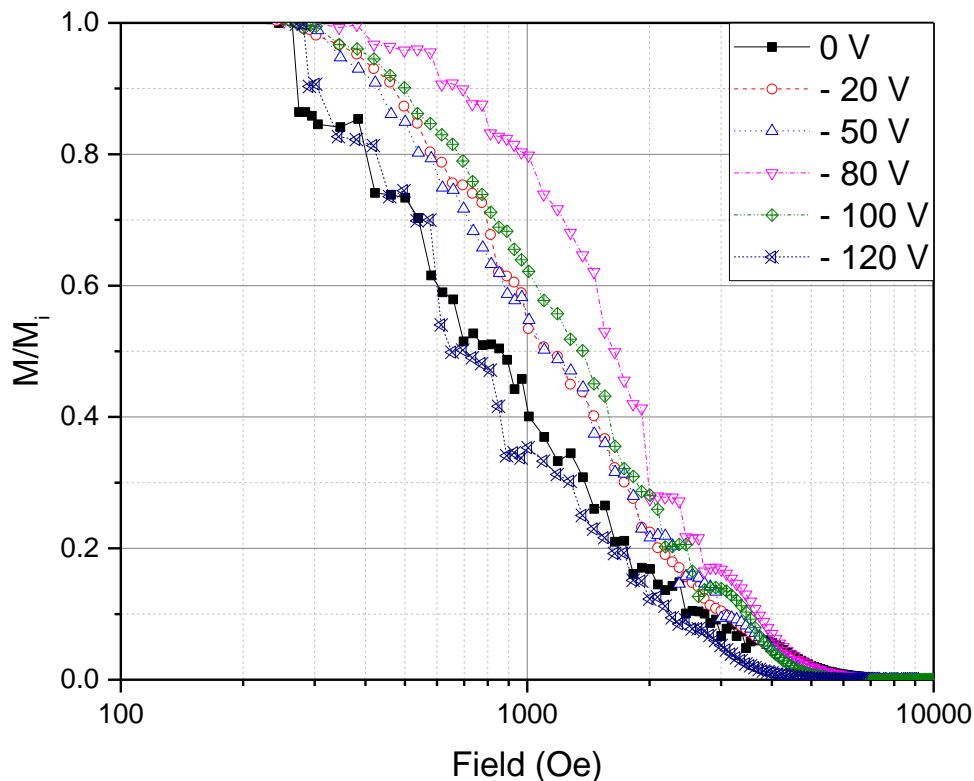


Figure 7.50. The normalised DC magnetic moment versus applied magnetic field for samples deposited at 500 °C with a DC substrate bias of 0 to – 120 V.

$M/M_i$  for all films deposited at 700 °C are shown in Figure 7.51.  $M/M_i$  was largest for the film deposited with -80 V bias and displayed the sharpest transition from the Meissner state to  $H_{C2}$  of any films deposited onto copper substrate during the study.  $M/M_i$  for the films deposited at -100 and -120 V displayed very similar properties over the entire curve. The smallest  $M/M_i$  was observed for the films deposited with bias voltages of either 0 or -20 V.

Figure 7.52 displays all  $M/M_i$  curves for films deposited at 800 °C. The film with the largest average  $M/M_i$  was deposited with a bias voltage of -100 V during deposition. The average  $M/M_i$  was larger for films biased at -20 V than at any other tested substrate temperature. The unbiased 800 °C film exhibited the smallest average  $M/M_i$  of any tested sample during the study.

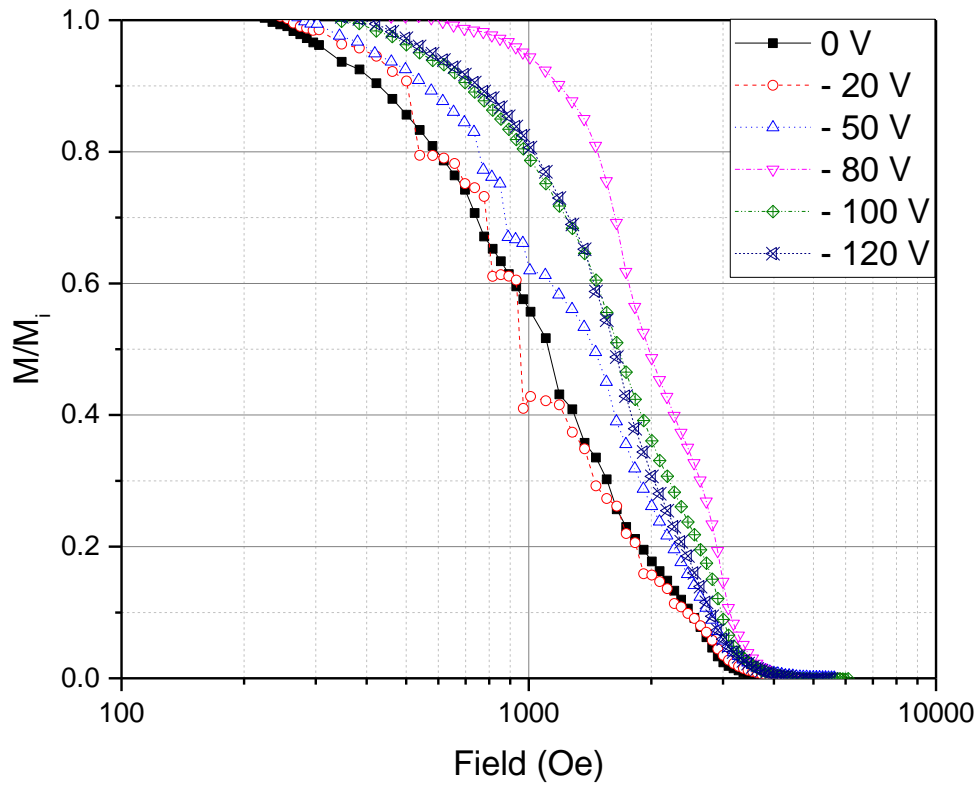


Figure 7.51. The normalised DC magnetic moment versus applied magnetic field for samples deposited at 700 °C with a DC substrate bias of 0 to – 120 V.

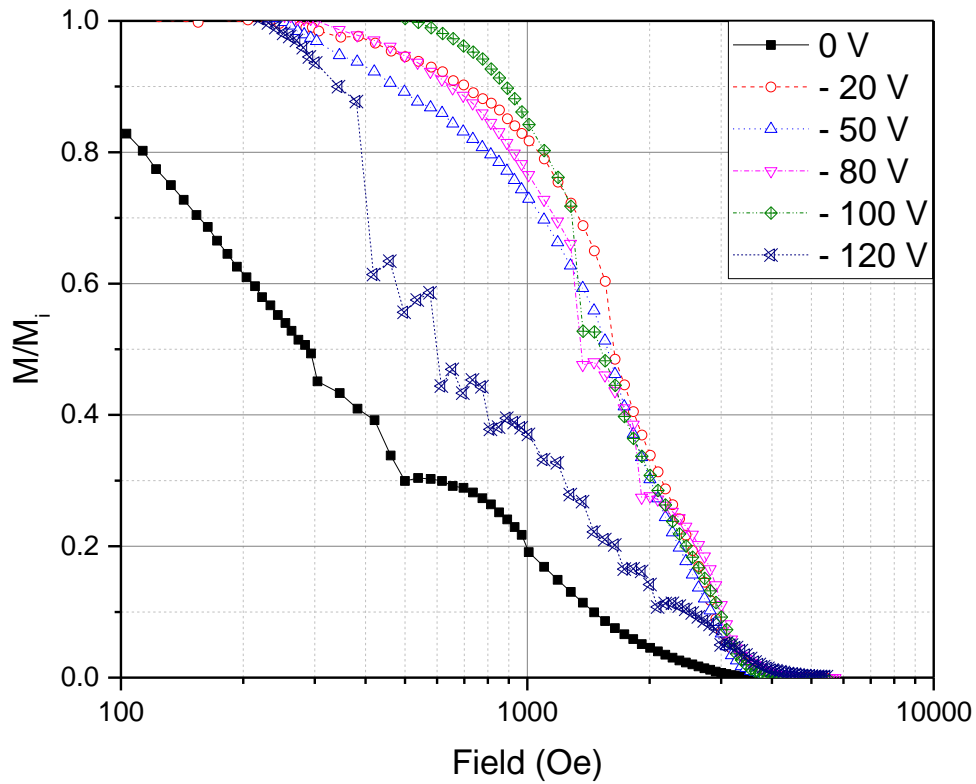


Figure 7.52. The normalised DC magnetic moment versus applied magnetic field for samples deposited at 800 °C with a DC substrate bias of 0 to – 120 V.

Figure 7.53 illustrates all deposited samples together at magnetic fields of 300, 600, 1000 and 1800 Oe. Repeated measurements of the same film and films deposited with similar process conditions display sample to sample variability in  $M/M_i$  of the order of the magnitude of any flux jumps in the measurement (repeated measurements are displayed in the next section of this report). Thus, errors have been set to the magnitude of flux jumps exhibited by samples. All films except for the unbiased 800 °C film achieve an  $M/M_i$  above 0.8 at 300 Oe.  $M/M_i$  is largest at bias voltages of -50 to -100 V for all temperatures at 300 Oe.

A distinct peak occurs at -80 V bias for films deposited at room temperature, 500 and 700 °C at an applied field strength of 600 Oe. The shape of the  $M/M_i$  curve is similar for films deposited at 500 and 700 °C with applied bias voltages of -20 to -100 V. However, the  $M/M_i$  for room temperature films deposited at -20 and -100 V is relatively smaller.  $M/M_i$  is considerably larger for films deposited at 700 °C for the unbiased sample and that biased at -120 V when compared to similar bias at room temperature and 500 °C. There is a broad peak in  $M/M_i$  for films deposited at 800 °C with bias voltages of -20 to -100 V.

$M/M_i$  is similar at 1000 Oe for films deposited with each bias voltage at room temperature and 500 °C, exhibiting a peak at -80 V.  $M/M_i$  has become greatly enhanced for films deposited at 700 °C relative to room temperature and 500 °C for the unbiased films and bias voltages of -80 to -120 V. The shape of the 800 °C  $M/M_i$  curve is unchanged at 1000 Oe relative to 600 Oe.

$M/M_i$  is no larger than 0.55 for any film at 1800 Oe. A peak of  $M/M_i$  can still be observed for films deposited with an applied bias of -80 V at room temperature, 500 and 700 °C whilst  $M/M_i$  peaks at bias voltages of -20 to -100 V for the films deposited at 800 °C.

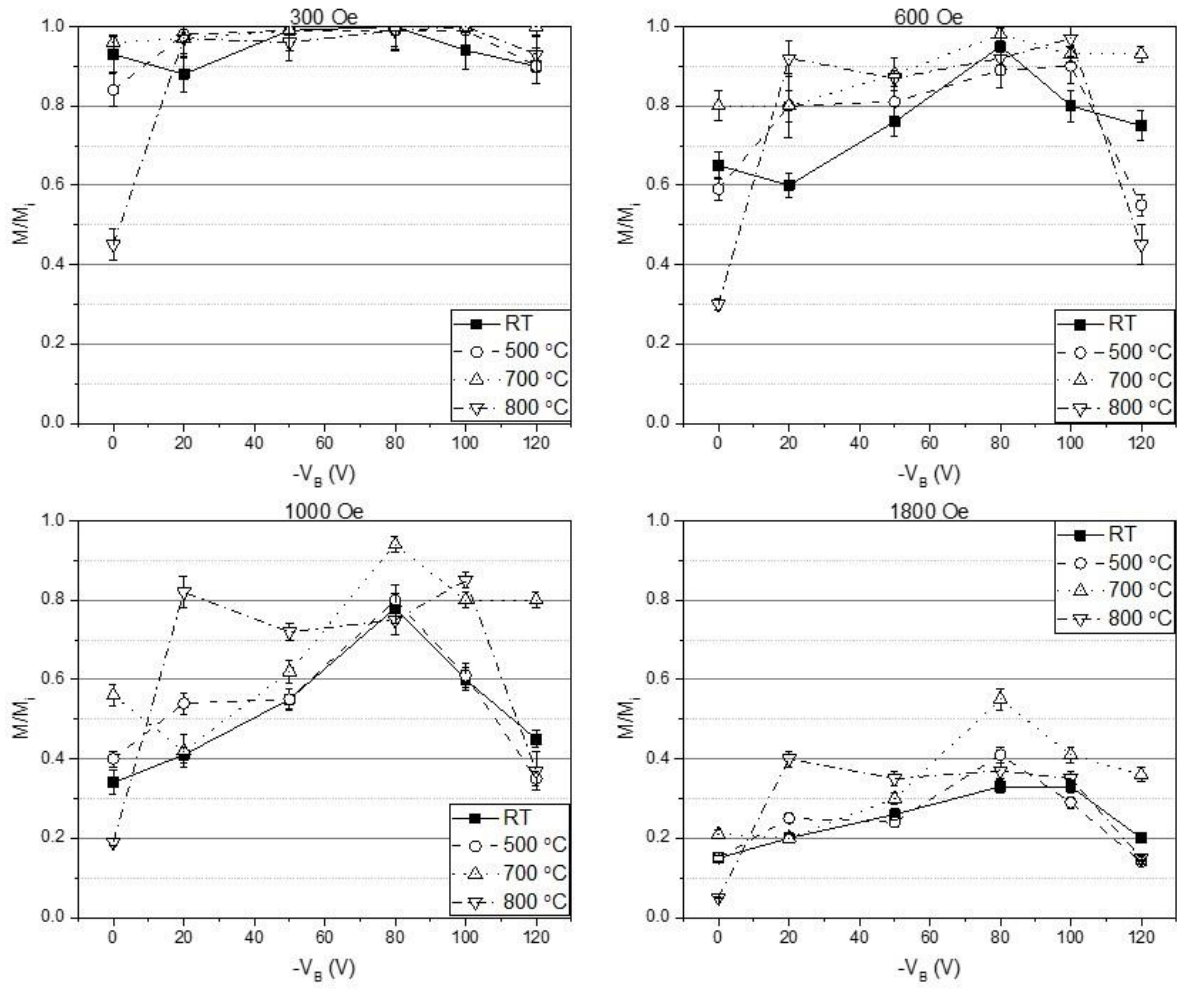


Figure 7.53. Compilation of the measured  $M/M_i$  versus applied bias voltage  $-V_B$ (V) for every sample at magnetic fields of 300, 600, 1000 and 1800 Oe.

### 7.2.2.9. Comparisons of repeated DC magnetisation measurements

As described in section 7.2.1, all the DC magnetisation measurements were for samples which first had the copper substrate etched from the film, allowing larger volumes of the film to be measured and increasing the signal to noise ratio. One film was later deposited for longer to see if it could be measured accurately as a single piece of film in the DC magnetometer and clarify what effects the etching or overlapping of multiple pieces of film had on the DC magnetic behaviour.

The thicker film was deposited for 8 hours onto as received substrate at a temperature of 700 °C with a -80 V DC bias and was a repeat of the process which deposited the film with both the largest average  $M/M_i$  and the largest  $H_{dev}$ , the sample also displayed stable flux pinning. The sample was measured using the DC magnetometer both as a single piece of film after the substrate was first etched away, i.e. using the same procedure as for the previous measurements, except for inserting only one piece of film and not three overlapping pieces, and as a similarly sized film which was still attached to the copper substrate.

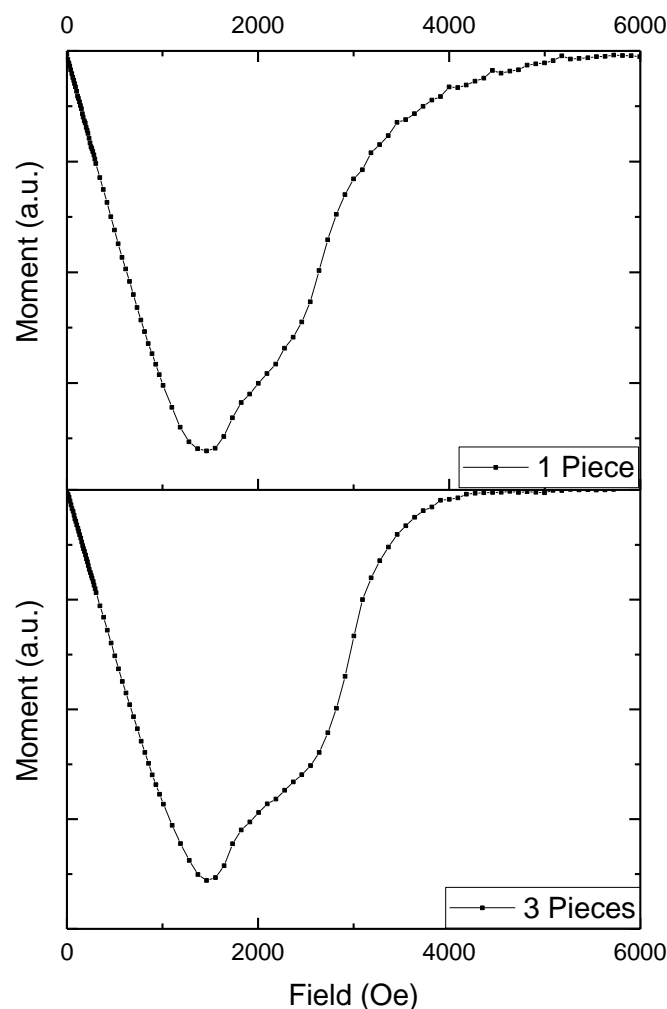
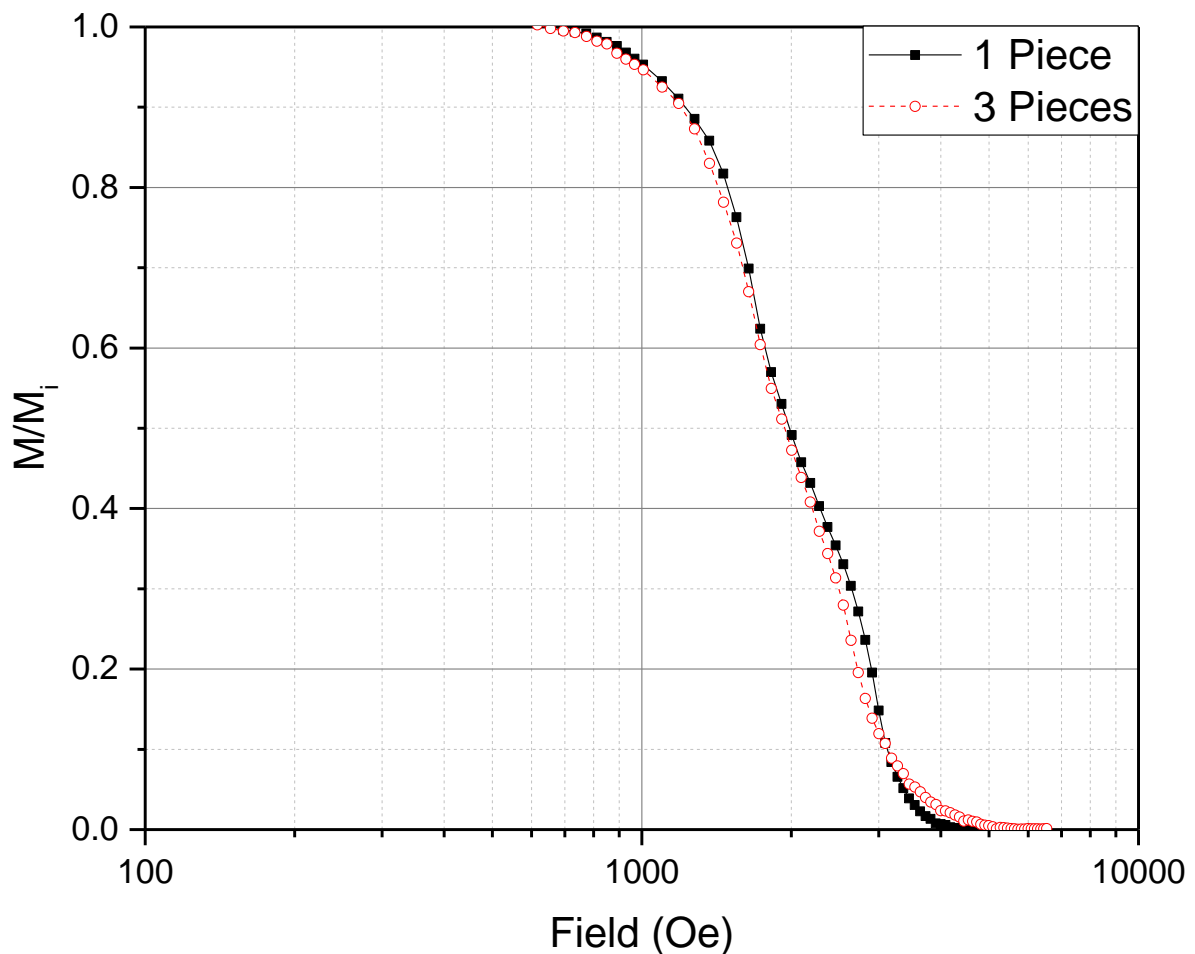


Figure 7.54. DC magnetisation data for two films deposited using the same deposition process. Measurement labelled 1 piece was deposited for 8 hours and contained only one piece of film whilst the measurement labelled 3 pieces was deposited for 4 hours and contained 3 overlapped pieces of the same film.

A comparison of the measured DC magnetic moment for either three pieces of overlapped film and one piece of thicker film is shown in figure 7.54. The shape of each measurement curve is very similar.  $H_{dev}$  is almost identical in each measurement,  $654 \pm 40$  Oe in the case of 3 pieces, and  $655 \pm 40$  Oe for 1 piece. The greatest variation of the two measurements comes from  $H_{C2}$  which was  $4630 \pm 450$  Oe for 3 pieces and  $5720 \pm 570$  Oe for 1 piece.  $M/M_i$  for both the 3 overlapped pieces of film and the single film is shown in figure 7.55. The result shows almost perfect correlation between each measurement with only a slight variation occurring at fields above 2500 Oe.



**Figure 7.55. Comparison of  $M/M_i$  versus applied magnetic field for both 1 piece and 3 pieces of niobium film deposited with similar process conditions.**

Comparisons of the DC magnetic moment of the film deposited at  $700^\circ\text{C}$  with an applied bias of  $-80$  V for 8 hours in both the etched condition and with the substrate still in place are shown in figure 7.56. The measured moment for the sample where the substrate is still in place exhibits a single smooth peak, whilst a distinct hump appears at approximately 1800 Oe for the sample where the substrate has been removed.  $H_{dev}$  was measured at  $655 \pm 40$  Oe for the etched sample whilst there was an increase up to  $1000 \pm 40$  Oe for the sample with the substrate still in place.  $H_{C2}$  remained constant

for both samples. Figure 7.57 displays  $M/M_i$  for both the film on copper and after etching and shows a reduction in the relative volume of the sample into which the applied magnetic field had penetrated for the film still attached to the copper substrate.

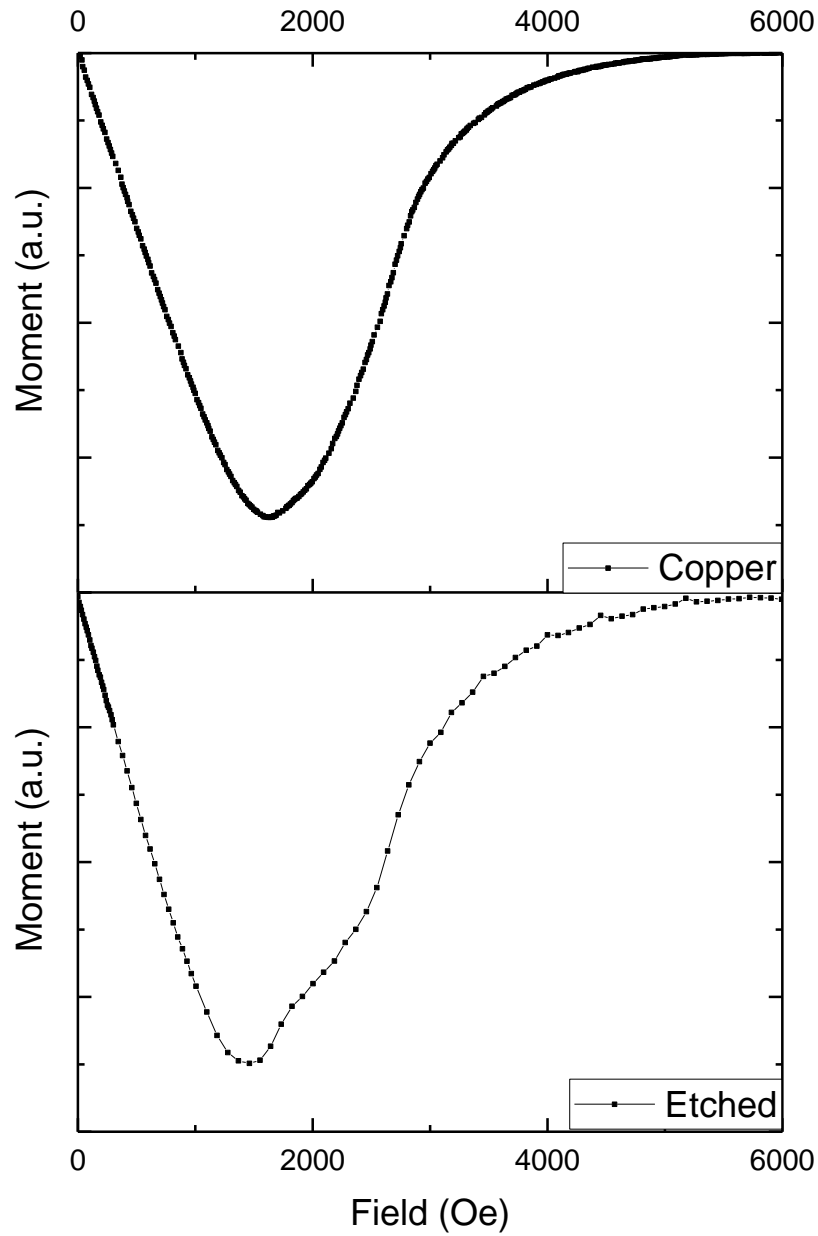


Figure 7.56. Comparison of the DC magnetic moment versus applied magnetic field of a film with copper substrate still in place and after the substrate has been removed by etching.

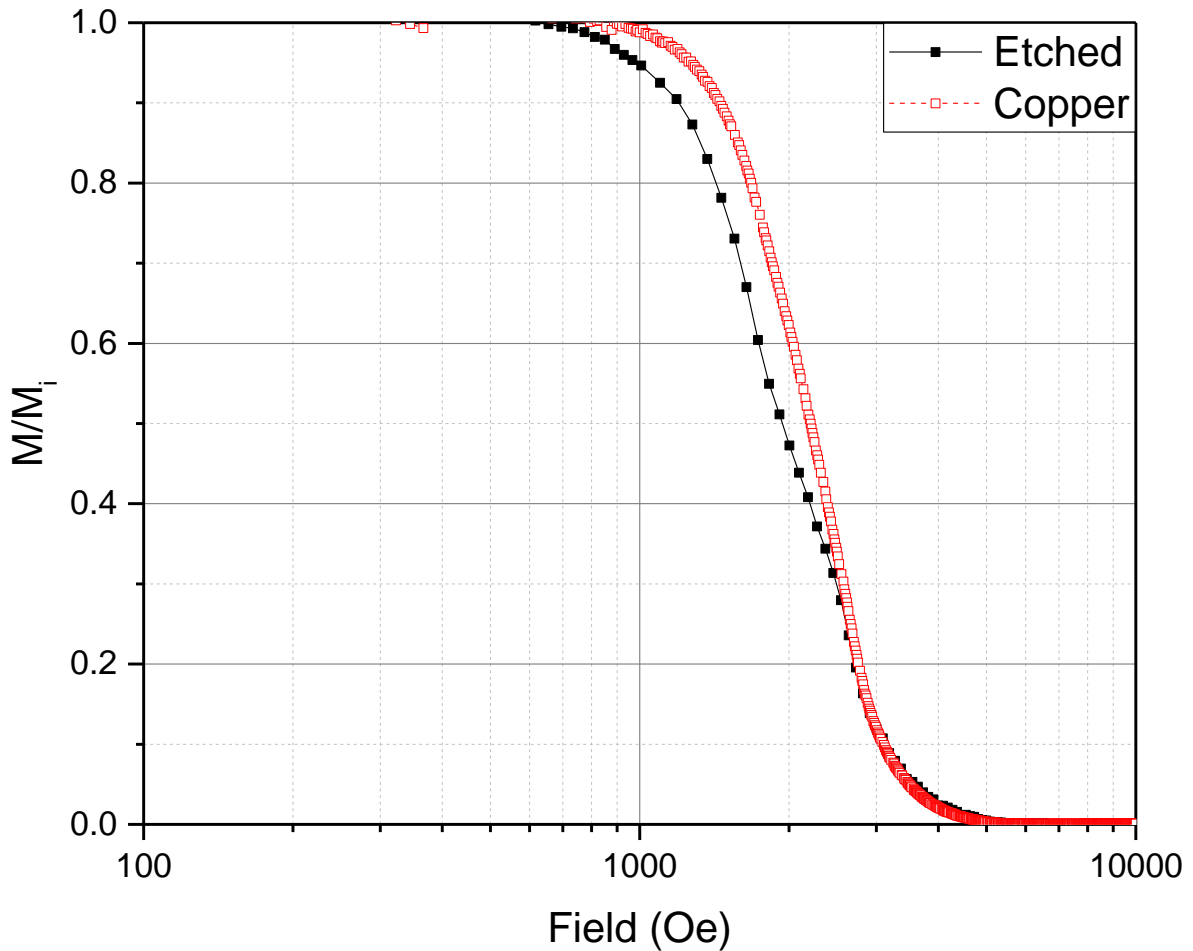


Figure 7.57. Comparison of the  $M/M_i$  versus applied magnetic field of a film with copper substrate still in place and after the substrate has been removed by etching.

Several other measurements using the DC magnetometer were repeated so that the repeatability could be quantified. The repeated measurements are shown in figures 7.58 to 7.61. Each repeated measurement used either pieces of the same film cut from different parts of the sample or was two different films deposited with similar conditions.

The films that were deposited and tested multiple times showed that the sample to sample variation in  $M/M_i$  was highly repeatable for samples which did not exhibit flux jumps, but the measured moment could fluctuate about the approximate magnitude of the flux jumps for those which did exhibit jumps.

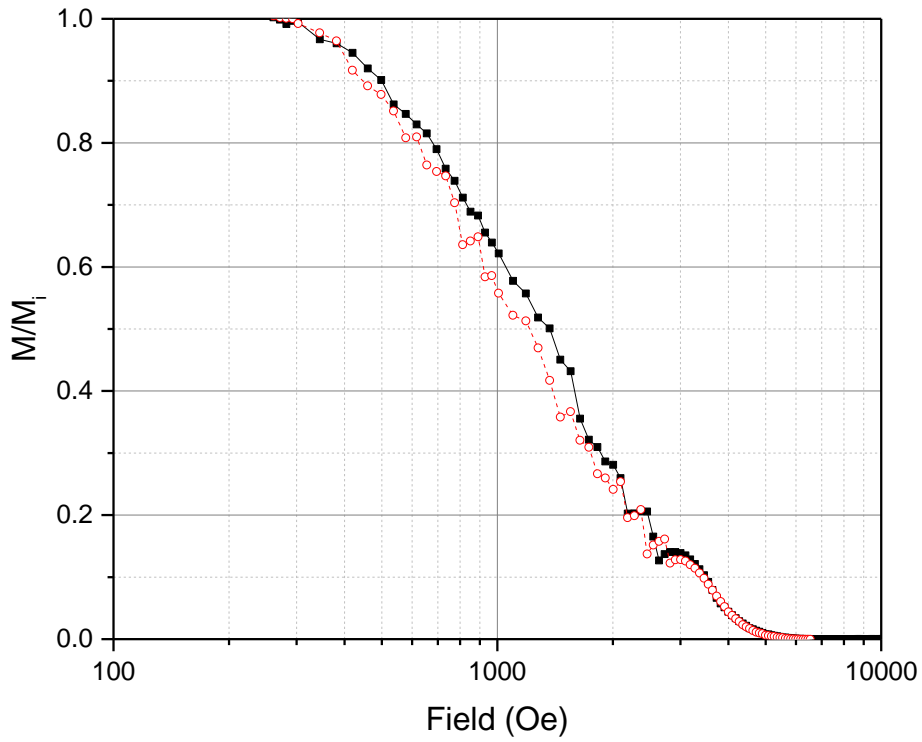


Figure 7.58. Repeated  $M/M_i$  versus applied magnetic field measurements of niobium thin film samples deposited at 500 °C with -100 V DC bias. Film was cut from different parts of the sample for each measurement. Small differences are seen in each measurement of the order of the magnitude of the flux jumps.

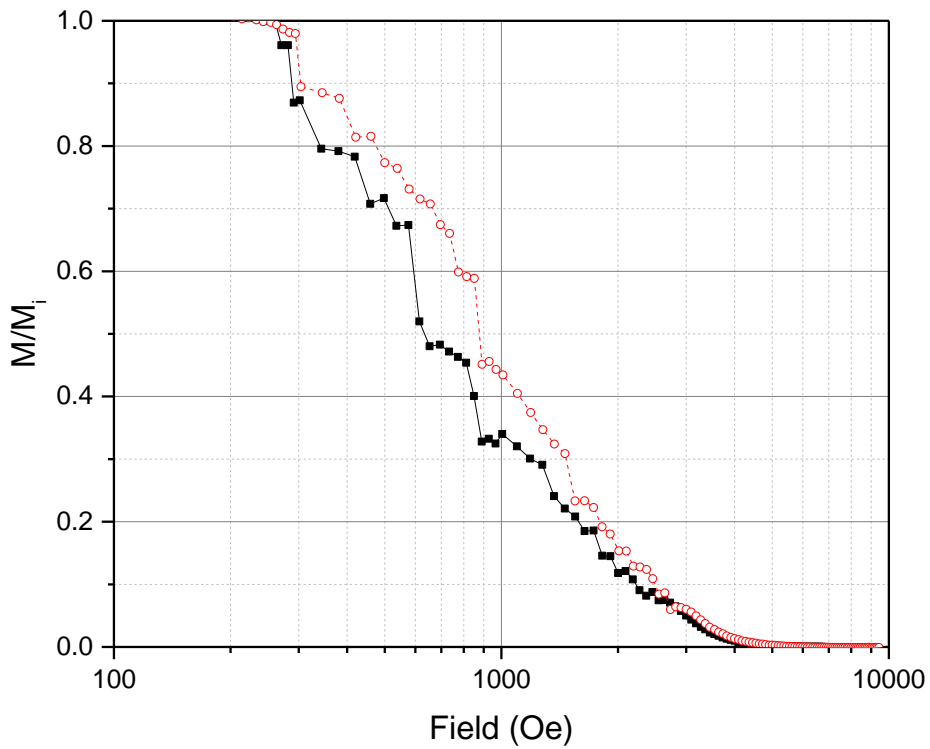


Figure 7.59. Repeated  $M/M_i$  versus applied magnetic field measurements of niobium thin film samples deposited at 500 °C with -120 V DC bias. Film was cut from different parts of the sample for each measurement. Small differences are seen in each measurement of the order of the magnitude of the flux jumps.

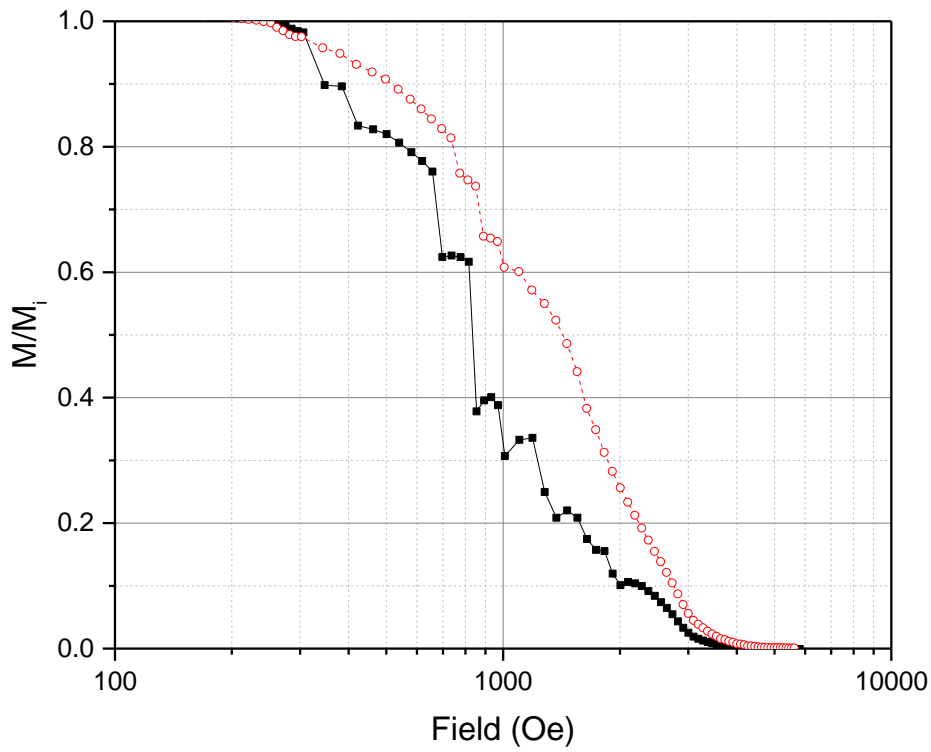


Figure 7.60. Repeated  $M/M_i$  versus applied magnetic field measurement of niobium thin film samples deposited at 700 °C with -50 V DC bias. Film was cut from different parts of the sample for each measurement. Large differences are seen in each measurement of the order of the magnitude of the flux jumps.

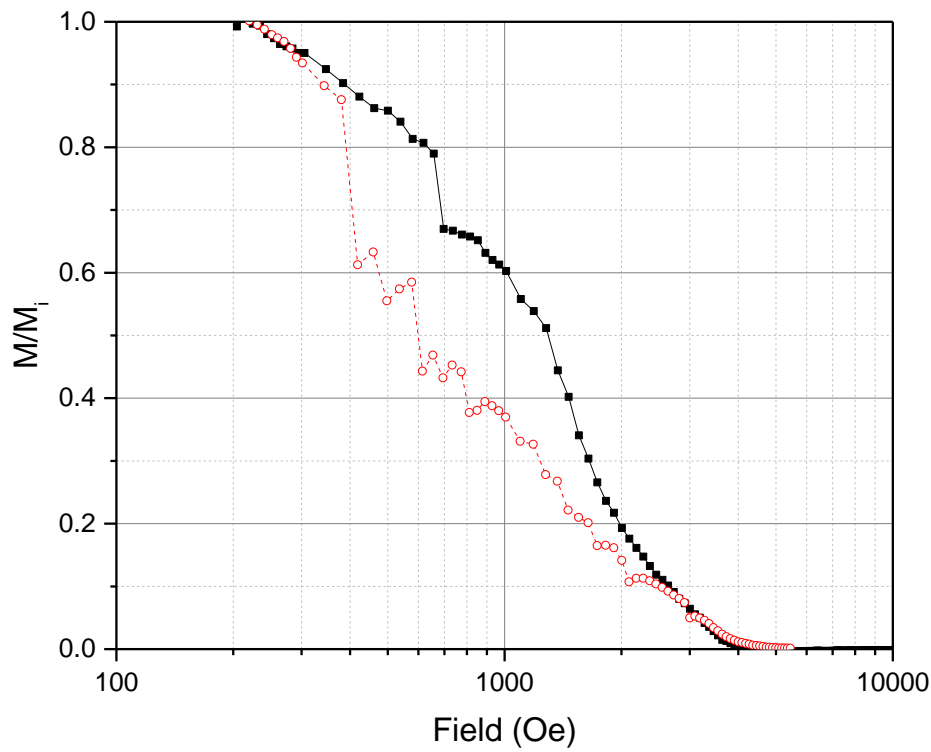


Figure 7.61. Repeated  $M/M_i$  versus applied magnetic field measurement of niobium thin film samples deposited at 800 °C with -120 V DC bias. Film was cut from different parts of the sample for each measurement. Large differences are seen in each measurement of the order of the magnitude of the flux jumps.

### 7.2.2.10. Discussion and conclusions

Plasma emission spectroscopy was used to verify that high energy niobium ions were present within the HiPIMS discharge. The results confirmed that there was considerably more niobium<sup>2+</sup> ions when compared to a DC magnetron sputtering discharge. This observation validated the expectation that biasing the substrate during HiPIMS deposition should result in changes to the properties of deposited thin films due to manipulation of the energies of bombarding ions. Krypton emission lines were similar for both DC magnetron sputtering and HiPIMS. It was not possible to quantify the presence of impurities such as oxygen, carbon or nitrogen within the plasma as any respective emission lines were not visible with a significant signal to noise ratio.

RGA monitoring was performed to verify that thin films were deposited within a clean environment. The results suggested that there was a possibility for oxygen, nitrogen or carbon contamination of up to 1 % of the elemental composition of the deposited film. This value was considered from the adsorption rate of residual gasses and the deposition rate of deposited films. The deposition rate was approximately half of what was typical of high power DC magnetron sputtering. This suggests that there is more chance of contamination by residual gas species during HiPIMS deposition compared to DC magnetron sputtering. However, RBS measurements displayed 100 % purity niobium films. It is possible that some elemental impurities were present within the thin films, but were below the  $10^{11} - 10^{15}$  at.cm<sup>-2</sup> detection limit of the RBS technique. It is highly likely that there is some krypton sputter gas which has been implanted by high energy ion bombardment into the films, especially at the highest applied bias voltages. More sensitive techniques would be required to measure the impurity concentrations, such as melting the film to measure the residual gasses that are released. Niobium melts at 2469 °C and is beyond the capabilities of any facilities to which this project had access.

The length of  $a_0$  gives an indication of the nature and distribution of the defects which may be present within films. Films that have similar  $a_0$  can be assumed to have similar internal strain and therefore comparable distributions of defects. Types of defect that could be consistent from sample to sample are the relative volume of the sample made up from grain boundaries and the abundancies of vacancies or substituted impurity atoms. Films that have seemingly random and varying lengths of  $a_0$  have comparatively random internal strain that acts to deform the crystal lattice in an uncontrolled manner. Types of defect that could randomly alter the length of  $a_0$  are random complex dislocations.

The measurements of  $a_0$  suggest two opposing trends; the most uniformity in  $a_0$  of films still attached to the substrate are deposited at room temperature and the most uniformity in  $a_0$  once the substrate is removed occurs for the films deposited at 700 °C. The opposing trends suggest that there

is a substrate related thermal stress at high temperature, most likely caused by different thermal expansion rates for copper and niobium, at  $16.5 \mu\text{m/mK}$  and  $7.3 \mu\text{m/mK}$  respectively.

Films deposited with bias voltages ranging -50 to -100 V display the smallest range of measured  $a_0$ ,  $0.02 \pm 0.01 \text{ \AA}$ , for every tested deposition temperature when measured for films after the substrate was etched away and for films deposited at room temperature to  $700 \text{ }^\circ\text{C}$  when measured on copper. This consistency in the sample to sample length of  $a_0$  suggests a consistency in the types of defect present within in the film microstructure for the films deposited with bias voltages of -50 to -100 V.

Films deposited with bias voltages of 0, -20 and -120 V display seemingly random distributions in the length of  $a_0$  for films deposited at a similar temperature when measured both on copper and after etching. All those films described as having seemingly random lengths of the  $a_0$  suggest unpredictable strain within the films, most likely caused by the presence of random complex dislocations.

The observations of the changing lengths of  $a_0$  as a function of applied bias, and subsequently the distribution of defects, can be explained using well known thin film growth theory [12]. Ion bombardment increases surface atom mobility and diffusion whilst annihilating surface defects. Films with relatively few defects will be deposited if the transferred energy due to ion bombardment is above the surface displacement energy, but below the bulk displacement energy of niobium [70]. The initial application of a bias voltage at -20 V accelerates charged ions towards the substrate and so promotes the breaking of atomic bonds at the films surface. Surface defects are annihilated but at a rate that is comparable to the rate of defect formation, thus the lengths of  $a_0$  for films deposited at 0 and -20 V bias exhibit seemingly random values. The rate of surface diffusion rises with increased bias voltage and minimises the number of random complex defects for the films deposited with bias voltages of -50 and -100 V, hence those films show the smallest range in the length of  $a_0$ . It is possible to produce more random complex defects, implant impurity atoms, and reduce film grain size, once the energy of bombarding ions becomes too large. Thus, there is a random variability in  $a_0$  for the films deposited at -120 V.

A small number of the grazing incidence XRD spectra displayed small peaks which correspond to fcc (111) copper. It is unlikely that these peaks could be observed directly from the substrate, as the x-ray grazing angle of  $2^\circ$  should prohibit a signal from the substrate.

A copper signal from the film itself would be an important finding as diffusion of copper into the film would be a definite cause of strain that would affect the length of  $a_0$ . The sample deposited at  $700 \text{ }^\circ\text{C}$  with applied bias of -120 V showed some of the largest copper peaks. However, the RBS measurement of the same sample showed that no copper was present within the film. Another

possible source of the small copper signal was at the film surface. Each sample was cut into smaller pieces using an 8 inch circular saw (the only available saw), so that the smaller pieces could be used for various analytical procedures. The coarse blade of the cutting saw may have left pieces of the copper substrate as dust at the film surface. SEM and EDX measurements (figure 7.62) were performed and showed that there was in fact copper dust present at the films surface after cutting and after the grazing incidence XRD measurements had been performed. Future experiments would require appropriate cutting tools so that copper dust was not left over after cutting.

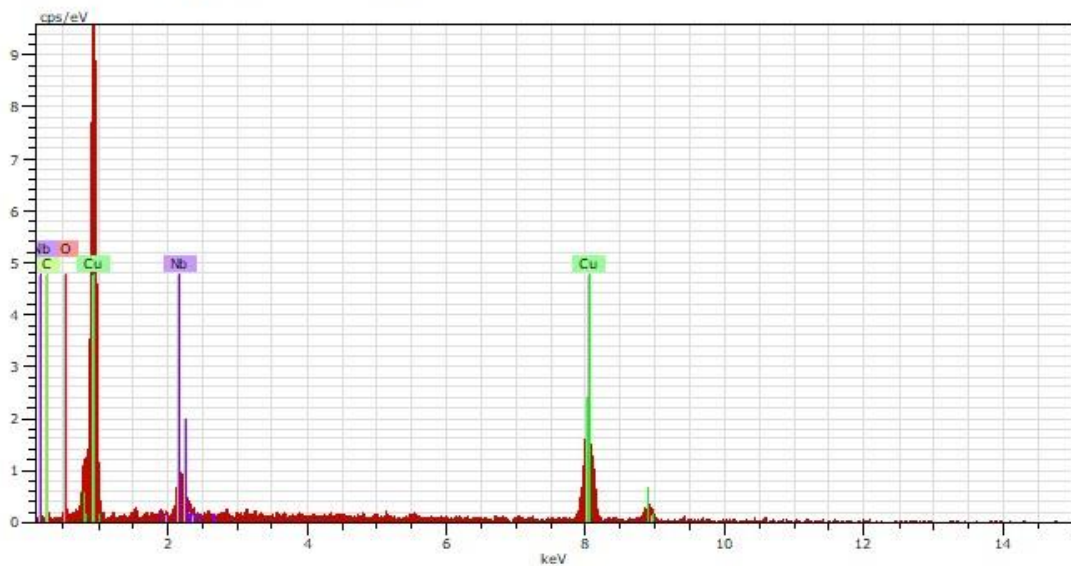
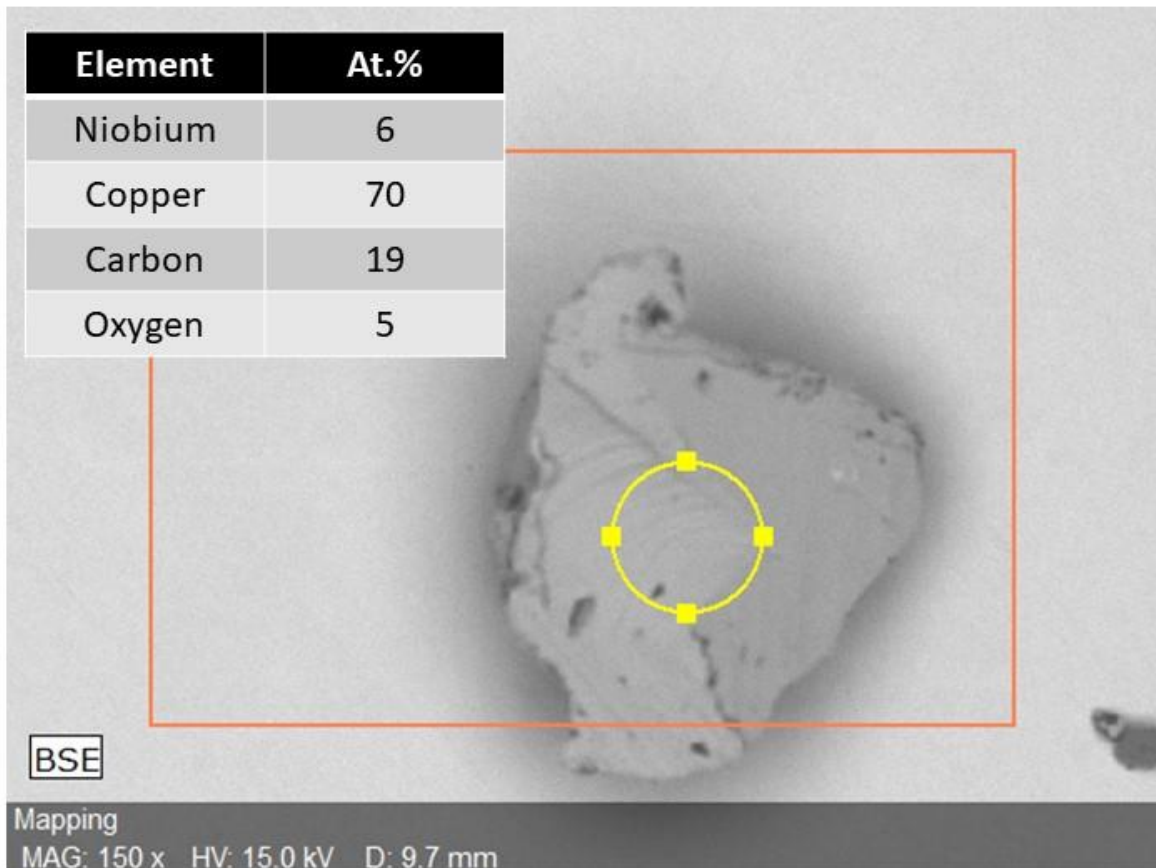


**Figure 7.62.** SEM and EDX data of copper dust found at the surface of some niobium thin films after cutting with the circular saw. The copper dust produced small GI-XRD peaks for the measured spectra.

The SEM images described in section 7.2.2.5 can be used to better understand the nature of defects that were suggested from the grazing incidence XRD measurements. SEM images showed how the films deposited at room temperature and 500 °C change from columnar films deposited with a grounded substrate to larger and more densely packed grains for films deposited with a bias of -80 V.

The different film's microstructure may explain why the length of  $a_0$  was more consistent for films deposited at room temperature and 500 °C with a bias voltage of -80 V, than was observed for the films deposited onto a grounded substrate at those temperatures. Thus, defects at grain boundaries may be more prevalent within the films deposited onto a grounded substrate at room temperature and 500 °C relative to those biased at -80 V during deposition.

SEM images of films deposited at 700 and 800 °C showed much larger grain size than for those deposited at the lower temperatures, with and without the application of a -80 V bias during deposition. The large grain size of films deposited at 700 °C suggests that heat energy has become large enough to drive significant rates of diffusion throughout the growing film, which is irrespective of the arrival energy of the sputtered material. The enlargement of grains at 700 °C relative to lower temperatures may also result, in part, by the initial substrate condition. Oxide free copper surfaces, as would be expected at 700 °C and above, have been shown to produce much larger niobium grain size than for films grown onto the native oxide of copper [2].

Average grains size was calculated using equation 5.1 and the FWHM of grazing incidence XRD peaks. The calculated average grain size was much smaller than was observed in the SEM images. There did not appear to be any trends which linked the calculated average grain size to the different process conditions. It is possible that the small average grain size is evidence of very small grains together with the larger grains shown in the SEM images. Another explanation of the difference between average grain size and the sizes of grains observed in SEM images is that the grazing incidence XRD peaks have become broadened by internal strain within the film microstructure, resulting in a similar FWHM for most films. Such an effect has been observed before for niobium thin films deposited by magnetron sputtering techniques [32].

3D optical microscopy and SEM images showed that some films displayed a characteristic "blistered" texture at the films surface. There is so far, no conclusive evidence that has explained what causes the different texture at some film surfaces. Initially, it was thought that the films become too energetic as the substrate temperature and bias voltage is increased, leading to delamination of the film. However, the films showed no delamination from the substrate in cross sectional SEM images. Films which exhibited the "blistered" texture at the surface were also tested for delamination using adhesive tape which again displayed no delamination. Further study of the film/substrate interface is necessary to conclude exactly what causes the "blisters", but was considered beyond the scope of this study. A future project is planned to probe the substrate/film interface in further detail. For now, it is proposed that films which exhibit many "blisters" at the surface should not be tested in SRF application until the feature is better understood. The present dataset suggests that the "blisters" only form once the substrate temperature during deposition reaches 500 °C and that the number, height and

diameter of the blisters increases with an applied bias voltage of -50 to -120 V for films deposited at 700 and 800 °C.

RRR is largest for niobium thin film samples that have the fewest lattice defects or numbers of substitutional impurity atoms. Therefore, the RRR can be considered a measure of a film's purity. The RRR of samples deposited at 500 °C increases in magnitude as the applied bias is increased during film deposition from 0 up to -80 V then drops at -100 and -120 V. The films deposited at room temperature showed a similar trend, with a rising RRR for films deposited with bias voltage of 0 up to -50 V, before a plateau in RRR up to a bias voltage of -120 V. It appears that ion bombardment can promote enough surface diffusion and annihilate sufficient numbers of lattice defects in a growing film so that RRR can increase up to a maximum value, which occurred at either -50 or -80 V applied bias, for the films deposited at the smaller deposition temperatures. This increase in RRR coincides with the densification of grain boundaries, as appears to occur in SEM images, of films deposited onto a substrate biased at -80 V. The degradation of RRR for the film deposited at 500 °C with bias voltage of -120 V is possibly a result of larger numbers of random complex dislocations within the film microstructure, brought about by very high energy ion bombardment, as suggested by the length of  $a_0$  of that film. It should be stressed that RRR was measured only once for each deposited film and therefore any statistical variation that could result from the inclusion of random complex defects would be difficult to predict from the single result. Conversely, the RRR of films with lengths of the  $a_0$  which suggest they contain fewer random complex, i.e. bias voltages of -50 to -100 V, should provide less variability in RRR for repeated measurements and for measurements of different films deposited with similar process conditions. RRR is consistently large at 700 °C when compared to films deposited at room temperature and 500 °C, with and without an applied bias. The larger RRR for films deposited at 700 °C is consistent with what would be expected for films that have grown with comparatively large grains. RRR was sometimes smaller at 800 °C relative to 700 °C. This was an unexpected result as it would be assumed that larger temperatures will anneal more defects from a deposited film. Although it is correct to assume that a larger temperature on the substrate heater will result in larger outgassing, possibly allowing greater volumes of impurity atoms to be substituted into the growing film, it is most likely that the RRR was smaller for some films deposited at 800 °C because of thermal stresses between film and substrate. This assumption is made because RGA measurements performed during deposition at both temperatures remained constant. Thus, it would be unlikely that film microstructure would be influenced by the exact same thermal stresses during repeated deposition of films using similar process conditions at 800 °C and so may explain the unexpected behaviour of RRR at that temperature.

The resistance versus temperature results presented here display no consistent trends which linked  $T_c$  to the process conditions used to deposit niobium thin films. Inconsistencies between  $T_c$  and the deposition process conditions have been reported previously in the literature [83].

The DC magnetic data will now be discussed. Multiple flux jumps were observed for all films deposited at room temperature and 500 °C and for a selection of films deposited at 700 and 800 °C. Such flux jumps represent unstable flux pinning and rapid reorientation of vortices into more energetically stable pinning locations as the magnetic field strength changes [125]. In extreme cases of multiple flux jumps, it can lead to the so-called vortex avalanches [126]. Types of pinning locations are precipitates of non-superconducting material, precipitates of superconducting material with reduced transition temperature, lattice dislocations and interplanar defects or grain boundaries. Vortices which move between pinning locations act as a viscous fluid and can produce areas of local heating which in turn can promote Cooper pair breaking. Enhanced numbers of unpaired electrons will increase the possibility of a quench [127]. Stable flux pinning was only observed for films deposited at 700 and 800 °C. There was no particular length of  $a_0$  that was unique to those films, but the SEM images did show a large increase in grain size relative to films deposited at room temperature and 500 °C. Thus, the results suggest that the most stable flux pinning occurs for large grain niobium films.

$H_{c2}$  is determined by the defect and impurity densities within films which act as magnetic pinning centres. Films with large  $H_{c2}$  must have the most abundant lattice defects and impurity atoms where a magnetic field can become trapped. A consistently small  $H_{c2}$  was measured for the films deposited at 700 and 800 °C where SEM images have shown that the grain size was largest. Thus, defects at grain boundaries appear to have a large impact on the magnitude of  $H_{c2}$ .

The field at which the gradient first changes for each DC magnetisation measurement indicates the first detectable change in the magnetic properties of the sample and is therefore the first detectable sign of flux entry into a sample. Results describe an enhancement in the field where the first flux penetration can be detected within sample films which were deposited at room temperature to 700 °C with bias voltages of -80 V and at 800 °C with a bias voltage of -100 V. The gradual increase in  $H_{dev}$  from no bias to -80 or -100 V bias, and subsequent reduction in  $H_{dev}$  at -120 V bias suggests that  $H_{dev}$  may be linked to distributions of defects within films. This assumption is made by linking the observations of  $H_{dev}$  to the RRR, measurements of  $a_0$  and SEM images. Results have described how films deposited at room temperature and 500 °C with applied bias voltages of -50 to -100 V, the same films which exhibit a peak in  $H_{dev}$ , displayed a peak in RRR and the most consistent lengths of  $a_0$ . Also, films deposited at room temperature and 500 °C with -80 V bias formed with more densely packed grains than films deposited onto a grounded substrate. Hence, the same thin film growth mechanisms that have already been described for both the observations of  $a_0$  and RRR should

explain the observations of  $H_{dev}$ . The application of a substrate bias increases the energy of ion bombardment, and therefore increases diffusion rate at the surface of the growing film up to a bias voltage of -80 to -100 V, resulting in the annihilation of defects. More defects are formed than are annihilated when the bombarding ions become too energetic, so  $H_{dev}$  decreases for films deposited with bias voltages of either -120 V.

$H_{dev}$  was relatively larger for films deposited with bias voltages of -100 and -120 V at 700 °C and -100 V at 800 °C relative to the same bias voltages at room temperature and 500 °C. The enhanced  $H_{dev}$  at the higher temperatures can be linked to the extra heat energy which enhances the probability of further annealing of complex random defects that can occur at the high bias voltages. The magnitude of  $H_{dev}$  for films deposited at 700 and 800 °C may also have been affected by reductions in the volume of grain boundaries, as shown by the large grain size in the SEM images of those samples.

$M/M_i$  is proportional to the fraction of the sample volume which contains magnetic vortices and gives a description of the behaviour of the flux entry into the sample between  $H_{dev}$  and  $H_{C2}$ . Films which have the largest  $M/M_i$  can be assumed to be more resistant to penetration by an applied magnetic field.

The  $M/M_i$  against bias voltage curves describe little difference between deposited films at fields of 300 Oe. However, differences can be observed once the field reaches 600 Oe. A pattern emerges where films deposited at room temperature to 700 °C show a maximum  $M/M_i$  for films deposited with a bias voltage of -80 V whereas there is a broader range of films displaying relatively large  $M/M_i$ , -20 to -100 V, at 800 °C.

A more distinct pattern can be observed at the higher field of 1000 Oe.  $M/M_i$  is similar for films deposited at room temperature and 500 °C with the same bias voltage, peaking at -80 V. The similarities in  $M/M_i$  for films deposited at room temperature and 500 °C suggest that the applied bias is more influential than the substrate temperature in deciding the magnitude of  $M/M_i$  at smaller substrate temperatures. The same thin film growth mechanisms described in detail for the observations of  $a_0$ , RRR and  $H_{dev}$  also apply for the  $M/M_i$  curves. The application of a bias will initially reduce defect densities up to a bias voltage of -80 V, before higher energy ion bombardment produces more defects than are being annihilated at higher bias voltage. The effects of heating the substrate to 700 and 800 °C during deposition become noticeable in the  $M/M_i$  curves at 1000 Oe, with enhanced  $M/M_i$  for a broad range of bias voltages. The enhanced  $M/M_i$  also coincides with a reduction in the number of observed flux jumps. The reduction in flux jumps at 700 and 800 °C has already been linked to an increase in grain size. Thus, enhanced grain size may also be responsible for the broad range of bias voltages which exhibit large  $M/M_i$  at the larger substrate temperatures.

Two films deposited at 800 °C produced unexpected  $M/M_i$  results. The unbiased film deposited at 800 °C showed the smallest  $M/M_i$  of all deposited films and the film deposited at 800 °C with an applied bias of -120 V displayed much smaller  $M/M_i$  than the film deposited with similar bias at 700 °C. Both observations are similar to the erratic nature of RRR and  $a_0$  of films deposited at 800 °C and are further evidence of the possibility of thermal stresses that can form between film and substrate at the highest temperatures. Also, the repeated DC magnetisation measurements described in section 7.2.2.9 show how the presence of flux jumps, like occurred for the films deposited at 800 °C with bias voltage of either 0 or -120 V, would lead to high sample to sample variability in  $M/M_i$ . Whereas measurements of films which did not exhibit flux jumps, such as those deposited at 700 °C with bias voltages of -80 to -120 V, displayed very little sample to sample variability.

Only one thin film sample was measured by the DC magnetometer when still attached to the copper substrate and after it had been etched away.  $H_{dev}$  and  $M/M_i$  was larger for the measurement when the substrate was still in place. Measurements of further samples with the substrate still in place would be required to make meaningful comparisons between films in each state.

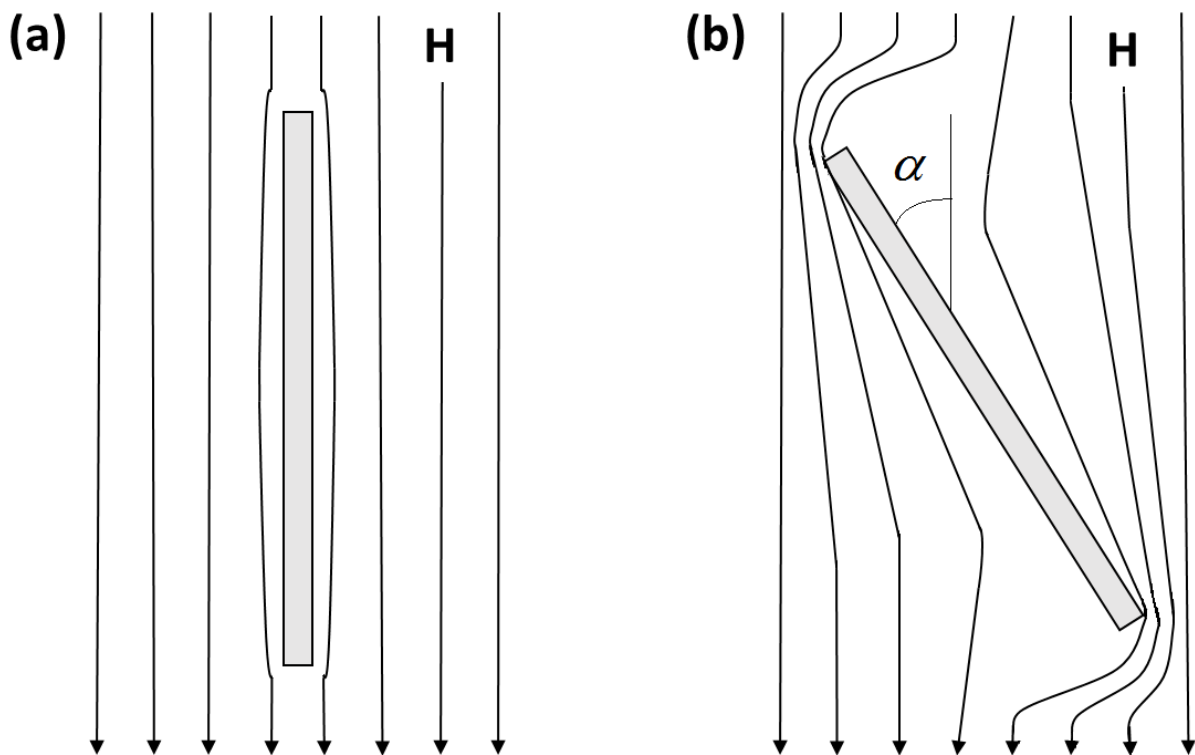


Figure 7.63. Schematic representation of magnetic field lines for (a) superconducting sample parallel to the applied magnetic field lines and (b) superconducting sample inclined with angle  $\alpha$ .

Next, the effects of sample alignment on the DC magnetic data will be discussed. When performing DC magnetometry measurements of thin film samples with the surface parallel to the magnetic field, care must be taken to align samples correctly to avoid early vortex penetration. The interpretation of the DC magnetometer measurements is perfectly valid and unambiguous only for cases when the thin film investigated is perfectly parallel to the applied magnetic field. Indeed, the magnetic behavior of superconducting thin films can be very different for samples which are aligned with the field and for films which are inclined to the magnetic field. Measurements of the DC magnetic moment of superconducting films with  $H$  parallel to the sample plane are fairly difficult to analyze because of the existence of a strong transverse signal, as shown in [128]. Moreover, regardless of any sample anisotropy, a purely geometric effect is to be expected due to edge effects. The magnetic moment is very sensitive to any small disorientation of the sample, which will have a dramatic effect on the signal intensity. Figure 7.63 illustrates a superconducting thin film oriented either parallel or inclined to the applied magnetic field. The area of samples which are perpendicular to the applied magnetic field are equal to  $A \sin\alpha$ . Therefore, the superconducting thin film ideally positioned parallel to the magnetic field will interfere much less than a thin film placed with an angle,  $\alpha > 0$ . The film can be considered parallel to the magnetic field if  $\alpha < d/L$ . We can use equation 7.2 to approximate an upper limit for  $\alpha$  in the parallel orientation to be 0.2 mrad, assuming a film thickness of 1  $\mu\text{m}$  and length of 5 mm.

$$\alpha(\text{rad}) \approx \frac{d}{L} \approx \frac{1 \mu\text{m}}{5000 \mu\text{m}} \approx 0.2 \text{ mra} \quad (7.2)$$

The value of 0.2 mrad is much smaller than the error in sample alignment of  $\pm 17$  mrad. Therefore, samples in our experiment cannot be considered parallel to the magnetic field. If the sample is not perfectly parallel to the magnetic field, then the magnetic field near the edges is enhanced with respect to the rest of the sample. Thus, the magnetic field penetrates early into the edges of the sample, whilst the rest of the sample remains in the Meissner state.

The limitations of the sample alignment dictate that it is difficult to separate the two phenomena of flux penetration due to edge effects and flux penetration due to whole sample properties. The results indicated that no film remained in the Meissner state above 654 Oe when measured after the copper substrate was etched away, which is well below the  $H_{SH}$  of niobium, at 2400 Oe. The early flux penetration may have occurred due to the sample geometry within the applied magnetic field which produced edge effects.

After considering the ramifications of imperfect alignment between sample and field within the DC magnetometer, it should be stressed that the discussion of the DC magnetic data that has been

presented is still valid. Repeated measurements of samples deposited by similar process conditions, or repeated measurements of the same sample, produced almost identical  $M/M_i$  results for samples that had the most stable flux pinning. Samples which displayed flux jumps displayed a sample to sample variation in  $M/M_i$  that was of the same magnitude as the flux jumps. Thus, samples with stable pinning had the most repeatable DC magnetic properties. Also, the act of measuring three overlapped films or one single film showed no effect on the DC magnetic properties of samples.

In conclusion; average increases of  $M/M_i$  and RRR for films deposited at 700 °C relative to room temperature and 500 °C reveal that the energy contribution towards diffusion within and at the surface of the film has become significant at the high temperature. There is a broad range of bias voltages which produces large  $M/M_i$  and RRR at 700 °C, suggesting that the effects of ion bombardment are less significant at larger temperatures. The films deposited at 700 °C also displayed the most stable flux pinning, smallest  $H_{C2}$  and most repeatable DC magnetic properties. The most likely cause of the enhancement of  $M/M_i$ , large RRR, small  $H_{C2}$  and most stable pinning properties at 700 °C is the enlargement of the niobium grain size as shown in SEM images. Enlargement of the niobium grains can be due to both enhanced diffusion rates at high temperature and the removal of the surface oxide layer from the copper substrate before the film is deposited.

Films deposited at room temperature and 500 °C displayed more consistency in the length of  $a_0$ , larger RRR, the biggest  $H_{dev}$  and greater average  $M/M_i$  when deposited with bias voltages ranging -50 to -100 V during deposition. The results suggest that increased rates of surface diffusion and defect annihilation occur due to ion bombardment, up to an applied bias of between -50 to -100 V. More random complex defects appear to form than are annihilated once the energy of bombarding ions becomes too large, as is suggested by measurements of the length in  $a_0$  of films deposited with a -120 V bias.

3D optical microscope images have shown that “blisters” occur at the surface of films when deposited at 500 °C with an applied bias of -80 V and at 700 and 800 °C with bias voltages of -80 to -120 V. The physical mechanism which produces the “blisters” is as yet unknown. However, it is suggested that films which exhibit the “blisters” should not be used within SRF application until the nature of the feature is better understood.

Properties of films deposited at 800 °C display less predictable properties than was observed for films deposited at 700 °C. Possibly due to enhanced thermal stresses between film and substrate at 800 °C. The results suggest that a copper substrate temperature of 800 °C is not advisable for any process which requires sample to sample repeatability

### **7.2.3. Testing the effects of substrate heating and an applied DC substrate bias when depositing onto pre-annealed copper substrate**

The results that were discussed in section 7.2.2 showed that niobium films deposited onto as received polycrystalline copper substrate displayed an average relative decrease in the volume of the sample which was penetrated by magnetic flux, more stable flux pinning and had a relatively small  $H_{C2}$  for films deposited at 700 °C when compared to similar bias voltages at room temperature and 500 °C. The study concluded that the observations resulted from enhanced mobility of sputtered material at high temperature and the possibility of substrate effects such as; the enlargement of grain size (both film and substrate), the removal of the native surface oxide layer of the substrate and substrate annealing. The next phase of the study was performed to better understand if the different properties exhibited by films deposited onto as received substrate were entirely due to thermalisation during deposition or also because of physical changes to the substrate that occur once it is heated to 700 °C.

A new batch of niobium films were deposited at substrate temperatures of room temperature and 500 °C and with bias voltages of 0, -20, -50, -80, -100 and -120 V. However, the substrate was first pre-heated to 700 °C for 12 hours before deposition. The substrate was allowed to cool from 700 °C down to the required temperature before each deposition was started. All niobium thin films were deposited by HiPIMS using the same process described for samples deposited onto as received copper substrate in section 7.2.2. Each film was then analysed using similar techniques and compared to the results that were discussed in section 7.2.2.

### 7.2.3.1. Grazing incidence x-ray diffraction

Grazing incidence XRD was performed on all films deposited onto pre-annealed substrate. All grazing incidence XRD measurements in this section of the report were analysed using a cobalt X-Ray source to produce an x-ray beam with  $K\alpha_1$  wavelength of 1.78901 Å with a glancing angle of 2°. Each film was measured when still attached to the copper substrate; no measurements were performed of films after the substrate was etched away.

The grazing incidence XRD measurements for all niobium films deposited onto pre-annealed copper substrate are shown in figure 7.64. All films formed with the bcc (110) preferred growth orientation with peaks between 44 and 46°. Smaller peaks denoting the following niobium bcc orientations were also observed in every deposited film; (200) at  $\approx 65^\circ$ , (211) at  $\approx 83^\circ$ , (220) at  $\approx 100^\circ$  and (310) at  $\approx 117^\circ$ . The peak distributions were similar of those observed for the samples deposited onto as received substrate. The (110) peaks were mostly regular in shape except for the films deposited at room temperature with bias voltages of -80 and -120 V, which exhibited doublet peaks.

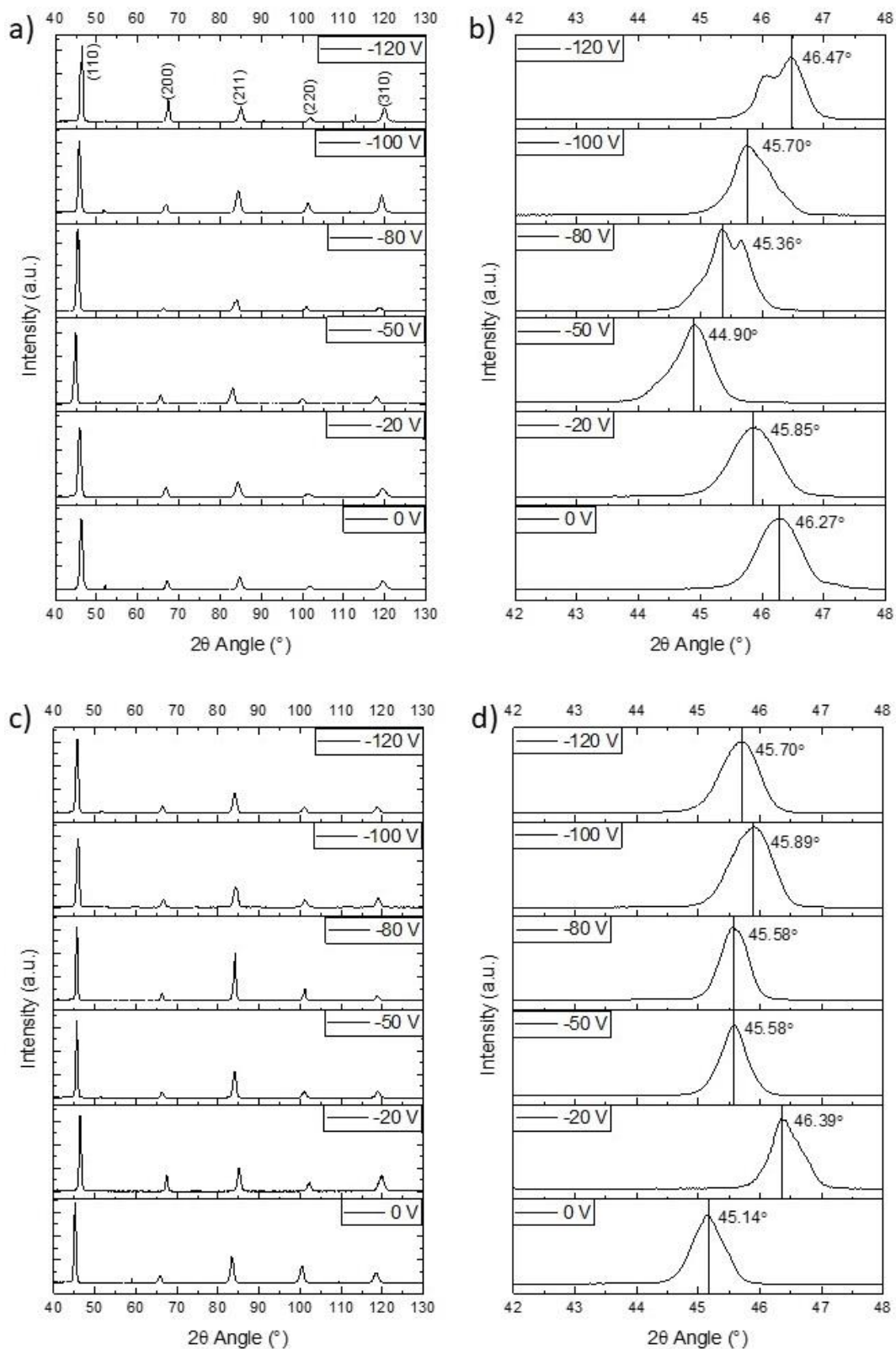


Figure 7.64. Grazing incidence XRD data for samples deposited onto pre-annealed substrate at room temperature and 500 °C. Data is shown in a) 40 to 130 ° measured on copper for films deposited at room temperature, b) the (110) peak at approximately 44 - 46° measured on copper for films deposited at room temperature, c) 40 to 130 ° measured on copper for films deposited at 500 °C and d) the (110) peak at approximately 44 - 46° measured on copper for films deposited at 500 °C.

The length of  $a_0$  of all films deposited at room temperature and 500 °C are shown in figure 7.65; results for films deposited onto as received and pre-annealed copper have been plotted together for comparison. The length of  $a_0$  for films deposited with substrate bias of 0, -20 and -120 V display a high variability depending on what temperature or substrate was used. The variability in lattice parameter is considerably less for films deposited with bias voltages of -50 and -100 V and is approximately constant at 3.27 to 3.28 Å for all films deposited with -80 V bias.

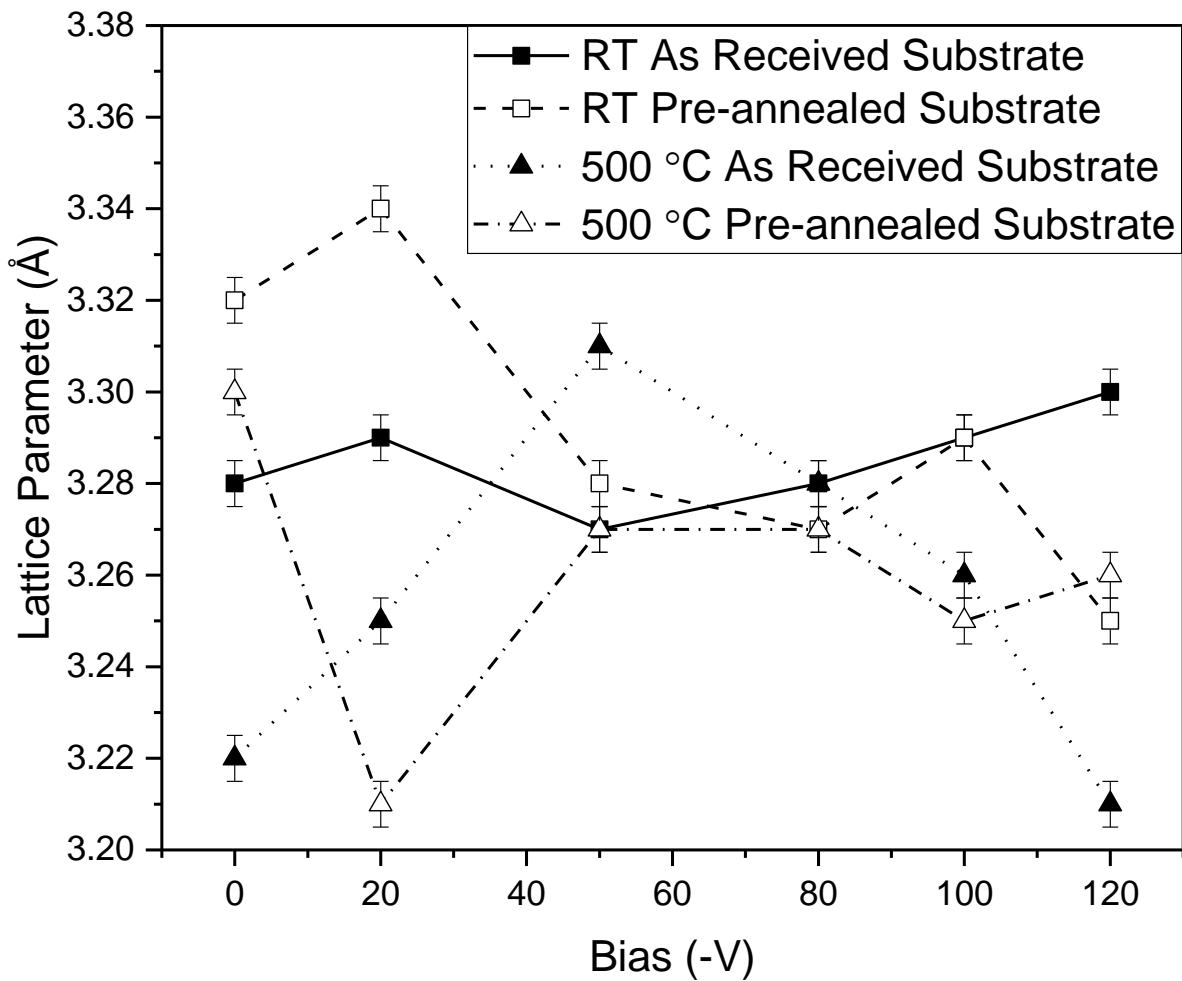


Figure 7.65. Lattice parameter versus applied bias voltage of niobium films deposited onto either as received or pre-annealed polycrystalline copper substrate.

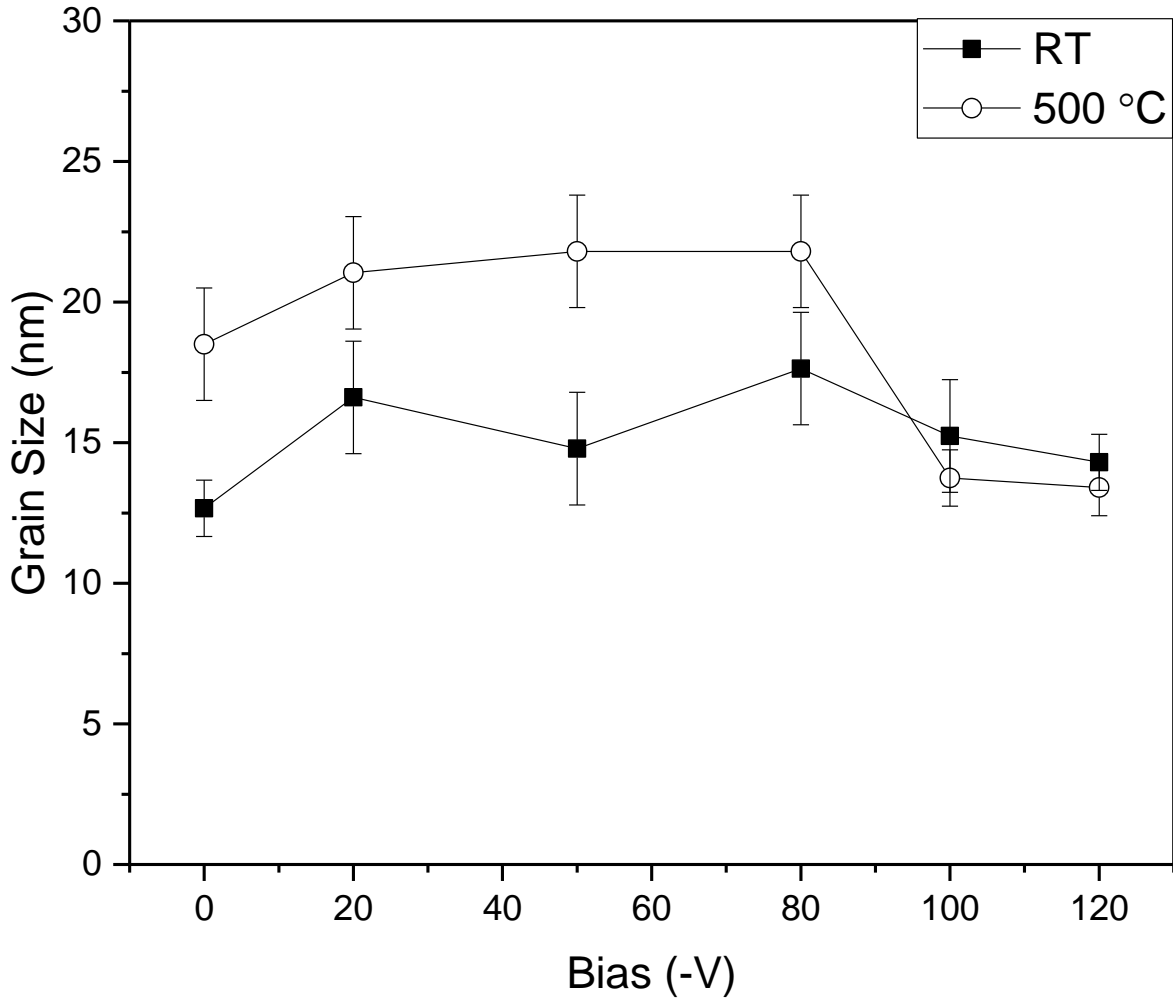


Figure 7.66. Average grain size against applied bias during deposition of niobium thin films deposited onto pre-annealed copper substrate.

The average grain size, as calculated by equation 5.1 and the FWHM of grazing incidence XRD peaks, of niobium films deposited onto pre-annealed substrate is shown in figure 7.66. The average grain size is ranges from 13 to 23 nm for all films.

### 7.2.3.2. Scanning electron microscopy and 3D optical microscopy

Backscatter detector SEM images were taken of all samples deposited at room temperature and 500 °C with applied bias voltage of 0, -80 and -120 V. Images were taken with beam energies of either 10 or 20 kV and with beam spot sizes of either 3 or 4.5 nm.

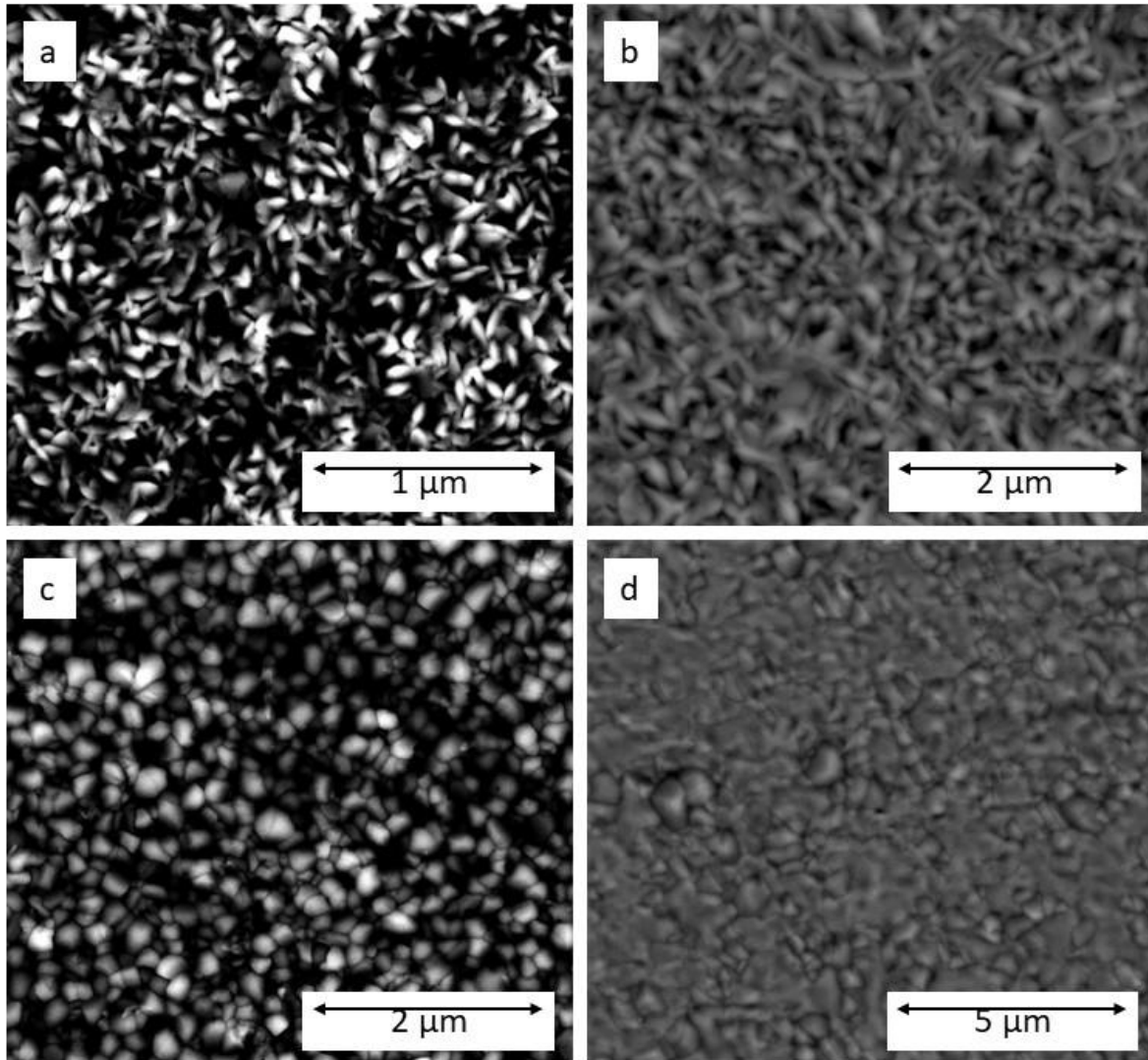
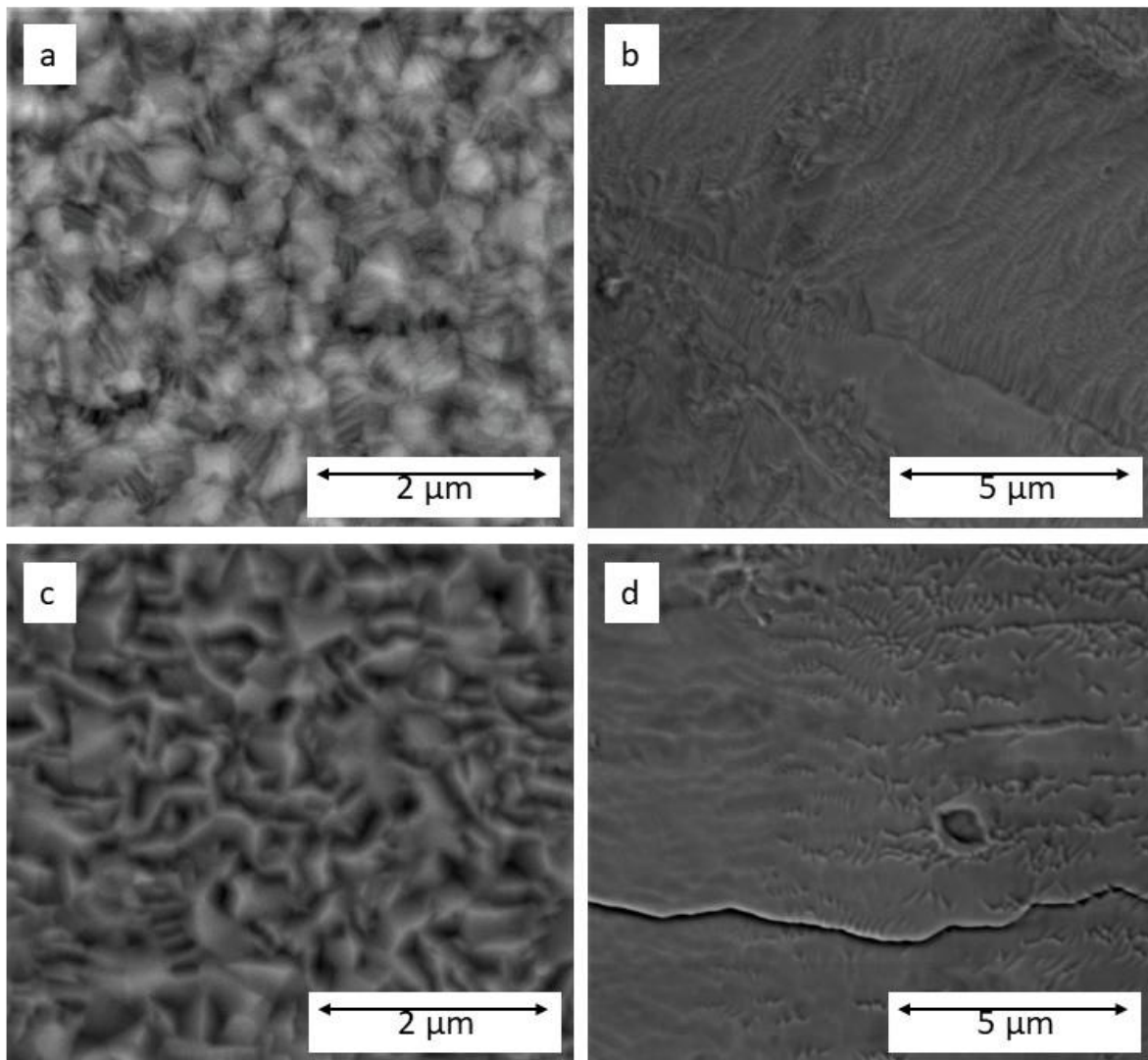


Figure 7.67. SEM images of niobium thin film samples deposited at a) room temperature without bias onto as received substrate, b) room temperature without bias onto pre-annealed substrate, c) 500 °C without bias onto as received substrate and d) 500 °C without bias onto pre-annealed substrate.

Figures 7.67 a and b displays a planar image of the niobium thin films deposited at room temperature without bias onto as received and pre-annealed substrate. Both films appear to have grains with maximum sizes of 100 – 200 nm across. Figures 7.67 c and d displays the niobium films deposited at 500 °C without bias onto either as received substrate or onto pre-annealed substrate. Grain sizes are slightly increased for the unbiased films deposited at 500 °C relative to room

temperature and show a small increase at 500 °C for the pre-annealed substrate when compared to the as received substrate.



**Figure 7.68.** SEM images of niobium thin film samples deposited at a) room temperature with -80 V substrate bias onto as received substrate, b) room temperature with -80 V substrate bias onto pre-annealed substrate, c) 500 °C with -80 V substrate bias onto as received substrate and d) 500 °C with -80 V substrate bias onto pre-annealed substrate.

Figures 7.68 a and b display the films deposited at room temperature with -80 V bias onto as received and pre-annealed copper substrate respectively. Grain boundaries are clearly visible for the films deposited onto as received substrate. However, no grain boundaries are seen on the pre-annealed substrate. The level of magnification is not as large in figures 7.68 b and d as in figures 7.68 a and b however increasing the magnification further did not reveal any further details. A large “crack” appears in figure 7.68 b which is most likely related to the topography of the underlying copper substrate.

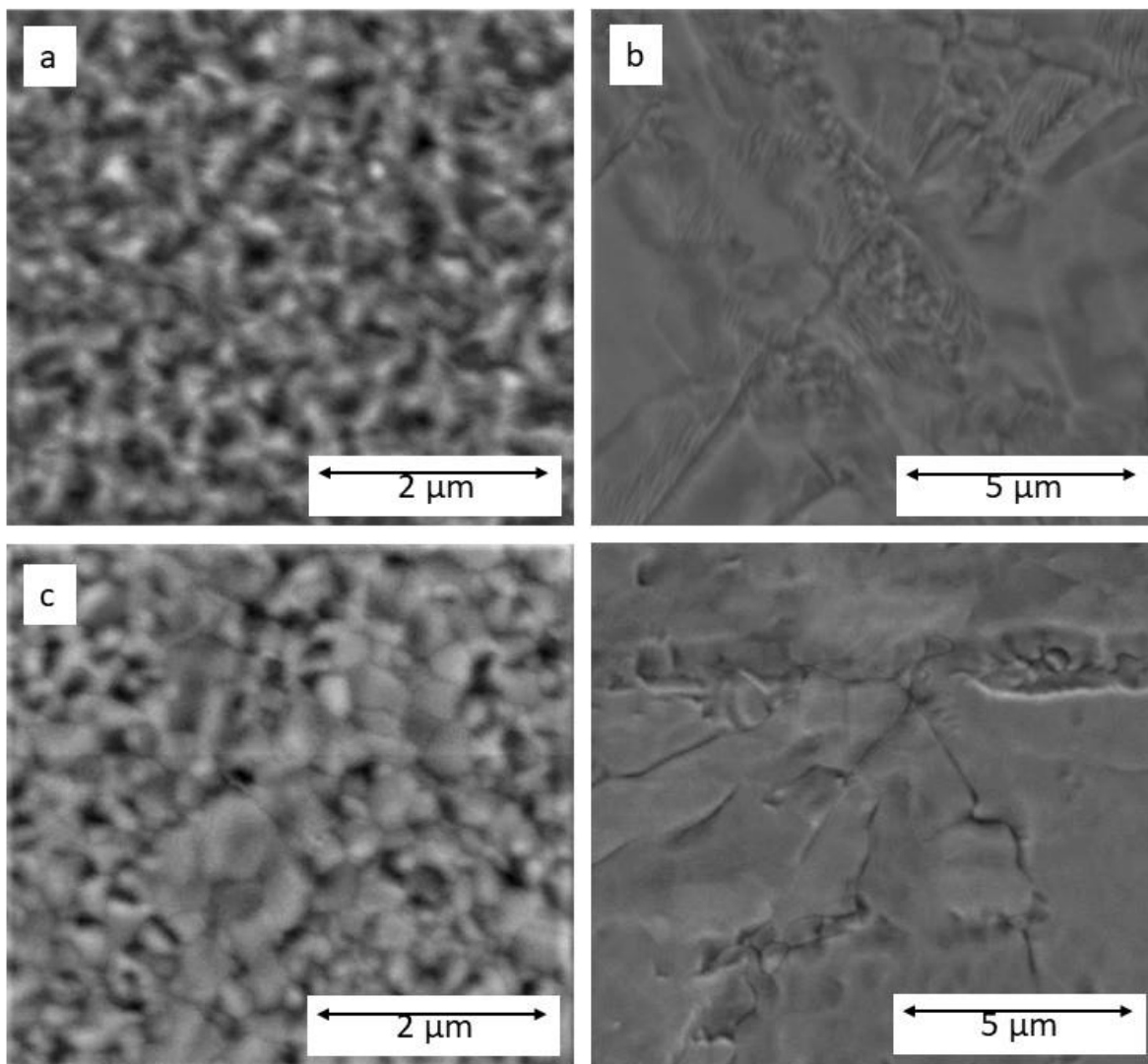
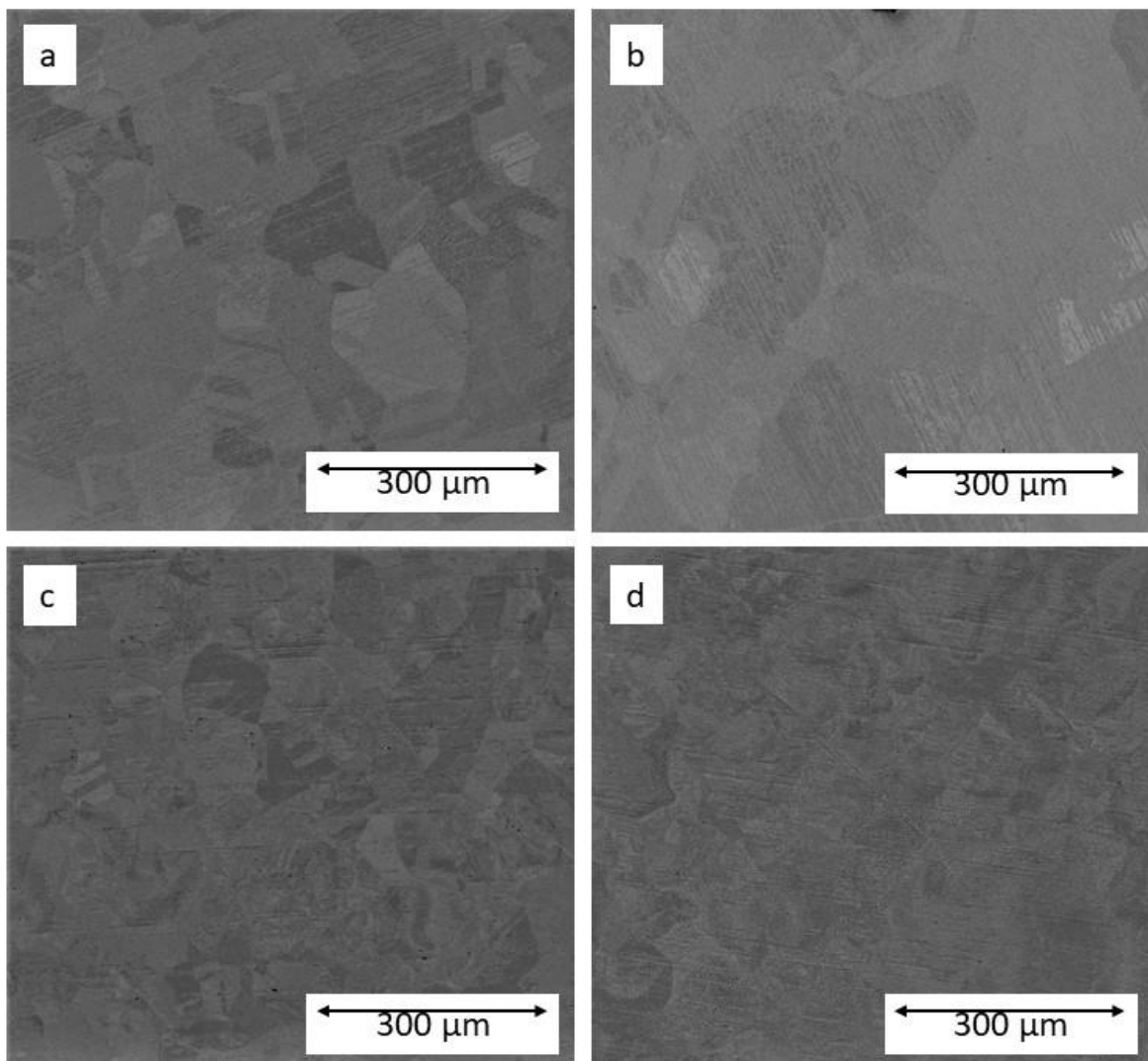


Figure 7.69. SEM images of niobium thin film samples deposited at a) room temperature with -120 V substrate bias onto as received substrate, b) room temperature with -120 V substrate bias onto pre-annealed substrate, c) 500 °C with -120 V substrate bias onto as received substrate and d) 500 °C with -120 V substrate bias onto pre-annealed substrate.

Figure 7.69 a, b, c, and d shows planar images of the films deposited at room temperature with -120 V bias onto as received and pre-annealed substrate and at 500 °C with -120 V bias onto as received and pre-annealed substrate respectively. The films deposited onto as received substrate with -120 V bias display comparable grain structure with sub-microns grain size. The films deposited onto pre-annealed substrate with -120 V bias do not display well defined grain boundaries, similar to those deposited at -80 V bias onto pre-annealed substrate.



**Figure 7.70.** SEM images of niobium thin films samples deposited at a) room temperature with -80 V substrate bias onto as pre-annealed substrate, b) room temperature with -120 V substrate bias onto pre-annealed substrate, c) 500 °C with -80 V substrate bias onto as pre-annealed substrate and d) 500 °C with -120 V bias onto pre-annealed substrate.

Figure 7.70 a, b, c and d display the films deposited onto pre-annealed substrate at room temperature with -80 and -120 V substrate bias and at 500 °C with -80 and -120 V substrate bias respectively. The channelling contrast of the backscatter SEM detector differentiates areas at the surface of the niobium film which have formed with differing growth orientation with respect to the direction of the detector. The largest of the similarly shaded areas in figure 7.70 are 100 – 200 microns across and are comparable in size for each image.

3D optical microscope images were taken of all niobium thin films deposited onto pre-annealed copper substrate and are shown in figures 7.71 and 7.72. All films deposited at room temperature and those deposited at 500 °C with bias voltages of 0 to -50 V have similar surface to that of the underlying copper substrate. Films deposited at 500 °C with bias voltages of -80 to -120 V display

a “blistered” texture, with heights ranging  $10\pm 2$  to  $15\pm 2$   $\mu\text{m}$  and diameter ranging 50 to 250  $\mu\text{m}$ , and the “blisters” occur more frequently as the bias voltage is increased during deposition. This observation is similar to those described in section 7.2.2.5 for films deposited at 700 and 800  $^{\circ}\text{C}$  with the same applied bias voltages.

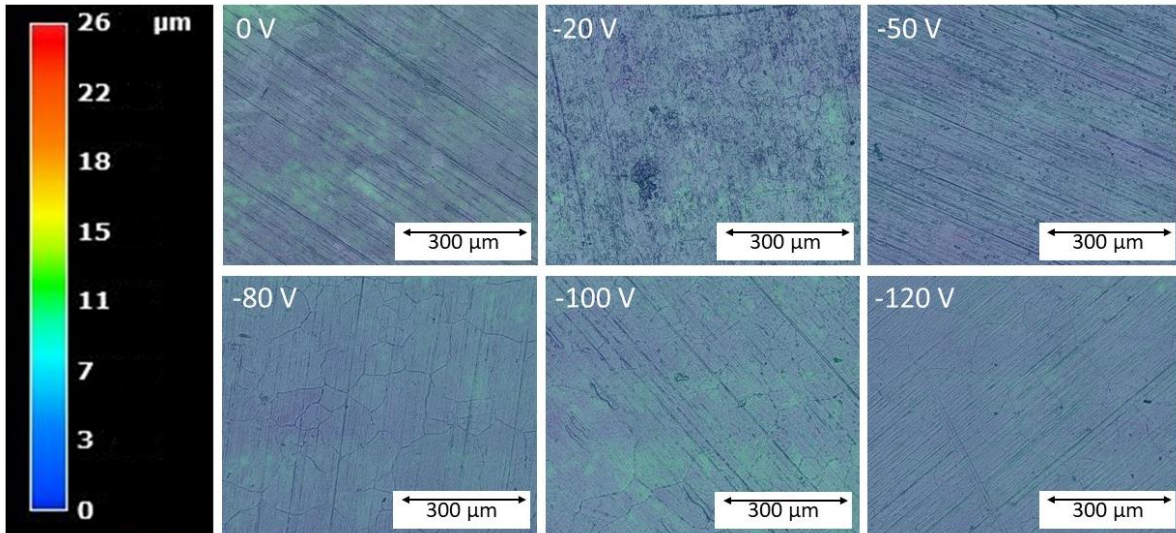


Figure 7.71. 3D Optical microscope images of the surface of niobium thin films deposited by HiPIMS at room temperature with bias voltages of 0 to -120 V onto pre-annealed substrate.

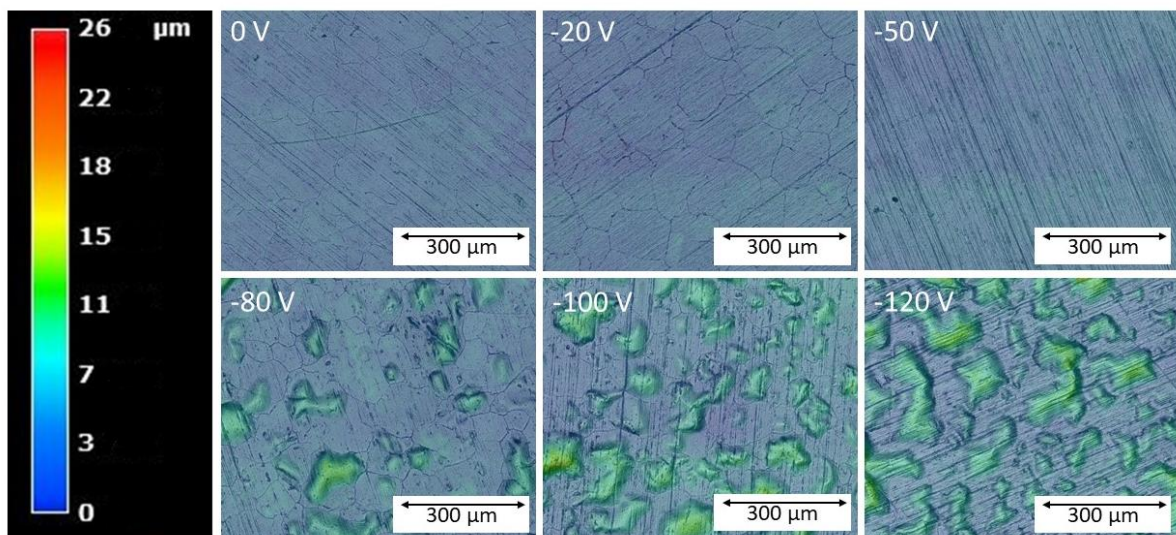


Figure 7.72. 3D Optical microscope images of the surface of niobium thin films deposited by HiPIMS at 500  $^{\circ}\text{C}$  with bias voltages of 0 to -120 V onto pre-annealed substrate.

### 7.2.3.3. Resistance versus temperature curves

The resistance versus temperature data for samples deposited onto pre-annealed copper substrate at room temperature is shown in figure 7.73a. The maximum normal state resistance at just above  $T_c$  occurred for the sample deposited without an applied bias at 0.0025 m $\Omega$ , films biased -20, -50 and -100 V exhibited a resistance of approximately 0.0016 m $\Omega$  and the smallest normal state resistance of approximately 0.0010 m $\Omega$  was measured for the films biased at -80 and -120 V during deposition.

The RRR versus temperature data for samples deposited onto pre-annealed copper substrate at room temperature is shown in figure 7.73b. The smallest RRR was 10 and occurred for the samples deposited with bias voltages of both 0 and -20 V, followed by the film biased at -50 with RRR of 25. The largest RRR was measured at 39 to 41 for the films deposited with bias voltages of -80 to -120 V.

The resistance versus temperature data for samples deposited onto pre-annealed copper substrate at 500 °C is shown in figure 7.74a. The maximum normal state resistance at just above  $T_c$  occurred for the sample deposited with -20 V bias at 0.0015 m $\Omega$ , the film biased -50 V exhibited a resistance of approximately 0.0012 m $\Omega$ , the films biased at 0 V displayed resistance of 0.0008 m $\Omega$  and the smallest normal state resistance of 0.0004 m $\Omega$  was measured for the films biased at -80 and -120 V during deposition.

The RRR versus temperature data for samples deposited onto pre-annealed copper substrate at 500 °C is shown in figure 7.74b. The smallest RRR was 32 and occurred for the sample deposited with -20 V bias, the film deposited without bias displayed RRR of 50. The films deposited with bias voltages of -50 and -120 displayed RRR of 84 and 91. The largest RRR occurred for the films deposited with bias voltages of -80 and -100 V with RRR of 129 and 110 respectively. RRR of 129 was the largest of any film deposited during this study.

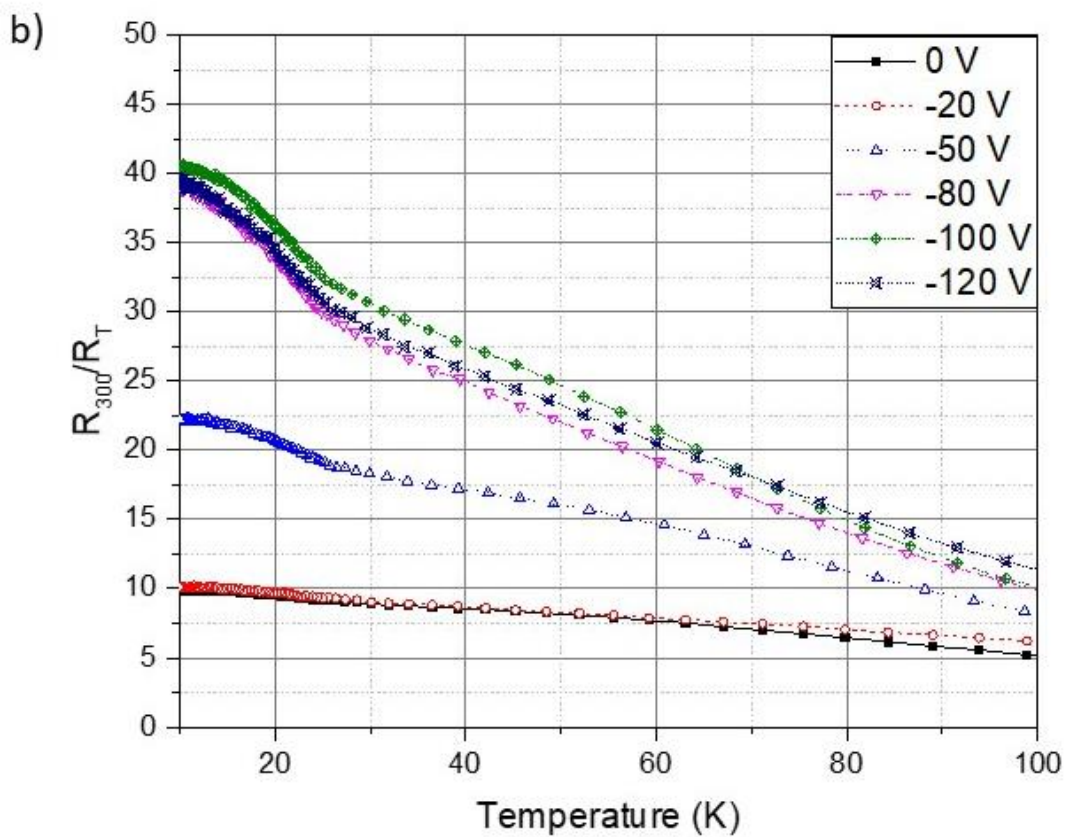
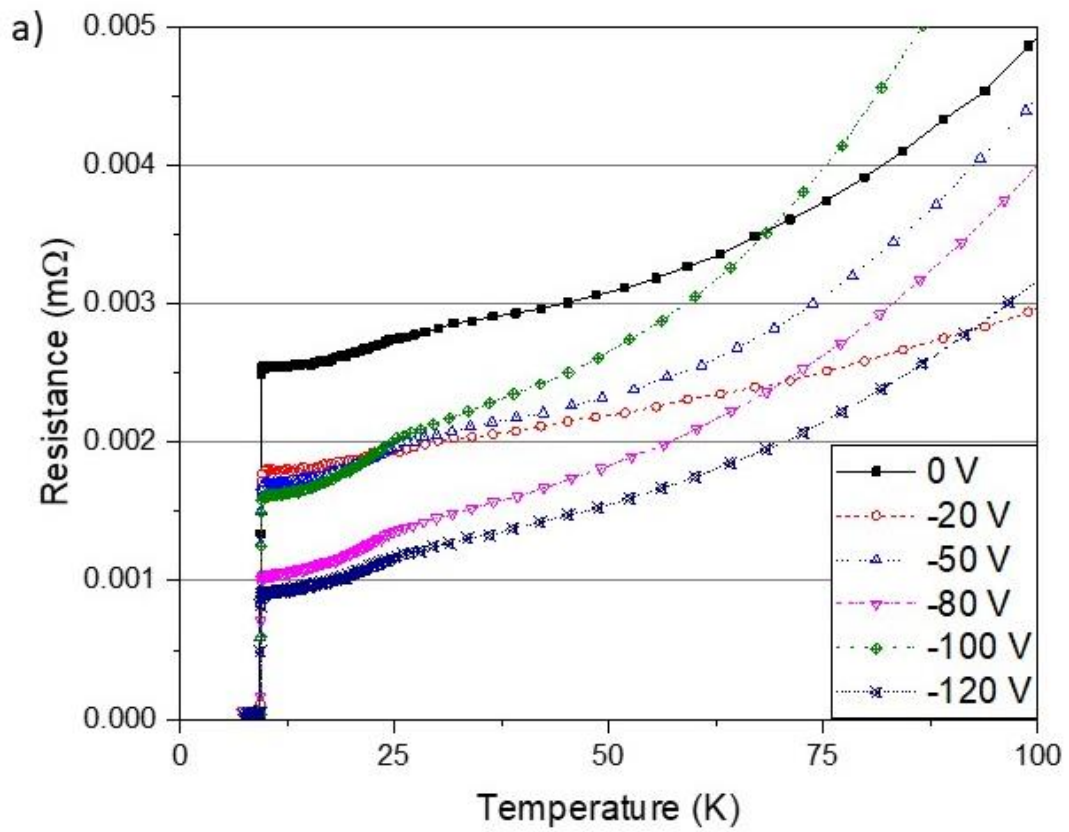


Figure 7.73. a) Resistance versus temperature from 0 to 100 K and b) RRR versus temperature for niobium films deposited onto pre-annealed polycrystalline copper substrate at room temperature with bias voltages ranging from 0 to -120 V.

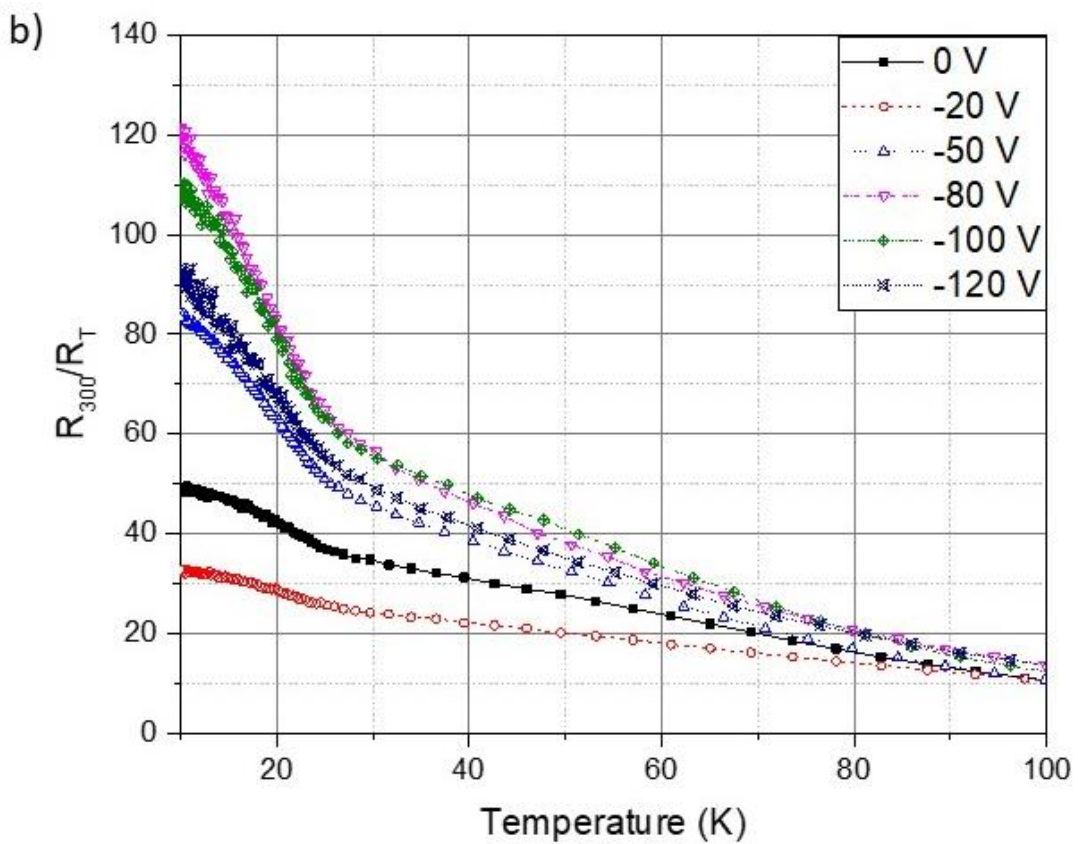
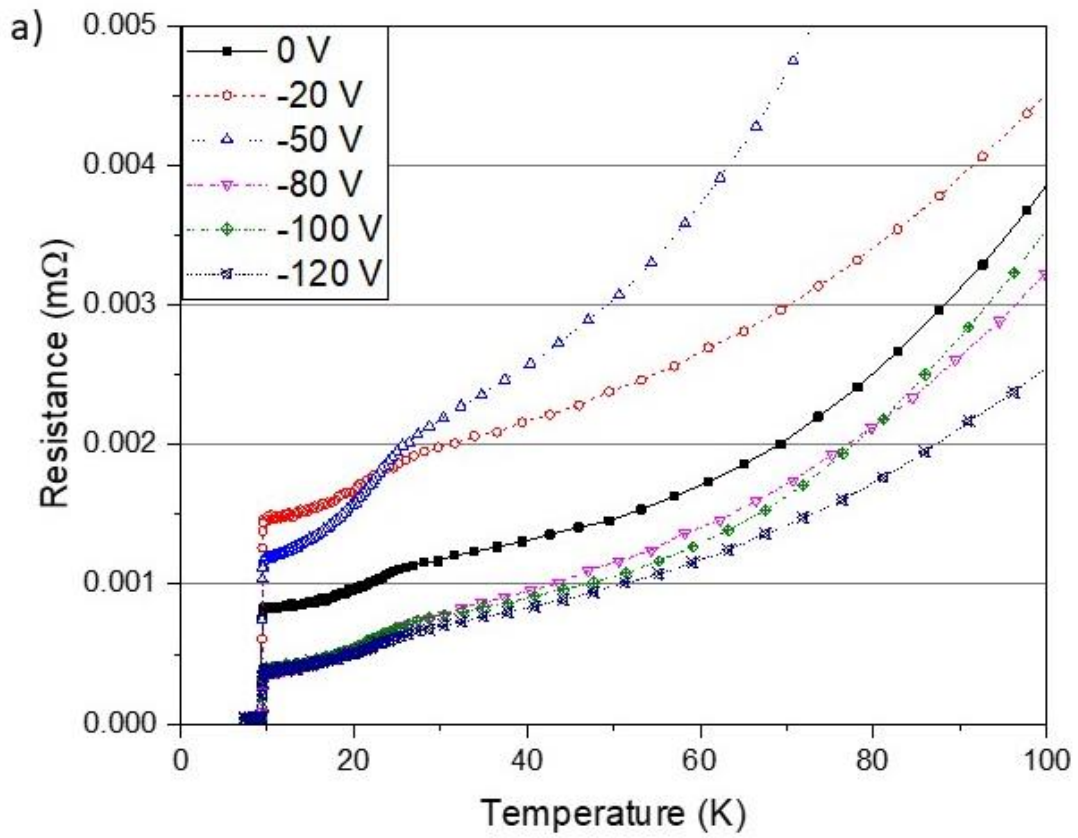


Figure 7.74. a) Resistance versus temperature from 0 to 100 K and b) RRR versus temperature for niobium films deposited onto pre-annealed polycrystalline copper substrate at 500 °C with bias voltages ranging from 0 to -120 V.

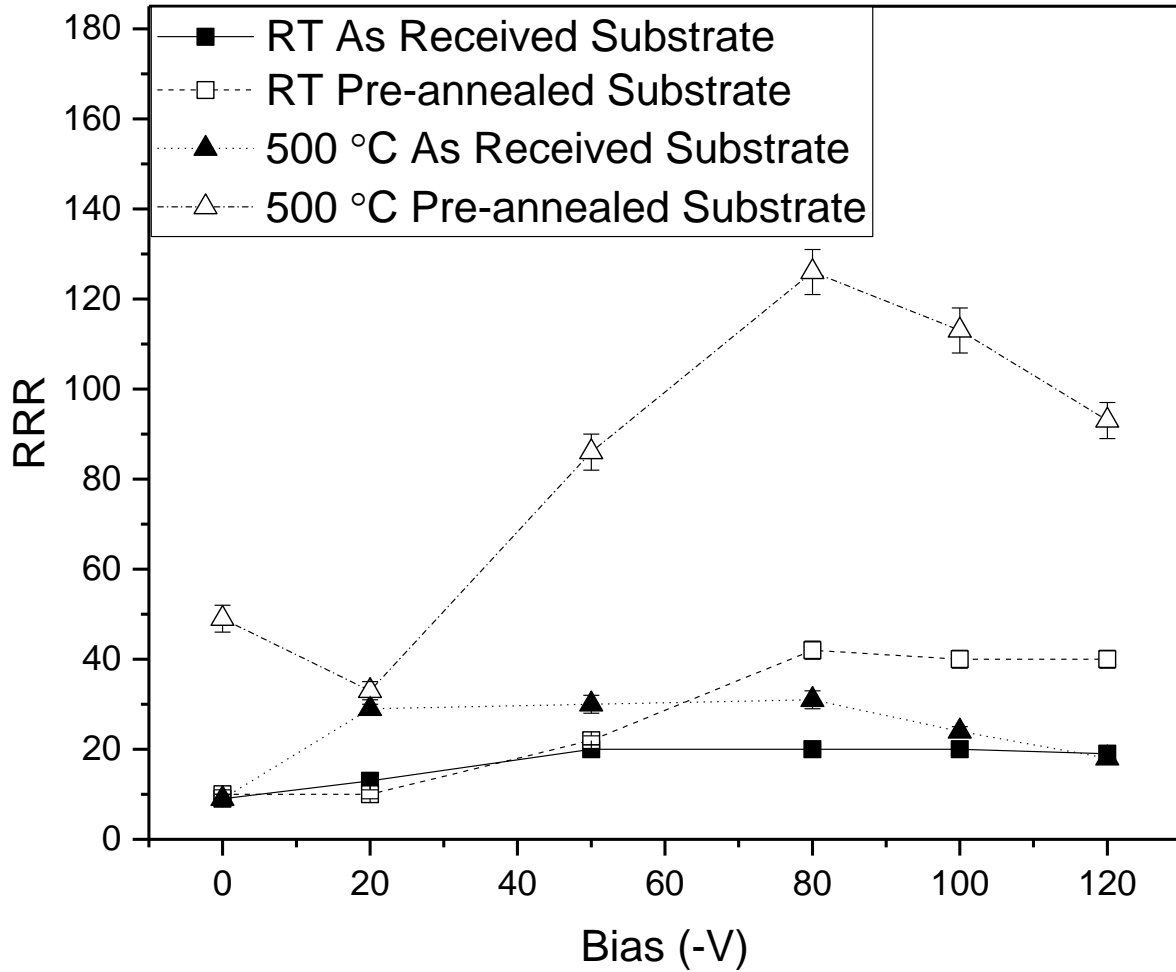


Figure 7.75. RRR versus applied bias voltage for niobium films deposited onto as received and pre-annealed polycrystalline copper substrate.

RRR data for all deposited films is shown in figure 7.75. RRR is similar for the films deposited at room temperature onto both as received and pre-annealed substrate at bias voltages of 0 to -50 V, increasing from 9 for the unbiased films to approximately 20 for the films biased at -50 V. RRR is approximately twice as large for the films deposited at room temperature onto pre-annealed substrate when compared to as received substrate at bias voltages of -80 to -120 V, increasing from 20 to over 40. RRR is greatly enlarged for all but the -20 V biased sample for films deposited at 500 °C onto pre-annealed substrate when compared to as received substrate. RRR peaks at 129 for the film deposited onto pre-heated substrate at 500 °C with applied -80 V bias.

### 7.2.3.4. DC magnetisation measurements

The DC magnetisation between 0 and 10000 Oe is shown in figure 7.76 for films deposited at room temperature and 500 °C onto pre-annealed substrate. The measured magnetic moment increases linearly before displaying a changing gradient up to the maximum magnetisation and finally dropping back to zero. As discussed in section 7.2.2.10, many small magnitude flux jumps were observed in all samples deposited at either room temperature or 500 °C onto as received substrate. Films deposited onto pre-annealed substrate at room temperature with bias voltages of 0, -20 and -50 V and at 500 °C with a bias voltage of -20 V display similar small magnitude flux jumps to those seen on as received substrate. All other films displayed either no flux jumps or just one flux jump.

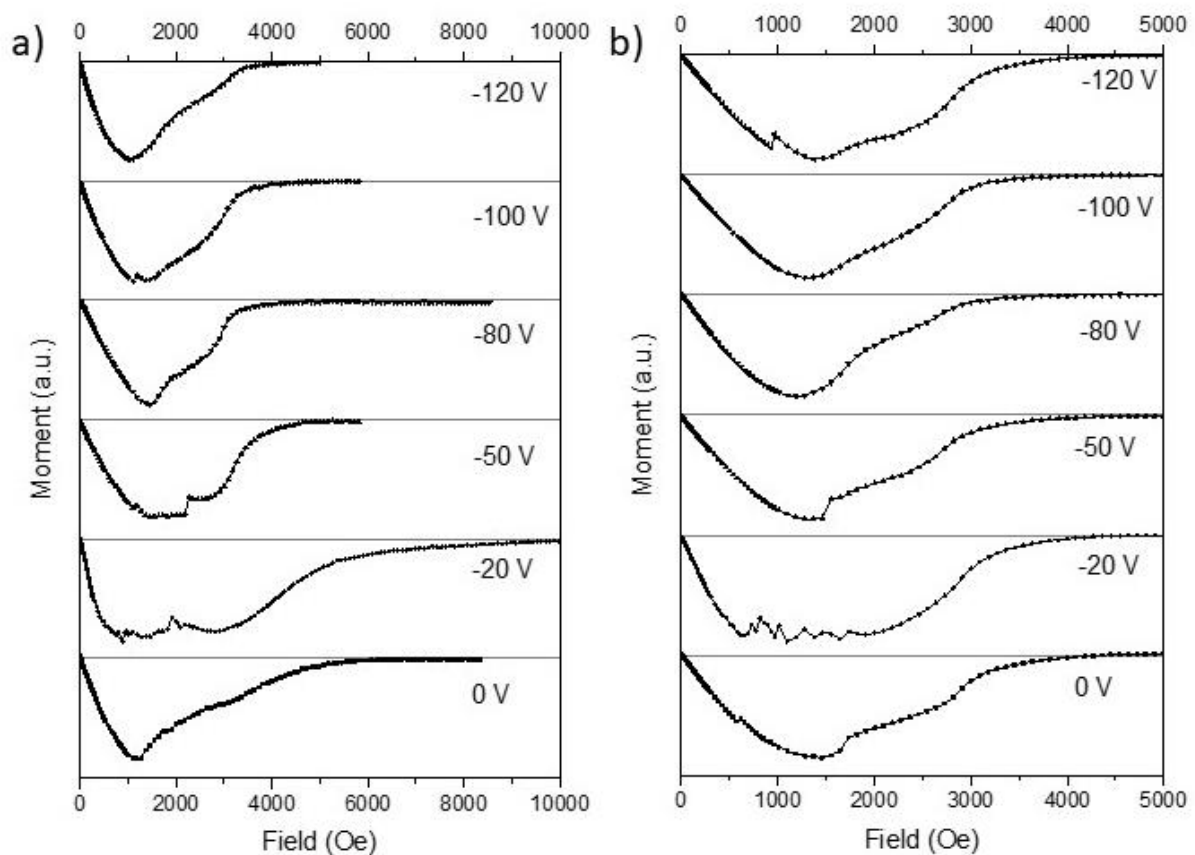


Figure 7.76. DC magnetic moment versus applied magnetic field for niobium thin film samples which were deposited at a) room temperature and b) 500 °C onto copper substrate which had been pre-annealed at 700 °C for 12 hours.

$H_{C2}$  is plotted for all films deposited at room temperature or 500 °C in figure 7.77. Only the film deposited at room temperature with a -20 V bias displayed similar  $H_{C2}$  when deposited onto either as received and pre-annealed copper substrate.  $H_{C2}$  dropped from 10000 Oe for films deposited onto as received copper substrate to 6000 Oe on pre-annealed copper substrate for the films deposited at room temperature without bias.  $H_{C2}$  of all other films dropped from approximately 8000 – 6000 Oe on as received copper substrate to approximately 4000 – 5000 Oe on pre-annealed copper substrate.

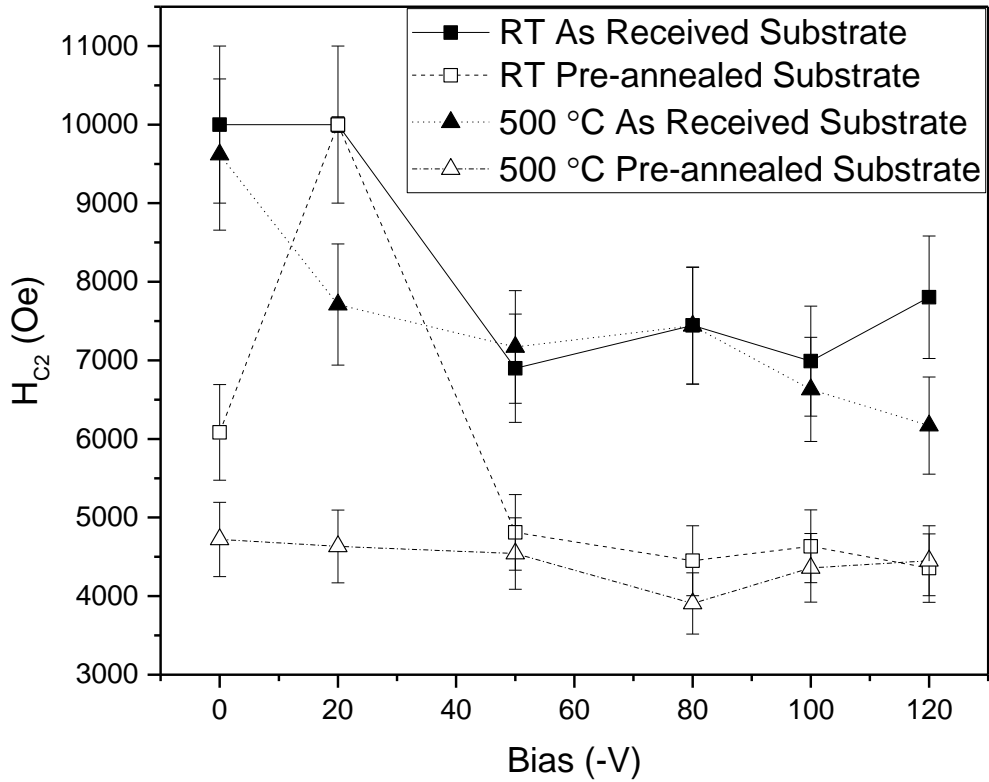


Figure 7.77.  $H_{C2}$  versus applied bias voltage for each deposited niobium thin film deposited onto either as received or pre-annealed copper substrate.

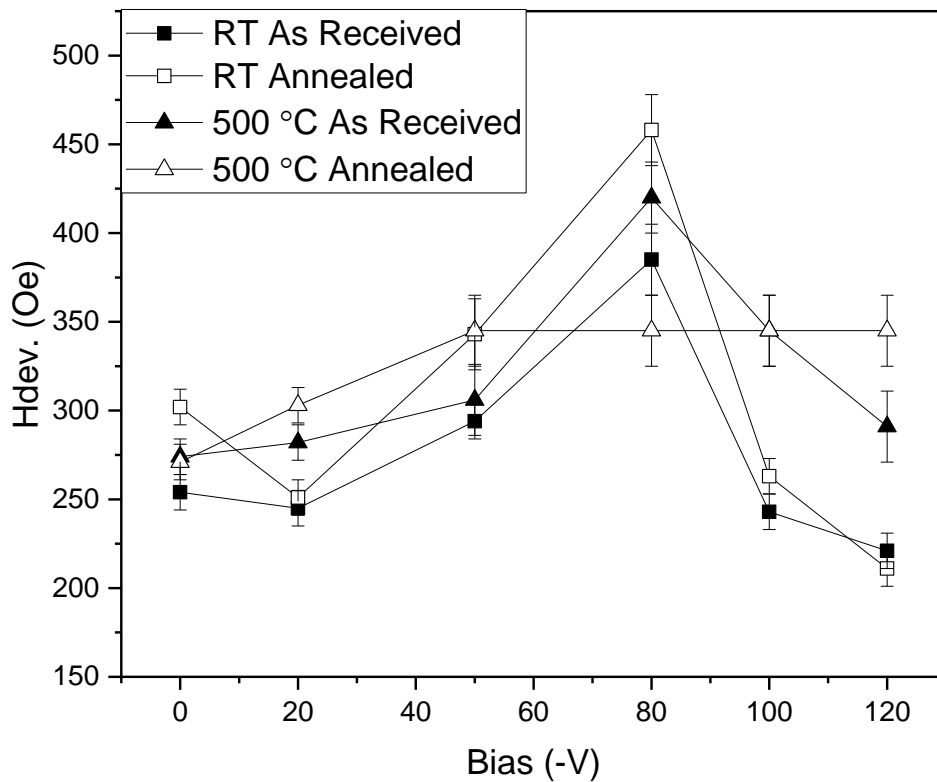


Figure 7.78.  $H_{dev.}$  (as defined in figure 7.45) versus applied bias voltage for samples deposited at room temperature and 500 °C onto either as received copper substrate or pre-annealed copper substrate.

$H_{dev}$  is plotted in figure 7.78 for films deposited at both room temperature and 500 °C onto either as received or pre-annealed copper substrate. Peaks in  $H_{dev}$  are seen at -80 V DC bias for films deposited at room temperature onto both as received copper substrate, at  $385\pm 20$  Oe, and pre-annealed copper substrate, at  $458\pm 20$  Oe.  $H_{dev}$  peaks at  $420\pm 20$  Oe for films deposited at 500 °C onto as received copper substrate for the film biased at -80 V but drops to  $345\pm 20$  Oe for each of the films biased at -50 to -120 V when deposited onto pre-annealed substrate.

$M/M_i$  for niobium thin films deposited at room temperature onto pre-annealed substrate is displayed in figure 7.79 and for those deposited at 500 °C onto pre-annealed substrate in figure 7.80. Films deposited at room temperature have the largest average  $M/M_i$  at -80 V bias followed by the next largest average values at 0, -50 and -100 V and the smallest average  $M/M_i$  occurs at -20 and -120 V. Films deposited at 500 °C onto pre-annealed copper substrate at bias voltages of 0, -50, -80, -100 and -120 V have a consistently large average  $M/M_i$  and is like the largest values observed for films deposited at 700 °C.  $M/M_i$  for the film deposited at 500 °C with a -20 V bias was smaller than for films deposited at other bias voltages.

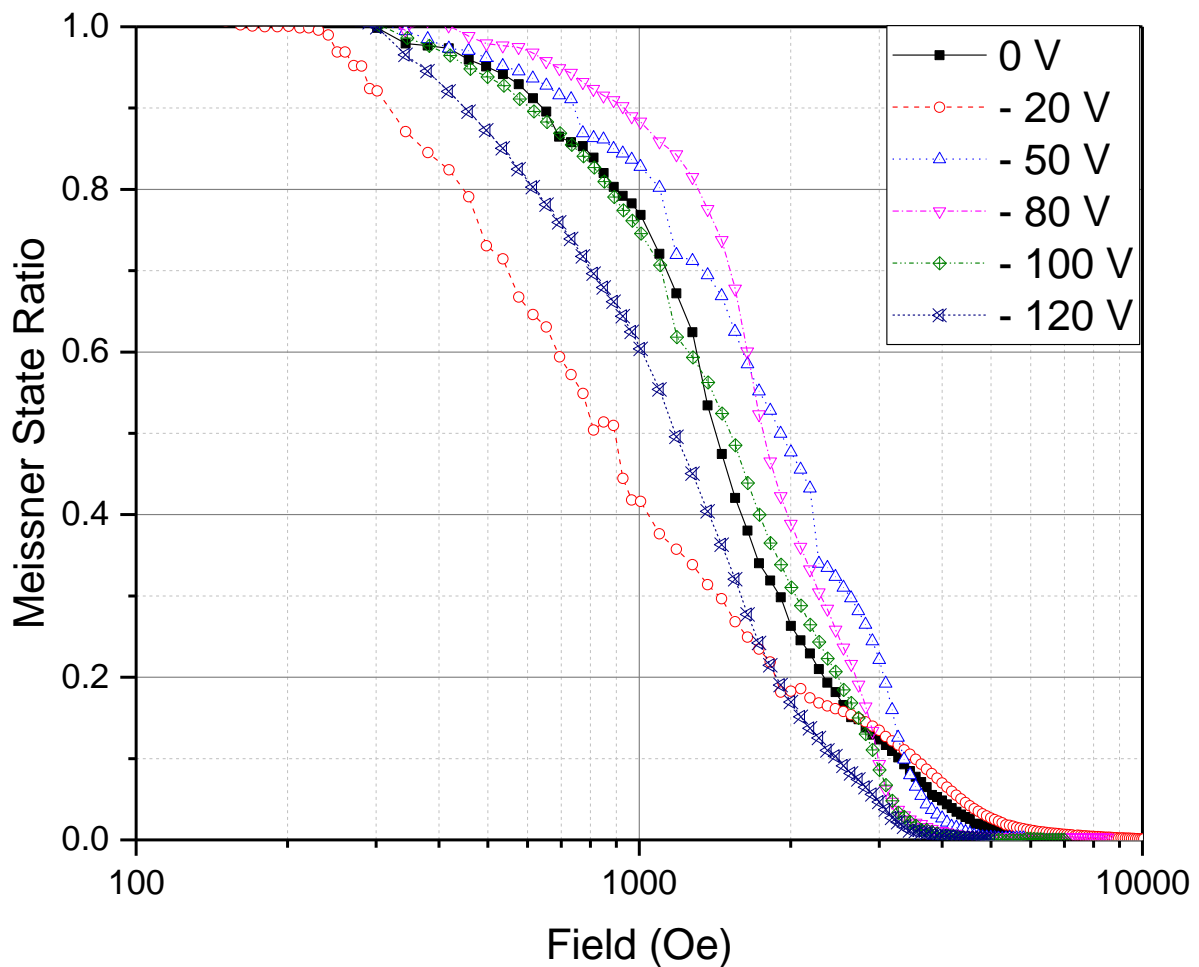


Figure 7.79.  $M/M_i$  versus applied magnetic field for niobium films deposited at room temperature onto copper substrate which was annealed at 700 °C prior to deposition.

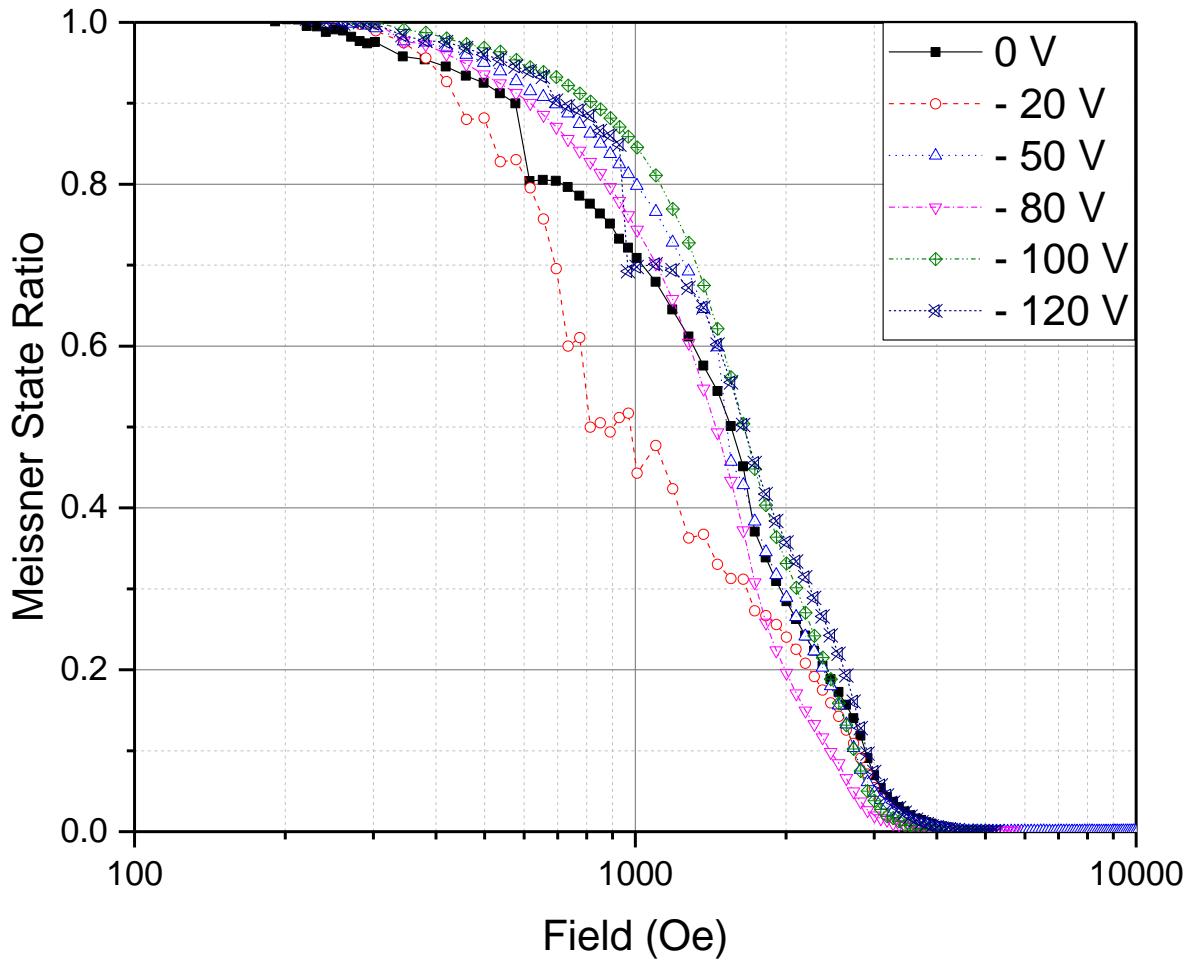


Figure 7.80.  $M/M_i$  versus applied magnetic field for niobium films deposited at 500 °C onto copper substrate which was annealed at 700 °C prior to deposition.

Figure 7.81 illustrates all samples deposited at either room temperature or 500 °C together at magnetic fields of 300, 600, 1000 and 1800 Oe. All films deposited with bias voltages of either -50 or -80 V have  $M/M_i = 1$  at 300 Oe.  $M/M_i$  peaks, and was similar in value, for all films deposited with an applied substrate bias of -80 V at 600 Oe. However,  $M/M_i$  was larger for films deposited with a wide range of applied bias voltage, the only exception being the films deposited at -20 V, onto pre-annealed substrate relative to as received substrate at 600 and 1000 Oe.  $M/M_i$  dropped to below 0.5 for all films at 1800 Oe.

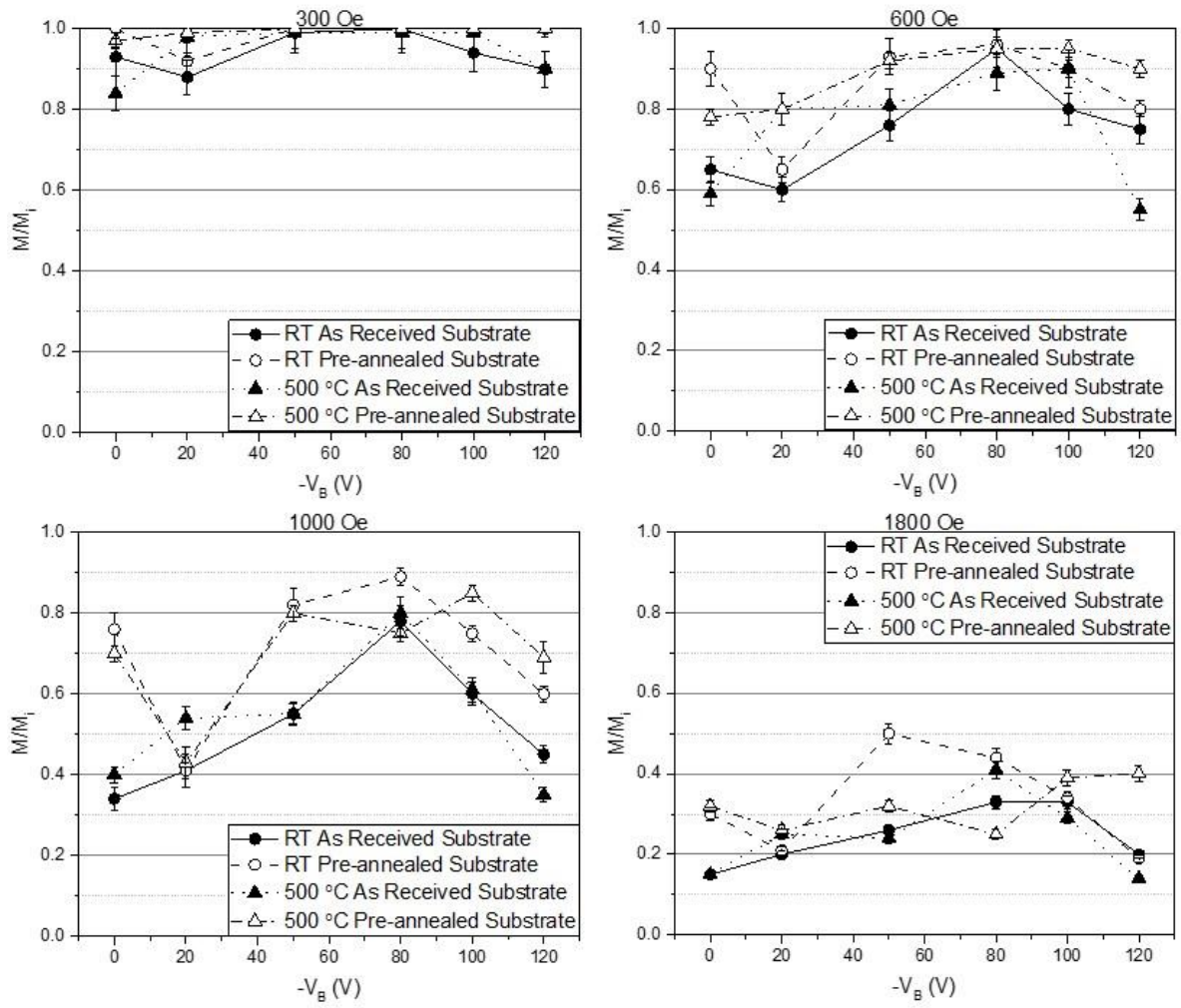


Figure 7.81. Compilation of the measured  $M/M_i$  versus applied bias voltage for niobium thin films at magnetic fields of 300, 600, 1000 and 1800 Oe. The bias voltage of each sample is denoted as  $-V_B$  (V).

### 7.2.3.5. Discussion and conclusions

The results described in section 7.2.3 will now be discussed. In particular, changes in the physical properties of films deposited with similar process conditions onto either as received or pre-annealed substrate will be analysed.

The SEM images show how the film microstructure changes as a function of the substrate preparation, the substrate deposition temperature and applied bias. The films deposited with a grounded substrate all show sub-micron grain size and only a very slight increase in grain size for films deposited at 500 °C when compared to room temperature; there is a small increase in grain size for films deposited onto a grounded and pre-annealed substrate relative to a grounded as received substrate. The films deposited onto pre-annealed substrate with an applied bias of -80 and -120 V display grain structure at scales of hundreds of  $\mu\text{m}$  across. This effect may be a result of the removal of the surface oxide layer from the copper substrate during the pre-anneal process. It has been shown in the literature that niobium films deposited onto oxide free copper surfaces have grain orientations which are decided by the orientation of the copper substrate [129]. It has been assumed that the backscatter SEM detector could not pick out individual niobium grains using channelling contrast because all grains are oriented in the same direction with respect to the underlying copper substrate. The fact that the niobium grains align with the copper grains over areas as large as 100 – 200  $\mu\text{m}$  across allows films to form with enhanced regularity of the lattice structure over larger scales than was observed for films deposited with similar conditions onto as received substrate.

The average grains sizes of films deposited onto pre-annealed substrate, as calculated using equation 5.1, were not consistent with the size of grains shown in the SEM images. This observation was typical of niobium films deposited onto as received copper substrate. It is possible that the small average grain size indicates the polycrystalline film microstructure is made up of both large and very small grains. It is also possible that the films exhibit grazing incidence XRD peak broadening due to the internal strain that is inherent to sputtered films, as already described in section 7.2.2.1.

Films deposited at room temperature onto pre-annealed copper form with stable flux pinning with either no or just one flux jump at bias voltages of -80 to -120 V. All films except for that biased at -20 V demonstrated stable pinning when deposited at 500 °C onto pre-annealed substrate. No films deposited at room temperature and 500 °C displayed stable flux pinning when deposited onto as received substrate. The absence of flux jumps in the DC magnetic moment indicates that the physical film properties are more repeatable when deposited onto pre-annealed substrate, compared to films deposited with similar conditions onto as received substrate.

Films deposited onto pre-annealed substrate display a reduction in  $H_{c2}$  relative to films deposited onto as received substrate for most tested deposition conditions. A relative reduction of

$H_{C2}$  would be expected of a film which had formed with relatively fewer defects or impurities which act as magnetic pinning centres. Thus, films deposited onto pre-annealed substrate are more likely to form with smaller volumes of pinning centres.

The films deposited onto pre-annealed substrate at 500 °C with applied bias voltages of -50 to -120 V displayed the largest RRR of any films deposited during the study; RRR peaked for the film deposited at 500 °C onto pre-annealed substrate with a bias voltage of -80 V, with RRR of 129. There was also an increase in RRR for films deposited at room temperature with applied bias of -80 to -120 V onto pre-annealed substrate relative to as received substrate. The results show that largest increases in RRR corresponds to those films which have grain orientations that have become aligned with the underlying copper substrate. Further, RRR was greatly increase for the films deposited at 500 °C relative to room temperature, suggesting enhanced rates of diffusion which acts to anneal defects within the films grown at the larger temperature.

$M/M_i$  peaked, and was similar for all films deposited with a -80 V bias. In contrast,  $M/M_i$  is larger for films deposited with a wide range of other bias voltages onto pre-annealed substrate when compared to similar conditions onto as received substrate. The enhancement of  $M/M_i$  for films deposited with a wide range of process conditions onto pre-annealed substrate is caused by the same physical processes that were described for the relative increases in RRR.

The only disparity between RRR and  $M/M_i$  results are for the films deposited at room temperature without bias and with -50 V bias onto pre-annealed substrate.  $M/M_i$  is enhanced for both films relative to films deposited with similar conditions onto as received substrate, whereas RRR remained constant. Although  $M/M_i$  was large for both films, they did display unstable flux pinning, and therefore  $M/M_i$  could vary by the magnitude of the flux jumps if the measurement was repeated multiple times. The repeatability of sample properties is discussed in more detail later in this chapter in relation to the observation of the  $a_0$ .

$H_{dev}$  was largest for the film deposited at room temperature with an applied bias of -80 V onto pre-annealed substrate. It was surprising that the film deposited at 500 °C with a bias voltage of -80 V did not have larger  $H_{dev}$  considering that it had by far the largest RRR. That said,  $H_{dev}$  was similar and relatively large for the films deposited on pre-annealed substrate at 500 °C with bias voltage of -50 to -120 V, suggesting a wider peak in  $H_{dev}$  relative to the films deposited at room temperature, and relative to films deposited with similar conditions onto as received substrate. Again, the results suggest that substrate heating to 500 °C result in higher rates of diffusion within growing films deposited onto pre-annealed substrate when compared to films deposited onto as received substrate.

Over the course of the study, there have been a number of instances where films deposited with an applied bias of -80 V have displayed the largest RRR or the largest  $M/M_i$ , and this has been

independent of the substrate preparation. The lengths of  $a_0$  as a function of applied bias may explain why that particular bias voltage is producing favourable results. The study found that the curves of  $a_0$  versus applied bias voltage converge at -80 V for films deposited at both room temperature and 500 °C onto both as received and pre-annealed copper substrate. This result indicates a clear correlation between the distribution in lengths of  $a_0$  and the applied bias voltage, which is not influenced by the initial substrate conditions. The convergence in the length of  $a_0$  for films deposited with a -80 V bias could only occur if there were consistent distributions of defects and internal strain within those films. This result suggests that fewer random complex dislocations are formed with an applied bias of -80 V when compared to the other tested bias voltages. The large variability of the lattice parameter of films deposited with an applied bias of -20 V, and to a lesser extent 0 and -120 V, is evidence that many random complex defects are present within those films. The proposed mechanism which leads to the observed results is that the energy of ion bombardment is increasing from 0 up to -80 V bias, resulting in larger rates of surface diffusion and defect annihilation. Once ion bombardment reaches an energy threshold, at applied bias of between 100 and -120 V, then more random complex defects are formed than are being annihilated. This mechanism is consistent with the observations of RRR and  $M/M_i$ . Thus, the most repeatable physical properties, including  $a_0$ , RRR and  $M/M_i$  should be expected of those films deposited with bias voltages of -50 to -100 V as these films form with the fewest random complex defects. Conversely,  $a_0$ , RRR and  $M/M_i$  may be expected to exhibit the most variability when measured for many films deposited with bias voltage of 0, -20 or -120 V as these films contain relatively more random complex defects.

Finally, 3D Optical microscope images showed that films deposited onto pre-annealed substrate at 500 °C with bias voltages of -80 to -120 V formed with a “blistered” texture at the films surface. Films deposited onto as received copper substrate displayed similar “blisters” when deposited at 500 °C with bias voltage of -80 V and 700 and 800 °C with bias voltage of -80 to -120 V. As was described in section 7.2.2.10, there is no explanation for what is causing the texture to appear at the film surface. The present dataset suggests that the “blisters” only begin to form once the substrate temperature reaches 500 °C and that they are larger and more frequent for the films deposited onto pre-annealed substrate with bias voltages of -80 to -120 V. Further analysis of the films which exhibit “blisters” is still required to fully understand its root cause and what effects it might have on a film used in SRF application.

In conclusion, pre-annealing copper substrate at 700 °C for 12 hours prior to deposition has a large impact on the properties of deposited niobium thin film microstructure. Films that were deposited onto a pre-annealed copper substrate with applied bias of -80 or -120 V appear to have grains that are oriented in a direction that is decided by the underlying copper substrate, whereas

films deposited with similar process conditions onto as received substrate do not. The change in film microstructure resulted in more stable magnetic pinning properties, larger RRR and enhanced  $M/M_i$  for the films deposited onto the pre-annealed substrate relative to the films deposited onto as received substrate.

Films deposited onto pre-annealed substrate that was grounded displayed a small increase in grain size with respect to films deposited with the same process conditions onto as received substrate. The small increase in grain size resulted in smaller increases of RRR and  $M/M_i$  than was observed at the higher bias voltages.

RRR and  $M/M_i$  was larger for films deposited at 500 °C relative to those deposited at room temperature onto pre-annealed substrate, suggesting that thermally induced diffusion within the growing films was significant at the higher temperature. In comparison,  $M/M_i$  was comparable in magnitude for films deposited onto as received substrate at room temperature and 500 °C with the same bias voltage.

RRR peaked at 129 for the film deposited onto pre-annealed copper substrate at 500 °C and with an applied bias of -80 V. Also, all of the films deposited with an applied bias of -80 V at either room temperature or 500 °C had similar  $a_0$  no matter what the substrate preparation conditions. These observations suggest that a bias of -80 V produced films which formed with fewer random complex defects than was observed for films deposited with the other tested bias voltages. It is assumed that ion bombardment increases the rate of surface diffusion and annihilation of lattice defects from a minimum rate for the grounded film, to a high rate at -80 V bias. Ion bombardment becomes too energetic at bias voltages of -100 to -120 V and a net increase in the number of random complex dislocations are formed.

Although the film deposited onto pre-annealed copper substrate at 500 °C with -80 to -120 V bias displayed the largest RRR, had very stable flux pinning and relatively large  $M/M_i$ , those samples also exhibit the unexplained “blisters” at the film surface.

The films deposited onto pre annealed copper substrate at room temperature with an applied bias of -80 V, and at 500 °C with an applied bias of 0 and -50 V all show stable pinning properties, and relatively large RRR and  $M/M_i$ , without the “blistered” texture at the film surface. Therefore, those samples seem the most appropriate for further SRF testing; due to a strong resistance to the onset of flux penetration and stable and repeatable flux pinning properties, without the risk of an undefined physical property.

#### 7.2.4. Comparison of the DC magnetic properties of thin film and bulk niobium

As has already been discussed in section 7.2.2.10, the physical properties of niobium thin films become difficult to predict when deposited at 800 °C onto copper substrate. A-plane sapphire has a much larger melting temperature than copper, 2050 °C when compared to 1085 °C, and was considered as an alternative substrate to test niobium thin film deposition at high temperatures.

A range of samples were deposited onto a-plane sapphire. Samples were deposited by DC magnetron sputtering, pulsed DC magnetron sputtering and HiPIMS with substrate temperatures of 500, 800 and 1000 °C with either a grounded substrate or biased at -80 V DC. The substrate was annealed at 700 °C for 12 hours in each instance before the start of the deposition. Films deposited by HiPIMS were pulsed with the same settings as discussed in section 7.2.2 and 7.2.3 and films deposited by pulsed DC magnetron sputtering were pulsed at 350 kHz with a 50% duty cycle. The power of the pulsed DC and DC power supply was maintained at 400 W for each deposition process. The krypton gas pressure was maintained at  $7 \times 10^{-3}$  mbar during deposition of all films. The aim of this section of the study was to test the properties of films where the high temperature thermal stresses at the interface between film and substrate should be at a minimum.

**Table 7.4. Niobium thin film samples deposited at a range of deposition temperatures and bias voltage using either the HiPIMS, DC or pulsed DC power supply.**

<b>Power Supply</b>	<b>Temp (°C)</b>	<b>Bias (-V)</b>	<b>RRR</b>
HiPIMS	800	0	150
Pulsed DC	800	0	117
DC	800	0	47
HiPIMS	800	80	229
Pulsed DC	800	80	86
DC	800	80	18
HiPIMS	500	0	124
Pulsed DC	500	0	172
DC	500	0	10
HiPIMS	500	80	13
Pulsed DC	500	80	121
DC	500	80	218
HiPIMS	1000	0	145
Pulsed DC	1000	0	45
DC	1000	0	43
HiPIMS	1000	80	51
Pulsed DC	1000	80	190
DC	1000	80	146

Only RRR was measured for every deposited film and is described in table 7.4. It was expected that there would be a systematic increase in RRR as the deposition temperature increased. However, this was not observed. RRR does not always increase with temperature when other deposition parameters remain the same and there is no correlation which shows that ion bombardment consistently affects RRR; all what would be expected from the findings of the study of niobium films deposited onto copper substrate. There has not been enough time remaining on the research project to fully investigate the reasons for the random distribution of RRR values for films deposited onto a plane sapphire substrate. The most obvious causes of the seemingly random nature of the measured RRR are inconsistent cleaning of each sample substrate before deposition, inconsistent substrate temperatures during deposition, inconsistent process gas pressures during deposition, an atmospheric leak into the vacuum system or error in the measurement of RRR. However, the cleaning procedure was consistent with all samples deposited previously. Process gas pressure and residual gas pressures were all monitored regularly during each deposition, showing no irregularities.

Error in the measurement of RRR was ruled out as a source of the unexpected results as repeated measurements were always consistent.

It is still possible to take some useful information from the seemingly random set of sample properties. The sample with the largest RRR of 229 was deposited by HiPIMS onto a-plane sapphire at 800 °C with a -80 V DC bias and had the smallest normal state resistance, at 0.0006 mΩ, of any sample during the study (figure 7.82). The resistance versus temperature curve shows a  $T_C$  of  $9.32 \pm 0.02$  K.

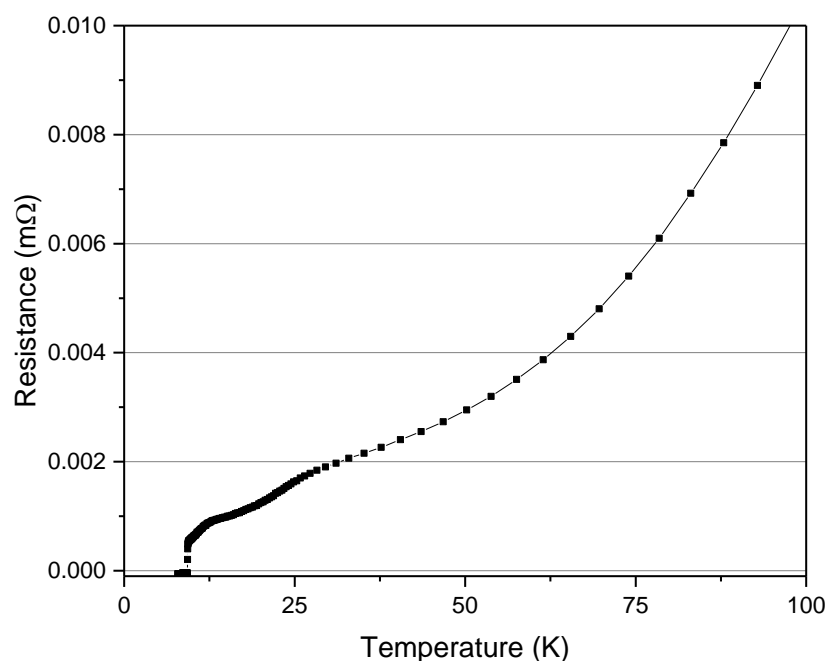


**Figure 7.82.** Resistance versus temperature for a niobium thin film deposited onto a-plane sapphire at 800 °C with -80 V DC bias. Sample displayed the smallest normal state resistance of any sample tested during the study at 0.0006 mΩ.

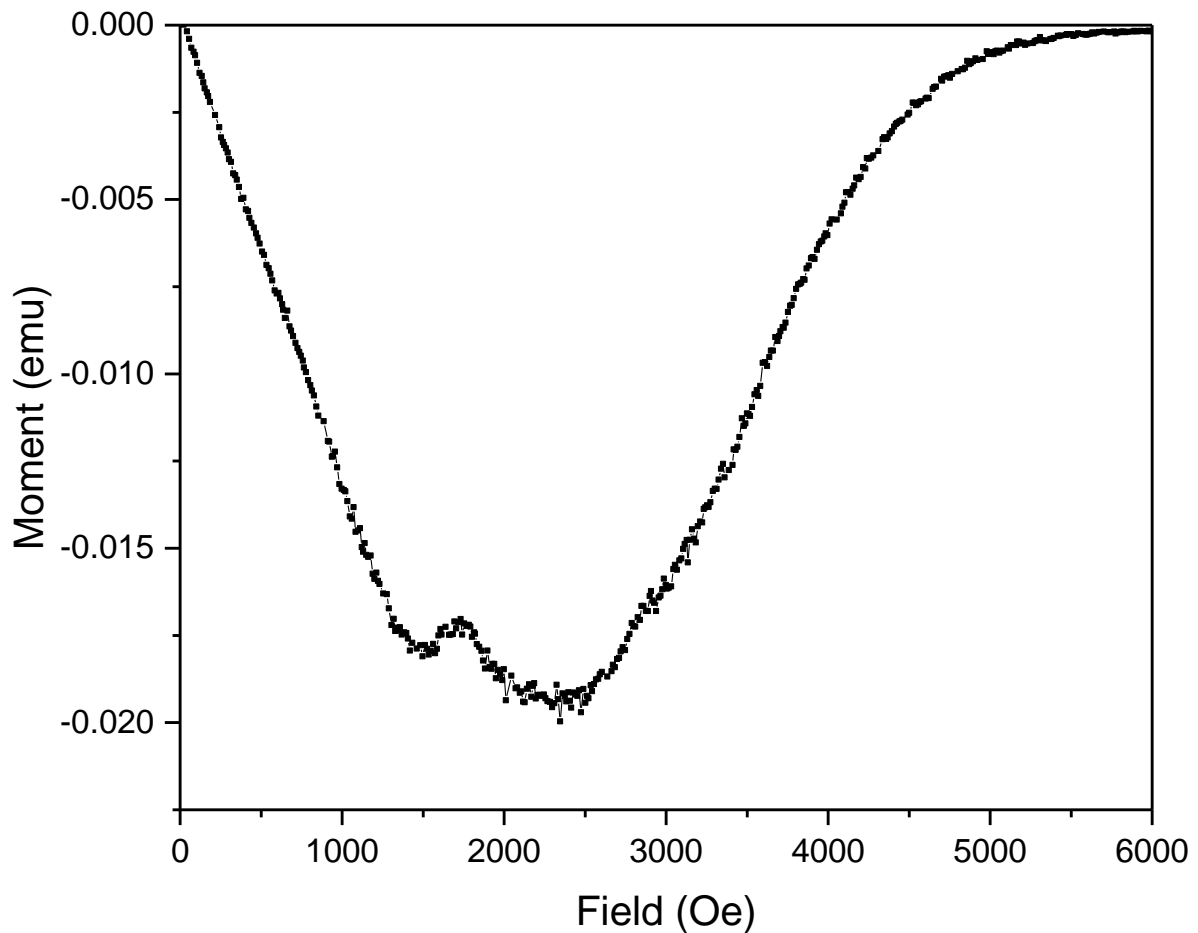


Figure 7.83. DC magnetic moment versus applied magnetic field of a niobium film with RRR of 229 deposited onto a-plane sapphire.

The thin film sample with the largest RRR was later measured by DC magnetometry at 4.2 K and is shown in figure 7.83. The most notable feature of the DC magnetic measurement is that  $H_{dev}$  extends to higher magnetic fields than for any other niobium film deposited during the study, at  $1200 \pm 60$  Oe. The  $M/M_i$  curve of the same film is shown in figure 7.84, also shown is the film with largest  $H_{dev}$  of the films deposited onto copper substrate and a theoretical line depicted the  $M/M_i$  of a bulk niobium sample with  $H_{dev}$  of 1800 Oe and  $H_{C2}$  of 2800 Oe, as has been reported in the literature [116]. For reference, the copper substrate sample was deposited at 700 °C with -80 V DC bias.

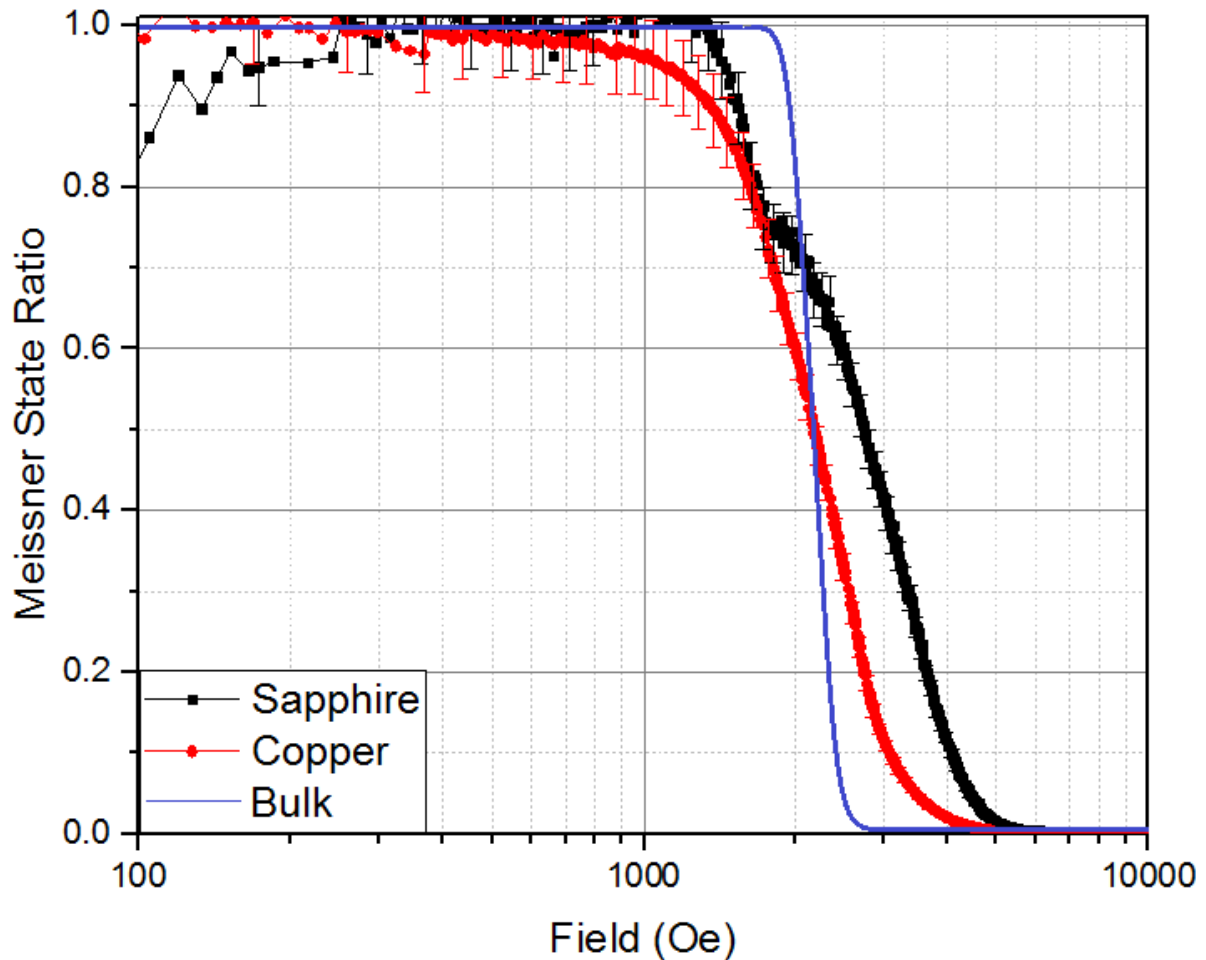


Figure 7.84.  $M/M_i$  versus applied magnetic field of niobium thin films deposited onto both sapphire or copper substrate and a theoretical line for a bulk niobium sample.

$M/M_i = 1$  up to fields of 1200 Oe for the niobium thin film on sapphire, 800 Oe for the film deposited onto copper and then 1800 Oe for the bulk material. The two films shown have sharper transitions from Meissner state to normal conducting than any of the other deposited films, but each transition is still much broader than would be expected of the bulk material. The cause of the extended mixed superconducting / normal conducting state within the film is trapped flux at either defects or impurity pinning locations.

A type II superconductor with large grains, small volumes of grain boundaries and few defects within the grain interior, such as the bulk niobium used for SRF cavity fabrication [130], would first allow Josephson vortices to penetrate and be pinned at grain boundaries. The magnetic field which is pinned at the grain boundaries then puts pressure on the grain interior. Once Abrikosov vortices begin to enter the grain interior then they move relatively easily due to the lack of pinning centres.  $H_{C2}$  in this instance is small and the transition from Meissner state to normal conducting is sharp.

Thin films deposited by magnetron sputtering inherently form with large volumes of grain boundaries and defects and interstitial impurities within the grain interiors [37, 2]. Even the highest quality niobium thin films deposited during this study are type II superconductors with large volumes of grain boundaries and internal strain related to either defects or the presence of impurity atoms. Josephson vortices still penetrate the thin films first at the grain boundaries but when the Abrikosov vortices enter the grain interior they can become pinned and  $H_{C2}$  becomes large.

The investigation suggests that the niobium thin films which have been tested cannot replicate the DC magnetic properties of bulk niobium. Although  $H_{dev}$  has been shown to be influenced by sample geometry for a thin film sample and could be a function of early flux penetration due to alignment with the applied magnetic field,  $H_{C2}$  has always been above 4000 Oe for every deposited thin film. Thus, the transition from Meissner state to  $H_{C2}$  could never be as sharp for any of the deposited films as would be expected for a bulk niobium sample. This phenomenon is most likely a result of the smaller grain size, internal film strain and higher concentrations of impurities within grain interiors when compared to bulk niobium. All of which are typical properties of films deposited by magnetron sputtering techniques.

### 7.2.5. RF surface resistance measurements of niobium thin films deposited by HiPIMS onto as received polycrystalline copper

Only two flat niobium thin film samples have been deposited and tested for their RF surface resistance. There are very few facilities in the world that are capable of performing such measurements and therefore access is limited. It should be stressed that the samples which were measured for their RF surface resistance were deposited at a time when the option to test them was made available; but which was before the process development of niobium thin films had been completed. Therefore, the deposition conditions used to produce the samples were not optimal when considering the conclusions discussed in the remainder of this report.

Samples were measured by J. T. Maniscalco using the sample host cavity at Cornell University. The host cavity is discussed in detail in [131]. Flat superconducting samples are disks with a diameter of 5 inches and thickness of 3 mm. The cavity allows a 4 GHz RF magnetic field up to 100 mT to be applied to the surface of the sample whilst  $R_S$  is measured.  $R_S$  is calculated using equation 7.3 where  $Q_{0.calib}$  is the component of the calibration quality factor corresponding to the cavity when a bulk niobium calibration disk is measured,  $Q_{sam.calib}$  is the component of the sample calibration Q factor corresponding to the bulk niobium calibration disk and  $Q_{sam}$  is the component of the experimental Q factor when a thin film sample is measured.

$$R_S = \frac{G}{Q_{0.calib}} \frac{Q_{sam.calib}}{Q_{sam}} \quad (7.3)$$

The area of each sample disk which is exposed to the RF field has a diameter of approximately 10 cm. Thermometers are used to produce a temperature map of the sample during the RF measurement and can therefore determine if the sample quenches due to local heating at defects.

Samples substrates were as received polycrystalline copper disks which were diamond turned to produce a mirrored surface with RA of 10 nm. The samples were then cleaned in ultrasonic baths of acetone and then isopropanol before being rinsed with deionised water using a high pressure rinse. The sample was finally blown dry using filtered compressed air. No clean room facilities were in place to transfer the sample to the deposition system. However, any dust visible by eye at the substrate surface was blown away using dry nitrogen gas before sample insertion. All HiPIMS deposition settings remained similar to those in sections 7.2.2 and 7.2.3.

The variable parameters of the experiment were the substrate temperature and the applied substrate bias. One sample was deposited at a substrate temperature of 500 °C with an applied DC bias of -100 V and one sample with a grounded substrate at 800 °C. Again, the parameters used were not optimal considering the conclusions of sections 7.2.2 and 7.2.3. However, the plan at the time of

the experiment was to deposit one film at high temperature then deposit a second film at a lower temperature with an applied substrate bias and see if the resulting films were comparable.

$R_S$  as a function of the applied magnetic field strength is shown for the sample deposited at 800 °C in figure 7.85. The sample was measured at 1.6 K and displayed very large  $R_S$  of 4  $\mu\Omega$ . The quench field of the superconductor was very small at 25 mT.

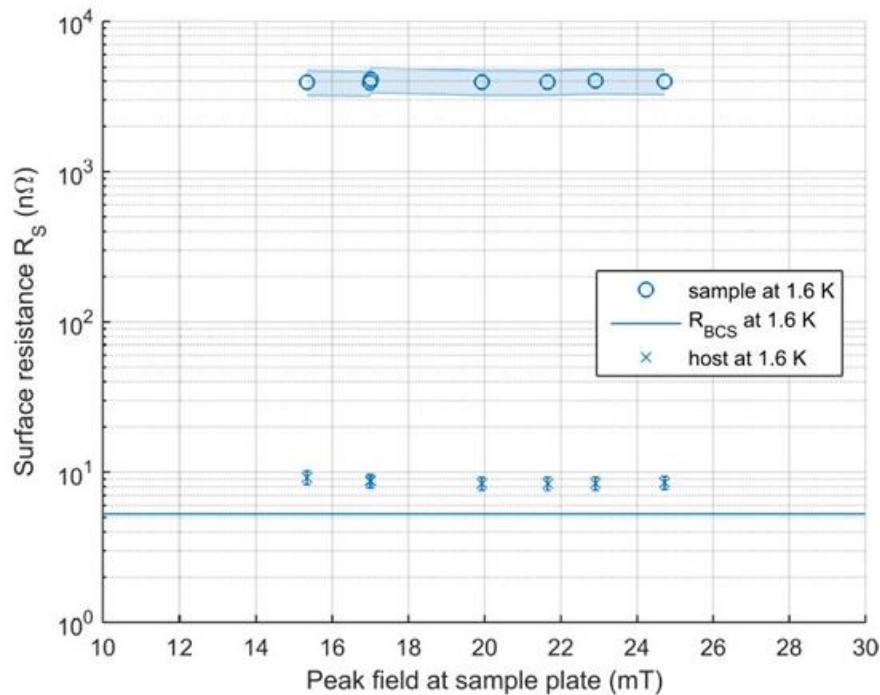


**Figure 7.85.**  $R_S$  versus magnetic field strength of a flat thin film niobium sample which was deposited at 800 °C with a grounded substrate.  $R_S$  of the host cavity and the predicted  $R_{BCS}$  of niobium at 1.6 K are also shown (measurement performed by J.T. Maniscalco, Cornell University).

$R_S$  as a function of the applied magnetic field strength is shown for the sample deposited at 500 °C with an applied substrate bias of -100 V in figure 7.86. The sample was measured at both 1.6 and 1.8 K.  $R_S$  at 1.8 K increases from 100 nΩ at 10 mT up to 200 nΩ at 55 mT, at which point the sample quenched. However, the error in the measurement of the sample at 1.8 K was very large. The large error was systematic during the measurement as the  $R_S$  of the host cavity itself was larger than expected.  $R_S$  at 1.6 K increased linearly from 200 nΩ at 15 mT to 300 nΩ at 60 mT, before a sharp increase in  $R_S$  up to 750 nΩ at 90 mT, where the sample quenched. The  $R_S$  of the host cavity was smaller at 1.6 K than at 1.8 K therefore the systematic error for the measurement of the thin film at 1.6 K was reduced with respect to the measurement performed at 1.8 K.

A temperature map was made for only the sample deposited at 500 °C with -100 V bias and is shown in figure 7.87. The temperature map showed that one thermometer displayed a temperature increase of up to 0.1 K, whereas all others increased by no larger than 0.02 K. The localised spike in

temperature is characteristic of a film that has quenched due to induced heating at a surface defect as the RF power is increased.

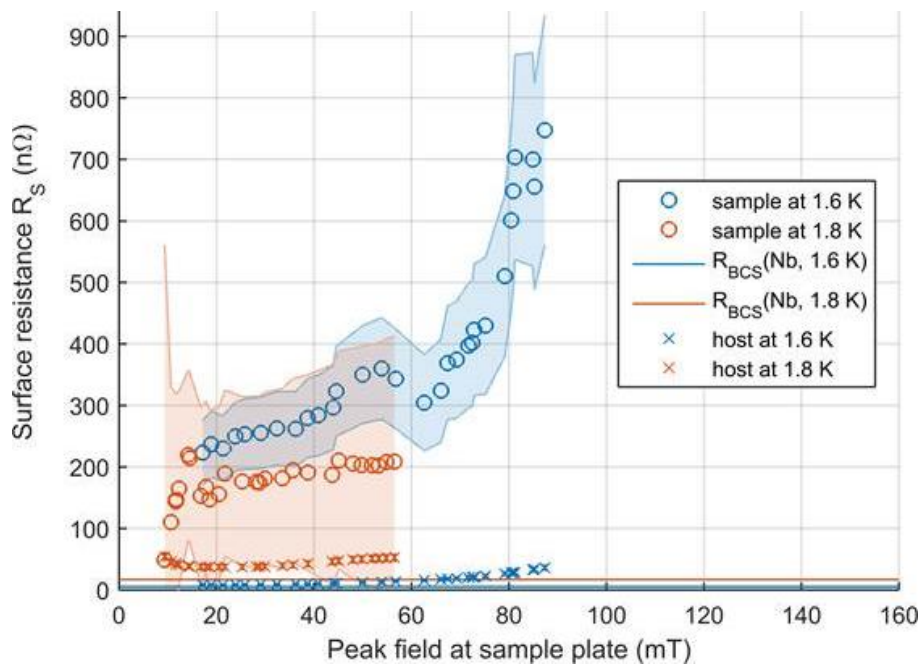


Figure 7.86.  $R_s$  versus magnetic field strength of a flat thin film niobium sample which was deposited at 500 °C with -100 V substrate bias.  $R_s$  of the host cavity and the predicted  $R_{BCS}$  of niobium at 1.6 K and 1.8 K are also shown (measurement performed by J.T. Maniscalco, Cornell University).

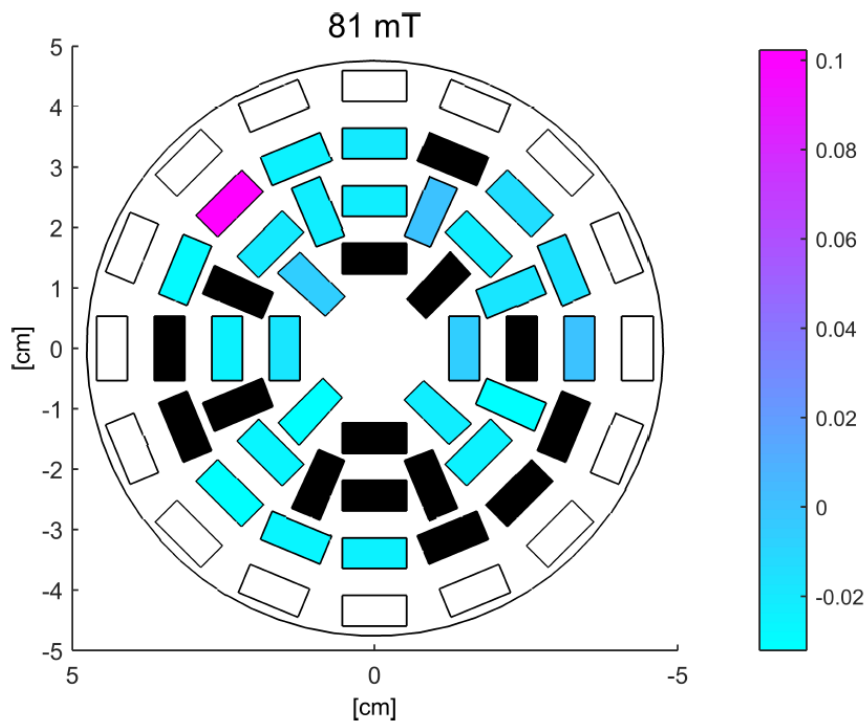


Figure 7.87. Temperature map during RF surface resistance test of flat thin film niobium sample which was deposited at 500 °C with -100 V substrate bias (measurement performed by J.T. Maniscalco, Cornell University).

It is difficult to make useful comparisons between the two measured samples due to the large disparity in  $R_s$ . The sample deposited at 800 °C displayed by far the largest  $R_s$  and smallest quench field. The poor RF performance should not come as too much of a surprise when relating to the DC magnetic measurements discussed in section 7.2.2 where the film deposited at 800 °C onto a grounded substrate displayed the smallest  $M/M_i$  of any sample tested during the study. The average  $M/M_i$  was much larger for the sample deposited at 500 °C with -100 V bias onto as received copper substrate. This would suggest that the sample deposited at 500 °C with -100 V bias was more resistant to flux entry and therefore should have the smallest  $R_s$ , as was observed. It is difficult to say that there is a true relation between the DC magnetic measurements and  $R_s$  as too few RF measurements were performed. Also, the findings of the temperature map suggest that local surface heating at a point defect has also contributed to  $R_s$ . The nature of the defect is as yet unknown; there was no noticeable defect at the sample surface.



## 8. Superconducting materials other than niobium

This section of the report focuses on the deposition of materials other than niobium. As discussed in chapters 2 and 4, superconductors with  $T_C > T_C^{Nb}$  have been shown to have a lower  $R_{BCS}$  than niobium at 4.2 K because  $R_{BCS} \propto e^{-T_C/T}$  [6]. Thus, the deposited thin films described in this chapter would be suitable for use as a single superconducting layer, or as part of an SIS multilayer, for SRF cavity application at 4.2 K.

### 8.1. Niobium Nitride thin films

Equation 4.1 shows that materials for use in SIS multilayers should have small  $\xi$  so that  $B_{C1}$  can be enhanced for a layer that is thinner than  $\lambda_0$ . Thus, niobium nitride is an appropriate candidate for use in an SIS multilayer as it has a relatively small  $\xi$  of 3 - 5 nm and has a large  $\lambda_0$  of 200 - 350 nm. For comparison, niobium has  $\xi$  of 36 nm and  $\lambda_0$  of 40 nm.

#### 8.1.1. Deposition of niobium nitride thin films

Films were deposited by reactive HiPIMS in a mixture of krypton and nitrogen gas at a pressure of  $7 \times 10^{-3}$  mbar. Films were deposited onto a grounded silicon (100) substrate that was maintained at 600 °C and continuously rotated at 4 rpm. The target of the magnetron was 99.95 % purity niobium and was maintained at 150 mm from the substrate surface. The variable parameter during the experiment was the composition of the process gas. The nitrogen partial pressure was varied between 11 and 22 %. The nitrogen partial pressure was adjusted for each deposition by changing the ratio of krypton and nitrogen that was let into the deposition chamber through a pair of mass flow controllers.

The HiPIMS power supply was set to pulse at 1000 Hz with a 50  $\mu$ s pulse length for each deposition. A short pulse length and high repetition rate was chosen to ensure that a stable plasma could be maintained at the target surface. Longer pulses with smaller repetition rates were tested but the plasma was unstable or even stopped altogether after only a few seconds of operation. The plasma instabilities were assumed to be due to insufficient voltage being applied to the target surface once too thick a nitride layer had formed.

#### 8.1.2. Analysis of deposited niobium nitride thin films

Each deposited film was measured using the four-point probe to provide a resistance versus temperature curve. Figure 8.1 shows the resistance versus temperature curves between 0 and 100 K for niobium nitride films deposited with nitrogen partial pressures ranging 11 to 22 %. The resistance was measured using a DC current of 1 mA. The largest normal state resistance at just above  $T_C$  of 8.5 m $\Omega$  occurred for the sample deposited in an 11 % nitrogen partial pressure, the smallest normal state

resistances of 3.7 and 3.8 mΩ occurred for the samples deposited in 21 and 14 % nitrogen partial pressures respectively.

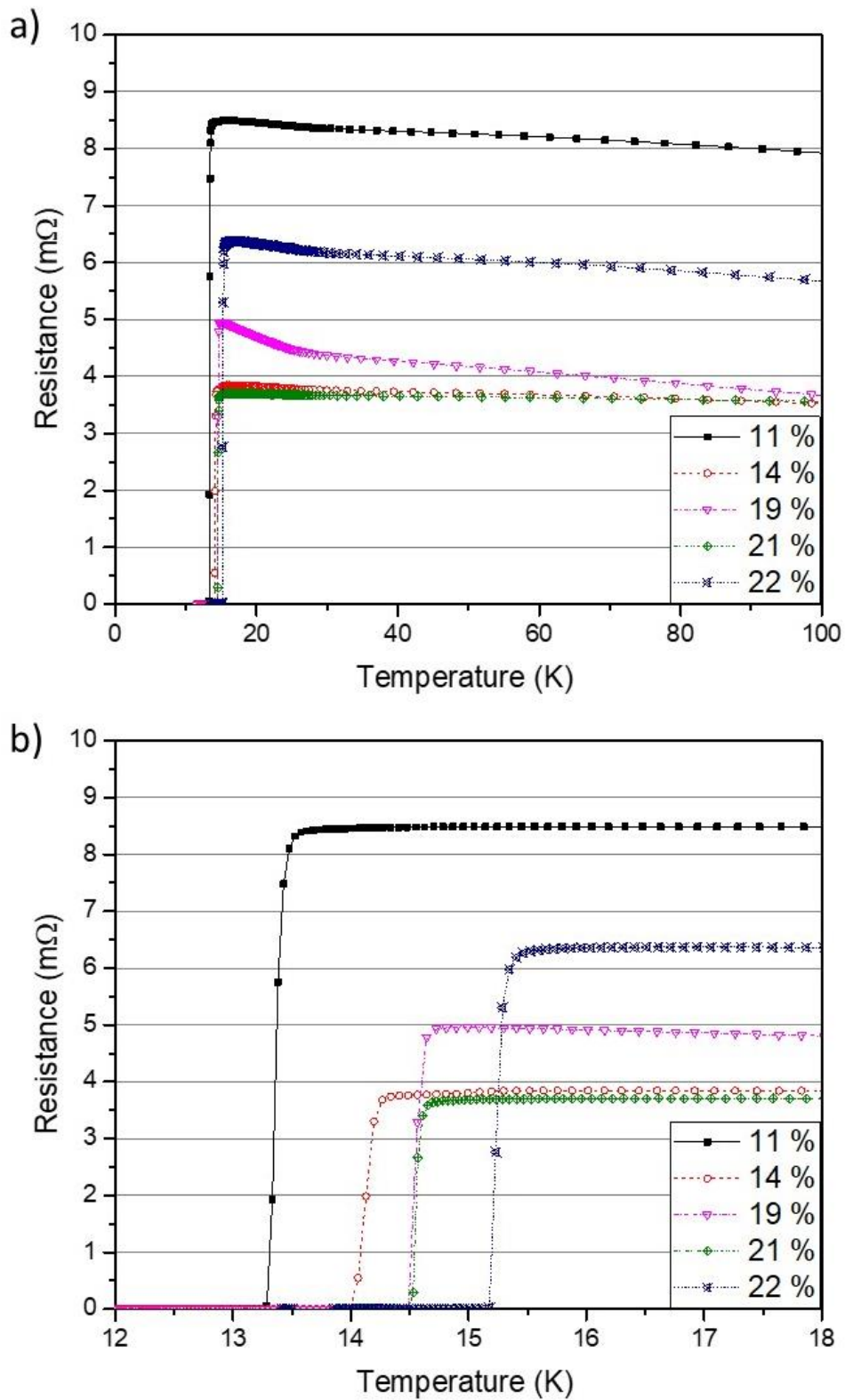


Figure 8.1. Resistance versus temperature curves for niobium nitride thin films deposited with a range of nitrogen partial pressures. a) displays the curve between 0 and 100 K whilst b) displays the superconducting transition.

Every tested niobium nitride sample displayed a normal state resistance which was inversely proportional to the sample temperature, with the steepest gradients for the samples deposited with 11, 19 and 22 % nitrogen partial pressure. No consistent trends appear to link the magnitude of the normal state resistance to the nitrogen partial pressure.

$T_c$  was taken from the resistance versus temperature curves and increased with nitrogen partial pressure, as shown in figure 8.2. All  $T_c$  measurements were taken as the onset of the superconducting state where the resistance of the sample was at approximately 90 % of the normal conducting state [114]. The smallest  $T_c$  of the tested samples was  $13.48 \pm 0.03$  K and occurred for the sample deposited with a nitrogen partial pressure of 11 %, while the largest  $T_c$  of  $15.35 \pm 0.03$  K was measured for the sample deposited in a nitrogen partial pressure of 22 %.

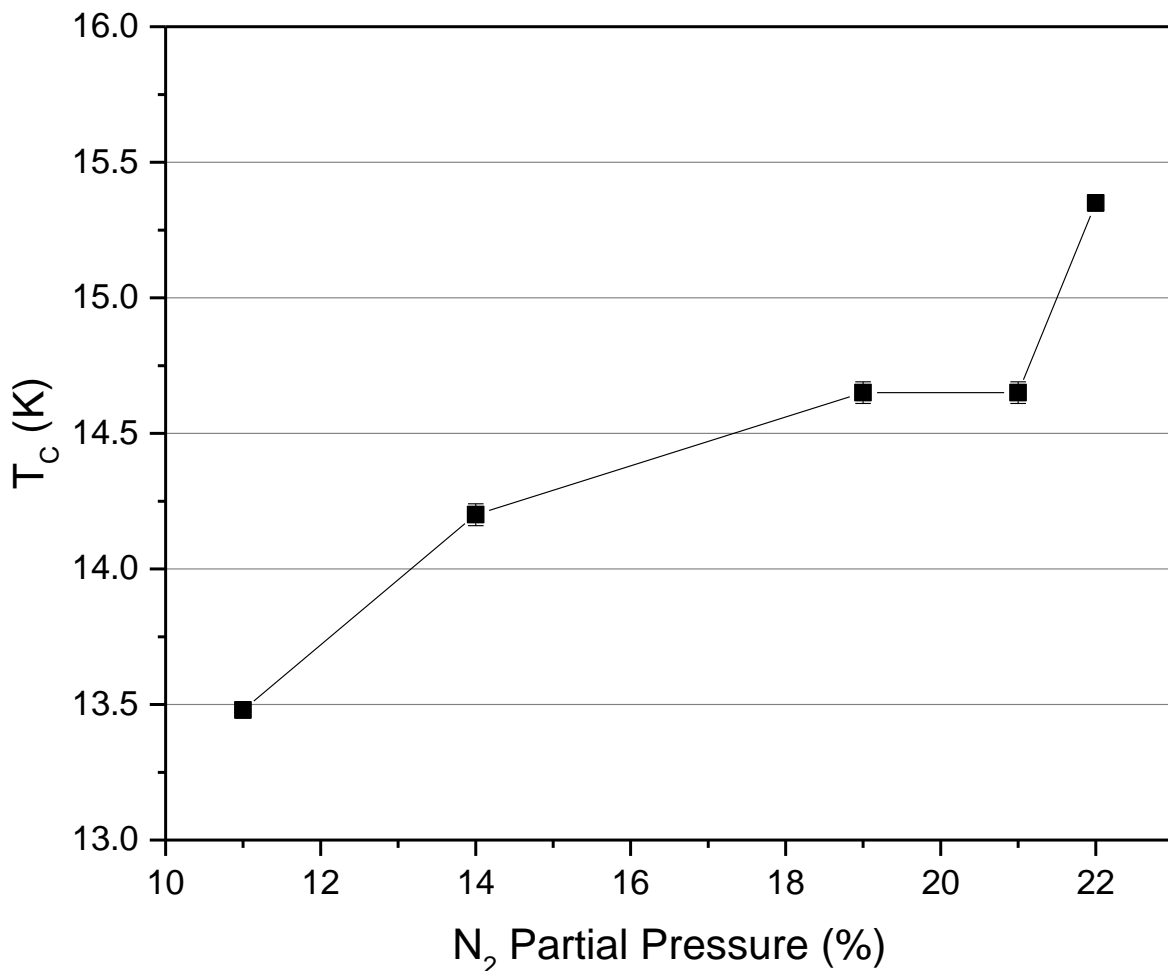


Figure 8.2. The  $T_c$  of niobium nitride thin films deposited with varying nitrogen partial pressure.

Figure 8.3 shows an XRD spectrum of the niobium nitride film which exhibited the largest  $T_c$ . XRD measurements in this chapter of the report were performed using a copper x-ray source to produce x-rays with  $K\alpha_1$  wavelength of  $1.54056 \text{ \AA}$ . The spectrum shows only a single peak at  $35.44^\circ$  and denotes the (111) cubic structure typical of high  $T_c$  niobium nitride [133]. The same film was also

imaged by SEM using a back-scatter detector and is shown in figure 8.4. The image shows columnar grains with many voids. The thickness of the film in figure 8.4 is approximately 1.5  $\mu\text{m}$  implying the resistivity to be  $800\pm 200 \mu\Omega\text{cm}$ .

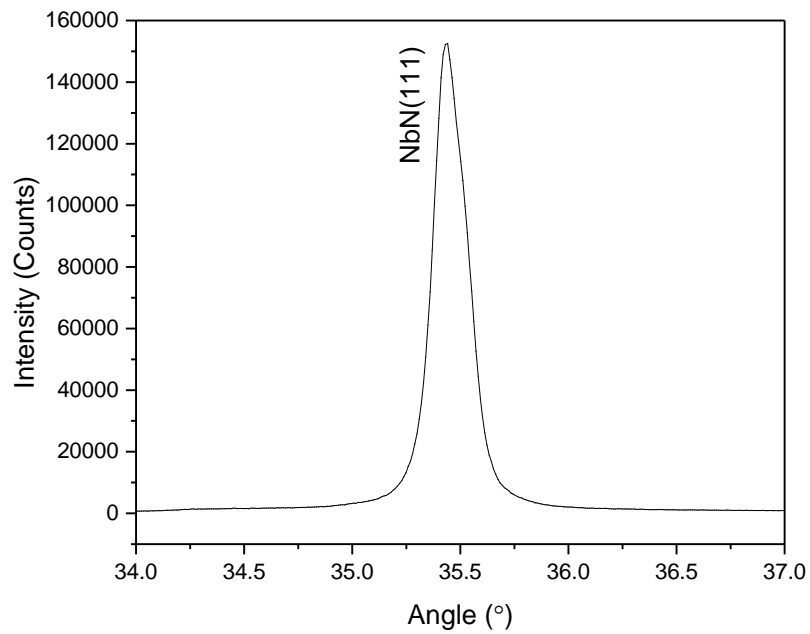


Figure 8.3. XRD data for a niobium nitride thin film with the largest measured  $T_c$  of  $15.35\pm 0.03$  K.

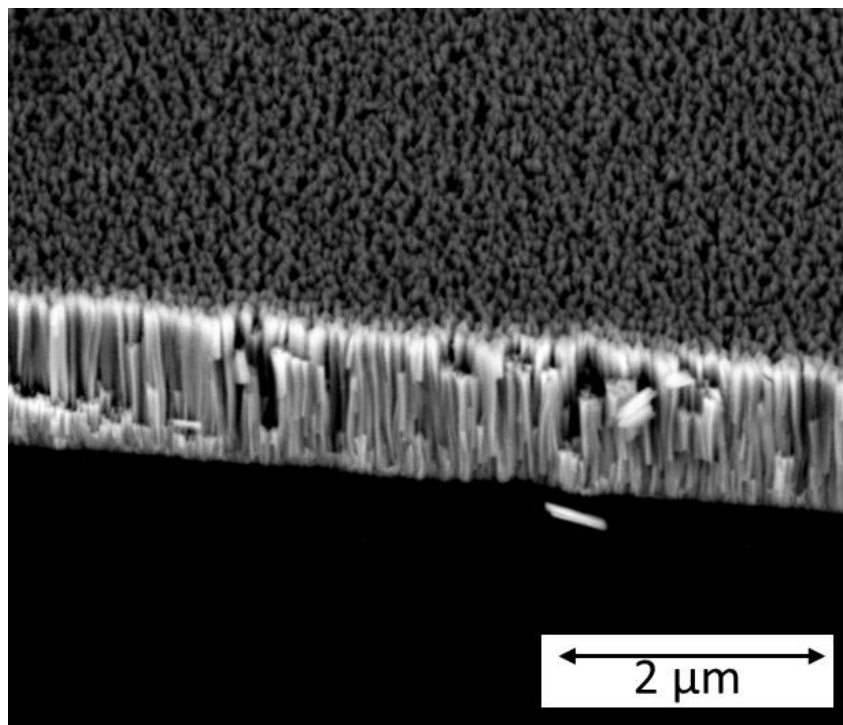


Figure 8.4. SEM image of a niobium nitride thin film with the largest measured  $T_c$  of  $15.35\pm 0.03$  K.

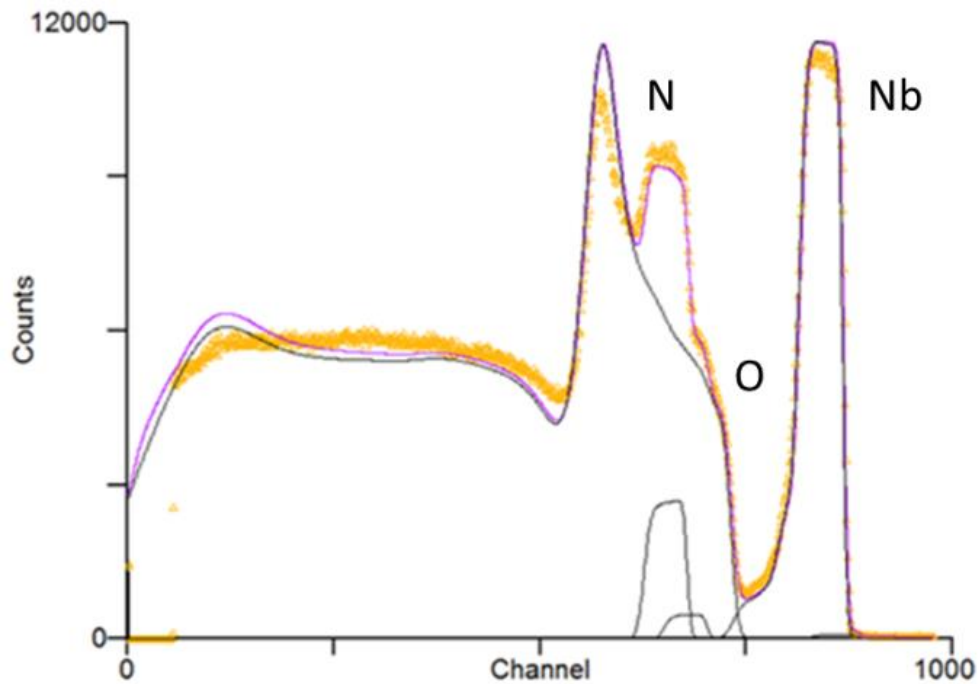


Figure 8.5. Rutherford backscattering spectroscopy data showing the elemental composition of the niobium nitride film with the largest  $T_c$ . Measurement was performed using a hydrogen beam with  $10^\circ$  angle of incidence,  $165^\circ$  scattering angle and  $25^\circ$  exit angle (measurement performed by E. Alves and N.P. Barradas, Lisbon, Portugal).

A perfect niobium nitride crystal should contain both 50 at.% niobium and 50 at.% nitrogen. However, an RBS measurement of the sample with the largest  $T_c$  showed that the elemental composition was 47.5 % niobium, 42.6 % nitrogen and 9.9 % oxygen. The RBS measurement was performed by E. Alves and N.P. Barradas at Lisbon, Portugal, and is shown in figure 8.5 where the yellow data points are the raw data, the purple line was fitted to the data after the measurement and the grey lines relate to the deconvoluted signal from the elemental composition. The oxygen was attributed to ex-situ oxidation of the porous columnar structure. Niobium nitride  $T_c$  has been strongly linked to nitrogen stoichiometry [88]. Thus, the depleted nitrogen content may have suppressed the  $T_c$  of the samples.

A search of the literature shows that niobium nitride thin films deposited by reactive DC magnetron sputtering typically form with an equiatomic composition of niobium<sub>0.987</sub> / nitrogen<sub>0.987</sub>; a 1:1 ratio of niobium to nitrogen is not formed due to vacancies in the sub-lattice of the film and results in high resistivity [132]. Thus, the niobium nitride films deposited by reactive HiPIMS and presented in this study display physical properties that are consistent with those deposited by reactive DC magnetron sputtering. The large normal state resistivity suggests the material would have large  $R_{BCS}$  and may be unsuitable for SRF application.

## 8.2. Niobium Titanium Nitride thin films

Niobium titanium nitride has been suggested as an alternative to niobium nitride as it has much smaller normal state resistivity, reported as low as  $37 \mu\Omega\text{cm}$ , and therefore would be expected to display small  $R_{BCS}$  at 4.2 K. The  $T_C$  of niobium titanium nitride is 17.3 K,  $\xi$  is 5 nm and  $\lambda_0$  is 150 - 200 nm [17].

### 8.2.1. Varying nitrogen partial pressure

Niobium titanium nitride films were deposited by dual magnetron sputtering. One magnetron, fitted with a 99.95 % niobium target, was powered by the HiPIMS power supply. A second magnetron, fitted with a 99.99 % titanium target, was powered by the pulsed DC power supply. Both targets were maintained at 150 mm from the substrate surface. The HiPIMS power supply was set to pulse with a repetition rate of 1000 Hz with 50  $\mu\text{s}$  pulse length whilst the pulsed DC supply was set to pulse at 350 kHz with a 50 % duty cycle. Films were deposited with a constant current of 590 mA supplied to the niobium cathode and 960 mA supplied to the titanium cathode. Other process conditions were similar to those used to deposit the niobium nitride films in section 8.1; the process gas was a mixture of krypton and nitrogen at  $7 \times 10^{-3}$  mbar and the silicon (100) substrate was heated to 600 °C. Similarly, the nitrogen partial pressure was varied between 11 and 21 % across the set of deposited samples.

Each deposited sample was measured using the four-point probe with a current of 1 mA. Figure 8.6 displays the resistance versus temperature data for the niobium titanium nitride films. The resistance versus temperature curves suggest that the normal state DC resistance of the niobium titanium nitride is inversely proportional to the nitrogen content for all partial pressures that were tested. The resistance measured across the four-point probe reduced with increasing nitrogen partial pressure from a maximum of 19.5 m $\Omega$  at 11 % nitrogen down to 0.4 m $\Omega$  at 21 % nitrogen.

Samples showed no superconductivity when deposited with a nitrogen partial pressure of 11 %. Samples were superconducting at a partial pressure of 14 % nitrogen upwards to 21 % and the maximum  $T_C$  of  $16.67 \pm 0.01$  K occurred at 20 % (Figure 8.7). The shape of the  $T_C$  versus nitrogen partial pressure curve displays a plateau where  $T_C$  did not vary by more than 0.3 K between nitrogen partial pressures of 17 and 21 %.

Figure 8.8 displays a cross sectional SEM image of the niobium titanium nitride sample with the largest  $T_C$ , deposited with a 20 % nitrogen partial pressure. The SEM image showed the film thickness to be  $350 \pm 30$  nm. Measurement of the film thickness allowed the resistivity of the sample to be calculated at  $45 \pm 7 \mu\Omega\text{cm}$ .

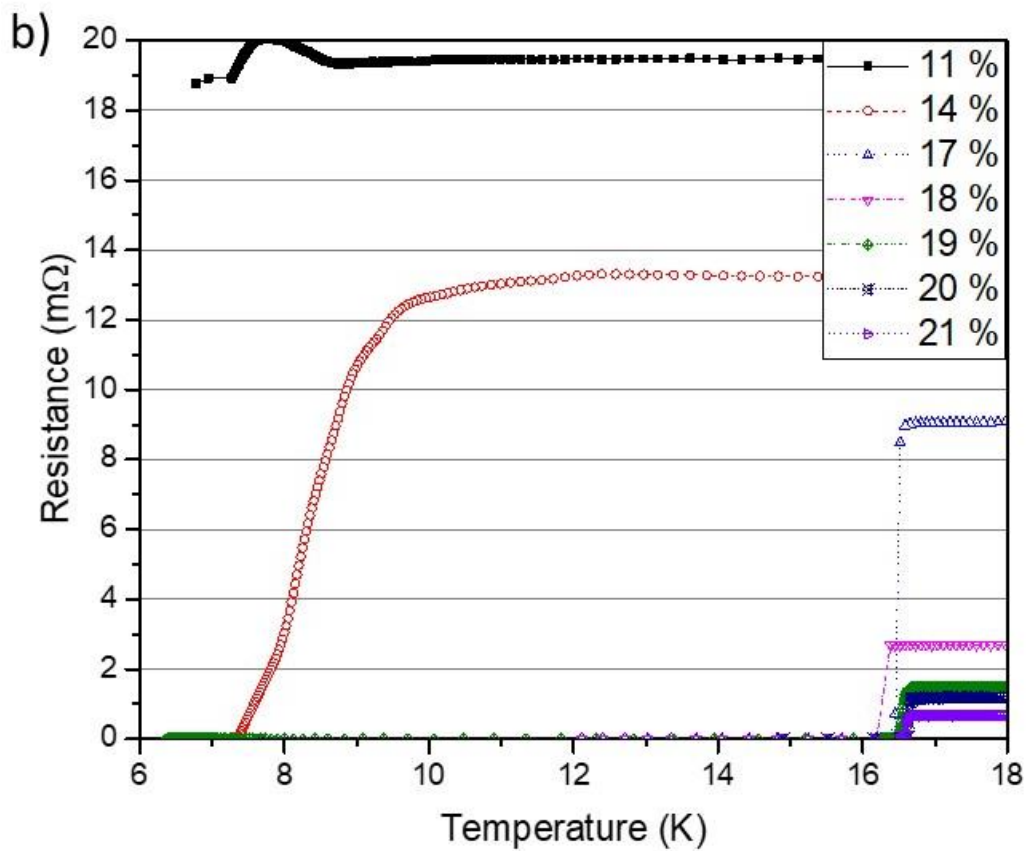
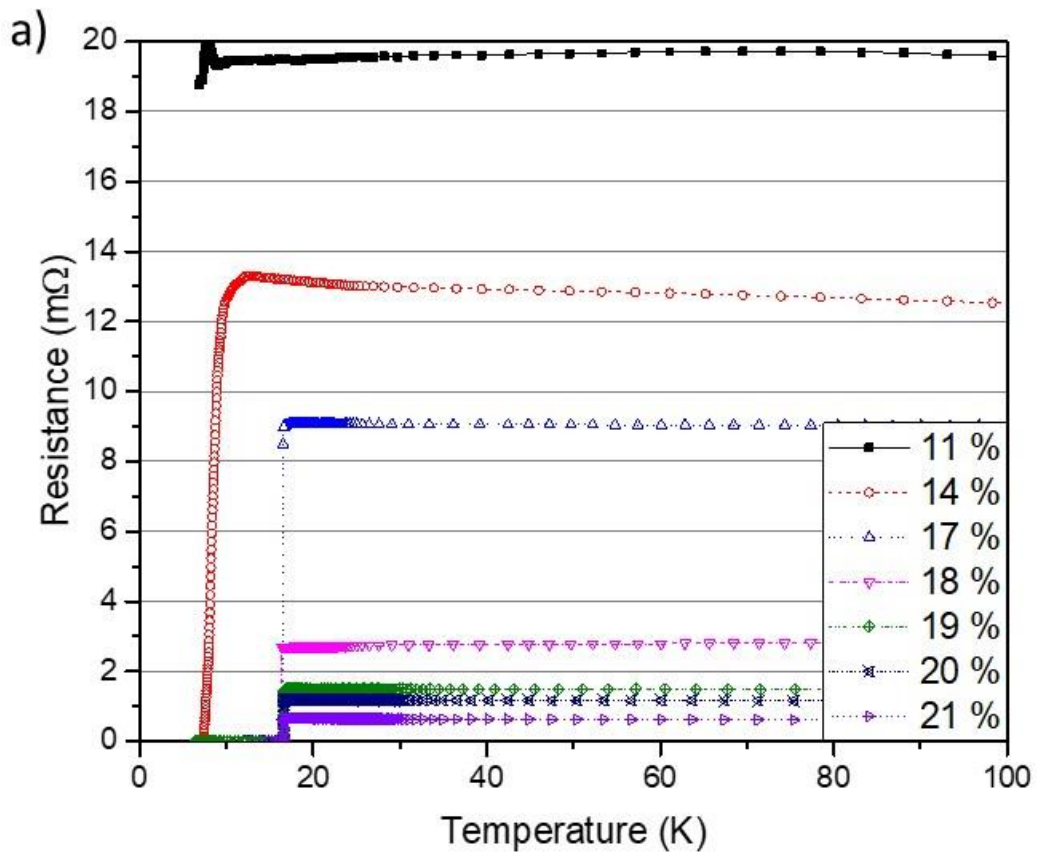


Figure 8.6. Resistance versus temperature curves for niobium titanium nitride thin films deposited with a range of nitrogen partial pressures. a) displays the curve between 0 and 100 K whilst b) displays the superconducting transition.

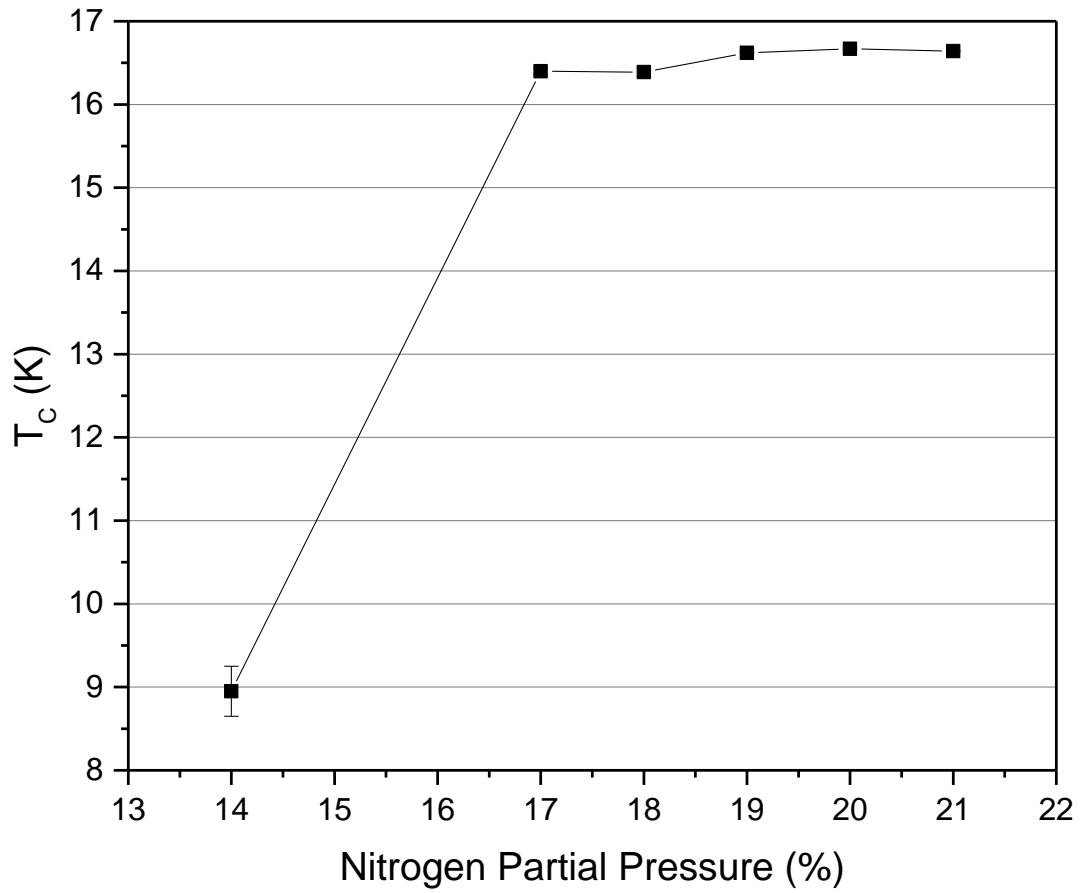


Figure 8.7. The  $T_c$  of niobium titanium nitride thin films with varying nitrogen partial pressure during deposition.

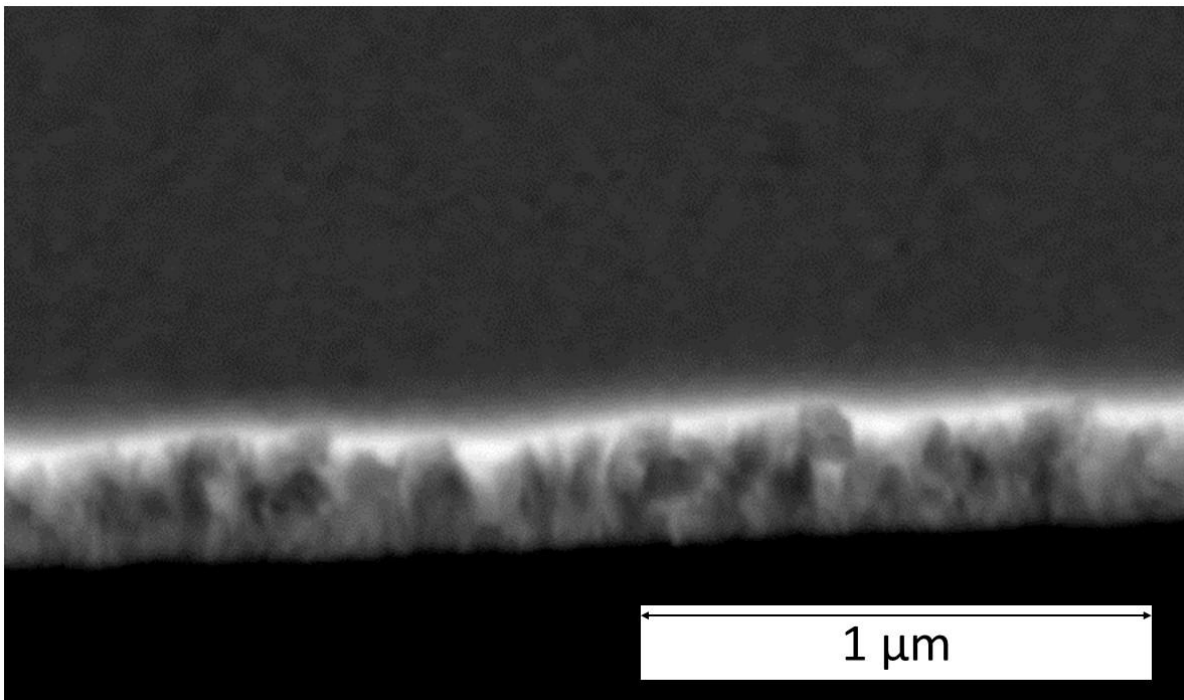


Figure 8.8. SEM image of a niobium titanium nitride thin film deposited with a niobium cathode current of 590 mA, a titanium cathode current of 960 mA and a nitrogen partial pressure of 20 %.  $T_c$  of the sample was  $16.67 \pm 0.01$  K.

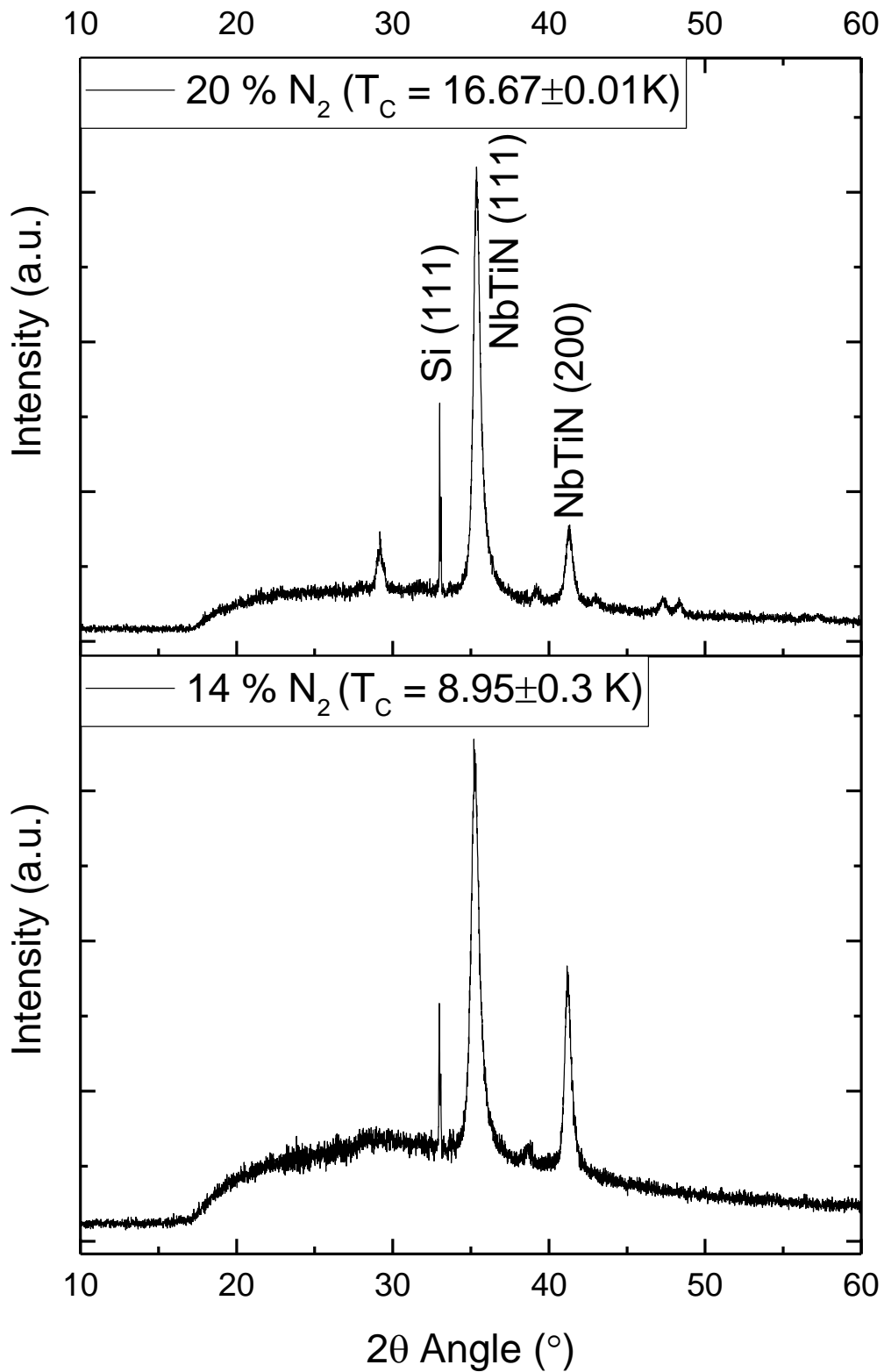


Figure 8.9. XRD data for niobium titanium nitride thin films deposited with a niobium cathode current of 590 mA, titanium cathode current of 960 mA and nitrogen partial pressure of either 14 or 20 %.

Only two niobium titanium nitride thin films were analysed using XRD; the measurements are shown in figure 8.9. The samples were deposited with constant niobium cathode current of 590 mA, constant titanium cathode current of 960 mA and either 14 or 20 % nitrogen partial pressure. Each

XRD measurement shows peaks indicating that the niobium titanium nitride has formed with a preferred fcc (111) orientation, with a smaller peak denoting the (200) orientation. The XRD spectra are similar for each of the tested samples. The length of  $a_0$  from the (111) peak results in  $4.39\pm 0.01$  and  $4.41\pm 0.01$  Å for the films deposited in nitrogen partial pressure of 14 or 20 % respectively.

RBS was used to analyse two niobium titanium nitride thin films to provide the elemental composition of the samples. The samples were deposited with either 18 or 20 % nitrogen partial pressure. The RBS measurement of the sample deposited in a partial pressure of 20 % nitrogen is shown in figure 8.10. The RBS measurement was performed by E. Alves and N.P. Barradas at Lisbon, Portugal, where the yellow data points are the raw data, the purple line was fitted to the data after the measurement and the grey lines relate to the deconvoluted signal from the elemental composition. The summary table in figure 8.10 describes how the titanium content remained constant but the niobium was replaced by nitrogen as its partial pressure was increased during deposition.

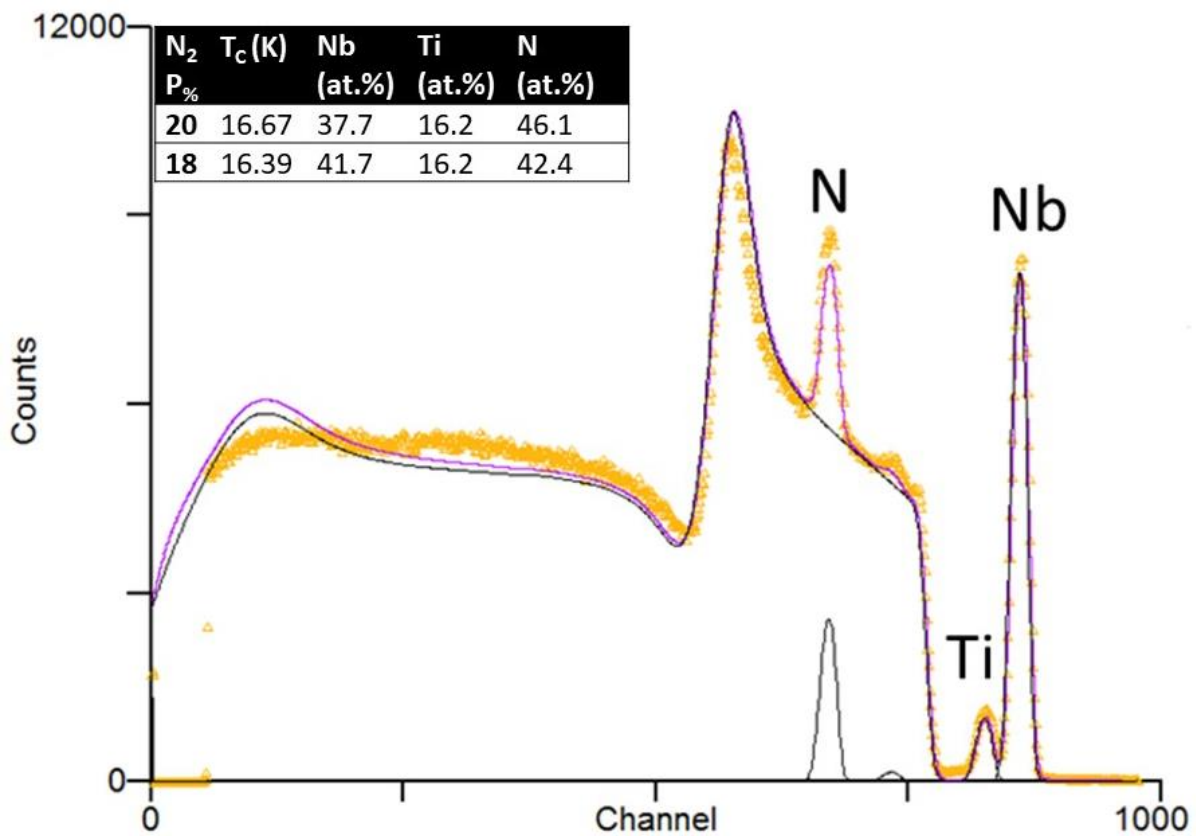


Figure 8.10. Rutherford backscattering spectroscopy measurement of a niobium titanium nitride thin film deposited with a niobium cathode current of 590 mA, a titanium cathode current of 960 mA and a nitrogen partial pressure of 20 %.  $T_c$  of the sample was  $16.67\pm 0.01$  K. RBS measurement was performed using a hydrogen beam with  $10^\circ$  angle of incidence,  $165^\circ$  scattering angle and  $25^\circ$  exit angle. Inset is a summary of two RBS measurements displaying the nitrogen partial pressure, N<sub>2</sub> P<sub>%</sub>,  $T_c$ , and at.% of niobium, titanium and nitrogen (measurement performed by E. Alves and N.P. Barradas, Lisbon, Portugal).

The results suggest that increasing the nitrogen content of the niobium titanium nitride thin films can result in a reduction in the normal state resistance. This effect has been reported before and was linked to a reduction in the number of nitrogen vacancies, hence a reduction in the number of defects [133]. However, there does not appear to be a strong correlation between normal state resistance and  $T_C$ . The samples with the largest normal state resistance at just above  $T_C$ , 19 and 14 m $\Omega$  respectively, were the samples with either no superconductivity or the smallest  $T_C$  of 8.95 K. However, there was very little difference in  $T_C$  for all other deposited samples, displaying a wide range of normal state resistances at just above  $T_C$  of 9 to 0.4 m $\Omega$ .

The two samples with measured lattice parameters were deposited with either low or high nitrogen partial pressure and showed that the lattice parameter was longest for the sample deposited in the larger nitrogen partial pressure. Similar studies have suggested that the lattice parameter will initially increase as the number of stoichiometric niobium titanium nitride grains increases within the thin film. However, there is always a threshold where the nitrogen content becomes so large that it is in excess and causes disorder through adjustments of the nitrogen atoms. Thus, the lattice parameter will rise proportionally with nitrogen content but there is a threshold where the resistivity of the sample begins to increase [133]. The normal state resistance of the samples deposited for this study decreased up to the largest tested nitrogen partial pressure suggesting that the nitrogen content did not reach optimal concentrations; this was confirmed by the RBS data. The stoichiometry for perfect niobium titanium nitride crystal would constitute 25 at.% of niobium, 25 at.% of titanium and 50 at.% of nitrogen. The closest to perfect composition from the measured films was 37.7 % niobium, 16.2% titanium and 46.1 % nitrogen for the sample with the largest  $T_C$  of  $16.67 \pm 0.01$  K.

The film with the largest  $T_C$  of 16.67 K had a thickness measured at 350 nm and therefore the resistivity of the sample could be calculated. The resistivity of the sample was  $45 \pm 7$   $\mu\Omega\text{cm}$  and was therefore considerably smaller than  $800 \pm 200$   $\mu\Omega\text{cm}$  as was observed for the niobium nitride film discussed in section 8.1. From figure 4.7, a  $T_C$  of 16.67 K and resistivity of  $45 \pm 7$   $\mu\Omega\text{cm}$  suggests an  $R_S$  of only 2 n $\Omega$  at a temperature of 4.2 K and frequency of 500 MHz. For comparison, niobium displays approximately 32 n $\Omega$  at 4.2 K and 500 MHz [87, 88]. This result suggests that niobium titanium nitride is a real alternative to niobium for SRF application at 4.2 K.

### **8.2.2. Varying the niobium or titanium cathode current**

Next, either the niobium or titanium cathode currents were varied whilst other deposition conditions remained constant, in the hope of achieving the correct stoichiometry required to increase  $T_C$  even further.

Films were deposited with a niobium cathode current that was varied between 510 and 590 mA with constant titanium current of 960 mA and constant nitrogen partial pressure of 20 %, followed by films deposited with a titanium current that was varied between 940 and 1020 mA with constant niobium current of 590 mA and 20 % nitrogen partial pressure. Pulse rates and off times remained like those described in section 8.2.1 for both the HiPIMS and pulsed DC power supplies.

The resistance versus temperature and  $T_c$  data is shown in figures 8.11 to 8.14. The range of measured DC resistances in the normal conducting state varied between 1.3 and 0.5 m $\Omega$  regardless of either niobium or titanium cathode current.  $T_c$  displayed little variation, between  $16.65\pm 0.01$  and  $16.70\pm 0.01$  K, for films deposited with niobium cathode currents between 510 and 590 mA.  $T_c$  varied between  $8.2\pm 0.01$  and  $16.67\pm 0.01$  K for films deposited with the range of tested titanium cathode currents.

The results showed that there was very little difference in the normal state resistance of all samples deposited with the constant nitrogen partial pressure of 20 %. This strengthens the argument from section 8.2.1 that the resistivity of niobium titanium nitride is largely dependent on the number of nitrogen vacancies present within the crystal lattice, or is affected by disorder brought about by displaced atoms if the nitrogen concentration becomes too large.

It was hoped that  $T_c$  could be increased above that of samples discussed in section 8.2.1 ( $16.67\pm 0.01$  K) by altering the niobium or titanium cathode current during deposition.  $T_c$  of  $16.64\pm 0.01$  -  $16.70\pm 0.01$  K occurred for a range of deposition parameters.  $T_c$  remained approximately the same for the films deposited at each tested niobium cathode current. However, there was a large range of  $T_c$  for the different titanium cathode currents which were tested. The results suggest that the  $T_c$  of niobium titanium nitride is more sensitive to changes in the titanium atom and ion arrival rates than for the niobium atom and ion arrival rates during deposition. An explanation for this phenomenon is that titanium is a good getter of nitrogen and therefore changes in the titanium ion and atoms arrival rate can also affect the arrival rates of nitrogen. Thus, altering the arrival rate of titanium atom and ions could alter the stoichiometry of the deposited films by more of an extent than changing the arrival rate of niobium atom and ions. However, changes in the nitrogen content would be expected to alter the normal state resistance of samples, which remained largely constant. Ideally more films should have been measured using the RBS to elucidate the relative stoichiometric changes from film to film but it was not possible to arrange further time on the machine.

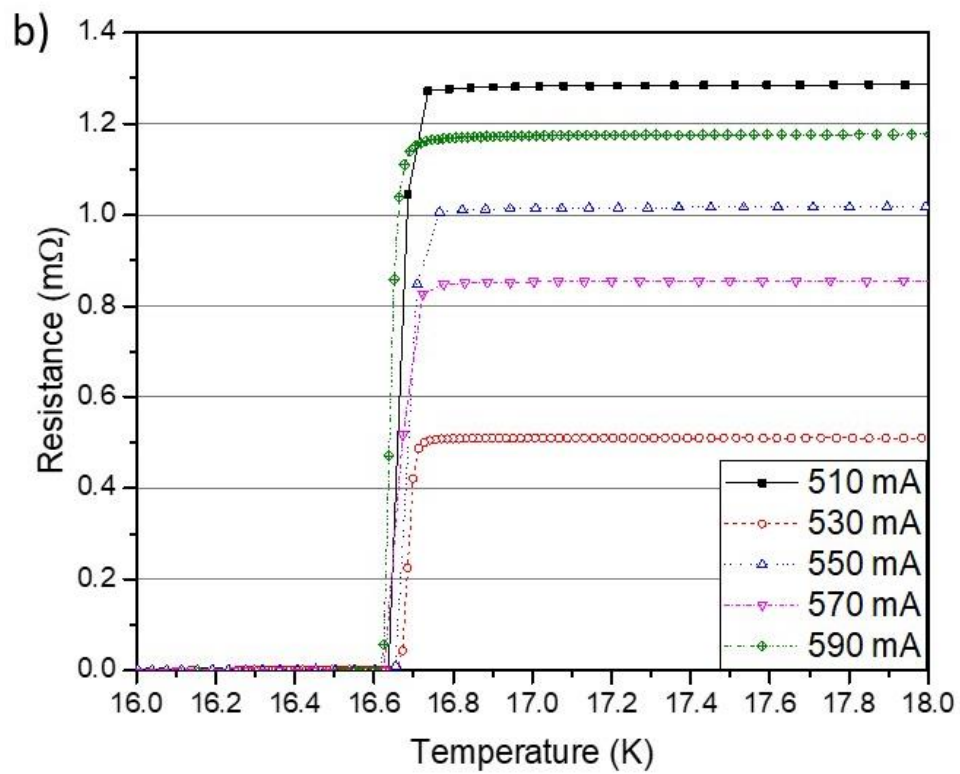
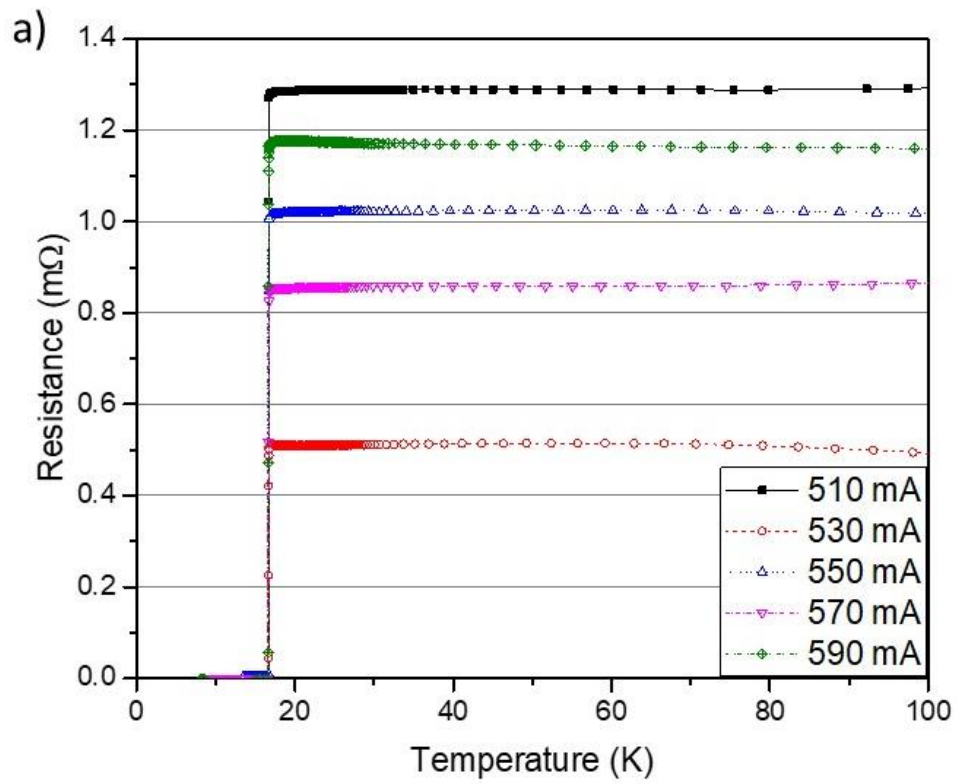


Figure 8.11. Resistance versus temperature profiles for niobium titanium nitride thin films deposited with a range of niobium cathode currents. a) displays the curve between 0 and 100 K whilst b) displays the superconducting transition.

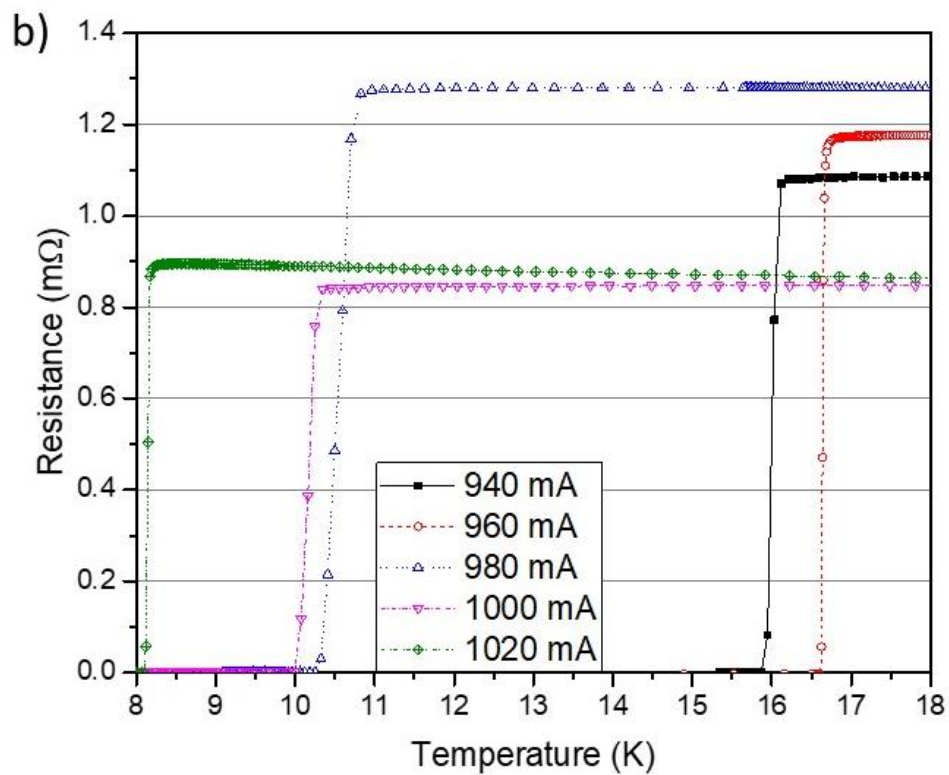
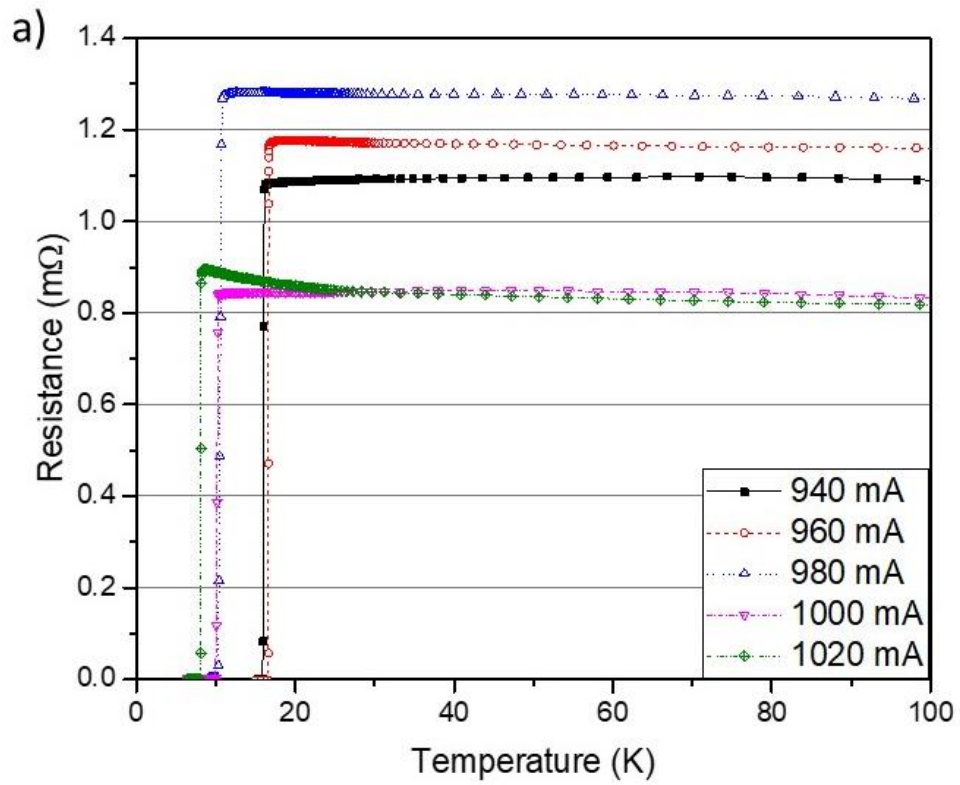


Figure 8.12. Resistance versus temperature profiles for niobium titanium nitride thin films deposited with a range of titanium cathode currents. a) displays the curve between 0 and 100 K whilst b) displays the superconducting transition.

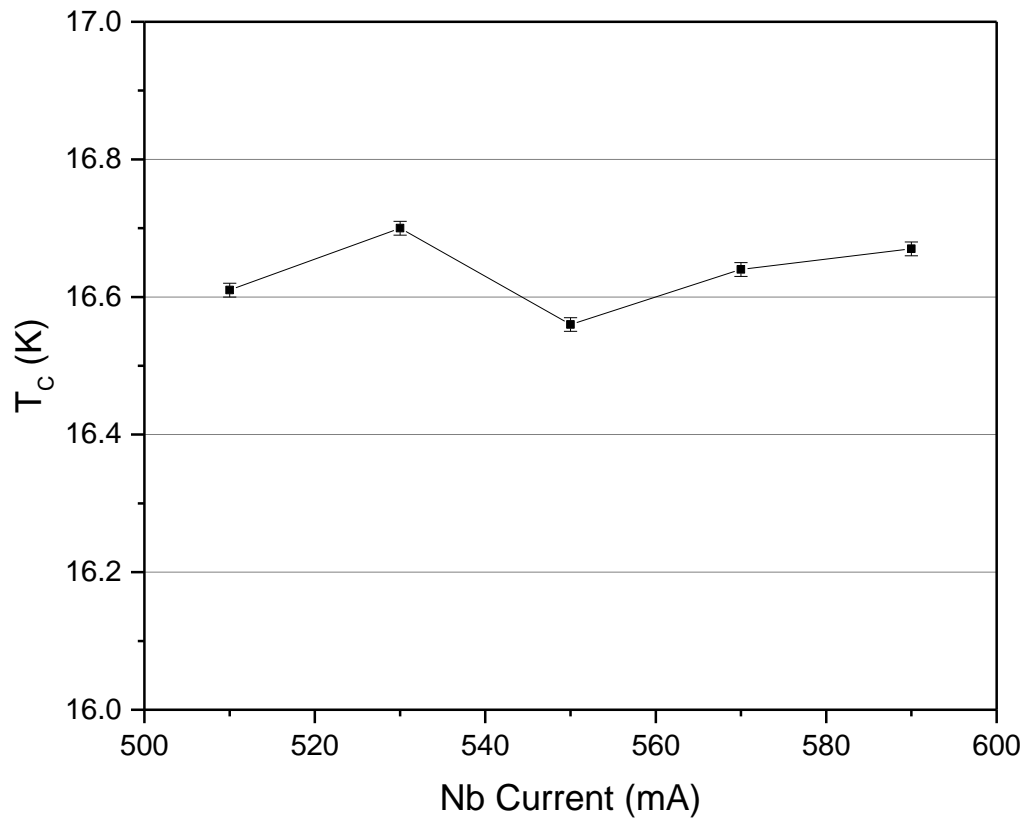


Figure 8.13. The  $T_c$  of niobium titanium nitride thin films with varying niobium cathode current during deposition.

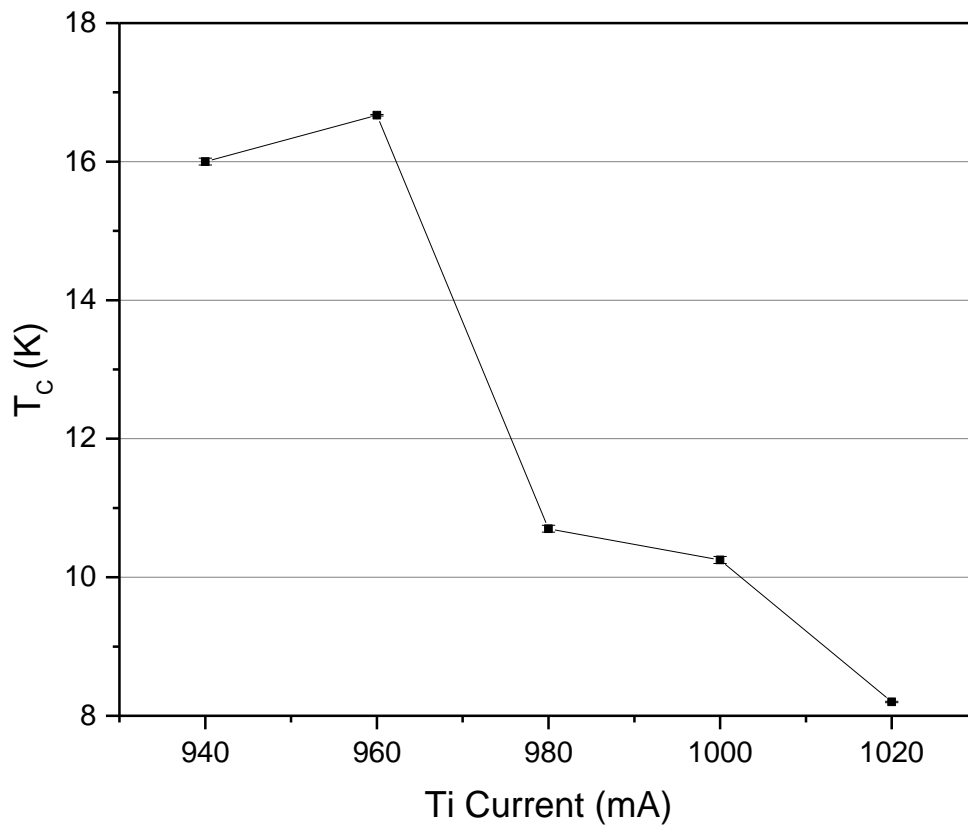


Figure 8.14. The  $T_c$  of niobium titanium nitride thin films with varying titanium cathode current during deposition.



## 9. Summary and future research

As already described, sputtered thin film SRF cavities suffer from a sharp  $Q$  slope. The reason for the onset of the sharp  $Q$  slope is, as yet, unknown. This study intended to improve the scientific understanding of the physical properties of superconducting thin films as a function of changing deposition process conditions in the hope that the knowledge could be used to better understand the  $Q$  slope. In particular, the study aimed to test the effects of substrate heating and an applied bias during HiPIMS deposition.

The study began with a short analysis of niobium films deposited by DC magnetron sputtering. DC magnetron sputtering produces small ion to atom arrival ratios of up to 5 %. However, an applied substrate bias had a significant effect on the physical properties of niobium films deposited by DC magnetron sputtering. Film grains were more densely packed together, displayed changes in the relative sizes of grazing incidence XRD peaks and had larger RRR when deposited with an applied bias of -50 V relative to a grounded substrate.

A HiPIMS discharge is known to produce more energetic niobium ions than occur for DC magnetron sputtering. The application of a substrate bias during HiPIMS deposition was expected to allow tuning of the physical properties of growing films by manipulation of the levels of ion bombardment. Thus, an experiment was devised which allowed to test the effects of both substrate heating and ion bombardment during HiPIMS deposition, as a function of a wide range of physical parameters.

Films deposited with a wide range of applied bias voltages onto as received polycrystalline copper substrate displayed the most repeatable and stable pinning properties for films deposited at 700 °C. The films deposited at 700 °C also displayed large RRR, had an enhanced resistance to the onset of DC magnetic flux penetration and displayed the smallest values of  $H_{c2}$ . The source of the listed properties of films deposited at 700 °C was assumed to be the formation of large niobium grains of up to 1 – 2 microns across. The origin of the large grain size was considered to be either; very high rates of diffusion and annealing of defects during film deposition at the high substrate temperature, or the physical properties of the substrate were altered at the high temperature, such as the removal of the surface oxide layer from the copper substrate and annealing of the copper substrate.

Further testing of films deposited onto copper substrate that was pre-annealed at 700 °C for 12 hours proved that the initial substrate conditions were the most important factor in deciding the physical properties of deposited niobium thin films. Films deposited at 500 °C onto pre-annealed copper substrate and with a wide range of applied bias voltages displayed larger RRR and similar DC magnetic properties to films deposited at 700 °C onto as received copper substrate.

An applied substrate bias was shown to have a significant influence on the properties of niobium thin films deposited by HiPIMS. With the most noticeable effects occurring for films deposited at room temperature. Results suggested that ion bombardment increases the rates of surface diffusion and defect annihilation up to a bias voltage of approximately -80 V. Increasing the applied substrate bias further resulted in ion bombardment that was too energetic and produced more random complex defects than were being annihilated. Thus, the investigation proved that it was possible to minimise the number of random complex defects that form in deposited niobium films by tuning the energy of bombarding ions. It should be stressed that a HiPIMS discharge can produce a range of target ion energies and that those energies will be affected by gas dynamics that are particular to a specific coating system. That said; it would be possible to find the specific bias requirements needed to reduce the numbers of random complex defects from deposited niobium films for any HiPIMS deposition facility, by following a similar systematic investigation to what has been presented here.

An unexplained “blistering” effect has been observed for a range of niobium thin films that were deposited at the higher substrate temperatures and at the larger applied substrate bias voltages that were tested. This effect is as yet unexplained. Observations of films in cross section did not show delamination of the film. Similarly, films did not exhibit delamination after testing with an adhesive tape. Further investigation is required to explain why the “blistering” effect is occurring and what effect it could have on thin films used in SRF application.

Niobium titanium nitride thin films were deposited successfully by dual HiPIMS/Pulsed DC magnetron sputtering. The niobium titanium nitride thin films had  $T_c$  up to 16.7 K with a normal state resistivity of  $45 \pm 7 \mu\Omega\text{cm}$ . The relatively small normal state resistivity suggests that the deposited niobium titanium nitride thin films may have smaller  $R_s$  than niobium at 4.2 K. Such a film may be effective if used in a SRF application as a monolayer or in an SIS multilayer.

It should be stressed that the main focus of this research project was on the development of niobium thin film coatings deposited by HiPIMS. The deposition of niobium titanium nitride was considered an extra addition and as such this part of the study was somewhat incomplete. This study tried to test the  $T_c$  of niobium titanium nitride thin films deposited by HiPIMS as a function of stoichiometry. However, the differences in stoichiometry were implied by the varied deposition parameters, but was not actually measured for every film. It is hoped that more of the deposited samples can be measured by RBS in the future to supplement the current dataset. Also, the effects of depositing from a single niobium titanium target should be tested and compared to the films deposited with two targets.

STFC intends to continue using HiPIMS to deposit other superconducting materials with  $T_C > T_C^{Nb}$  in the hope of producing films with small  $R_{BCS}$  at 4.2 K and which can be used within SIS multilayer films. The proposed materials are niobium germanium, niobium tin and vanadium silicon.

Finally, it was unfortunate that too few SRF measurements were performed to make meaningful comparisons between morphological, DC superconducting properties and the SRF properties of deposited films. A new test facility is in development at STFC that will allow flat 100 mm disks to be tested for  $R_S$  at 3.9 GHz. Similar films to those discussed in this report will be tested in the new facility once it is fully commissioned.

It is hoped that the wide range of niobium thin film properties that have been described in this report may help future researchers to eradicate the thin film  $Q$  slope, as has already been achieved for the  $Q$  slope of bulk niobium. For now, the DC magnetic behaviour that has been presented here implies that bulk niobium should display a sharper transition from the full Meissner state to no superconductivity, as a reaction to an increasing DC magnetic field, than has been observed for sputtered niobium thin films. Thus, the density of magnetic pinning centres must be larger for the sputtered niobium films than occurs within the bulk niobium. Unfortunately, this observation cannot be used to argue for or against any of the proposed  $Q$  drop mechanisms that were described in section 4.7.

## List of Publications

- S. Wilde, R. Valizadeh, O. B. Malyshev, G. B. G. Stenning, A. Hannah, S. Pattalwar, N. Pattalwar, N. P. Barradas, E. Alves and B. Chesca, "Physical vapour deposition of NbTiN thin films for superconducting RF cavities", in Proceedings of 8th International Particle Accelerator Conference, Copenhagen, Denmark, 2017.
- S. Wilde, R. Valizadeh, O. B. Malyshev, N. P. Barradas, E. Alves, G. B. G. Stenning, A. Hannah, S. Pattalwar and B. Chesca, "High power impulse magnetron sputtering of thin films for superconducting rf cavities", in Proceedings of 17th International conference on RF superconductivity, Whistler, Canada, 2015.
- S. Wilde, R. Valizadeh, O. B. Malyshev, G. B. G. Stenning, A. Hannah, D. O. Malyshev, S. Pattalwar and B. Chesca, "Physical vapour deposition of thin films for use in superconducting rf cavities," in Proceedings of the 6th international particle accelerator conference, Richmond, USA, 2015.
- S. Wilde, R. Valizadeh, O. B. Malyshev, A. Hannah, D. O. Malyshev, S. Pattalwar, G. B. G. Stenning and B. Chesca, "Development of thin films for superconducting rf cavities," in Proceedings of the 5th international particle accelerator conference, Dresden, Germany, 2014.



## 10. References

- [1] V. Arbert-Engels, C. Benvenuti, S. Calatroni, P. Darriulat, M. A. Peck, A. M. Valente and C. A. Van't Hof, "Superconducting niobium cavities, a case for the film technology," *Nuclear Instruments and Methods in Physics Research Section A: Accelerators, Spectrometers, Detectors and Associated Equipment*, vol. 463, no. 1 - 2, pp. 1 - 8, 2001.
- [2] C. Benvenuti, S. Calatroni, I. E. Campisi, P. Darriulat, M. A. Peck, R. Russo and A. M. Valente, "Study of the surface resistance of superconducting niobium films at 1.5 GHz," *Physica C: Superconductivity*, vol. 316, no. 3, 1999.
- [3] C. James, M. Krishnan, B. Bures, T. Tajima, L. Civale, R. Edwards, J. Spradlin and H. Inoue, "Superconducting Nb Thin Films on Cu for Applications in SRF Accelerators," *IEEE Transactions on Applied Superconductivity*, vol. 23, no. 3, 2013.
- [4] T. L. Hylton, A. Kapitulnik, M. R. Beasley, J. P. Carini, L. Drabek and G. Gruner, "Weakly coupled grain model of high-frequency losses in high T<sub>c</sub> superconducting thin films," *Applied physics letters*, vol. 53, no. 14, pp. 1343 - 1345, 1988.
- [5] B. Bonin and H. Safa, "Power dissipation at high fields in granular RF superconductivity," *Superconducting Science and Technology*, vol. 4, pp. 257 - 261, 1991.
- [6] C. Attanasio, L. Maritato and R. Vaglio, "Residual surface resistance of polycrystalline superconductors," *Physical Review B*, vol. 43, no. 7, pp. 6128 - 6131, 1991.
- [7] V. Palmieri and R. Vaglio, "Thermal contact resistance at the Nb/Cu interface as a limiting factor for sputtered thin film RF superconducting cavities," *Superconducting Science and Technology*, vol. 29, no. 1, p. 015004, 2016.
- [8] R. L. Geng, H. Padamsee, A. Seaman and V. D. Shemelin, "World record accelerating gradient achieved in a superconducting niobium RF cavity," in *Particle Accelerator Conference*, Knoxville, 2005.
- [9] A. Grassellino, A. Romanenko, D. Sergatskov, O. Melnychuk, Y. Trenikhina, A. Crawford, A. Rowe, M. Wong, T. Khabiboulline and F. Barkov, "Nitrogen and argon doping of niobium for superconducting radio frequency cavities: a pathway to highly efficient accelerating structures," *Superconducting Science and Technology*, vol. 26, pp. 1 - 6, 2013.
- [10] A. Gurevich, "Enhancement of rf breakdown field of superconductors by multilayer coating," *Applied Physics Letters*, vol. 88, p. 012511, 2006.
- [11] A. Anders, J. Andersson and A. Ehasarian, "High power impulse magnetron sputtering: Current-voltage-time characteristics indicate the onset of sustained self-sputtering," *Journal of applied physics*, vol. 102, p. 113303, 2007.
- [12] A. Anders, "Generalised structure zone diagram," *Thin solid films*, vol. 518, p. 4087, 2010.

- [13] H. K. Onnes, "Further experiments with liquid helium. C. On the change of electric resistance of pure metals at very low temperatures, etc. IV. The resistance of pure mercury at helium temperatures," vol. 120b, 2011.
- [14] J. Bardeen, L. N. Cooper and J. R. Schrieffer, "Theory of Superconductivity," *Physical Review*, vol. 108, p. 1175, 1957.
- [15] W. Buckel and R. Kleiner, *Superconductivity. Fundamentals and Applications.*, Germany, : WILEY-VCH, 2004.
- [16] P. Esquinazi, A. Setzer, D. Fuchs, Y. Kopelevich, E. Zeldov and C. Assmann, "Vortex avalanches in Nb thin films: Global and local magnetization measurements," *Phys.Rev.B*, vol. 60, no. 17, pp. 12454-12461, Nov 1999.
- [17] A. M. Valente-Feliciano, "Superconducting RF materials other than bulk niobium: a review," *Superconducting Science and Technology*, vol. 29, p. 113002, 2016.
- [18] H. Padamsee, "The science and technology of superconducting cavities for accelerators," *Superconductor Science and Technology*, vol. 14, pp. R28 - R51, 2001.
- [19] F. Lockwood Estrin, *The study of spokes in HiPIMS discharges with applications to the production of superconducting thin films*, Liverpool: University of Liverpool, 2016.
- [20] D. R. Pellemounter, D. J. Christie and B. D. Fries, "Pulsed DC Power for Magnetron Sputtering: Strategies for Maximising Quality and Flexibility," Chicago, USA, 2014.
- [21] V. Kouznetsov, K. Macak, J. M. Schneider, U. Helmersson and I. Petrov, "A novel pulsed magnetron sputter technique utilizing very high target power densities," *Surface and Coatings Technology*, vol. 122, no. 2 - 3, pp. 290-293, 12/15 1999.
- [22] J. E. Mahan, *Physical Vapour Deposition of Thin Films*, John Wiley & Sons, 2000.
- [23] P. Poolcharuansin and J. W. Bradley, "Short and long term plasma phenomena in a HiPIMS discharge," *Plasma Sources Science and Technology*, vol. 19, p. 025010, 2010.
- [24] N. Brenning, I. Axnas, M. a. Raadu, D. Lundin and U. Helmersson, "A bulk plasma model for DC and HiPIMS magnetrons," *Plasma Sources Science and Technology*, vol. 17, no. 4, p. 045009, 2008.
- [25] K. Macak, V. Kouznetsov, J. Schneider, U. Helmersson and I. Petrov, "Ionized sputter deposition using an extremely high plasma density pulsed magnetron discharge," *Journal of Vacuum Science & Technology A: Vacuum, Surfaces, and Films*, vol. 18, p. 1533, 2000.
- [26] J. Bohlmark, J. Alami, C. Christou, P. Ehasarian and U. Helmersson, "Ionisation of sputtered metals in high power pulsed magnetron sputtering," *Journal of Vacuum Science & Technology A: Vacuum, Surfaces, and Films*, vol. 18, 2005.
- [27] A. P. Ehasarian, W. D. Munz, L. Hultman, U. Helmersson and I. Petrov, "High power pulsed magnetron sputtered CrN films," *Surface and Coatings Technology*, Vols. 163 - 164, pp. 267 - 272, 2003.

- [28] A. D. Palczewski, G. Ciovati, R. L. Geng and Y. Li, "Exploration of material removal rate of SRF elliptical cavities as a function of media type and cavity shape on niobium and copper using centrifugal barrel polishing (CBP)," in *SRF*, Paris, 2013.
- [29] M. Tauhiduzzaman and S. C. Veldhuis, "Surface generation in ultra precision single point diamond turning of aluminum," in *Proceedings of the American Society for Precision Engineering Annual Meeting*, 2008.
- [30] V. Palmieri, V. L. Ruzinov, S. Y. Stark and F. Stivanello, "Electropolishing of seamless 1.5 GHz OFHC copper cavities," in *Workshop on RF superconductivity*, Gif-sur-Yvette, 1995.
- [31] V. Palmieri, F. Stivanello and S. Y. Stark, "Besides the standard niobium bath chemical polishing," in *Workshop on RF superconductivity*, Tsukuba, 2001.
- [32] R. Russo, "Quality measurement of niobium thin films for Nb / Cu superconducting RF cavities," *Measurement Science and Technology*, vol. 18, pp. 2299 - 2313, 2007.
- [33] D. Beringer and C. Reece, "Anomalous morphological scaling in epitaxial niobium thin films on MgO (001)," in *Proceedings of IPAC*, 2014.
- [34] E. Chiaveri, "Production by industry of a large number of superconducting cavities," *Part.Accel.*, vol. 53, no. CERN-SL-95-122-RF-2, pp. 253-268, 1995.
- [35] E. Chiaveri, "Superconducting RF Cavities," *IEEE Trans.Appl.Supercond.*, vol. 13, no. CERN-SL-2002-052-ECT, pp. 1199-1204, 2002.
- [36] D. M. Mattox, "Substrate preparation for thin film deposition - a survey," *Thin Solid Films*, vol. 124, pp. 3 - 10, 1985.
- [37] J. A. Venables, *Introduction to Surface and Thin Film Processes*, Cambridge: Cambridge University Press, 2003.
- [38] D. L. Smith, *Thin Film Deposition Principles and practices*, Boston: McGraw Hill, 1995.
- [39] H. Luth, *Solid Surfaces, Interfaces and Thin Films*, New York: Springer, 2010.
- [40] J. D. Weeks and G. H. Gilmer, "Dynamics in crystal growth," *Advances in chemical physics*, vol. 40, pp. 157 - 227, 1979.
- [41] B. A. Movchan and A. V. Demchishin, *Fiz. Met. Metalloved*, vol. 28, p. 653, 1969.
- [42] A. Anders, "A structure zone diagram including plasma-based deposition and ion etching," *Thin Solid Films*, vol. 518, no. 15, pp. 4087 - 4090, 2010.
- [43] R. F. Bunshah, *Handbook of Hard Coatings*, New York: Noyes, 2001.
- [44] I. Petrov, P. B. Barna, L. Hultman and J. E. Greene, "Microstructural evolution during film growth," *Journal of vacuum science and technology*, vol. 25, no. 5, p. S117, 2003.
- [45] M. Peiniger and H. Piel, "A superconducting Nb<sub>3</sub>Sn Coated Multicell Accelerating Cavity," *IEEE Transactions on Nuclear Science*, vol. 32, no. 5, pp. 3610 - 3612, 1985.

- [46] E. Sarhammar, E. Stradberg, N. Martin and T. Nyberg, "Sputter rate distribution and compositional variations in films sputtered from elemental and multi-elemental targets at different pressures," *International Journal of Materials Science and Applications*, vol. 3, no. 2, pp. 29-36, 2014.
- [47] G. Ciovati, P. Dhakal and A. Gurevich, "Decrease of the surface resistance in superconducting niobium resonator cavities by the microwave field," *Applied Physics Letters*, vol. 104, p. 092601, 2014.
- [48] H. Padamsee, J. Knoblock and T. Hays, *RF Superconductivity for Accelerators*, New York: Wiley, 1998.
- [49] C. Benvenuti, S. Calatroni, I. E. Campisi, P. Darriulat, M. A. Peck and A. M. Valente, "Influence of the nature of the substrate on the growth of superconducting niobium films," CERN internal report, Geneva, Switzerland, 2000.
- [50] C. Benvenuti, S. Calatroni, P. Durriulat, M. A. Peck and A. M. Valente, "Fluxon pinning in niobium films," *Physica C*, vol. 351, p. 429, 2001.
- [51] C. Benvenuti, S. Calatroni, M. Hakovirta, H. Neupert, M. Prada and A. M. Valente, "CERN studies on niobium-coated 1.5 GHz copper cavities," in *IPAC*, Tsukuba, 2001.
- [52] J. Spradlin, A. M. Valente-Feliciano, H. Phillips, C. Reece, X. Zhao, D. Gu and K. Seo, "Structural properties of niobium thin films deposited on metallic substrates," in *Proceedings of SRF*, 2011.
- [53] W. Roach, D. Beringer, J. Skuza, W. Oliver, C. Clavero, C. Reece and R. Lukaszew, "Niobium thin film deposition studies on copper surfaces for superconducting radio frequency cavity applications," *Physical Review Special Topics-Accelerators and Beams*, vol. 15, no. 6, p. 062002, 2012.
- [54] N. Jecklin, S. Calatroni, B. Delaup, L. Ferreira, I. Mondino, A. Sublet, M. Therasse and W. Venturini Desolaro, "Niobium coatings for the HIE-ISOLDE QWR superconducting accelerating cavities," in *Proceedings of SRF 2013*, Paris, 2013.
- [55] A. M. Valente-Feliciano, "Nb films: Substrates, nucleation & crystal growth," in *Proceedings of SRF 2011*, Chicago, 2011.
- [56] X. Zhao, L. Phillips, C. E. Reece, K. Seo, M. Krishnan and E. Valderrama, "Twin symmetry texture of energetically condensed niobium thin films on sapphire substrate (a-plane Al<sub>2</sub>O<sub>3</sub>)," *Journal of Applied Physics*, vol. 110, p. 033523, 2011.
- [57] C. Surgers, C. Strunk and H. V. Lohneysen, "Effect of substrate temperature on the microstructure of thin niobium films," *Thin Solid Films*, vol. 239, pp. 51 - 56, 1994.
- [58] M. Krishnan, E. Valderrama, B. Bures, K. Wilson-Elliott, X. Zhao, L. Phillips, A.-M. Valente-Feliciano, J. Spradlin, C. Reece and K. Seo, "Very high residual resistivity ratios of heteroepitaxial superconducting niobium films on MgO substrates," *Superconductor Science and Technology*, vol. 24, no. 11, p. 115002, 2011.

- [59] C. Benvenuti, P. Bernard, D. Bloess, G. Cavallari, E. Chiaveri and E. Hachel, "Superconducting niobium sputter-coated copper cavity modules for the LEP energy upgrade," in *Proceedings of PAC*, 1991.
- [60] D. Bloess, "Sputter-coated superconducting RF cavities for LEP: technological challenge," *Vacuum*, vol. 47, pp. 597 - 600, 1996.
- [61] E. Chiaveri and W. Weingarten, "Industrial production of superconducting niobium sputter coated copper cavities for LEP," in *Proceedings of the Sixth Workshop on RF Superconductivity*, Virginia, USA, 1993.
- [62] S. Calatroni, "20 Years of experience with the Nb/Cu technology for superconducting cavities and perspectives for future developments," *Physica C*, vol. 441, pp. 95 - 101, 2006.
- [63] R. Russo and S. Sgobba, "Influence on coating temperature on niobium films," in *Proceedings of the workshop on RF superconductivity*, Padova, 1997.
- [64] C. Benvenuti, S. Calatroni, P. Darriulat, A. M. Valente and C. A. Van't Hof, "Study of the Residual Resistance of Superconducting Niobium Films at 1.5 GHz," in *Proceedings of the 1999 Workshop on RF Superconductivity*, New Mexico, 1999.
- [65] V. Palmieri and R. Vaglio, "Thermal contact resistance at the Nb/Cu interface as a limiting factor for sputtered thin film RF superconducting cavities," *Superconducting science and technology*, vol. 29, p. 015004, 2015.
- [66] A. M. Porcellato, S. Stark, V. Palmieri, L. Bertazzo, A. Capuzzo, F. Stivanello, A. Beltramin, T. Contran and M. De Lazzari, "Completion of ALPI medium beta section upgrading," in *Proceedings of 11th Workshop on RF Superconductivity*, DESY, 2003.
- [67] A. Sublet, I. Aviles Santillana, B. Bartova, S. Calatroni, N. Jecklin, I. Mondino, M. Therasse, W. Venturini Delsolaro and P. Zhang, "Nb coated HI-ISOLDE QWR superconducting accelerating cavities: from process development to series production," in *Proceedings of IPAC 2014*, Dresden, 2014.
- [68] G. Lanza, S. Calatroni, L. Marques Antunes Ferreira, A. Gustafsson, M. Pasini, P. Trilhe and V. Palmieri, "The HIE-ISOLDE superconducting cavities: surface treatment and niobium thin film coating," in *Proceedings of SRF 2009*, Berlin, 2009.
- [69] M. M. M. Bilek and D. R. McKenzie, "A comprehensive model of stress generation and relief processes in thin films deposited with energetic ions," *Surface and Coatings Technology*, vol. 200, no. 14 - 15, pp. 4345 - 4354, 2006.
- [70] D. K. Brice, J. Y. Tsao and S. T. Picraux, "Partitioning of ion-induced surface and bulk displacements," *Nuclear Instruments and Methods B*, vol. 44, pp. 68 - 78, 1989.
- [71] L. Hultman and J. E. Sundgren, *Handbook of Hard Coatings*, Noyes, 2001.
- [72] A. Anders, "Self-Sputtering Far above the Runaway Threshold: An Extraordinary Metal-Ion Generator," *Physical Review Letters*, vol. 102, no. 4, p. 045003, 2009.

- [73] A. Hecimovic and A. P. Ehasarian, "Temporal evolution of the ion fluxes for various elements in HiPIMS plasma discharge," *IEEE Transactions on plasma science*, vol. 39, no. 4, p. 1154, 2011.
- [74] A. Anders and G. Y. Yushkov, "Plasma "anti-assistance" and "self-assistance" to high power impulse magnetron sputtering," *Journal of Applied Physics*, vol. 105, no. 7, p. 073301, 2009.
- [75] A. Anders, "Discharge physics of high power impulse magnetron sputtering," *Surface and Coatings Technology*, vol. 205, no. 2, pp. S1 - S9, 2011.
- [76] G. Terenziani, S. Calatroni and A. P. Ehasarian, "Nb Coatings for superconducting RF applications by HiPIMS," CERN, Geneva, 2013.
- [77] G. Terenziani, S. Calatroni, T. Junginger, I. A. Santillana and A. P. Ehasarian, "Nb Coating developments with HiPIMS for SRF applications," in *Proceedings of SRF*, Paris, 2013.
- [78] T. Junginger, "Field dependant surface resistance of niobium on copper cavities," *Physical review special topics - accelerators and beams*, vol. 18, p. 072001, 2015.
- [79] G. Rosaz, G. Terenziani, D. Sonato, S. Calatroni, A. Ehasarian, T. Junginger and M. Taborelli, "Biased HiPIMS technology for superconducting RF accelerating cavities coating," in *6th International Conference on HiPIMS*, Braunschweig, 2015.
- [80] G. Rosaz, K. Ilyina, S. Calatroni, W. Vollenberg, A. Sublet, F. Leaux and D. Richter, "A15 materials thin films and HiPIMS progress at CERN for SRF cavities," in *EuCARD-2 3rd Annual WP12 Meeting*, Daresbury Laboratory, 2016.
- [81] A. Anders, R. J. Mendelsberg, S. Lim, M. Mentink, J. L. Slack, J. G. Wallig, A. V. Nollau and G. Y. Yushkov, "Deposition of niobium and other superconducting materials with high power impulse magnetron sputtering: concept and first results," in *Proceedings of SRF 2011*, Chicago, 2011.
- [82] A. Anders, "Atomic scale heating in cathodeic arc plasma deposition," *Applied Physics Letters*, vol. 80, no. 6, pp. 1100 - 1102, 2002.
- [83] J. Langner, R. Mirowski, M. J. Sadowski, P. Strzyzewski, J. Witkowski, S. Tazzari, L. Catani, A. Cianchi, J. Lorkiewicz and R. Russo, "Deposition of superconducting niobium films for RF cavities by means of UHV cathodic arc," *Vacuum*, vol. 80, no. 11 - 12, pp. 1288 - 1293, 2006.
- [84] G. Wu, A. M. Valente, H. L. Phillips, H. Wang, A. T. Wu, T. J. Renk and P. Provencio, "Studies of niobium thin film produced by energetic vacuum deposition," *Thin solid films*, vol. 489, pp. 56 - 62, 2005.
- [85] A. M. Valente-Feliciano, G. Ereemeev, C. Reece, J. Spradlin, S. Aull and T. Proslie, "Material quality & srf performance of Nb films grown on Cu via ECR plasma energetic condensation," in *SRF*, Whistler, 2015.
- [86] H. Ji, G. S. Was, J. W. Jones and N. R. Moody, "Effect of ion bombardment on in-plane texture, surface morphology, and microstructure of vapor deposited Nb thin films," *Journal of applied physics*, vol. 81, no. 10, pp. 6754 - 6761, 1997.

- [87] A. M. Valente-Feliciano, *SRF Materials other than niobium*, Beijing: 13th International Workshop on RF Superconductivity, 2007.
- [88] V. Palmieri, "New materials for superconducting radiofrequency cavities," in *The 10th Workshop on RF Superconductivity*, Tsukuba, 2001.
- [89] A. Sublet, S. Aull, B. Bartova, S. Calatroni, T. Richard, G. Rosaz, M. Taborelli, M. Therasse, W. Venturini Delsolaro and P. Zhang, "Developments on SRF coatings at CERN," in *Proceedings of SRF*, Whistler, Canada, 2015.
- [90] P. Fabbriatore, P. Fernandes, G. C. Gualco, F. Merlo, R. Musenich and R. Parodi, "Study of niobium nitrides for superconducting rf cavities," *Journal of applied physics*, vol. 66, p. 5944, 1989.
- [91] A. Nigro, G. Nobile, V. Palmieri, G. Rubino and R. Vaglio, "Superconducting and normal state properties of niobium-nitride thin films," *Physica Scripta*, vol. 38, no. 3, pp. 483 - 485, 1988.
- [92] R. Di Leo, A. Nigro, G. Nobile and R. Vaglio, "Niobium-titanium nitride thin films for superconducting rf accelerating cavities," *Journal of Low Temperature Physics*, vol. 78, no. 1 - 2, pp. 41 - 50, 1990.
- [93] M. Marino, "Study of NbTiN coatings by reactive magnetron sputtering for the production of 1.5 GHz accelerating cavities," in *Proceedings of the 8th Workshop on RF Superconductivity*, Padova, 1997.
- [94] A. Gurevich, "Maximum screening field of superconducting multilayer structures," *AIP Advances*, vol. 5, p. 017112, 2015.
- [95] A. Andreone, A. Cassinese, A. DiChiara, M. Salluzzo, R. Vaglio, C. Attanasio and L. Maritato, "Surface impedance measurements of superconductor V3Si films by a microstrip resonator technique," *Journal of Applied Physics*, vol. 78, no. 3, p. 1862, 1995.
- [96] C. Buzea and T. Yamashita, "Review of the superconducting properties of MgB<sub>2</sub>," *Superconducting Science and Technology*, vol. 14, pp. R115 - R146, 2001.
- [97] X. X. Xi, A. V. Pogrebnyakov, S. Y. Xu, K. Chen, Y. Cui, E. C. Maertz, C. G. Zhuang, Q. Li, D. R. Lamborn, J. M. Redwing, Z. K. Liu, A. Soukiassian, D. G. Schlom, X. J. Weng, E. C. Dickey, Y. B. Chen, W. Tian, X. Q. Pan, S. A. Cybart and R. C. Dynes, "MgB<sub>2</sub> thin films by hybrid physical-chemical vapour deposition," *Physica C*, vol. 456, pp. 22 - 37, 2007.
- [98] A. Gurevich, "Enhancement of rf breakdown field of superconductors by multilayer coating," *Applied Physics Letters*, vol. 88, no. 1, pp. 012511-012511-3, 2006.
- [99] T. Kubo, Y. Iwashita and T. Saeki, "Radio-frequency electromagnetic field and vortex penetration in multilayered superconductors," *Applied Physics Letters*, vol. 104, p. 032603, 2014.
- [100] A. M. Valente - Feliciano, *Development of SRF monolayer / multilayer thin film materials to increase the performance of SRF accelerating structures beyond bulk Nb*, Paris: Universite Paris Sud - Paris XI, 2014.

- [101] A. Grassellino, A. Romanenko, D. Sergatskov, O. Melnychuk, Y. Trenikhina, A. Crawford, A. Rowe, M. Wong, T. Khabiboulline and F. Barkov, "Nitrogen and argon doping of niobium for superconducting radio frequency cavities: a pathway to highly efficient accelerating structures," arXiv.org, 2013.
- [102] T. L. Hylton, A. Kapitulnik and M. R. Beasley, "Weakly coupled grain model of high-frequency losses in high T<sub>c</sub> superconducting thin films," *Applied physics letters*, vol. 53, p. 1343, 1988.
- [103] B. Bonin and H. Safa, "Power dissipation at high fields in granular RF superconductivity," *Superconducting science and technology*, vol. 4, pp. 257 - 261, 1991.
- [104] C. Attanasio, L. Maritato and R. Vaglio, "Physical Review B," vol. 43, 1991.
- [105] C. Benvenuti, S. Calatroni, I. E. Campisi, P. Darriulat, M. A. Peck, R. Russo and A. M. Valente, "IEEE Transactions of applied superconductivity," vol. 9, 1999.
- [106] I. O. Kulik and V. Palmieri, "Theory of Q degradation and nonlinear effects in Nb-coated superconducting cavities," *Particle accelerators*, vol. 60, p. 257, 1998.
- [107] B. E. Warren, *X-Ray Diffraction*, Reading: Addison - Wesley, 1969.
- [108] A. L. Patterson, "The Scherrer Formula for X-Ray Particle Size Determination," *Phys.Rev.*, vol. 56, no. 10, pp. 978-982, Nov 1939.
- [109] M. Chabinyč, "Stanford Synchrotron Radiation Laboratory Material Scattering," 28 June 2010. [Online]. Available: <http://ssrl.slac.stanford.edu/materialscatter/scatter-grazing.html>. [Accessed 23 September 2017].
- [110] Oxford Instruments, *EBSD Explained*, 2015.
- [111] J. F. Moulder, W. F. Stickle, P. E. Sobol and K. D. Bomben, *Handbook of X-ray Photoelectron Spectroscopy*, Chigasaki: Physical Electronics Inc., 1995.
- [112] B. Hafner, "Energy dispersive spectroscopy on the SEM: a primer," University of Minnesota, Minnesota.
- [113] F. Paszti, A. Kotai, M. Jaksic and S. Fazinic, *Instrumentation for PIXE and RBS*, Vienna: IAEA, 2000.
- [114] PHYWE SYSTEME GMBH, "Physics Laboratory Experiments".
- [115] Quantum Design, *Magnetic Property Measurement System SQUID VSM User's Manual*, San Diego: Quantum Design, 2009.
- [116] M. Bahte, F. Herrmann and P. Schmuser, "Magnetisation and susceptibility measurements on niobium samples for cavity production," in *Workshop on RF Superconductivity*, Padova, 1997.
- [117] Pfeiffer, *Vacuum Technology Book Volume II*, Berlin: Pfeiffer Vacuum GmbH, 2013.
- [118] W. Singer, A. Ermakov and X. Singer, "RRR - Measurement Techniques on High Purity Niobium," DESY, 2010.

- [119] A. M. Valente-Feliciano, "HiPIMS: A new generation of film deposition techniques for SRF applications," in *SRF*, Paris, 2013.
- [120] L. van Loyen, D. Elefant, V. Palmieri, W. Venturini and J. Halbritter, "Topography and electrical properties of sputtered niobium films," in *Workshop on RF Superconductivity*, Abano Terme, 1997.
- [121] J. Colt, K. Mahadevan, B. Bures and T. Tajima, "Superconducting Nb Thin Films on Cu for Applications in SRF Accelerators," *IEEE Transactions on Applied Superconductivity*, vol. 23, no. 3, p. 2300205, 2013.
- [122] X. Zhao, J. Spradlin, A. M. Valente-Feliciano, L. Phillips and C. E. Reece, "Energetic condensation growth of Nb thin films," *Physical Review Special Topics - Accelerators and Beams*, vol. 15, p. 032001, 2012.
- [123] F. Lockwood Estrin, *Private Communication*, 2015.
- [124] M. C. Burton, M. R. Beebe, K. Yang, R. A. Lukaszew, A. M. Valente-Feliciano and C. Reece, "Superconducting NbTiN thin films for superconducting radio frequency accelerator cavity applications," *Journal of Vacuum Science & Technology A*, vol. 34, p. 021518, 2016.
- [125] R. Kleiner and W. Buckel, *Superconductivity*, Weinheim: Wiley-VCH, 2016.
- [126] P. Esquinazi, A. Setzer, D. Fuchs, Y. Kopelevich, E. Zeldov and C. Assmann, "Vortex avalanches in Nb thin films: Global and local magnetization measurements," *Physical Review B*, vol. 60, p. 12454, 1999.
- [127] R. B. Goldfarb, L. F. Goodrich, T. Pyon and E. Gregory, "Suppression of Flux Jumps in Marginally Stable Niobium-Tin Superconductors," *IEEE Transactions on Applied Superconductivity*, vol. 11, pp. 3679 - 3682, 2001.
- [128] A. A. Zhukov, G. K. Perkins, V. Yu, V. Bugoslavsky and A. D. Caplin, "Geometrical locking of the irreversible magnetic moment to the normal of a thin-plate superconductor," *Physical Review B*, pp. 2809 - 2819, 1997.
- [129] W. M. Roach, D. B. Beringer, J. R. Skuza, W. A. Oliver, C. Clavero, C. E. Reece and R. A. Lukaszew, "Niobium thin film deposition studies on copper surfaces for superconducting radio frequency cavity applications," *Physical Review Special Topics - Accelerators and Beams*, vol. 15, p. 062002, 2012.
- [130] H. Padamsee, *RF Superconductivity*, Wiley, 2009.
- [131] J. T. Maniscalco, D. L. Hall and M. Liepe, "RF Performance studies of thin-film superconductors using a sample host cavity," in *Proceedings of IPAC*, Richmond, 2015.
- [132] A. M. Valente-Feliciano, "New Materials for SRF Cavities," in *SRF Materials Workshop*, 2007.
- [133] K. Makise, H. Terai, M. Takeda, Y. Uzawa and Z. Wang, "Characterization of NbTiN Thin Films Deposited," *IEEE TRANSACTIONS ON APPLIED SUPERCONDUCTIVITY*, vol. 21, no. 3, pp. 139 - 142, 2011.

